Enabling Techniques for Future Broadband High Speed Wireless Communications

vorgelegt von M. Sc.
Jian Luo
aus Guangdong, VR China

von der Fakultät IV - Elektrotechnik und Informatik
der Technischen Universitt Berlin
zur Erlangung des akademischen Grades

Doktor der Ingenieurwissenschaften
- Dr.-Ing.-

genehmigte Dissertation

Promotionsausschuss:

Vorsitzender: Prof. Dr.-Ing. Adam Wolisz
Berichter: Prof. Dr.-Ing. Hans-Joachim Grallert
Berichter: Prof. Dr. Mikko Valkama (Tampere University of Technology, Finnland)
Berichter: Prof. Dr. Andreas Springer (Johannes Kepler Universität Linz, Österreich)

Tag der wissenschaftlichen Aussprache: 01. Feb. 2012

Berlin 2012
D 83

To my parents

Acknowledgements

The research work for this PhD thesis was carried out during the years 2007-2011 at the Wireless Communication and Network department (WN, earlier Broadband Mobile Communication department, BM) of Fraunhofer Heinrich-Hertz-Institut (HHI), Berlin. This place has provided me excellent conditions and great atmosphere for the scientific research. Moreover, Berlin University of Technology (TU Berlin) has provided me the chance for PhD study.

First of all, I would like to thank Prof. Holger Boche. Although he has left HHI and TU Berlin in 2010, it was him who has invited me to start the research work in wireless communications. I owe my deepest gratitude to Dr. Andreas Kortke and Dr. Wilhelm Keusgen, who lead my research group in HHI. They have guided me into the research world of wireless communications and have been abundantly helpful. Their continuous encouragement, inspiration and support have led to the valuable results of this thesis.

I am very grateful to Prof. Hans-Joachim Grallert, Prof. Mikko Valkama and Prof. Andreas Springer for taking their valuable time to supervise this thesis and providing invaluable comments on my research work. Especially, I would like to thank Prof. Mikko Valkama again for visiting HHI in 2009 and for giving me the chance to visit his research group in Tampere, Finland in 2011. These are very precious experience to me, which helped to extend my knowledge and knowhow.

In addition, I would like to thank my colleagues Michael Peter, Benjamin Schubert and Jacek Liszewski for the very nice collaboration in project works and their support. Furthermore, I would like to express my special thanks to our department head, Dr. Thomas Haustein, as well as all other colleagues in the whole WN department of HHI, since they are always kind and helpful. Because of them, the working environment at HHI is very comfortable.

Finally, I would like to express my deepest thanks to my whole family in China, especially my parents and my grandma, and to Xiaodan Wu for their continuous love and support.

Berlin, Oct. 29. 2011

Jian Luo

Zusammenfassung

Diese Dissertation beschäftigt sich mit der Herausforderung der sehr schnell wachsenden Datenrate-Anforderungen in zukünftigen drahtlosen Kommunikationssystemen. Dabei liegt der Schwerpunkt auf Kompensierung von RF-Fehlern und Systemdesign. Zwei Anwendungsbereiche wurden betrachtet: der zellulare Mobilfunk und das drahtlose lokale Netzwerk (WLAN).

Im zellularen Mobilfunk wurde das Konzept von Multi-Band- und Multi-Standard-Basis-Stationen (BS) diskutiert. Solche BS ermöglicht die Beherrschung der Koexistenz verschiedener Technologie-Generationen (2G/3G/4G) mit angemessenen Kosten. Für die Realisierung solcher BS ist die RF-Fehler-Kompensierung benötigt, insbesondere für den Sender mit Direktmischarchitektur. In dieser Dissertation wurden praktische Konzepte für die digitale Kompensierung der frequenz-selektiven I/Q-Fehler und Modulator-DC-Offset-Fehler im Sender solcher BS untersucht. Sowohl die digitale Kompensierungsschaltung als auch die Parameterschätz- und Tracking-Verfahren wurden entwickelt. Die entsprechende RF-Fehler-Kompensierung ist flexibel, standard-unabhängige und benötigt wenig Komplexität. Die Effektivität und die Vorteile der entwickelten Verfahren wurden sowohl durch numerische Simulationen als auch durch Labor-Experimente verifiziert.

Im Anwendungsbereich des WLANs wurde die Nutzung der 60 GHz-Bänder studiert. Ein neues Entwurfskonzept wurde für 60 GHz WLAN vorgeschlagen, welches hohe Datenrate und hohe Nutzerdichte gleichzeitig unterstützen soll. Ein In-Flight-Entertainment (IFE) System wäre ein Beispiel der Anwendung. Zuerst wurde der allgemeine Systementwurf vorgestellt. Zum Parametrisieren der Abwärtsstrecke wurde die Optimierung der Zeitbereichsfensterung und der Schutzbandgröe von OFDM-Signalen untersucht. Danach konzentriert sich die Dissertation auf die Kompensierung der Sende- und Empfänger- RF-Fehler in der Abwärtsstrecke mithilfe der empfangsseitigen digitalen Signalverarbeitung. Die betrachteten RF-Fehler enthalten Trägerfrequenzversatz und Sende- und Empfänger-I/Q-Fehler. MIMO OFDM bertragung wurde angenommen. Für die Kompensierung dieser RF-Fehler wurde passender Präambel-Entwurf sowie effiziente und effektive Parameterschätzverfahren entwickelt. Zuletzt wurde die Mehrnutzerentzerrung in der Aufwärtsstrecke auch untersucht.

Alle Ergebnisse in beiden Anwendungsbereichen können zur Datenrateerhöhung in zukünftigen drahtlosen Kommunikationssystemen beitragen.

Abstract

This thesis addresses the challenges of rapidly increasing data rate requirements in future wireless communication systems, where the emphasis is on RF impairment compensation and system design. Two scenarios are considered: the mobile cellular scenario and the Wireless Local Access Network (WLAN) scenario.

In the mobile cellular scenario, the concept of multi-band-/multi-standard Base Station (BS) is discussed, which allows to manage the coexistence of different technological standards (2G/3G/4G) with reasonable installation and operation costs. For the realization of such BSs, the issue of RF impairment compensation has to be addressed, especially at the transmitter with direct conversion architecture. In this thesis, practical concepts for digital compensation of frequency selective I/Q-imbalance and modulator DC-offset are proposed for such BS transmitters. Both digital pre-equalization circuit and parameter estimation/tracking schemes are developed, which allow flexible and standard independent impairment compensation with comparatively low-complexity. The effectiveness and advantages of these schemes are verified by both numerical simulations and laboratory experiments.

In the WLAN scenario, the exploitation of the 60 GHz band is studied. A new design concept for 60 GHz WLAN systems is proposed to support both high data rate and high user density for potential applications e.g. the In-Flight Entertainment (IFE) systems. First, the general system design is described. For the parameterization in the downlink (DL), the optimization between the guardband size and time domain windowing of OFDM signals is studied. Afterwards, the focus is on the compensation of both Tx- and Rx RF impairments in the DL via Rx side digital signal processing. The considered RF impairments include Carrier Frequency Offset (CFO) and Tx-/Rx I/Q-imbalance. MIMO OFDM transmission is assumed. For impairment compensation, sophisticated preamble designs as well as efficient and effective parameter estimation schemes are developed, which require comparatively low computational complexity. Finally, the uplink is also studied, with the emphasis on efficient Multi-User Detection (MUD) using MIMO configuration.

All results in both scenarios contribute to the data rate enhancement in future wireless communication systems.

Contents

List of Figures

LIST OF FIGURES

List of Tables

Notations

Abbreviations

ACF	Auto-Correlation Function
AD	Antenna Diversity
ADC	Analog-to-Digital Converter
ADD	ADDition
AGC	Automatic Gain Control
ALP	Anti-aliasing Low-Pass
AP	Access Point
AST	Adaptive Symbol Training
AWGN	Additive White Gaussian Noise
BB	Baseband
BER	Bit Error Rate
BP	BandPass
BS	BaseStation
BW	BandWidth
CACF	Complementary Auto-Correlation Function
CAZAC	Constant Amplitude Zero Auto Correlation
CCF	Cross-Correlation Function
CC	Cancellation Carrier
CDF	Cumulative Distribution Function
CDMA	Code Division Multiple Access
CESAR	CEllular Small Area Radio
CF	Crest Factor
CFO	Common Frequency Offset
CoCI	Co-Channel Interference
CP	Cyclic Prefix
CPE	Common Phase Error
CRLB	Cramer-Rao Lower Bound
DAC	Digital-to-Analog Converter

DCA	Direct Conversion Architecture
DCD	DL Channel Descriptor
DCO	DC-Offset
DFT	Discrete Fourier Transform
DTFT	Discrete Time Fourier Transform
DL	DownLink
DMOD	Demodulator
DS-CDMA	Direct-Sequence Code Division Multiple Access
DTFT	Discrete Time Fourier Transform
EVM	Error Vector Magnitude
FCH	Frame Control Header
FDE	Frequency Domain Equalization
FDS	Frequency Domain Separation
FDMA	Frequency Division Multiple Access
FIR	Finite Impulse Response
FUSC	Full Usage of SubChannels
FPGA	Field Programmable Gate Array
FR	Frequency Response
GB	Guard-Band
Gbps	Gigabits per second
GI	Guard-Interval
GSM	Global System for Mobile Communications
HIL	Hardware-In-the-Loop
IAI	Inter-Antenna-Interference
ICI	Inter-Carrier Interference
IDFT	Inverse Discrete Fourier Transform
IDTFT	Inverse Discrete Time Fourier Transform
IF	Intermediate-Frequency
IFDE	Iterative Frequency Domain Estimation
IFE	In-Flight Entertainment
IIR	Infinite Impulse Response
INTP	INTerPolation
IR	Impulse Response
IRR	Image Rejection Ratio
ItCI	Inter-Channel Interference
LES	Linear Equation System
LLS	Linear Least Square
LMMSE	Linear Minimum Mean Square Error
LNA	Low Noise Amplifier

LO	Local Oscillator
LOS	Line-Of-Sight
LS	Least-Square
LSE	Least-Square Estimation
LTE	Long Time Evolution
MAC	Medium Access Control layer
MAP	Media Access Protocol
MAT	Multiple Antenna Technique
MB	Multi-Band
MCS	Multiple Choice Sequence
MFI	Mirror-Frequency Interference
MOD	Modulator
MIMO	Multiple Input Multiple Output
MISO	Multiple Input Single Output
MFB	Matched Filter Bound
MLE	Maximum Likelihood Estimation
MMSE	Minimum Mean Square Error
MRC	Maximum Ratio Combining
MSE	Mean Square Error
MT	Mobile Terminal
MU	Multi-User
MUD	Multi-User Detection
MUI	Multi-User Interference
MUL	MULtiplication
Nr.	Number
NLS	Non-linear Least-Square
OFDM	Orthogonal Frequency-Division Multiplexing
OLOS	Obstructed Line-Of-Sight
PA	Power Amplifier
PACF	Periodical-Auto-Correlation-Function
PAPR	Peak-to-Average-Power-Ratio
PB	Pilot Based
PC	Personal Computer
PCCF	Periodical-Cross-Correlation-Function
PCI	Peripheral Component Interconnect
PDS	Power Density Spectrum
PDU	Packet Data Unit
PHY	Physical layer
PL	Path Loss

PSD	Power Spectral Density
PTEQ	Per-Tone-EQualization
PUSC	Partial Usage of SubChannels
RAM	Random-Access-Memory
RC	Raised Cosine
RF	Radio Frequency
RLP	Reconstruction Low-Pass
ROF	Roll-Off-Factor
Rx	Receiver
SB	Single Band
Sc.	Subcarrier
SC	Single Carrier
SC-FDMA	Single-carrier Frequency-Division Multiple Access
SCH	SCHeme
SEP	SEParation
SIC	Successive Interference Cancellation
SIMO	Single Input Multiple Output
SINR	Signal-to-Interference-and-Noise Ratio
SIPS	SuperImposed Pilot Signal
SIR	Signal-to-Interference Ratio
SISO	Single Input Single Output
SM	Spatial Multiplexing
SNR	Signal-to-Noise Ratio
SSB	Single-Side-Band
STC	Space Time Code
TDMA	Time Division Multiple Access
TDS	Time Domain Separation
Tx	Transmitter
UCD	UL Channel Descriptor
UL	UpLink
UMTS	Universal Mobile Telecommunications System
UT	User-Terminal
VHT	Very High Throughput
VR	Variable Gain
WiMAX	Worldwide Interoperability for Microwave Access
WLAN	Wireless Local Access Network
w.r.t.	with respect to
WPAN	Wireless Personal Access Network
WWS	Wide-Sense-Stationary

ZF	Zero-Forcing

Mathematical Notations

In the following, the principal mathematical notations are listed. Note that Bold-type letters denote vectors or matrices.

$(\cdot)^*$	complex conjugate
$(\cdot)^T$	transpose
$(\cdot)^H$	conjugate transpose
$((\cdot))_N$ or $\mathrm{mod}(\cdot, N)$	modulo by N operation
$(\cdot)^\dagger$	pseudo-inverse
$\mathrm{cond}(\cdot)$	condition number of a matrix
$\mathrm{sum}(\cdot)$	sum of the vector elements
$\mathrm{sgn}(\cdot)$	sign/signum function
$\|\|\cdot\|\|_2$	the Euclidean norm
$\|\|\cdot\|\|_F$	the Frobenius norm
$\lambda_m(\boldsymbol{A})$	the m^{th} eigenvalue of $\boldsymbol{A}$
$\sigma_m(\boldsymbol{B})$	the m^{th} singular value of $\boldsymbol{B}$
$\lfloor c \rfloor$	the largest integer smaller than c
$\lceil c \rceil$	the smallest integer greater than c
$*$	convolution
$\circledast_N$	circular convolution with block length N
$\hat{(\cdot)}$	if not specified, the estimate of a parameter or a parameter vector/matrix
$\vec{\boldsymbol{a}}_M$	a length-M vector $[a_0, \ldots, a_{M-1}]$
$(\boldsymbol{A})_{m,n}$	the $(m,n)^{\text{th}}$ element of the matrix $\boldsymbol{A}$, where the row/column indexes can be negative valued
$\mathcal{OR}(\vec{\boldsymbol{a}}_M)$	cyclically right-shifted oder reversed version of a vector $\vec{\boldsymbol{a}}_M$ i.e. $[a_0, a_{M-1}, a_{M-2}, \ldots, a_1]$
$\boldsymbol{A}_{(\mathcal{R},\mathcal{C})}$	a submatrix obtained from $\boldsymbol{A}$ by eliminating the rows and columns that are not within index sets $\mathcal{R}$ and $\mathcal{C}$, respectively
$\boldsymbol{V}_{\mathcal{R}}$	a subvector obtained from $\boldsymbol{V}$ by eliminating the elements that are not within $\mathcal{R}$
$\boldsymbol{F}$ or $\boldsymbol{F}^N$	$N \times N$ Fourier transform matrix with elements $(\boldsymbol{F})_{k,n} = e^{-j\frac{2\pi kn}{N}}$, $\forall k = -\frac{N}{2}, \ldots, \frac{N}{2} - 1; n = 0, \ldots, N-1$
$\mathbf{1}_{M\times N}$	a length-N all ones matrix
$\mathbf{0}_{M\times N}$	an $M \times N$ zero matrix
$\boldsymbol{I}_N$	an identity matrix of size N
$-\mathcal{I}$	order-reversed and component-wise negated version of the set $\mathcal{I}$

$:$	the whole index set
$\mathcal{I}(\kappa)$	the κ^{th} element of the set $\mathcal{I}$
$\{a:d:b\}$	an arithmetic sequence with common difference d, which starts from a and ends with an integer $\leq b$
$\mathcal{F}\{x[n]\}\|_{\omega}$	DTFT i.e. $X(\omega)=\mathcal{F}\{x[n]\}\|_{\omega}=\sum_{n=-\infty}^{\infty}x[n]e^{-j\omega n}$
$\mathcal{F}^{-1}\{X(\omega)\}\|_{n}$	IDTFT i.e. $x[n]=\mathcal{F}^{-1}\{X(\omega)\}\|_{n}=\frac{1}{2\pi}\int_{-\pi}^{\pi}X(\omega)e^{j\omega n}d\omega$
$\mathcal{F}_N\{x[n]\}$	N-point DFT i.e. $X[k]=\mathcal{F}_N\{x[n]\}=\sum_{n=0}^{N-1}x[n]e^{-j\frac{2\pi kn}{N}}$, $\forall k=-N/2,\ldots,N/2-1$
$\mathcal{F}_N^{-1}\{X[k]\}$	N-point IDFT i.e. $x[n]=\mathcal{F}_N^{-1}\{X[k]\}=\frac{1}{N}\sum_{k=-N/2}^{N/2-1}X[k]e^{j\frac{2\pi kn}{N}}$, $\forall n=0,\ldots,N-1$
$\mathcal{R}e\{\cdot\}$	real part
$\mathcal{I}m\{\cdot\}$	imaginary part
subscript re	real part
subscript im	imaginary
$X^{Re}[k]$	$\mathcal{F}_N\{x_{\text{re}}[n]\}$
$X^{Im}[k]$	$\mathcal{F}_N\{x_{\text{im}}[n]\}$
$X^{Re}(\omega)$	$\mathcal{F}\{x_{\text{re}}(t)\}$
$X^{Im}(\omega)$	$\mathcal{F}\{x_{\text{im}}(t)\}$
superscript (i)	i^{th} TX
superscript $\langle r\rangle$	r^{th} RX
";" in sub-/superscripts	"or", e.g. $h_{\text{D;I}}$ indicates h_{D} or h_{I}
$\Delta_{2\pi}(\omega)$	Dirac comb function with period 2π
$\delta[n]$	unit impulse i.e. $\delta[0]=1,\delta[n]=0,\forall n\neq 0$
$\delta(t)$	dirac delta distribution
$\mathbb{C}$	complex number set
$\mathbb{R}$	real number set
μ_x	the mean value of x
$\overrightarrow{(\bullet)}$	$(\bullet)e^{-j\frac{2\pi}{N}\epsilon n}$
$\overleftarrow{(\bullet)}$	$(\bullet)e^{j\frac{2\pi}{N}\epsilon n}$

For OFDM systems, the following notations are used:

N	total number of subcarriers
N_0	the number of NULL subcarriers for guardband reservation
N_D	the number of used subcarriers i.e. $N_D=N-N_0-1$ (excluding DC-subcarrier)
$\mathcal{N}$	$\{0,\ldots,N-1\}$
$\mathcal{N}_1$	$\{0,\ldots,\frac{N}{2}-1\}$
$\mathcal{N}_2$	$\{\frac{N}{2},\ldots,N-1\}$
$\mathcal{I}_D$	$\{-\frac{N_D}{2},\ldots,-1,1,\ldots,\frac{N_D}{2}\}$

Chapter 1

Introduction

1.1 Background and Motivation

Wireless communication is playing a more and more important role in our life. During the last decades, the service areas of wireless communication have been expanding with an exponentially increasing rate. Compared to simple voice application in the early 1990s, wireless communication systems nowadays can provide service for voice, text, image, multimedia, video streaming, wireless teleconferencing, internet surfing etc. Along with the expanding service area, rapidly increasing requirements for wireless communication systems can be observed, including data rate, coverage, latency, mobility, link quality, spectral efficiency, cost etc. These requirements have driven the evolution of wireless communication systems. The evolution of wireless communication systems as well as the development trend can be strongly reflected by the data rate roadmap in wireless communications, which is shown in Fig. 1.1. In this figure, three main application cases are included: cellular mobile systems, Wireless Local Area Network (WLAN) and Wireless Personal Area Network (WPAN). While cellular mobile systems are designed to cover up to 15 kilometers per cell, WLAN and WPAN are intended for coverage of up to 150 meters and 10 meters per Access Point (AP), respectively. As shown, the data rate requirements for all application cases have been increased by a factor of 10 in every five years. In the near future, these data rate requirements can approach 100 Mbps, 10 Gbps and 100 Gbps for cellular mobile, WLAN and WPAN, respectively [4]. Such high data rate requirements give big technical challenges to future wireless communication systems. There are generally three ways to increase data rate: to increase the spectral efficiency, to extend transmission bandwidth and to exploit frequency resources that were not used for wireless communication so far.

In cellular mobile application, the increasing data rate requirement has driven the evolution from the 2^{nd} Generation (2G, GSM), the 3^{rd} Generation (3G, UMTS, CDMA2000 etc.) towards the 4^{th} Generation (4G, LTE, LTE-advanced), which is expected to provide up to 1 Gbps peak data rate. To achieve such high data rate, 4G has deployed advanced transmission techniques

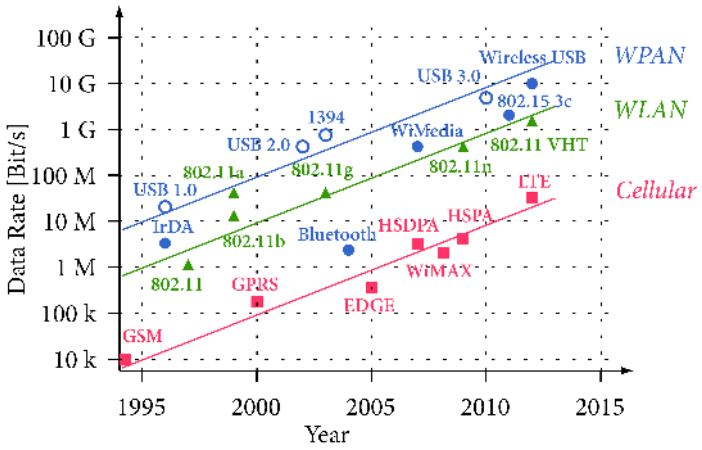

Figure 1.1: Roadmap of data rate in wireless communications, where several wired communication standards are included for comparison. Cited from [1]

including Multiple Input Multiple Output (MIMO), Orthogonal Frequency Division Multiplexing (OFDM) and advanced scheduling techniques etc. Moreover, bandwidth of up to 20 MHz is supported. Except for part of the 2G/3G frequency bands, some new frequency bands are exploited, including the 2.6 GHz band and the 800 MHz band (digital dividend).

Since the migration from 2G/3G to 4G is a very long process, a big challenge in cellular systems is to handle the coexistence of different generations of technical standards (2G/3G/4G) with limited installation and operation costs. On the one hand, Mobile Terminals (MT) should be able to operate with different standards in different frequency bands (see [5, 6, 7, 8, 9, 10, 11, 12] etc.). On the other hand, the cost of Base Stations (BS) should be restricted, which is one of the major costs of the mobile operators. Currently, separate BSs are deployed for 2G and 3G, which is very inefficient due to doubled costs for site, hardware and energy consumption etc. To reduce the BS costs and to facilitate the migration to LTE, multi-band multi-standard BSs or in other words, universal BSs, are desired (see [13, 14, 15] etc.). Such BSs are expected to be very flexible and efficient. They should be able to operate in a wide range of frequency bands and to handle multiple standards simultaneously. The realization of such BSs require both multi-technology BaseBand (BB) unit and multi-band-/broadband RF-frontends e.g. antenna and Power Amplifier (PA). Moreover, the cooperation between digital BB and analog components is a key element to reduce frontend costs and to enhance energy efficiency, flexibility and transmission quality. To be more concrete, advanced digital signal processing techniques should be applied to compensate for the impairments of the RF-frontends and analog BB components (called “dirty RF” effects [5, 12, 16, 17, 18, 19, 20, 21, 22] etc.). Such a concept is called “Smart RF”, which was investigated in a German project with the same name [23].

In WLAN and WPAN applications, the extremely high data rate requirements and the

relatively low coverage range have inspired the exploitation of unlicensed band from 57 to 64 GHz, which is generally called the "60 GHz" band (see [1, 24, 24, 25, 26, 27, 28, 29, 30] etc.). The specific advantages of this frequency band are the large unlicensed available bandwidth and the short wavelength, allowing very high data rates and small antenna dimensions, respectively. Furthermore, there is no interference to the existing wireless systems. Due to high free space attenuation of such high frequency electromagnetic waves[1] as well as their strong penetration loss in common materials, the system coverage as well as the interference range is relatively small. Thus, better frequency reuse and higher user density are allowed. Furthermore, according to recent advances in silicon semiconductor technology, 60 GHz transceivers will soon be able to be implemented in powerful and marketable integrated circuits.

Currently, the most advanced WLAN standards IEEE 802.11n[2] is being extended to the 60 GHz version IEEE 802.11ad for VHT (Very High Throughput), which is supposed to support rates beyond 1 Gbps [31]. Meanwhile, the high rate WPAN standard IEEE 802.15.3 is being extended with a millimeter-wave-based alternative Physical Layer (PHY), which is indicated as IEEE 802.15.3c and should provide data rates above 2 Gbps.

However, there are certain 60 GHz WLAN/WPAN applications which can not be covered by IEEE 802.11 VHT or IEEE 802.15.3c. One application is the indoor high-user-density WLAN e.g. an In-Flight Entertainment (IFE) system for aircrafts, which requires a sum data rate in the order of several Gbps with user densities of up to thousand passengers per system. None of the existing wireless standards can support such high data rate and high user density at the same time. Another application is the indoor short-range Point-to-Point (P2P) data transmission with data rates up to 10 Gbps and transmission range of up to 1 meter. Such applications give challenge to system design and are being intensively investigated in current 60 GHz research (e.g. [29, 30, 32, 33] etc.).

1.2 Scope and Contributions of This Thesis

The challenges in cellular and WLAN application cases of wireless communication in Sec. 1.1 are investigated in this thesis.

1.2.1 Cellular Mobile Application Case

In the cellular mobile application case, the "Smart-RF" concept is investigated at BSs. The desire for low-cost, low power (consumption) and flexible BSs motivates the deployment of the Direct Conversion Architecture (DCA,see [34]), which is nowadays a trend of transceiver development. However, it is well known that the performance of DCA can be severely limited by impairments of analog components, which are called "dirty RF effects". These effects include sampling jitter, I/Q-imbalance, oscillator phase noise, Local Oscillator (LO) signal leakage as

[1] The LOS path loss of 60 GHz waves at 1 meter distance is 68 dB.
[2] published on Oct. 29. 2009.

well as non-linearity of the PA, the LNA, the mixer, the ADC and other analog components. In this thesis, the investigation is restricted to the Tx part of the DownLink (DL). Among the impairments at Tx, I/Q-imbalance and PA non-linearity put the most severe performance limitation on DCA. While I/Q-imbalance generates Mirror-Frequency Interference (MFI) within the transmission bandwidth [3], PA non-linearity causes both in-band and out-of-band interference [35, 36]. Thus, both effects can significantly degrade the achievable spectral efficiency and thus, the system performance. One of the most effective solution is to compensate these impairments in the digital BB[1]. Since the digital compensation at the Tx takes place before the signals are passed to the analog front-ends, it is called "digital pre-equalization" or "digital pre-distortion". Except for effectiveness of compensation, digital compensation has the advantages of flexibility and reconfigurability and can easily cope with changes in operation frequency band and the bandwidth. Note that digital compensation puts high performance requirements on the DAC/ADC with regard to BW and resolution. Fortunately, with today's technology, such requirements can be fulfilled [12].

In this thesis, advanced digital compensation techniques are proposed for the compensation of I/Q-imbalance at broadband DCA transmitters. One of the challenges for the compensation is that the I/Q-imbalance effect in broadband systems shows frequency-selectivity. An even bigger challenge is that the digital compensation should be able to track the parameter changes (in time) during the normal operation of the Tx, i.e., when the BS is transmitting normal communication signals. This means that parameter estimation has to be carried out periodically without using any dedicated pilot sequence. Instead, the communication signal should be used as reference for parameter estimation. Such estimation is called "semi-blind" estimation and should work with communication signals of different characteristics. Finally, the complexity of both the pre-equalizer and the parameter estimation should be kept low. Based on the considerations above, two estimation and compensation schemes are proposed. Compared to the state-of-the-art schemes, improved robustness and lower complexity are achieved. Both numerical simulation and Hardware-In-the-Loop (HIL) experiments were conducted to test the effectiveness of these schemes. According to the results, the most effective and practical scheme among them can be identified.

1.2.2 60 GHz WLAN Application Case

In the 60 GHz WLAN application case, a wireless IFE system design concept is proposed. A wireless IFE system is a typical example of indoor high-user-density WLAN and requires a sum data rate in the order of several Gbps with user densities of up to thousand passengers per system. By exploiting the 60 GHz band, both high data rate and high user density can be achieved. Compared to the existing IFE systems with wired connections, high flexibility, significantly reduced weight and low installation cost can be achieved. The proposed system

[1] Alternative solution to pure digital BB compensation is the digital-assisted hybrid compensation e.g. feed-forward or mixer IP2 calibration, which are also very effective and viable.

concept is called "CEllular Small Area Radio (CESAR)", which is cellular based, with a cell diameter of about 5 meters and a frequency reuse factor of 8. In the DownLink (DL), MIMO OFDM is applied to achieve high spectral efficiency and diversity. In the Up-Link (UL), Cyclic-Prefix (CP) assisted Direct-Sequence Code-Division-Multiple-Access (DS-CDMA) is applied. With this design concept, several technical challenges were investigated.

First, the sidelobes of the OFDM spectrum was reduced by applying Raised Cosine (RC) windowing in the time domain. On the one hand, a higher Roll-Off Factor (ROF) of the RC-window leads to better sidelobe suppression and allows a smaller GuardBand (GB) size, increasing the spectral efficiency. On the other hand, high ROF requires large Guard-Interval (GI) in time, decreasing the data rate. Based on this phenomenon, a joint optimization technique for the ROF and guardband size is presented, which maximizes the achievable data rate.

Afterwards, digital compensation of RF-impairments in MIMO OFDM systems are investigated. Two different concepts are considered: 1) Joint estimation and compensation of frequency selective I/Q-imbalance and the MIMO channel; 2) Joint estimation and compensation of Carrier-Frequency-Offset (CFO), frequency selective I/Q-imbalance and the MIMO channel. For each concept, effective schemes are proposed. Compared to state-of-the-art schemes, better performance can be achieved with lower preamble overhead and/or lower computational complexity. The advantages of the proposed schemes are verified by simulation results.

Finally, novel antenna diversity schemes are proposed for the Multi-User-Detection (MUD) in the UL, incl. SIMO, MISO and MIMO. The proposed schemes operate in the frequency domain and allow efficient implementation. The performance of the schemes of different antenna diversity configurations are compared based on numerical simulation. It was found out that the SIMO scheme achieves the best tradeoff between performance and complexity (both RF-hardware and computational complexity). Moreover, compared to the most state-of-the-art scheme, better performance can be achieved requiring slightly higher hardware complexity but much lower computational complexity.

1.3 Previous Publications and New Contributions

This thesis is partly based on the author's previous publications [37, 38, 39, 40, 41, 42, 43, 44]. The relations between this thesis and the previous publications are listed below:

- The joint I/Q-imbalance and modulator DC-offset compensation concept, the Least-Square (LS) based parameter estimation and -tracking method in Ch. 2 have been partly published in [37];
- The overall system design of the 60 GHz WLAN in Sec. 3.2 has been published in [39];
- The optimization of time domain windowing and GB size for cellular OFDM systems in Sec. 3.3 has been published in [40];

- The TDS- and FDS- based joint I/Q-imbalance- and MIMO channel estimation schemes in Sec. 3.4.5 and Sec. 3.4.6, respectively, have been published in [42];
- The joint CFO, I/Q-imbalance and MIMO channel estimation scheme (based on closed-form CFO estimator) in Sec. 3.5.4 has been published in [44];
- The antenna diversity schemes for uplink multi-user detection in Sec. 3.6 has been published in [43].

In all previous publications, the co-authors[1] have provided very valuable comments to improve the presentation. Moreover, the co-authors have used their expertise in RF circuits to help the author derive system models, develop ideas and define simulation parameters. For the 60 GHz WLAN system design in [39], the co-authors have provided the basic system configuration including frequency allocation, frequency plan, downlink- and uplink waveforms etc., which serves as a basis for the work in Ch. 3.

Except for the contributions in the previous publications, this thesis also includes the following new (unpublished) contributions:

- In Sec. 2, the work in [37] has been extended. Both matrix condition analysis and a practical solution for ill-conditioned matrix problem are presented. Moreover, a new simplified two-phase parameter estimation scheme is proposed. Hardware-In-the-Loop results are also included;
- In Sec. 3.3, the work in [40] has been extended in this thesis with instantaneous interference analysis (Sec. 3.3.6);
- In Sec. 3.4.7, the design and application of a multi-functional preamble for the joint estimation of I/Q-imbalance and the MIMO channel is proposed;
- In Sec. 3.5.5, an iterative scheme for the estimation of CFO, I/Q-imbalance and the MIMO channel is proposed;
- The simulation results in Sec. 3.4 and Sec. 3.5 are more detailed and extensive than those in [42] and [44], respectively.

[1] Including Dr. Andreas Kortke, Dr. Wilhelm Keusgen and Michael Peter.

Chapter 2

Smart-RF Concept for Cellular Mobile Systems

2.1 Introduction

As mentioned in Chapter 1.2.1, the desire for low-cost, low power (consumption) and flexible BSs motivates the deployment of the Direct Conversion Architecture (DCA), which is a trend of transceiver development (see [2, 12, 45, 46] etc.).

One advantage of the DCA is that the number, the size and the cost of the required analog components (e.g. MOD and DMOD) can be significantly reduced compared to those with the conventional multi-stage (superheterodyne) conversion architecture. Correspondingly, highly integrated implementation and low power consumption are allowed.

Another advantage is that high flexibility of the communication systems is allowed with respect to the RF signal generation and demodulation in different frequency bands [47]. This serves as a basis for "Software Defined Radio (SDR)". This advantage is especially beneficial for the implementation of multi-band multi-standard BSs. Traditionally, multi-band multi-standard transceivers are implemented by applying parallel dedicated RF chains for the different bands and standards. However, such implementation requires a large number of RF- and BB analog components, leading to high hardware cost, high power consumption and low integration degree. Moreover, such implementation is not flexible. A significant improvement can be achieved by applying the SDR concept based on DCA with broadband analog frontends and high sampling rate in the digital BB. Without loss of generality, we describe this concept at the Tx. First, in the digital BB, individual signal streams are properly oversampled, converted to different IFs and then overlapped. These signal streams may stem from different communication standards. The resulting BB signal is called "Multi-Band (MB) IF signal"[1] and can be converted to the radio frequency via a single RF-chain. In this way, easy adjustment of the IFs and the

[1] It is also called "multi-carrier IF signal" in the literature e.g. [48].

BW of the individual signal streams as well as the radio carrier frequency are allowed[1]. The number of RF- and BB analog components as well as the hardware cost can also be significantly reduced. A similar concept applies to the Rx.

However, it is well known that the performance of DCA can be severely limited by impairments of analog components i.e. the "dirty RF effects", which include sampling jitter, I/Q-imbalance, oscillator phase noise, Local Oscillator (LO) signal leakage as well as non-linearity of the PA, the LNA, the mixer, the ADC and other analog components. These impairments become stronger, as the cost and size of the analog components decrease and also as the bandwidth and the carrier frequency are increased [16]. Moreover, the parameters of these impairments can vary with the operation frequency band. In this Chapter, the investigation is restricted to the DCA transmitters, for which the key performance limiting impairments are PA non-linearity, I/Q-imbalance and MOD DC-offset error. These impairments will be described in detail in the following. As will be shown, they can severely degrade the DCA transmitter performance and are especially critical for the application of multi-band IF signals.

2.1.1 PA Non-linearity

The non-linearity problem of the PA becomes evident as larger bandwidth and higher order modulation schemes are deployed to achieve high data rate. As a result, the Peak-to-Average-Power-Ratio (PAPR) of communication signals increases considerably. To keep both the cost and the energy consumption of the PA on a reasonable level, the transmitter has to operate beyond the linear region of the PA and cause inter-modulation due to nonlinearity effects. Inter-modulation results in both inband distortion and spectral regrowth of the communication signals. While inband distortion increases the Error Vector Magnitude (EVM) of the transmitted signal, spectral regrowth causes interference to adjacent channels. Moreover, in broadband systems, the non-linearity has memory effect, giving more challenge to the modeling and compensation [46, 49, 50, 51, 52, 53].

Specifically, due to power control, the signals in different subbands of a multi-band IF signal may have different transmit power. Due to spectral regrowth, a strong subband signal can generate strong interference to the other subband signals, as illustrated in Fig. 2.1. As a result, the weak subband signals will suffer from high detection error.

There are generally two digital methods to cope with non-linear distortion: PAPR reduction and pre-distortion. While many of the PAPR reduction techniques assume certain signal characteristics (e.g. OFDM, see [54, 55, 56, 57, 58] etc.), pre-distortion can generally be applied to arbitrary signal waveforms and provides high flexibility [35, 46, 51, 59, 60]. There is also work on the combination of PAPR reduction and pre-distortion [61][2]. Except for digital methods, feedforward linearizer (see [62, 63]) can also be applied, which operates both in digital- and

[1] However, this concept is only suitable when the carrier frequency difference of the individual signal streams are within the allowable range of digital BB BW. For signal streams with very large carrier frequency difference (e.g. larger than 1 GHz), multiple RF chains are still needed.

[2] The PAPR reduction technique in this paper is independent of the signal characteristic.

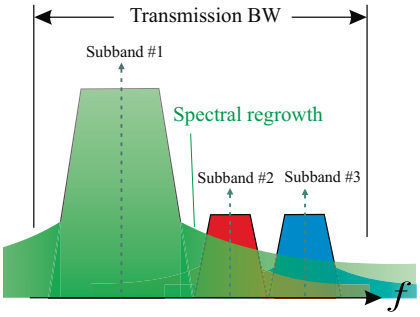

Figure 2.1: Influence of spectral regrowth on multi-band IF signal.

analog domains.

2.1.2 I/Q-Imbalance and Modulator DC-Offset Error

There are generally two I/Q-imbalance effects in DCA-transmitters. The first one is the I/Q-imbalance in the MOD, which stems from the imperfect quadrature splitting of the LO signal in the MOD. This imperfect splitting results in two LO signal branches which have unequal amplitude and a phase difference deviating from 90°. For a given LO frequency, this effect can be regarded as constant over the whole signal BW and is called "frequency independent I/Q-imbalance" in this thesis (however, it may be slowly time-variant). The other I/Q-imbalance effect stems from unequal Frequency Response (FR) of the I- and Q-signal path analog BB components, among which the analog Low-Pass (LP) filters for signal reconstruction are most typical. This effect is generally frequency-selective within the signal BW. In this thesis, the overall effect including both I/Q-imbalance effects is referred to as "frequency selective I/Q-imbalance". In broadband communication systems, the frequency selectivity of I/Q-imbalance should be taken in to account.

I/Q-imbalance limits the performance of DCA by generating MFI [3]. Fig. 2.2 illustrates MFI in Single-Band (SB) signals and multi-band IF signals. As shown, especially in the multi-band case, a strong subband signal can generate strong interference to the subbands in the mirror positions, resulting in high detection error of the signals on those subbands. Except for MFI, I/Q-imbalance can significantly degrade the performance of the digital pre-distortion for PA linearization [47].

MOD DC-offset is an unwished effect caused by the LO signal leakage to the RF output. It may cause high power density at the carrier frequency and impairs the spectral mask. Moreover, it will affect the I/Q-imbalance parameter estimation and thus, must be compensated for.

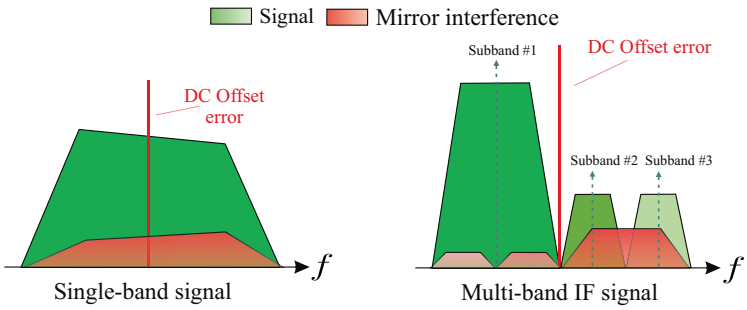

Figure 2.2: Influence of I/Q-imbalance on single-band signal and multi-band IF signal, respectively.

2.1.3 Different Concepts for the Compensation of PA Non-Linearity, Modulator DC-offset and I/Q-imbalance

As shown in Fig. 2.3, there are two different concepts for the compensation of PA non-linearity, I/Q-imbalance and MOD DC-offset. The first one is the separate compensation of DC-offset, I/Q-imbalance and PA non-linearity. In this case, I/Q-imbalance and DC-offset are first estimated and compensated for. Afterwards, PA-identification and PA-predistortion are carried out. Both pre-compensation units are cascaded. The second one is the joint identification and predistortion of PA non-linearity, I/Q-imbalance and MOD DC-offset. On the one hand, for parameter estimation, the separate concept requires both feedback signals from the MOD output and the PA output, while the joint concept requires only one feedback signal from the PA output. As a result, the separate concept requires higher hardware complexity (mainly an RF-switch). On the other hand, the joint concept requires higher complexity both in the computation of the pre-distortion coefficients and pre-distortion circuit.

The investigations of the separate concept and the joint concept can be found in [3, 37, 47, 64, 65, 66] etc. and [46, 53, 66, 67, 68] etc., respectively. So far, there is no systematical hardware-based performance comparison of both concepts.

In this thesis, the separate concept is applied. The joint I/Q-imbalance and DC-offset compensation is investigated.

2.1.4 Pilot-based- and Semi-blind Parameter Estimation Principle

Generally, the parameters of all these effects can vary slowly in time due to environment factors e.g. temperature. Thus, the parameters have to be estimated periodically (with relatively long periods).

In the case when the transmitter is not transmitting communication signals e.g. right after device booting, dedicated pilot sequence can be transmitted for parameter estimation. Such estimation is called **"pilot-based" estimation**. In [69], such pilot-based estimation and the

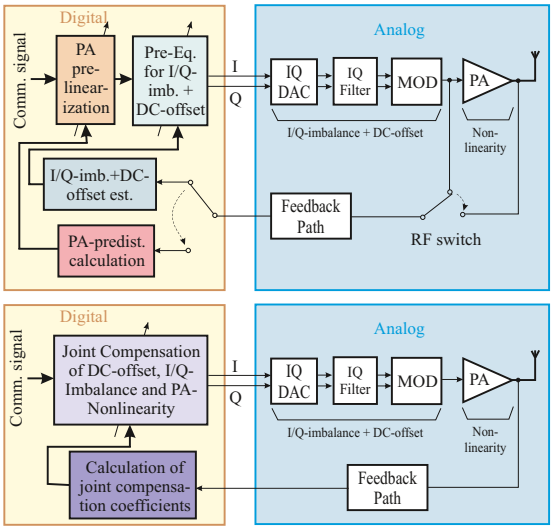

Figure 2.3: Two different concepts for the compensation of PA non-linearity, I/Q-imbalance and MOD DC-offset: (a) Separate estimation and compensation; (b) Joint estimation and compensation.

corresponding impairment compensation are called "off-line" calibration.

However, the estimation has to be carried out also when the transmitter is transmitting communication signals. This transmission should not be interrupted by the parameter estimation. Thus, instead of dedicated pilot sequence, the transmitted communication signal has to be used for parameter estimation. Although the transmitted signal is known at the transmitter, little influence can be taken on its characteristic, which can affect the estimation quality. The parameter estimation under such condition is called **"semi-blind" estimation**, which should be flexible and standard independent. Furthermore, once the compensation coefficients are available, the digital pre-compensation should be applied, even during the estimation for parameter updates. Thus, the digital pre-compensation circuit should be taken into account for the parameter update estimation. Such a concept of parameter estimation, update and impairment compensation is called "on-line" calibration in [69].

2.1.5 Related Works and Overview of This Chapter

There are a number of works considering the I/Q-imbalance compensation in DCA transmitters, including [2, 3, 37, 38, 42, 44, 45, 46, 47, 64, 65, 67, 68, 69, 70, 71, 72, 73, 74, 75, 76, 77, 78, 79, 80, 81, 82, 83, 84, 85, 86, 87, 88, 89, 90, 91], etc.

A considerable part of the reported works have focused on the compensation of Tx I/Q-imbalance at the Rx (in digital domain), either jointly with Rx I/Q-imbalance [42, 76, 77, 79, 82, 83, 84, 85, 86] or separately [44, 74, 81, 90][1]. Although these works have shown promising

[1]The compensation of Tx I/Q-imbalance is separated from that of Rx I/Q-imbalance. But the Tx I/Q-

results, they have all assumed perfect linearity of the PA. When PA-nonlinearity is present, all schemes in these works will suffer from performance degradation. The reason is that the PA-nonlinearity occurs after the Tx-I/Q-imbalance and can lead to significant model mismatch of these schemes. Thus, if feedback paths (e.g. those shown in Sec. 2.1.3) are available at the Tx, it would be more favorable to compensate the Tx-I/Q-imbalance at the Tx. Moreover, Tx-side I/Q-imbalance compensation is necessary, anyway, for effective PA-predistortion. A further advantage of Tx side compensation of Tx-I/Q-imbalance is the relaxation of the Rx signal processing complexity. This is especially true when considering a cellular multi-user UL scenario (although this is not the target scenario in this thesis).

The Tx-side Tx-I/Q-imbalance compensation have also been studied by a number of works, including [2, 3, 37, 38, 45, 46, 47, 53, 64, 65, 67, 68, 69, 70, 71, 72, 73, 75, 78, 80, 87, 88, 89, 91] etc. All of these works assume that there are feedback paths available from the output of the MOD, PA or the LP filters. Many of these works i.e. [64, 65, 67, 69, 70, 71, 72, 73, 87] only considered frequency independent I/Q-imbalance (of the MOD). Among these works, [70, 71, 73] rely on training signals for parameter estimation, while [64, 65, 67, 69, 72, 75, 80, 87] have presented blind compensation schemes. Most of these works have applied adaptive algorithm for parameter estimation.

However, in broadband wireless communication, the I/Q-imbalance effect is generally frequency selective. As will be shown in Sec. 2.5.7 and Sec. 2.8, ignoring the frequency selectivity of I/Q-imbalance in broadband systems can result in significant performance degradation. Thus, the frequency independent compensation schemes mentioned above are unsuitable for our target scenario, where broadband DCA transmitters are used.

Frequency selective I/Q-imbalance has been taken into account in [2, 3, 37, 38, 45, 46, 47, 53, 68, 78, 88, 89, 91]. Among these works, [78] only considers the I/Q-imbalance between BB LP-filters in the I- and Q-branches. The corresponding parameter estimation scheme requires two feedback paths from the outputs of both LP-filters. Considering the need for additional compensation of MOD I/Q-imbalance, which probably requires an extra feedback path, the hardware complexity is unnecessarily increased. In contrast, the works [2, 3, 37, 38, 45, 46, 47, 53, 68, 88, 89, 91] consider I/Q-imbalance effects of both the MOD and the BB analog components, allowing more efficient and effective compensation. In our previous work [88], a self-calibration method is proposed to compensate Tx- and Rx frequency selective I/Q-imbalance at the Tx and the Rx of the same device, respectively. However, this method requires the transmission of special training sequences through a calibration path which connects the MOD output and the DMOD input. This implies that the regular communication signal transmission has to be interrupted during calibration. Thus, "on-line" calibration is not allowed. Furthermore, this method requires symmetric Tx- and Rx structures as well as two LOs at each transceiver device, which are generally not fulfilled in cellular systems (e.g. in BSs). The work [45] has proposed a pilot-based compensation scheme for OFDM transmitters. Since dedicated pilot signals are

imbalance may be compensated jointly with the radio channel.

necessary, this scheme is also not suitable for "on-line" calibration. Moreover, since OFDM is assumed, it is not suitable for multi-band multi-standard BSs.

For multi-band multi-standard BSs in cellular mobile communications, the works [2, 3, 37, 38, 46, 47, 53, 68, 89, 91] are more appropriate, since no dedicated training signal is necessary. The works [46, 53, 68] have proposed joint predistortion schemes for frequency selective I/Q-imbalance and PA-nonlinarity. As mentioned in Sec. 2.1.3, we focus on the separate compensation of I/Q-imbalance and PA-nonlinearity in this thesis. Thus, the other works are more relevant. In [2, 47], a Least-Square (LS) based parameter estimation scheme was proposed, while a second-order-statistics based scheme and a Widely-Linear (WL) LS scheme were proposed in [3]. Furthermore, the WL-LS scheme was implemented in DSP and reported in [91]. In [89], a non-linear modeling approach was proposed for I/Q-imbalance compensation. In this approach, non-linearities of analog components e.g. DAC and LP filters, are included in the signal model. Although promising results were shown in [89], the complexity of both the pre-compensation circuit and the parameter estimation (identification) is very high (from I/Q-imbalance compensation point of view).

Our previous work [37] is an improvement of the LS-based scheme in [2, 47]. First, a simplified pre-equalization circuit is proposed. Second, the time variations of both the I/Q-imbalance parameters and the FR of the RF components are considered. Accordingly, a parameter tracking scheme is proposed, which was not considered in most of the above mentioned works i.e. [2, 3, 47, 89, 91]. Note that parameter tracking is a key enabling component for "on-line" calibration (see Sec. 2.1.4 or [69]). Compared to [3, 89, 91], MOD DC-offset error is included in our work. In [38], we have further proposed an Iterative Frequency Domain Estimation (IFDE) method to solve the problem caused by ill-conditioned data matrices in the LS-estimation. However, the computational complexity of this scheme could be quite high.

In this thesis chapter, we have extended and improved our previous work [37, 38]. The extension and new contributions are listed below:

- Optimal sequence design for the LS-based scheme in the initial calibration;
- Condition analysis is conducted for the LS-based scheme in the tracking phase. The cause of ill-conditioned matrix problem is identified;
- Practical solutions are proposed to solve the ill-conditioned matrix problem in the LS-estimation;
- A simplified two-phase calibration scheme is proposed[1], which is more advantageous than the LS-based scheme and is free from the ill-conditioned matrix problem[2].
- HIL-experiment results are shown for verification of the proposed schemes.

[1] While the LS-based scheme is an improvement of the scheme in [2, 47], the simplified two-phase calibration scheme is totally novel.

[2] If assuming no time synchronization error between the transmitted and feedback signal.

The novelty of the proposed schemes in this thesis against the previous schemes in the literature can be summarized as follows:

- The proposed pre-equalization circuit is less complex than those in the literature;
- Except for initial calibration, the proposed schemes also consider parameter tracking;
- The proposed schemes can cope with the ill-conditioned matrix problem (caused by spectral gaps in the transmit signal) in parameter estimation;
- The simplified two-phase calibration scheme has lower computational complexity than both the LS-based scheme and the reference schemes.

This chapter is organized as follows: In Sec. 2.2, the signal-and-system model of a DCA transmitter with frequency selective I/Q-imbalance is described. In Sec. 2.3, a simple pre-equalizer circuit is derived for the joint compensation of frequency selective I/Q-imbalance and DC-offset. In Sec. 2.4, the structure of the I/Q-imbalance-free feedback path is described. Sec. 2.5 and Sec. 2.6 present different algorithms for flexible parameter estimation, which can work with communication signals of different characteristics. The corresponding numerical simulation results were also presented in these two sections. Sec. 2.7 and Sec. 2.8 provide complexity analysis and HIL results, respectively. Sec. 2.9 summaries this chapter.

2.2 Signal-and-System Model

Fig. 2.4 shows the structure of the direct-up-conversion Tx, where f_c is the carrier frequency. The amplitude and phase imbalance of the MOD are represented by g^T and φ^T, respectively. The frequency-selectivity of the I/Q-imbalance is modeled to be caused by the Reconstruction Low-Pass (RLP) filters in the I- and Q-branches, which have different Impulse Response (IR) $h^{T_I}(t)$ and $h^{T_Q}(t)$, respectively. Since the imbalance parameters are only very slowly time variant, we first model them as time-invariant for simplicity. The extension to time-variant parameters will be given later. In the feedback loop, a single branch low IF down-conversion, a broadband ADC and a digital I/Q-DMOD are used to avoid additional I/Q-imbalance (see Sec. 2.4 for more details). Furthermore, both FRs of the MOD[1] and the feedback path (including LP and ADC) should be taken into account, since they will affect the parameter estimation (see Sec. 2.5 and 2.6). However, they don't have to be compensated by the calibration scheme, since they don't cause any I/Q-imbalance and will be generally compensated by channel equalization at the Rx. Furthermore, these FRs can be jointly modeled. Finally, as shown in Fig. 2.4, the DC-offset and I/Q-imbalance parameters are jointly estimated from the known transmitted signal and the corresponding feedback signal. After the estimation, these parameters are fed to the digital signal pre-equalization unit.

[1]Indicated as $H_m(f)$ in Fig. 2.4, which may also co-model the FR of other RF components.

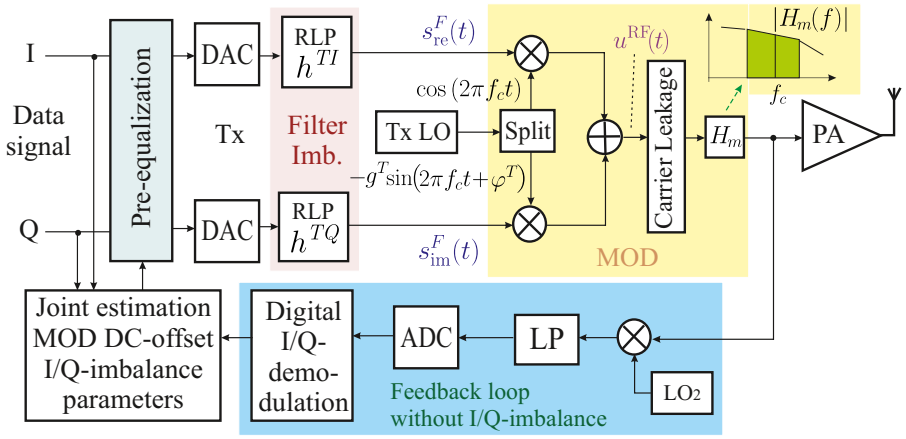

Figure 2.4: System model of a DCA transmitter

For simplicity of analysis, an equivalent BB signal model should be derived. From Fig. 2.4, the relation between the MOD inputs $s^F_{\mathrm{re}}(t)$ and $s^F_{\mathrm{im}}(t)$ and the modulated signal $u^{\mathrm{RF}}(t)$ can be derived as follows:

$$\begin{aligned} u^{\mathrm{RF}}(t) &= s^F_{\mathrm{re}}(t)\cos(\omega_c t) - s^F_{\mathrm{im}}(t) g^T \sin(\omega_c t + \varphi^T) \\ &= \mathcal{R}e\left\{ \left(u_{\mathrm{re}}(t) + j u_{\mathrm{im}}(t)\right) e^{j\omega_c t} \right\}, \end{aligned} \tag{2.1}$$

where $\omega_c := 2\pi f_c$. Moreover, $u_{\mathrm{re}}(t) + j u_{\mathrm{im}}(t)$ is the equivalent BB representation of the modulated signal with $u_{\mathrm{re}}(t) = s^F_{\mathrm{re}}(t) - s^F_{\mathrm{im}}(t) g^T \sin\varphi^T$ and $u_{\mathrm{im}}(t) = s^F_{\mathrm{im}}(t) g^T \cos\varphi^T$. Accordingly, the MOD-imbalance can be represented in BB as shown in Fig. 2.5, where discrete time notation is applied. The equivalent BB IR of the MOD and that of the feedback loop are both included in $h[n]$, which will affect the parameter estimation but need not to be compensated for[1]. It will be shown that the desired pre-equalization coefficients can be obtained without explicitly estimating $h[n]$. In Fig. 2.5, $s[n]$, d and $v[n]$ are the transmitted data signal, the complex DC-offset value and the feedback signal.

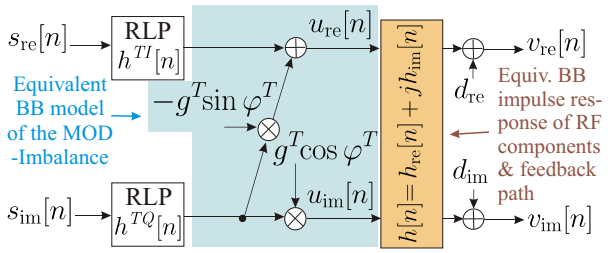

Figure 2.5: Equivalent baseband signal model

[1]Note that the common-mode IR of h^{T_I} and $h^{T_Q}[n]$ can actually be co-modeled by $h[n]$. However, this does not work conversely, since the common-mode IR of h^{T_I} and $h^{T_Q}[n]$ is real valued and can not co-model $h[n]$, which is generally complex valued.

Based on Fig. 2.5, a further BB model can be derived. We express $v[n]$ as:

$$\begin{aligned} v[n] &= s_{\mathrm{re}}[n] * h_\alpha[n] + j s_{\mathrm{im}}[n] * h_\beta[n] + d \\ &= (s_{\mathrm{re}}[n] * h_1[n] + s_{\mathrm{im}}[n] * h_2[n]) \\ &+ j\,(s_{\mathrm{re}}[n] * h_3[n] + s_{\mathrm{im}}[n] * h_4[n]) \\ &+ d_{\mathrm{re}} + j d_{\mathrm{im}}, \end{aligned} \tag{2.2}$$

where

$$\begin{aligned} h_\alpha[n] &= h_1[n] + j h_3[n] = h^{T_I}[n] * h[n] \\ h_\beta[n] &= h_4[n] - j h_2[n] = g^T e^{j\varphi^T} h^{T_Q}[n] * h[n] \end{aligned} \tag{2.3}$$

and $h_1[n]$, $h_2[n]$, $h_3[n]$ and $h_4[n]$ are real FIR filters. Note that since the power of the feedback signal is relatively high compared to the received communication signals, the additive noise contribution is neglected in our analysis. The corresponding signal model is depicted in Fig. 2.6. As will be shown later, the estimation of $h_1[n]$, $h_2[n]$, $h_3[n]$, $h_4[n]$, d_{re} and d_{im} are crucial for the calculation of the pre-equalization coefficients.

Finally, we remark that similar signal models have been used in the literature e.g. [2, 3, 47].

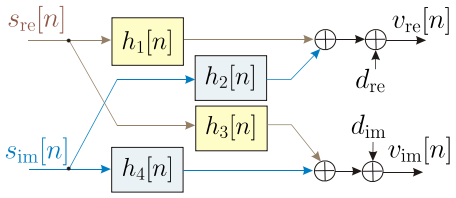

Figure 2.6: Equivalent baseband representation with real FIR filters

2.3 Digital Compensation of Frequency-Selective I/Q- Imbalance and MOD DC-Offset Error

First, we consider the compensation of I/Q-imbalance. As shown in Fig. 2.5, all the I/Q-imbalance sources are included in the signal path between $s[n]$ and $u[n]$. Thus, it is sufficient that the pre-equalization compensates for the influence of I/Q-imbalance in $u[n]$[1]. This has significantly reduced the pre-equalization complexity compared to the scheme in [2, 47, 89], which compensates both the I/Q-imbalance and $h[n]$. In the following, the pre-equalization circuit will be derived by maximizing the system Image Rejection Ratio (IRR), which is an important measure of the I/Q-imbalance corruption.

[1]In contrast, $v[n]$ contains both influences of I/Q-imbalance and $h[n]$. Thus, deriving compensation scheme based on $u[n]$ is easier than from $v[n]$.

Let $U(\omega) := \mathcal{F}\{u[n]\}|_\omega$. From Fig. 2.5, we have:

$$U(\omega) = S^{Re}(\omega)H^{T_I}(\omega) + jS^{Im}(\omega)\tilde{H}^{T_Q}(\omega), \tag{2.4}$$

where $\tilde{H}^{T_Q}(\omega) = H^{T_Q}(\omega)g^T e^{j\varphi^T}$ and $S^{Re}(\omega)$, $S^{Im}(\omega)$, $H^{T_I}(\omega)$ and $H^{T_Q}(\omega)$ are the DTFTs of $s_{\text{re}}[n]$, $s_{\text{im}}[n]$, $h^{T_I}[n]$ and $h^{T_Q}[n]$, respectively. With $S(\omega) = \mathcal{F}\{s[n]\}|_\omega$ and $S^{Re}(\omega) = 0.5\left(S(\omega) + S^*(-\omega)\right)$ and $S^{Im}(\omega) = -0.5j\left(S(\omega) - S^*(-\omega)\right)$ (see [92]), we can write $U(\omega)$ in terms of the transmitted signal and its image:

$$U(\omega) = S(\omega)\frac{H^{T_I}(\omega) + \tilde{H}^{T_Q}(\omega)}{2} + S^*(-\omega)\frac{H^{T_I}(\omega) - \tilde{H}^{T_Q}(\omega)}{2}. \tag{2.5}$$

Then, according to the definition in [3], the IRR of $U(\omega)$ is the power ratio between the image part and the desired signal part. From (2.5), this IRR can be expressed as follows as a function of ω:

$$IRR(U(\omega)) = 10\log\left(\frac{\left|H^{T_I}(\omega) + \tilde{H}^{T_Q}(\omega)\right|^2}{\left|H^{T_I}(\omega) - \tilde{H}^{T_Q}(\omega)\right|^2}\right). \tag{2.6}$$

Due to I/Q-imbalance, $H^{T_I}(\omega) \neq \tilde{H}^{T_Q}(\omega)$ and $IRR(U(\omega))$ may be insufficient. In order to compensate for the I/Q-imbalance, we can multiply a correction term $C(\omega)$ to $S^{Im}(\omega)$ to maximize the IRR. Now, the new MOD output becomes

$$\hat{U}(\omega) = S^{Re}(\omega)H^{T_I}(\omega) + jS^{Im}(\omega)C(\omega)\tilde{H}^{T_Q}(\omega), \tag{2.7}$$

and the new IRR becomes

$$IRR(\hat{U}(\omega)) = 10\log\left(\frac{\left|H^{T_I}(\omega) + C(\omega)\tilde{H}^{T_Q}(\omega)\right|^2}{\left|H^{T_I}(\omega) - C(\omega)\tilde{H}^{T_Q}(\omega)\right|^2}\right). \tag{2.8}$$

By setting $H^{T_I}(\omega) = C(\omega)\tilde{H}^{T_Q}(\omega)$, the new IRR becomes infinite, which is equivalent to the case without I/Q-imbalance. The corresponding expression for $C(\omega)$ can be easily obtained:

$$C^{Re}(\omega) = \frac{H^{T_I}(\omega)}{H^{T_Q}(\omega)g^T\cos\varphi^T}, \quad C^{Im}(\omega) = -\frac{\sin\varphi^T}{\cos\varphi^T}. \tag{2.9}$$

Note that $C^{Re}(\omega), H^{T_I}(\omega), H^{T_Q}(\omega)$ are probably all complex quantities. However, they all have real valued IDTFTs. Moreover, $C^{Im}(\omega)$ is a real valued constant (independent of ω), which simplifies the pre-equalization.

Now, we consider the compensation of DC-offset, which can be achieved by adding a complex correction term ζ to the equivalent BB input of the MOD. According to [47], the following

relation should be satisfied:

$$\begin{bmatrix} \zeta_{\mathrm{re}} \\ \zeta_{\mathrm{im}} \end{bmatrix} = \begin{bmatrix} \sum_{n=0}^{L-1} h_1[n], & \sum_{n=0}^{L-1} h_2[n] \\ \sum_{n=0}^{L-1} h_3[n], & \sum_{n=0}^{L-1} h_4[n] \end{bmatrix}^{-1} \begin{bmatrix} -d_{\mathrm{re}} \\ -d_{\mathrm{im}} \end{bmatrix}. \tag{2.10}$$

Finally, the pre-equalized data signal is:

$$\begin{aligned} \hat{S}(\omega) &= S^{Re}(\omega) + jS^{Im}(\omega)C(\omega) + \zeta\Delta_{2\pi}(\omega) \\ &= S^{Re}(\omega) + jS^{Im}(\omega)(C^{Re}(\omega) + jC^{Im}(\omega)) + \zeta\Delta_{2\pi}(\omega) \\ &= \left(S^{Re}(\omega) - S^{Im}(\omega)C^{Im}(\omega)\right) + jS^{Im}(\omega)C^{Re}(\omega) + \zeta\Delta_{2\pi}(\omega), \end{aligned} \tag{2.11}$$

where $\Delta_{2\pi}(\omega)$ is the Dirac comb function with period 2π. The IDTFT of (2.11) is:

$$\hat{s}[n] = s_{\mathrm{re}}[n] + cs_{\mathrm{im}}[n] + js_{\mathrm{im}}[n] * h^C[n] + \zeta_{\mathrm{re}} + j\zeta_{\mathrm{im}}, \tag{2.12}$$

with

$$c := -C^{Im}(\omega) = \frac{\sin\varphi^T}{\cos\varphi^T} \tag{2.13}$$

$$h^C[n] := \mathcal{F}^{-1}\left\{C^{Re}(\omega)\right\}\Big|_n \tag{2.14}$$

Since spectrum inversion is involved in the calculation of $h^C[n]$ with (2.9) and (2.14), $h^C[n]$ is an anti-causal filter i.e. has coefficients at negative indices. In practice, a shift towards the positive index direction is introduced to attain causality:

$$h^C[n] = \mathcal{F}^{-1}\left\{\frac{H^{T_I}(\omega)}{H^{T_Q}(\omega)g^T\cos\varphi^T}\right\}\Bigg|_{n-n_\tau}, \tag{2.15}$$

where n_τ is length of the IR part of (2.14) at negative indices. Accordingly, a delay block should be applied in the I-branch to equalize this shift. Based on (2.12), (2.13) and (2.15), the pre-equalization structure is depicted in Fig. 2.7. Note that the pre-equalizer is pretty simple, since only an FIR filter $h^C[n]$ and some minor operations are required.

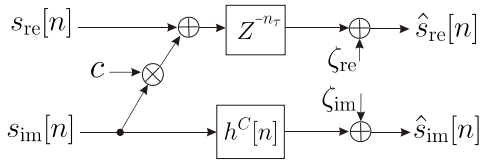

Figure 2.7: Pre-equalization structure

2.4 Feedback-Path with Low-IF Structure

2.4.1 Receiver Architecture

It is crucial for the parameter estimation that the feedback path does not introduce additional I/Q-imbalance. To achieve this, the single-branch low IF Rx architecture (i.e. superheterodyne Rx with digital quadrature downconverter) should be applied. Although this feedback Rx architecture was already used in earlier literature e.g. [2, 3, 46, 47, 69], we will describe and discuss this architecture in more details.

First, the modulated signal with signal BW B_S is down-converted to a low IF frequency f_I via a single branch converter as shown in Fig. 2.4 and Fig. 2.8. Since no image rejection is provided by a single branch converter, the image signal (with regard to the DC-frequency) is down-converted to $-f_I$ as shown in Fig. 2.8. After the LP filtering, the IF signal is converted to the digital domain via an ADC whose BW is larger than $2f_I + B_S$. In digital domain, the IF signal is perfectly I/Q-demodulated. Due to aliasing of the signal spectrum caused by sampling, the image parts will appear next to the desired signal in the spectrum, as shown in Fig. 2.8. These image parts can be easily suppressed by a digital filter (probably IIR). In this way, a feedback path without I/Q-imbalance can be realized.

Considering that the feedback path requires an ADC with relative large BW, the following question may arise: why not use a DAC with a comparable BW instead and apply a single branch up conversion which does not involve I/Q-imbalance (corresponds to a superheterodyne Tx)? The answer is illustrated in Fig. 2.8. After the BB signal is digitally modulated to the IF, only the I-branch of the digital signal is converted to analog signal, resulting in an image part (with regard to the DC-frequency) at $-f_I$. This image is also up converted to the HF frequency and causes severe interference to adjacent channels. To suppress this image part, a HF BP filter is required. Since the DAC BW is limited by technical and cost factors, the frequency separation between the desired signal and the image signal may be small, resulting in difficulties for the BP filter. Furthermore, if the Tx should operate in multiple frequency bands, multiple BP filters (maybe tunable) are required. This results in cost enhancement and flexibility degradation of the Tx.

2.4.2 Synchronization Issue

One practical consideration is the synchronization between the transmit signal and the feedback signal. Since both the LO signals for the corresponding up- and down-conversion are generated from the same reference clock in the Tx device, frequency synchronization is straightforward. However, tiny frequency offset may still be present, which could be the reason for the limited achievable IRR in practice (see Sec. 2.8).

In contrast, time synchronization may be treated differently in different cases. In the case of pilot-based estimation, dedicated pilot sequence can be applied for time synchronization. In the case of semi-blind estimation, the time synchronization has to be carried out based on

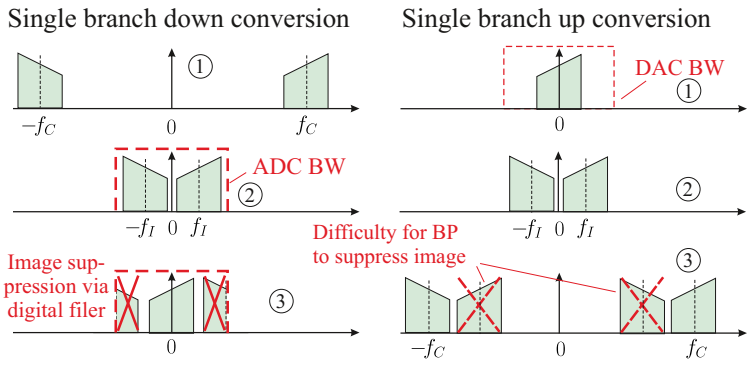

Figure 2.8: Principles of low-IF single branch up/down conversion

the transmitted and feedback versions of the communication signal, probably via correlation between the two versions. The time synchronization accuracy may depend on the characteristic of the communication signal. Generally, the higher the spectral occupancy (see Sec. 2.5) of the communication signal, the better the time synchronization. It will be shown that the parameter estimation algorithms proposed in this chapter are capable of tolerating certain range of time synchronization error.

2.5 Least-Squares (LS) Based Parameter Estimation

2.5.1 Parameter Estimation

From Fig. 2.7, the coefficients to be calculated for the pre-equalization are c, $h^C[n]$ and ζ. According to (2.3), (2.13), (2.15) and (2.10), the desired coefficients can be calculated from $h_\alpha[n]$, $h_\beta[n]$ and d. Since $h_\alpha[n]$ and $h_\beta[n]$ consist of $h_1[n]$, $h_2[n]$, $h_3[n]$ and $h_4[n]$, we just need to jointly estimate the latter four IRs and d. Considering the linear structure of (2.2), LS method is suitable for the estimation.

First, we rewrite (2.2) into the following two equations:

$$v_{\mathrm{re}}[n] = s_{\mathrm{re}}[n] * h_1[n] + s_{\mathrm{im}}[n] * h_2[n] + d_{\mathrm{re}} \tag{2.16}$$

$$v_{\mathrm{im}}[n] = s_{\mathrm{re}}[n] * h_3[n] + s_{\mathrm{im}}[n] * h_4[n] + d_{\mathrm{im}}. \tag{2.17}$$

Then, we concentrate on the estimation of $h_1[n]$, $h_2[n]$ and d_{re} based on (2.16). The estimation of $h_3[n]$, $h_4[n]$ and d_{im} based on (2.17) follows the same principle. Now, we switch to

blockwise observation and extend Eq. (2.16) to the following matrix equations:

$$\boldsymbol{v}_{\mathrm{re}} = \boldsymbol{S}_{\mathrm{Toep,re}}\boldsymbol{h}_1 + \boldsymbol{S}_{\mathrm{Toep,im}}\boldsymbol{h}_2 + d_{\mathrm{re}}\mathbf{1}_{N\times 1}, \tag{2.18}$$

$$\boldsymbol{v}_{\mathrm{im}} = \boldsymbol{S}_{\mathrm{Toep,re}}\boldsymbol{h}_3 + \boldsymbol{S}_{\mathrm{Toep,im}}\boldsymbol{h}_4 + d_{\mathrm{im}}\mathbf{1}_{N\times 1}, \tag{2.19}$$

with $\boldsymbol{v}_{\mathrm{re;im}} = [v_{\mathrm{re;im}}[0], \cdots, v_{\mathrm{re;im}}[N-1]]^T$, $\boldsymbol{h}_{1;2;3;4} = [h_{1;2;3;4}[0], \cdots, h_{1;2;3;4}[L-1]]^T$. N is the observed feedback block length with $N \geq 2L+1$. L is the maximal possible filter length of $h_1[n]$ and $h_2[n]$. $\boldsymbol{S}_{\mathrm{Toep,re;im}}$ is a Toeplitz matrix constructed from the samples $s_{\mathrm{re;im}}[n]$:

$$\boldsymbol{S}_{\mathrm{Toep,re;im}} := \begin{bmatrix} s_{\mathrm{re;im}}[0] & s_{\mathrm{re;im}}[-1] & \cdots & s_{\mathrm{re;im}}[-L+1] \\ s_{\mathrm{re;im}}[1] & s_{\mathrm{re;im}}[0] & \cdots & s_{\mathrm{re;im}}[-L+2] \\ \vdots & \vdots & \ddots & \vdots \\ s_{\mathrm{re;im}}[N-1] & s_{\mathrm{re;im}}[N-2] & \cdots & s_{\mathrm{re;im}}[N-L] \end{bmatrix}. \tag{2.20}$$

Note that the number of required data samples is $N+L-1$, where the number of required feedback samples is N. The index 0 is just defined as the starting time point of the observed signal block and the negative indexes indicate the samples prior to it. Eq. (2.18) can be further rewritten as:

$$\boldsymbol{v}_{\mathrm{re}} = \underbrace{\begin{bmatrix} \eta\mathbf{1}_{N\times 1} & \boldsymbol{S}_{\mathrm{Toep,re}} & \boldsymbol{S}_{\mathrm{Toep,im}} \end{bmatrix}}_{\boldsymbol{S}_{\mathrm{LS}}} \boldsymbol{h}_{12} \tag{2.21}$$

where $\boldsymbol{h}_{12} = \left[\frac{d_{\mathrm{re}}}{\eta}, \boldsymbol{h}_1{}^T, \boldsymbol{h}_2{}^T\right]^T$ with η a real valued scaling factor for adjusting the condition number of $\boldsymbol{S}_{\mathrm{LS}}$ (see Sec. 2.5.4 and 2.5.5). The LS-estimate of $\boldsymbol{h}_{12}$ can be obtained by:

$$\hat{\boldsymbol{h}}_{12} = \boldsymbol{S}_{\mathrm{LS}}^{\dagger}\boldsymbol{v}_{\mathrm{re}}, \tag{2.22}$$

where the estimates of $h_1[n]$, $h_2[n]$ and d_{re} can be extracted from $\hat{\boldsymbol{h}}_{12}$.

In a similar way, $h_3[n]$, $h_4[n]$ and d_{im} can be estimated by:

$$\hat{\boldsymbol{h}}_{34} = \boldsymbol{S}_{\mathrm{LS}}^{\dagger}\boldsymbol{v}_{\mathrm{im}}, \tag{2.23}$$

where $\boldsymbol{h}_{12} = \left[\frac{d_{\mathrm{im}}}{\eta}, \boldsymbol{h}_3{}^T, \boldsymbol{h}_4{}^T\right]^T$. In practice, we can repeat the estimation with many different data signal blocks and then average the results to mitigate random estimation error caused by measurement noise. Compared to the application of very large signal blocks (e.g. $N = 10240$), the application of averaging with relatively small signal blocks (e.g. $N = 64$) may allow simpler implementation.

2.5.2 Calculation of Pre-equalization Coefficients

After the parameter estimation, the coefficient ζ can be easily calculated from (2.10). Let $H_\alpha(\omega)$ and $H_\beta(\omega)$ be the DTFTs of $h_\alpha[n]$ and $h_\beta[n]$, which can be obtained using (2.3). We

define $W(\omega) := H_\beta(\omega)/H_\alpha(\omega)$. From (2.3), we have:

$$W(\omega) = \frac{H_\beta(\omega)}{H_\alpha(\omega)} = \frac{H^{TQ}(\omega) g^T e^{j\varphi^T}}{H^{TI}(\omega)}. \tag{2.24}$$

With (2.13), (2.15) and (2.24), c and $h^C[n]$ can be obtained by:

$$c = \frac{W^{Im}(\omega)}{W^{Re}(\omega)}, \quad h^C[n] = \mathcal{F}^{-1}\left\{\frac{1}{W^{Re}(\omega)}\right\}\Big|_{n-n_\tau}. \tag{2.25}$$

Note that (2.24) and (2.25) imply the following linear convolutions:

$$w[n] * h_\alpha[n] = h_\beta[n], \quad h^C[n+n_\tau] * w_{\mathrm{re}}[n] = \delta[n], \tag{2.26}$$

with $w[n] = \mathcal{F}^{-1}\{W(\omega)\}$. Since DTFTs are unavailable in practice, we have to calculate with DFTs. First, the sequences $h_\alpha[n]$ and $h_\beta[n]$ are zero-padded before their DFTs, $H_\alpha[k]$ and $H_\beta[k]$, are calculated. The number of padded zeros has to be sufficiently large so that the DFT convolution theorem [92] can be applied to the linear convolutions of (2.26). According to (2.24), we calculate $W[k] = H_\beta[k]/H_\alpha[k]$. Finally, with $W^{Re}[k] = 0.5\,(W[k] + W^*[-k])$ and $W^{Im}[k] = -0.5j\,(W[k] - W^*[-k])$, the desired coefficients are obtained:

$$c = \frac{1}{L_F} \sum_{k=-L_F/2}^{L_F/2-1} \frac{W^{Im}[k]}{W^{Re}[k]}, \tag{2.27}$$

$$h^C[n] = \mathcal{F}_{L_F}^{-1}\left\{\mathring{H}^C[k]\right\}\Big|_{((n-n_\tau))_{L_F}}, \tag{2.28}$$

$$\text{with} \quad \mathring{H}^C[k] := \frac{1}{W^{Re}[k]}, \tag{2.29}$$

where L_F is the DFT-length. Moreover, the notation $\mathring{(\bullet)}$ for $\mathring{H}^C[k]$ is used to indicate that it is the transfer function of an anti-causal system. Note that when using DFTs, the linear shift by n_τ in (2.25) corresponds to the circular shift by n_τ with block length L_F in (2.28). In practice, small values at the tail of $h^C[n]$ can be omitted to reduce its length.

In practice, due to the limited steepness of the transfer function of the RLP filters[1], $H_{\alpha;\beta}[k]$ will contain a part of the transition area of the RLPs. Due to the filter attenuation, this part of $H_{\alpha;\beta}[k]$ as well as $W[k]$ may suffer strongly from additive noise. In communication systems, a GB is usually reserved to avoid the transition area of the RLPs. Thus, when calculating c and $h^C[n]$, this area of $W[k]$ does not need to be taken into account, since they do not affect the signal transmission. Based on this consideration, we can select a symmetrical frequency index set $\mathcal{I}_a$ with $|\mathcal{I}_a| = L'$, which excludes the DC frequency and the GBs. Afterwards, c and $h^C[n]$

[1] In the HIL platform in Sec. 2.8, the DACs have internal rate-doubler with digital interpolation filter, so that the steepness requirement for the RLPs is relaxed. However, even the digital interpolation filter has limited steepness in the transition frequency area.

can be calculated by:

$$\begin{aligned} c &= \frac{1}{L'} \sum_{k \in \mathcal{I}_\mathrm{a}} \frac{W^{Im}[k]}{W^{Re}[k]} \\ \hat{\boldsymbol{h}}^C &= \left(\boldsymbol{F}_{(\mathcal{I}_\mathrm{a}, \mathcal{L}^C)}\right)^\dagger \mathring{\boldsymbol{H}}^C_{\mathcal{I}_\mathrm{a}}, \end{aligned} \tag{2.30}$$

where $\mathring{\boldsymbol{H}}^C_{\mathcal{I}_\mathrm{a}} = [\mathring{H}^C[\mathcal{I}_\mathrm{a}(1)], \ldots, \mathring{H}^C[\mathcal{I}_\mathrm{a}(L')]]^T$, $\mathcal{L}^C = \{N - n_\tau, \ldots, N-1, 0, 1, \ldots, L - n_\tau - 1\}$ and $\boldsymbol{h}^C = [h^C[0], \ldots, h^C[L-1]]^T$[1].

2.5.3 Parameter Tracking

The algorithm described in Sec. 2.5.1 and 2.5.2 assumes that the pre-equalizer is not activated and is only suitable for initial calibration. Now, we develop an algorithm to track the parameter changes. Since the parameter change is very slow, we divide the time index into intervals, which should be chosen small enough so that the parameters can be regarded as constant within each interval and the parameter change between consecutive intervals is very small[2]. In each new interval, parameter estimation and coefficient calculation needs only to be carried out once to enable seamless parameter tracking. We denote the old coefficients (in the previous interval) with the notation $\tilde{(\cdot)}$ and the new parameters (in the current interval) without $\tilde{(\cdot)}$, as shown in Fig. 2.9. To maintain sufficient IRR of the system, the pre-equalization should not be shut off during the parameter estimation. Thus, the pre-equalization block must be taken into account in the parameter estimation and coefficient calculation. More concretely, the new coefficients should be obtained based on the $s[n]$, $v[n]$ and the previous pre-equalization coefficients $\tilde{c}$, $\tilde{h}^C[n]$ and $\tilde{\zeta}$. Actually, due to the small intervals, the previous and the new coefficients only have very small difference. However, in the long term, parameter changes can be tracked. Note that $\hat{s}[n]$ is not used as reference signal, because the pre-equalization introduces correlation between its I- and Q-branches and offsets, which can lead to unreliable parameter estimates.

As shown in Fig. 2.10, the equivalent BB models with and without the pre-equalizer can have the same structure i.e. with four FIR filters. To distinguish both models, we use the notation $\breve{(\bullet)}$ for the FIR filters in the model with pre-equalizer, which can be written as:

$$\begin{aligned} v[n] &= \Big(s_\mathrm{re}[n] * \breve{h}_1[n] + s_\mathrm{im}[n] * \breve{h}_2[n]\Big) \\ &\quad + j\Big(s_\mathrm{re}[n] * \breve{h}_3[n] + s_\mathrm{im}[n] * \breve{h}_4[n]\Big) + \breve{d} \\ &= s_\mathrm{re}[n] * \breve{h}_\alpha[n] + j s_\mathrm{im}[n] * \breve{h}_\beta[n] + \breve{d}. \end{aligned} \tag{2.31}$$

[1] The estimation of $\boldsymbol{h}^C$ in (2.30) is based on the observation $\mathring{\boldsymbol{H}}^C_{\mathcal{I}_\mathrm{a}} = \boldsymbol{F}_{(\mathcal{I}_\mathrm{a}, \mathcal{L}^C)} \boldsymbol{h}^C$.

[2] Small in the sense that the calibration at the end of an interval using parameters estimated at the beginning of this interval has only negligible performance degradation (compared to the beginning of this interval).

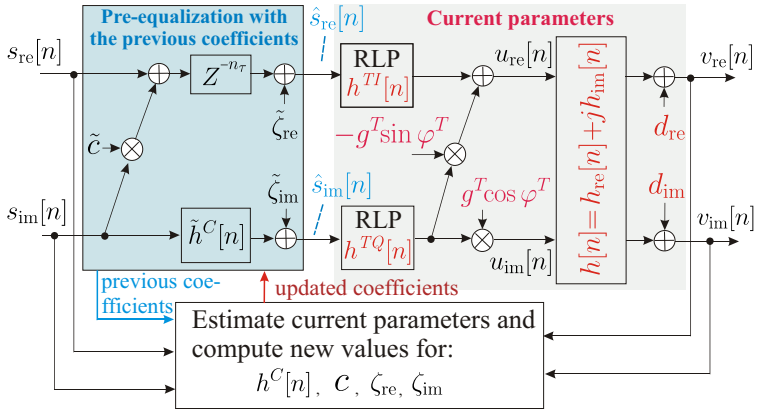

Figure 2.9: Adaptive parameter tracking scheme

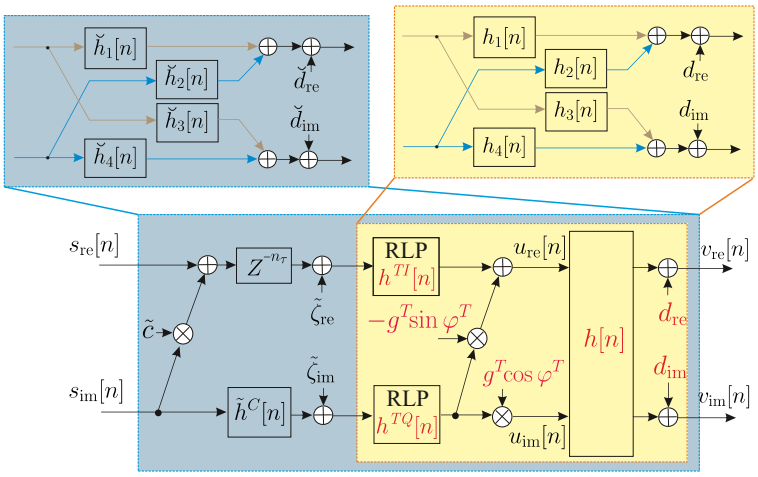

Figure 2.10: Equivalent signal models for parameter tracking

Furthermore, the following relations exist:

$$\begin{aligned}
\breve{h}_\alpha[n] &= \breve{h}_1[n] + j\breve{h}_3[n] = h_\alpha[n - n_\tau] \\
\breve{h}_\beta[n] &= \breve{h}_4[n] - j\breve{h}_2[n] = \tilde{h}^C[n] * h_\beta[n] + j\tilde{c}\breve{h}_\alpha[n] \\
\breve{d} &= \tilde{\zeta}_{\mathrm{re}} \sum_{n=0}^{L_0-1} h_\alpha[n] + j\tilde{\zeta}_{\mathrm{im}} \sum_{n=0}^{L_0-1} h_\beta[n] + d_{\mathrm{re}} + jd_{\mathrm{im}}
\end{aligned} \tag{2.32}$$

with $h_\alpha[n]$ and $h_\beta[n]$ defined as in (2.3). With the LS method in section 2.5.1, $\breve{h}_\alpha[n]$, $\breve{h}_\beta[n]$ and $\breve{d}$ can be estimated. From (2.32), we can compute the following quantities:

$$\begin{aligned}
&h_\alpha[n] = \breve{h}_\alpha[n + n_\tau], \\
&h_\theta[n] := \breve{h}^C[n] * h_\beta[n] = \breve{h}_\beta[n] - j\tilde{c}\breve{h}_\alpha[n].
\end{aligned} \tag{2.33}$$

Let $H_\theta(\omega)$ and $\tilde{H}^C(\omega)$ be the DTFTs of $h_\theta[n]$ and $\tilde{h}^C[n]$, respectively. From (2.33), we have:

$$H_\beta(\omega) = \frac{H_\theta(\omega)}{\tilde{H}^C(\omega)}. \tag{2.34}$$

With (2.34) and (2.24), we obtain

$$W(\omega) = \frac{H_\theta(\omega)}{\tilde{H}^C(\omega) H_\alpha(\omega)}. \tag{2.35}$$

Then, the desired coefficients for I/Q-imbalance compensation can be calculated with (2.25). In practice, DFT-based methods are used as described in section 2.5.2.

Now, the coefficients for DC-offset compensation should be calculated from $\breve{d}$. We first aim at obtaining $d = d_{\mathrm{re}} + jd_{\mathrm{im}}$ from (2.32). Instead of directly calculating $h_\beta[n]$, we only have to calculate $\sum_{n=0}^{L_0-1} h_\beta[n]$. With (2.33), the following relation can be derived:

$$\begin{aligned}
\sum_{n=0}^{2L_0-1} h_\theta[n] &= \sum_{n=0}^{2L_0-1} \left(\tilde{h}^C[n] * h_\beta[n] \right) \\
&= \sum_{n=0}^{L_0-1} h_\beta[n] \sum_{n=0}^{L_0-1} \tilde{h}^C[n],
\end{aligned} \tag{2.36}$$

with which we can compute $\sum_{n=0}^{L_0-1} h_\beta[n]$ from $h_\theta[n]$. With (2.32) and (2.36), d can be easily computed:

$$d = \breve{d} - \tilde{\zeta}_{\mathrm{re}} \sum_{n=0}^{L_0-1} h_\alpha[n] - j\tilde{\zeta}_{\mathrm{im}} \frac{\sum_{n=0}^{2L_0-1} h_\theta[n]}{\sum_{n=0}^{L_0-1} \tilde{h}^C[n]}. \tag{2.37}$$

Then, we will compute ζ with (2.10), which requires the terms $\sum_{n=0}^{L_0-1} h_{1;2;3;4}[n]$. While $h_1[n]$ and $h_3[n]$ can be directly obtained from $h_\alpha[n]$, the terms $\sum_{n=0}^{L_0-1} h_2[n]$ and $\sum_{n=0}^{L_0-1} h_4[n]$

are computed according to (2.3) and (2.36) as:

$$\begin{aligned}\sum_{n=0}^{L_0-1} h_2[n] &= -\frac{\mathcal{I}m\left\{\sum_{n=0}^{2L_0-1} h_\theta[n]\right\}}{\sum_{n=0}^{L_0-1} \tilde{h}^C[n]} \\ \sum_{n=0}^{L_0-1} h_4[n] &= \frac{\mathcal{R}e\left\{\sum_{n=0}^{2L_0-1} h_\theta[n]\right\}}{\sum_{n=0}^{L_0-1} \tilde{h}^C[n]}.\end{aligned} \tag{2.38}$$

Finally, ζ is computed with (2.10) and the new coefficients are fed to the pre-equalization block. In this way, seamless and simple parameter tracking is realized.

2.5.4 Matrix Condition Improvement for Pilot-Based Estimation

The condition number of matrix $\boldsymbol{S}_{\mathrm{LS}}$ in the LSE of (2.22) and (2.23) has significant influence on the reliability of the parameter estimates, which is crucial for the compensation performance. Actually, this is a general problem of the LSE. Here, we will analyze this problem in the context of joint I/Q-imbalance and DC-offset estimation and provide practical solution in this section and also Sec. 2.5.5.

In the case of pilot-based estimation, the pilot signal can be optimized to achieve the minimum condition number of $\boldsymbol{S}_{\mathrm{LS}}$ i.e. $\mathrm{cond}\left(\boldsymbol{S}_{\mathrm{LS}}\right) = 1$. In this case, the columns of $\boldsymbol{S}_{\mathrm{LS}}$ are all orthonormal to each other. Thus, $\boldsymbol{S}_{\mathrm{LS}}^{\dagger} = \boldsymbol{S}_{\mathrm{LS}}^{T}$. By defining

$$\boldsymbol{s}_{\mathrm{re;im}}[n] := [s_{\mathrm{re;im}}[n], \ldots, s_{\mathrm{re;im}}[n+N-1]]^T$$

, this orthonormality can be expressed as the following four conditions:

$$\begin{aligned}&\boldsymbol{s}_{\mathrm{re;im}}[n]^T \boldsymbol{s}_{\mathrm{re;im}}[m] = 0, n, m \in [-L+1, 0], n \neq m, \\ &\boldsymbol{s}_{\mathrm{re}}[n]^T \boldsymbol{s}_{\mathrm{im}}[m] = 0, \forall n, m \in [-L+1, 0], \\ &\mathbf{1}_{1\times N} \boldsymbol{s}_{\mathrm{re;im}}[n] = \mathrm{sum}(\boldsymbol{s}_{\mathrm{re;im}}[n]) = 0, n \in [-L+1, 0], \\ &||\boldsymbol{s}_{\mathrm{re;im}}[n]||_2 = ||\eta \mathbf{1}_{N\times 1}||_2 = \eta\sqrt{N}, n \in [-L+1, 0].\end{aligned} \tag{2.39}$$

Let $s[n], \forall n = 0, \ldots, N-1$ be the pilot sequence. If a CP of length $L-1$ can be attached to this pilot sequence, the columns $\boldsymbol{s}_{\mathrm{re;im}}[m], \forall m = -L+1, \ldots, -1$ are just the circularly shifted versions of $\boldsymbol{s}_{\mathrm{re;im}}[0]$ by a shift m. This inspires the idea of using sequences with perfect Periodical-Auto-Correlation-Function (PACF). Since perfect PACF is equivalent to DFT with constant magnitude, we can construct such sequences easily in the frequency domain. First, we construct a length-N DFT sequence $S_{\mathrm{P},1}[k], \forall k = -\frac{N}{2}, \ldots, \frac{N}{2} - 1$ with $|S_{\mathrm{P},1}[k]| = 1, \forall k$ and a conjugate symmetric structure. Its IDFT is a real valued sequence $s_{\mathrm{P},1}[n], \forall n = 0, \ldots, N-1$ with PACF. Afterwards, we can construct another real valued sequence $s_{\mathrm{P},2}[n] = s_{\mathrm{P},1}[((n-L))_N]$ and use $s[n] = s_{\mathrm{P},1}[n] + j s_{\mathrm{P},2}[n]$ as the pilot sequence, which is attached a CP. By setting $\eta = 1$, the columns of $\boldsymbol{S}_{\mathrm{LS}}$ consist of $\mathbf{1}_{N\times 1}$ and circularly shifted versions of the sequence

$s_{\mathrm{P},1}[n]$ with $2L$ different shifts. Due to the PACF of $s_{\mathrm{P},1}[n]$, the first two requirements in (2.39) are fulfilled. The third requirement of (2.39) implies that $s_{\mathrm{P},1}[n]$ has zero mean. This can be achieved by setting $S_{\mathrm{P},1}[0] = 0$. After this modification, the PACF values of $s_{\mathrm{P},1}[n]$ will have a small offset of $-\frac{1}{N}$. Since this offset is relatively small, the first two requirements in (2.39) are still approximately fulfilled. The fourth requirement in (2.39) can be easily achieved by scaling $s_{\mathrm{P},1}[n]$ with $\sqrt{N}$.

2.5.5 Matrix Condition Improvement for Semi-Blind Estimation

In the case of semi-blind estimation, the condition number depends on the characteristics of the communication signal $s[n]$. In the following, we will first give an analysis of the condition number according to the signal characteristics and then provide a practical way to solve the ill-conditioned problem.

Although asymptotic bounds on the eigenvalues and the condition numbers of auto-correlation matrices were already given in text books e.g. [93], they can not be applied here directly to analyze $\boldsymbol{S}_{\mathrm{LS}}$, since $\boldsymbol{S}_{\mathrm{LS}}$ has a different structure. In the following, we will find out the relation between the condition number of $\boldsymbol{S}_{\mathrm{LS}}$ and the spectral characteristic of $s[n]$. Furthermore, we will show that the filter order L plays an important role on the matrix condition.

2.5.5.1 Matrix Condition Analysis

First, we assume that $N \geq 2L+1$ and denote the $2L+1$ singular values of $\boldsymbol{S}_{\mathrm{LS}}$ as:

$$\sigma_1\left(\boldsymbol{S}_{\mathrm{LS}}\right) \geq \sigma_2\left(\boldsymbol{S}_{\mathrm{LS}}\right) \geq \ldots \geq \sigma_{2L+1}\left(\boldsymbol{S}_{\mathrm{LS}}\right), \tag{2.40}$$

with $\sigma_m\left(\boldsymbol{S}_{\mathrm{LS}}\right) \geq 0, \forall m$ [1]. The condition number of $\boldsymbol{S}_{\mathrm{LS}}$ can be expressed as:

$$\kappa\left(\boldsymbol{S}_{\mathrm{LS}}\right) = \frac{\sigma_1\left(\boldsymbol{S}_{\mathrm{LS}}\right)}{\sigma_{2L+1}\left(\boldsymbol{S}_{\mathrm{LS}}\right)}. \tag{2.41}$$

For further analysis, we define $\boldsymbol{R} := \frac{1}{N}\boldsymbol{S}_{\mathrm{LS}}^H\boldsymbol{S}_{\mathrm{LS}}$, which is a $(2L+1)\times(2L+1)$ positive semi-definite symmetric matrix. Let $\lambda_m\left(\boldsymbol{R}\right), m = 1, \ldots, 2L+1$ be the eigenvalues of $\boldsymbol{R}$ in descending order (w.r.t m). We have $\lambda_m\left(\boldsymbol{R}\right) \in \Re$ and $\lambda_m\left(\boldsymbol{R}\right) = \frac{1}{N}\sigma_m^2\left(\boldsymbol{S}_{\mathrm{LS}}\right)$. Thus, the following relation of condition numbers exists:

$$\kappa\left(\boldsymbol{R}\right) = \frac{\lambda_1\left(\boldsymbol{R}\right)}{\lambda_{2L+1}\left(\boldsymbol{R}\right)} = \kappa^2\left(\boldsymbol{S}_{\mathrm{LS}}\right), \tag{2.42}$$

which implies that the condition number of $\boldsymbol{S}_{\mathrm{LS}}$ can be revealed by that of $\boldsymbol{R}$. It will be shown that using the matrix $\boldsymbol{R}$ favors the condition number analysis based on the statistical characteristics of $s[n]$, e.g. the Auto-Correlation Function (ACF) of $s_{\mathrm{re;im}}[n]$ and the Cross-Correlation Function (CCF) between $s_{\mathrm{re}}[n]$ and $s_{\mathrm{im}}[n]$.

[1] Singular values are non-negative real numbers.

Now, we rewrite $\boldsymbol{R}$ as following:

$$\boldsymbol{R} = \begin{bmatrix} \eta^2 & \boldsymbol{\mu}_{s_{\mathrm{re}}}^T & \boldsymbol{\mu}_{s_{\mathrm{im}}}^T \\ \boldsymbol{\mu}_{s_{\mathrm{re}}} & \boldsymbol{R}_{s_{\mathrm{re}},s_{\mathrm{re}}} & \boldsymbol{R}_{s_{\mathrm{re}},s_{\mathrm{im}}} \\ \boldsymbol{\mu}_{s_{\mathrm{im}}} & \boldsymbol{R}_{s_{\mathrm{im}},s_{\mathrm{re}}} & \boldsymbol{R}_{s_{\mathrm{im}},s_{\mathrm{im}}} \end{bmatrix}, \tag{2.43}$$

where

$$\begin{aligned} \boldsymbol{\mu}_{s_{\mathrm{re;im}}} &:= \frac{\eta}{N} \left[\mathbf{1}_{1\times N} \boldsymbol{s}_{\mathrm{re;im}}[0], \ldots, \mathbf{1}_{1\times N} \boldsymbol{s}_{\mathrm{re;im}}[-L+1] \right]^T, \\ \boldsymbol{R}_{s_\Pi, s_\Lambda} &:= \frac{1}{N} \boldsymbol{S}_{\mathrm{Toep},\Pi}^T \boldsymbol{S}_{\mathrm{Toep},\Lambda}, \forall \Pi, \Lambda \in \{\mathrm{re}, \mathrm{im}\}, \\ \boldsymbol{s}_{\mathrm{re;im}}[n] &:= \left[s_{\mathrm{re;im}}[n], \ldots, s_{\mathrm{re;im}}[n+N-1] \right]^T. \end{aligned} \tag{2.44}$$

Note that $\boldsymbol{R}_{s_\Pi, s_\Lambda}, \forall \Pi, \Lambda \in \{\mathrm{re}, \mathrm{im}\}$, i.e. $\boldsymbol{R}_{s_{\mathrm{re}},s_{\mathrm{re}}}, \boldsymbol{R}_{s_{\mathrm{im}},s_{\mathrm{im}}}, \boldsymbol{R}_{s_{\mathrm{re}},s_{\mathrm{im}}}, \boldsymbol{R}_{s_{\mathrm{im}},s_{\mathrm{re}}}$, are Toeplitz matrices. Specifically, $\boldsymbol{R}_{s_\Pi, s_\Pi}, \forall \Pi \in \{\mathrm{re}, \mathrm{im}\}$ is a positive semi-definite symmetric Toeplitz matrix. Assuming $s[n]$ to be a zero-mean Wide-Sense-Stationary (WSS) stochastic process and $N \to \infty$, we have

$$\begin{aligned} \boldsymbol{\mu}_{s_{\mathrm{re}}} &= \boldsymbol{\mu}_{s_{\mathrm{im}}} = \mathbf{0}_{L\times 1}, \\ \left(\boldsymbol{R}_{s_\Pi, s_\Lambda}\right)_{k,l} &= R_{s_\Pi, s_\Lambda}[k-l], \forall k, l \in [0, L-1], \forall \Pi, \Lambda \in \{\mathrm{re}, \mathrm{im}\}, \end{aligned} \tag{2.45}$$

where

$$R_{s_\Pi, s_\Lambda}[l] := E\left\{ s_\Pi[n] s_\Lambda[n+l] \right\}, \forall \Pi, \Lambda \in \{\mathrm{re}, \mathrm{im}\} \tag{2.46}$$

is the correlation function between $s_\Pi[n]$ and $s_\Lambda[n]$ [1]. With (2.45), $\boldsymbol{R}$ can be further rewritten as:

$$\boldsymbol{R} = \begin{bmatrix} \eta^2 & \mathbf{0}_{2L\times 1}^T \\ \mathbf{0}_{2L\times 1} & \check{\boldsymbol{R}} \end{bmatrix}. \tag{2.47}$$

where

$$\check{\boldsymbol{R}} := \begin{bmatrix} \boldsymbol{R}_{s_{\mathrm{re}},s_{\mathrm{re}}} & \boldsymbol{R}_{s_{\mathrm{re}},s_{\mathrm{im}}} \\ \boldsymbol{R}_{s_{\mathrm{im}},s_{\mathrm{re}}} & \boldsymbol{R}_{s_{\mathrm{im}},s_{\mathrm{im}}} \end{bmatrix}. \tag{2.48}$$

Lemma 1. *From (2.47), the set of eigenvalues of $\boldsymbol{R}$ consists of η^2 and all eigenvalues of $\check{\boldsymbol{R}}$.*

The proof of Lemma 1 is given in App. A.2.

Lemma 2. *With the following value of η:*

$$\eta = \frac{1}{\sqrt{2NL}} \left|\left| \check{\boldsymbol{S}}_{\mathrm{LS}} \right|\right|_F, \tag{2.49}$$

[1] From (2.44), we have $\left(\boldsymbol{R}_{s_\Pi, s_\Lambda}\right)_{k,l} = \frac{1}{N} \sum_{n=0}^{N-1} s_\Pi[n-k] s_\Lambda[n-l]$. Here, we assumed that the correlation functions can be approximated by $R_{s_\Pi, s_\Lambda}[l] = \lim_{N\to\infty} \frac{1}{N} \sum_{n=0}^{N-1} s_\Pi[n] s_\Lambda[n+l]$.

we can ensure $\lambda_{2L}\left(\check{\boldsymbol{R}}\right) \leq \eta^2 \leq \lambda_1\left(\check{\boldsymbol{R}}\right)$ *and thus*

$$\kappa\left(\boldsymbol{R}\right) = \kappa\left(\check{\boldsymbol{R}}\right) = \frac{\lambda_1\left(\check{\boldsymbol{R}}\right)}{\lambda_{2L}\left(\check{\boldsymbol{R}}\right)}, \tag{2.50}$$

which implies that we just need to concentrate on the condition number analysis of $\check{\boldsymbol{R}}$*.*

The proof of Lemma 2 is given in App. A.3.

Considering that $\check{\boldsymbol{R}}$ is a symmetric (Hermitian) block matrix with Toeplitz blocks, as defined in Eq. (4) of [94], the eigenvalue bounds of [94] can be applied. To apply these bounds, we first define:

$$\acute{\Phi}_{s_\Pi,s_\Lambda}(\omega, L) := \sum_{l=-L+1}^{L-1} R_{s_\Pi,s_\Lambda}[l] e^{-j\omega n}, \forall \Pi, \Lambda \in \{\mathrm{re}, \mathrm{im}\}, \tag{2.51}$$

$$\acute{\Phi}_{s,s}(\omega, L) := \sum_{l=-L+1}^{L-1} R_{s,s}[l] e^{-j\omega n} = \acute{\Phi}_{s_{\mathrm{re}},s_{\mathrm{re}}}(\omega, L) + \jmath m\left\{\acute{\Phi}_{s_{\mathrm{re}},s_{\mathrm{im}}}(\omega, L)\right\}, \tag{2.52}$$

with $R_{s,s}[l] := \frac{1}{2} E\left\{s[n] s^*[n+l]\right\}$ the ACF of $s[n]$. Note that

$$\begin{aligned} \lim_{L\to\infty} \acute{\Phi}_{s_\Pi,s_\Lambda}(\omega, L) &= \Phi_{s_\Pi,s_\Lambda}(\omega), \forall \Pi, \Lambda \in \{\mathrm{re}, \mathrm{im}\}, \\ \lim_{L\to\infty} \acute{\Phi}_{s,s}(\omega, L) &= \Phi_{s,s}(\omega), \end{aligned} \tag{2.53}$$

where $\Phi_{s_\Pi,s_\Lambda}(\omega), \forall \Pi, \Lambda \in \{\mathrm{re}, \mathrm{im}\}$ and $\Phi_{s,s}(\omega, L)$ are Power Spectral Densities (PSD) as defined in (A.1.6) of App. A.1. Moreover, we assume that $s[n]$ is a proper stochastic process [95][1]. Thus, the properties of $\Phi_{s_\Pi,s_\Lambda}(\omega), \forall \Pi, \Lambda \in \{\mathrm{re}, \mathrm{im}\}$ and $\Phi_{s,s}(\omega, L)$ in App. A.1, e.g. (A.1.8), (A.1.9), (A.1.11), (A.1.12) and (A.1.13) can be applied, which also hold for $\acute{\Phi}_{s_\Pi,s_\Lambda}(\omega, L), \forall \Pi, \Lambda \in \{\mathrm{re}, \mathrm{im}\}$ and $\acute{\Phi}_{s,s}(\omega, L)$[2]. According to [94], the eigenvalues of $\check{\boldsymbol{R}}$ is bounded by:

$$\min_\omega \lambda_2\left(\acute{\boldsymbol{\Phi}}(\omega, L)\right) \leq \lambda_m\left(\check{\boldsymbol{R}}\right) \leq \max_\omega \lambda_1\left(\acute{\boldsymbol{\Phi}}(\omega, L)\right), \forall 1 \leq m \leq 2L, \tag{2.54}$$

where

$$\acute{\boldsymbol{\Phi}}(\omega, L) := \begin{bmatrix} \acute{\Phi}_{s_{\mathrm{re}},s_{\mathrm{re}}}(\omega, L) & \acute{\Phi}_{s_{\mathrm{re}},s_{\mathrm{im}}}(\omega, L) \\ \acute{\Phi}_{s_{\mathrm{im}},s_{\mathrm{re}}}(\omega, L) & \acute{\Phi}_{s_{\mathrm{im}},s_{\mathrm{im}}}(\omega, L) \end{bmatrix} \tag{2.55}$$

is a 2×2 matrix and $\lambda_{1;2}\left(\acute{\boldsymbol{\Phi}}(\omega, L)\right)$ are the eigenvalues of $\acute{\boldsymbol{\Phi}}(\omega, L)$. To characterize the eigenvalue bounds, the characteristics of $\lambda_{1;2}\left(\acute{\boldsymbol{\Phi}}(\omega, L)\right)$ are desired. From (A.1.9) and (A.1.11) in App.

[1] Most practical complex-alphabet-based communication signals are approximately proper[96]. Moreover, according to [97], the baseband representation of a band-pass stationary stochastic process has to be proper.

[2] $\acute{\Phi}_{s_\Pi,s_\Lambda}(\omega, L)$ and $\acute{\Phi}_{s,s}(\omega, L)$ can be seen as the DFT of the symmetrically windowed versions of $R_{s_\Pi,s_\Lambda}[l]$ and $R_{s,s}[l]$, respectively. Since the symmetrical windowing does not change the properties from (A.1.1) to (A.1.5), $\acute{\Phi}_{s_\Pi,s_\Lambda}(\omega, L)$ and $\acute{\Phi}_{s,s}(\omega, L)$ follow the corresponding properties of $\Phi_{s_\Pi,s_\Lambda}(\omega)$ and $\Phi_{s,s}(\omega)$, respectively.

A.1,

$$\acute{\Phi}_{s_{\mathrm{im}},s_{\mathrm{re}}}(\omega,L)=-\acute{\Phi}_{s_{\mathrm{re}},s_{\mathrm{im}}}(\omega,L), \tag{2.56}$$

which yields

$$\acute{\boldsymbol{\Phi}}(\omega,L)=\begin{bmatrix}\acute{\Phi}_{s_{\mathrm{re}},s_{\mathrm{re}}}(\omega,L) & \acute{\Phi}_{s_{\mathrm{re}},s_{\mathrm{im}}}(\omega,L)\\ -\acute{\Phi}_{s_{\mathrm{re}},s_{\mathrm{im}}}(\omega,L) & \acute{\Phi}_{s_{\mathrm{re}},s_{\mathrm{re}}}(\omega,L)\end{bmatrix}. \tag{2.57}$$

From (2.57), the eigenvalues of $\acute{\boldsymbol{\Phi}}(\omega,L)$ can be expressed as:

$$\lambda_{1;2}\left(\acute{\boldsymbol{\Phi}}(\omega,L)\right)\in\left\{\acute{\Phi}_{s_{\mathrm{re}},s_{\mathrm{re}}}(\omega,L)\pm j\acute{\Phi}_{s_{\mathrm{re}},s_{\mathrm{im}}}(\omega,L)\right\}. \tag{2.58}$$

By definition, we have $\lambda_1\left(\acute{\boldsymbol{\Phi}}(\omega,L)\right)\geq\lambda_2\left(\acute{\boldsymbol{\Phi}}(\omega,L)\right)$. Recalling from App. A.1 that $\acute{\Phi}_{s_{\mathrm{re}},s_{\mathrm{im}}}(\omega,L)\in\mathbb{I}$ and $\acute{\Phi}_{s_{\mathrm{re}},s_{\mathrm{im}}}(-\omega,L)=-\acute{\Phi}_{s_{\mathrm{re}},s_{\mathrm{im}}}(\omega,L)$, we obtain

$$\begin{aligned}\lambda_1\left(\acute{\boldsymbol{\Phi}}(\omega,L)\right)&=\acute{\Phi}_{s_{\mathrm{re}},s_{\mathrm{re}}}(\omega,L)+\left|\acute{\Phi}_{s_{\mathrm{re}},s_{\mathrm{im}}}(\omega,L)\right|,\\ \lambda_2\left(\acute{\boldsymbol{\Phi}}(\omega,L)\right)&=\acute{\Phi}_{s_{\mathrm{re}},s_{\mathrm{re}}}(\omega,L)-\left|\acute{\Phi}_{s_{\mathrm{re}},s_{\mathrm{im}}}(\omega,L)\right|.\end{aligned} \tag{2.59}$$

Finally, combining (A.1.13) in App. A.1 and Eq. (2.54), (2.59), the following eigenvalue bounds can be derived:

$$\min_{\omega}\acute{\Phi}_{s,s}(\omega,L)\leq\lambda_m\left(\check{\boldsymbol{R}}\right)\leq\max_{\omega}\acute{\Phi}_{s,s}(\omega,L),\ \forall 1\leq m\leq 2L. \tag{2.60}$$

According to (2.50), (2.42) and (2.60), the condition numbers of $\boldsymbol{R}$ and $\boldsymbol{S}_{\mathrm{LS}}$ are bounded by

$$\kappa\left(\boldsymbol{R}\right)\leq\frac{\max_{\omega}\acute{\Phi}_{s,s}(\omega,L)}{\min_{\omega}\acute{\Phi}_{s,s}(\omega,L)}\quad\text{and}\quad\kappa\left(\boldsymbol{S}_{\mathrm{LS}}\right)\leq\sqrt{\frac{\max_{\omega}\acute{\Phi}_{s,s}(\omega,L)}{\min_{\omega}\acute{\Phi}_{s,s}(\omega,L)}}, \tag{2.61}$$

respectively. Furthermore, the following equations can be obtained from [94],

$$\begin{aligned}&\lim_{L\to\infty}\lambda_{2L}\left(\check{\boldsymbol{R}}\right)=\min_{\omega}\Phi_{s,s}(\omega),\quad\lim_{L\to\infty}\lambda_1\left(\check{\boldsymbol{R}}\right)=\max_{\omega}\Phi_{s,s}(\omega),\\ &\lim_{L\to\infty}\kappa\left(\boldsymbol{R}\right)=\frac{\max_{\omega}\Phi_{s,s}(\omega)}{\min_{\omega}\Phi_{s,s}(\omega)},\quad\lim_{L\to\infty}\kappa\left(\boldsymbol{S}_{\mathrm{LS}}\right)=\sqrt{\frac{\max_{\omega}\Phi_{s,s}(\omega)}{\min_{\omega}\Phi_{s,s}(\omega)}},\end{aligned} \tag{2.62}$$

which provide the convergence trends of the corresponding eigenvalues and condition numbers.

2.5.5.2 Practical Interpretation of the Condition Number Bound

In practice, if N is large enough, Eq. (2.61) provides an asymptotic bound on the condition number. From (2.61), we can see that if $\max_{\omega}\acute{\Phi}_{s,s}(\omega)=\infty$ or $\min_{\omega}\acute{\Phi}_{s,s}(\omega)=0$, we may have $\kappa\left(\boldsymbol{S}_{\mathrm{LS}}\right)\to\infty$ i.e. $\boldsymbol{R}$ becomes singular. Since practical communication signals have finite PSD, spectral gaps in the communication signals is the main reason for ill-conditioned data matrix

in the LSE[1]. This problem can be interpreted as follows: Within the spectral gaps of the input signal, no signal components are available for the estimation of the corresponding frequency components of the desired transfer functions. Thus, the estimation error at these frequency components can be arbitrarily large. When applying LSE, estimation errors at these frequency components may propagate to the entire signal band, resulting in severe overall estimation error.

Interestingly, when $L \neq \infty$, $\acute{\Phi}_{s,s}(\omega, L)$ (instead of $\Phi_{s,s}(\omega)$) determines the bound of the condition number. Actually, Eq. (2.52) can be viewed as the Fourier transform of a windowed version of the sequence $R_{s,s}[l]$. Thus, $\acute{\Phi}_{s,s}(\omega)$ is actually the convolution result of $\Phi_{s,s}(\omega)$ and the DFT of a length-$2L-1$ rectangular window function. Since the DFT of the rectangular window function is sinc($\bullet$) shaped and has relative strong sidelobes, the spectral convolution results in a slightly spreading of the spectral power of the signal (also called "spectral leakage"). Thus, the spectral gaps in $\Phi_{s,s}(\omega)$ can be slightly "filled" by this spreading, resulting in a reduced condition number (compared to $L = \infty$). The condition number reduction due to this spreading is dependent on the size of the spectral gaps. Generally, the smaller the spectral gaps, the stronger the condition number reduction.

Fig. 2.11 shows the condition number as a function of the number of active subbands in an MB UMTS signal[2], where different L values were applied. The MB UMTS signal has a total BW of 40 MHz, while the BW of each subband is 5 MHz. For illustration, the corresponding spectra of MB UMTS signals with only one active subband and with 8 active subbands are shown in Fig. 2.12 and Fig. 2.13, respectively. For the results in Fig. 2.11, $N = 4096$ was used. As shown in Fig. 2.11, the higher the number of active subbands, the less spectral gaps there are in the signal, resulting in a lower condition number. Moreover, the smaller L is, the smaller the condition number.

Fig. 2.14 shows the condition number as a function of L for different signal types, which have different amount of spectral gaps. The "RAND" signal is a complex valued random sequence, which has no spectral gaps. The LTE signal was generated according to the 3GPP standard. It is an OFDM signal with 20 MHz BW, 30.72 MHz sampling frequency, 2048 subcarriers and CPs of 144 samples. The corresponding signal spectrum is shown in Fig. 2.15. The relatively large GB can be regarded as a relatively large spectral gap. The "MB UMTS-F"- and "MB UMTS-S" signals are those shown in Fig. 2.13 and Fig. 2.12, respectively. For all signals, $N = 4096$ was used. As shown in Fig. 2.14, the larger the value of L, the higher the condition number. The increase rate of the condition number differs from signal to signal. Generally, the more spectral gaps a signal has, the faster the initial condition number increase. Furthermore, the

[1] In practice, the PSD within the spectral gaps can not be exactly zero. Generally, the closer the PSD in the spectral gaps to zero, the higher the condition number.

[2] The active subband indexes are listed as follows: $\{3\}$ for 1 subband; $\{-1, 1\}$ for 2 subbands; $\{-1, 1, 2\}$ for 3 subbands; $\{-2 : 1 : 2\}$ for 4 subbands; $\{-2 : 1 : 3\}$ for 5 subbands; $\{-3 : 1 : 3\}$ for 6 subbands; $\{-3 : 1 : 4\}$ for 7 subbands; $\{-4 : 1 : 4\}$ for 8 subbands. Note that even with the same number of active subbands, the variation of the active subband locations can lead to variation of the condition number, since the effect of spectral spreading (due to a limited L) would be different.

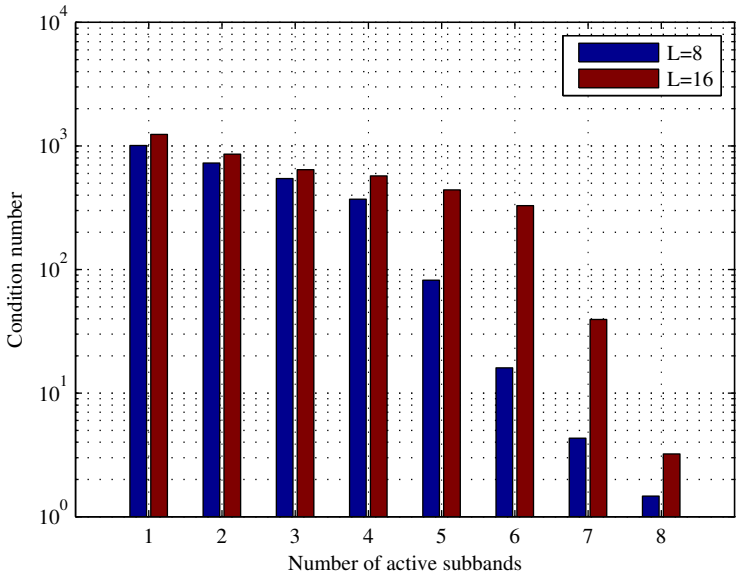

Figure 2.11: Condition number as a function of the number of active subbands in an MB UMTS signal. Different L values were applied. Furthermore, $N = 4096$.

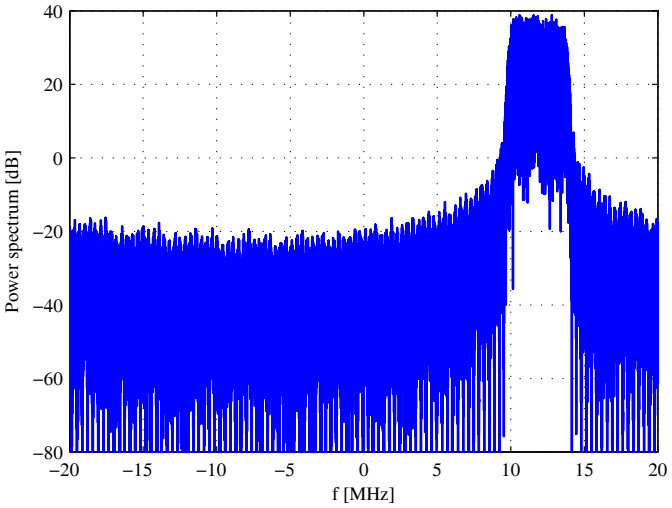

Figure 2.12: PSD of a MB UMTS signal where only one subband is active

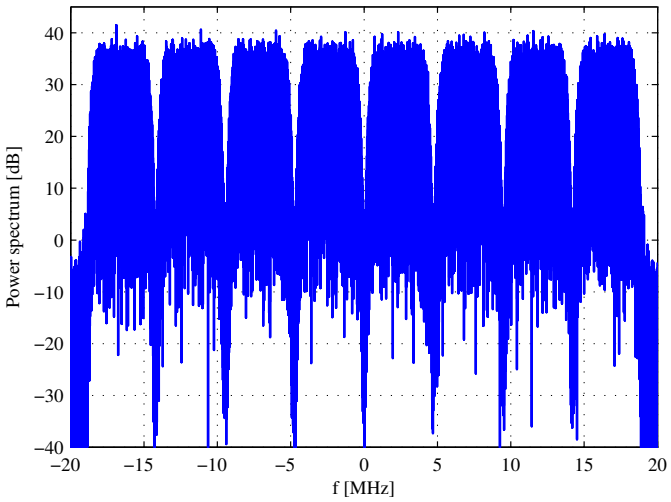

Figure 2.13: PSD of a MB UMTS signal where all 8 subbands are active

condition number increase corresponding to the signals with larger spectral gaps, e.g. LTE and MB UMTS-S, tend to reach saturation with smaller L.

Finally, Fig. 2.16 shows the influence of the block length N on the condition number. As shown, except for the LTE signal, the influence of N is quite small. Thus, the eigenvalue analysis results can also be applied for small N values. For the LTE signal, there exists a threshold for N. When N is below this threshold, the condition number of the LTE signal is even higher than that of the "MB UMTS-S" signal. The reason was that with such N values, the spectral power within the GB of the LTE signal was lower than that within the spectral gaps of an MB UMTS-S signal[1].

2.5.5.3 Practical Solution for Ill-Conditioned Problem

Based on the discussion in Sec. 2.5.5.2, the ill-conditioned matrix problem can be generally solved by refilling the spectral gaps of the Tx signal before it is passed to the DACs or to the pre-equalizer. It was suggested in [47] to add "artificial" low level white circular noise to the Tx signal and the feedback signal before the LS estimation is carried out. Note that such "artificial" noise is not transmitted and is used to obtain a flat frequency response of the pre-equalizer in the spectral gaps. As a result, the I/Q-imbalance in the spectral gaps remains uncompensated [2]. Moreover, if the spectral gaps are asymmetric (w.r.t. the DC-frequency), a part of the I/Q-imbalance within the active signal frequency will remain uncompensated. Based on the above considerations, we propose an improved approach.

Before the parameter estimation, a power spectrum estimation of the Tx signal is performed,

[1]For an OFDM signal, the longer the observation length, the more symbol switching there are at each subcarrier, causing more power leakage. As a result, more sidelobe, i.e. higher power within the GB, can be observed. Thus, a longer signal block can lead to lower condition number.

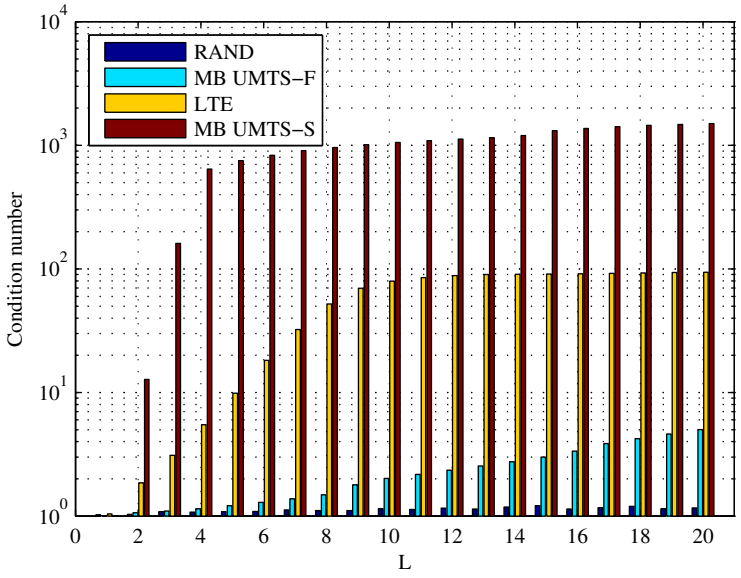

Figure 2.14: Condition number as a function of L. Different signal types were shown. Furthermore, $N = 4096$.

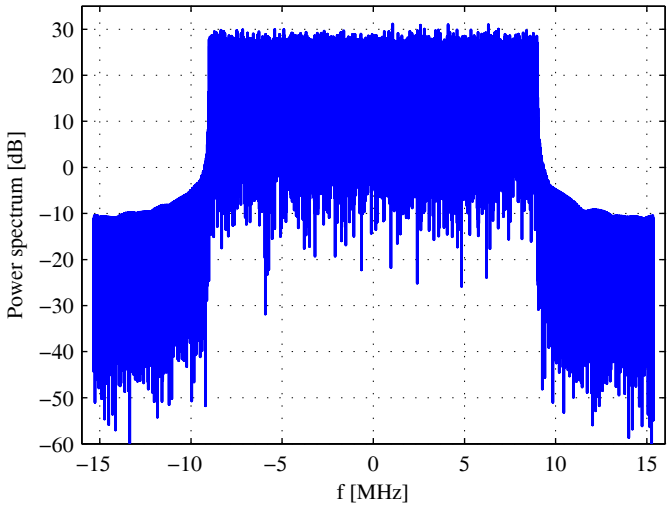

Figure 2.15: PSD of an SB LTE signal with BW of 20 MHz, 16 QAM, $f_s = 30.72$ MHz

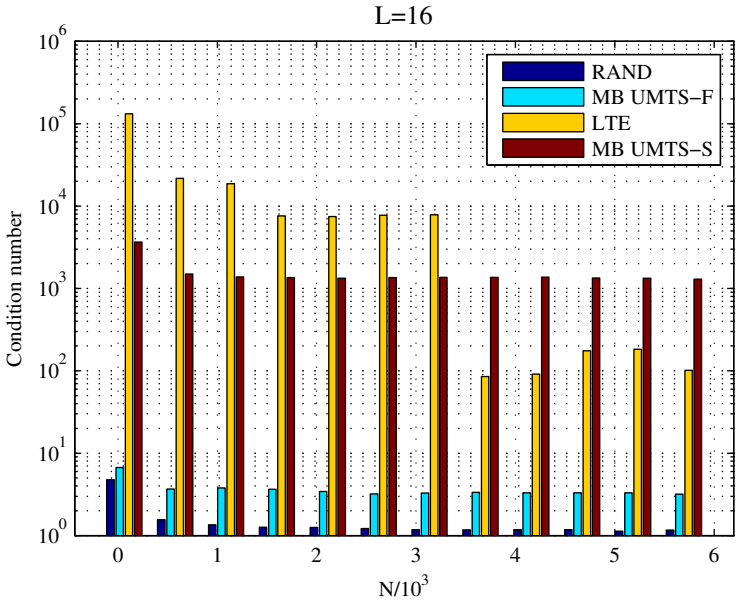

Figure 2.16: Condition number as a function of N with $L = 16$.

which can be efficiently implemented with DFT [98]. From the spectrum estimation, the areas of spectral gaps in the Tx signal can be identified. Afterwards, a length-N OFDM symbol is generated and superimposed on the Tx signal. Afterwards, the superimposed Tx signal is transmitted. This OFDM symbol is called "Super-Imposed Pilot Signal (SIPS)". The Tx signal with SIPS will be used as the system input for the LS estimation. The SIPS should only have spectral components with constant magnitude in the spectral gaps of the Tx signal and can be easily suppressed by digital filtering at the Rx. A CP is attached to this OFDM symbol to relax the time synchronization requirement of the feedback signal and maintain its periodicity after passing through linear systems. The time domain OFDM symbol should be properly windowed (e.g. with an RC window, see Sec. 3.3) to reduce the out-of-band radiation, which causes interference to the Tx signal. Moreover, GBs should be reserved between the OFDM spectrum edges and the Tx signal spectrum edges to further reduce interference. These GBs will not affect the condition number reduction, since they will be filled by the spectral spreading (leakage) mentioned in Sec. 2.5.5.3. Fig. 2.17 illustrates the attachment of an SIPS both in time- and frequency domains.

The power of the SIPS should generally be kept low (compared to the transmitted communication signal in terms of PSD). We consider the following two application scenario classes: SB- and MB transmissions (see also Sec. 2.1). In SB scenario, spectral gaps are mainly caused by GB reservation. In this case, the SIPS power must be kept low to minimize the interference to adjacent channels. More averaging should be done to reduce noise influence in parameter estimation. In MB scenario, spectral gaps are mainly caused by temporarily inactive subbands.

If we assume the inactive subbands are licensed by the BS owner[1], the SIPS power can be higher, since no adjacent channel interference will be generated. To make this solution standard independent, an algorithm should be developed, which can distinguish different scenarios from the spectral analysis and adaptively adjust the power level of the SIPS and the averaging number.

Note that in spite of the above measures, applying SIPS could still cause interference to both the communication signal the own channel (e.g. due to spectral leakage) and adjacent channels. Moreover, a tiny amount of Tx power is consumed by transmitting SIPS. However, both the interference power and the increase of the Tx power consumption are generally very small. Furthermore, SIPS is only applied when estimation is carried out i.e. in a quite small amount of time. Anyway, analysis of the its influence on the EVM of the transmitted communication signals as well as the adjacent channel interference would be an interesting topic, which remains future work.

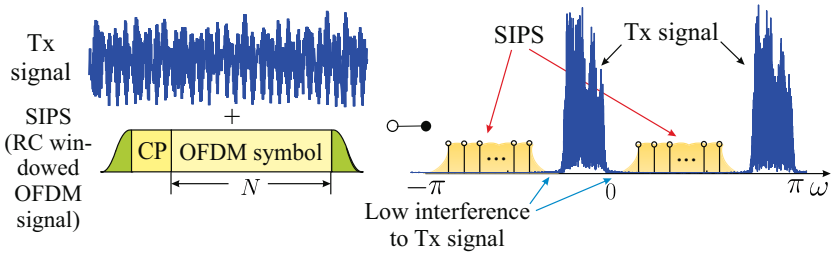

Figure 2.17: Illustration of attaching SIPS.

2.5.6 Other Practical Issues

2.5.6.1 Filter Order Estimation

The assumed filter order L of $h_1 \sim h_4$ should be properly determined. Let L_{act} indicate the actual filter order of $h_1 \sim h_4$ [2]. If $L < L_{\text{act}}$, the LSE suffers from under-parametrization. If $L >> L_{\text{act}}$, the computational complexity is unnecessarily increased. Moreover, a larger L may result in a larger condition number of $\boldsymbol{S}_{\text{LS}}$.

One practical solution is to apply a relatively large L in the initial estimation, where the optimal sequence in Sec. 2.5.4 is applied. With this sequence and a proper averaging number, relatively high estimation accuracy can be achieved. The proper filter order can be determined by omitting the trivial coefficients at the beginning and the tail of the estimated IRs. Afterwards, this proper filter order is used in the following estimation process.

[1] Spectrum aggregation is a counter-example.

[2] From (2.3) and the fact that h^{T_I} and h^{T_Q} do not differ from each other too much, $h_1 \sim h_4$ generally have the same order.

2.5.6.2 Influence of Time Synchronization Error

By choosing $L > L_{\text{act}}$, the proposed LSE can inherently tolerate time synchronization error (between the transmitted- and feedback signal blocks) within a certain range. In this case, time synchronization error within the tolerable range just causes a common shift of the taps in the estimated IRs [1]. According to Eq. (2.24) in Sec. 2.5.2, such a shift has no influence on the pre-equalization coefficients.

2.5.7 Numerical Results

The effectiveness of the proposed schemes was evaluated by numerical simulations. First, the I/Q-imbalance and DC offset parameters are modeled as time invariant. The amplitude and phase imbalance of the MOD are set to be around 2% and 2° as in [99], respectively. The transfer functions of the LPs in the I- and Q-branches have amplitude mismatch of up to 10% and phase difference of up to 10°. The higher the frequency, the larger the mismatch values[2]. For all the simulations, IRR is used as the evaluation criterion.

Fig. 2.18 compares the cases with no calibration, with a calibration which models the I/Q-imbalance as frequency non-selective ("MOD cal.") and the proposed frequency selective I/Q-imbalance calibration. For simplicity, we first assume no additive noise in the feedback signal. The Tx signal was a random signal without spectral gaps. As shown, in the case of no calibration, the IRRs are quite weak, especially at the spectrum edges. This complies with the filter imbalance parameter setup. For the frequency non-selective calibration, a multiplication by a coefficient $\frac{H^{T_I}(0)}{H^{T_Q}(0) g^T \cos \varphi^T}$ (can be computed with $\mathcal{F}\left\{h^C[n]\right\}\big|_0$) is applied instead of the filtering with h^C in Fig. 2.7. Actually, this only compensates for the I/Q-imbalance effect at the DC frequency. Thus, we can see in Fig. 2.18 that the resulting IRR values remain low except near $f = 0$ MHz. Therefore, frequency non-selective calibration is noneffective. For the frequency selective I/Q-imbalance calibration, different numbers of taps of the calibration filter h^C were applied for the pre-equalization. As shown in Fig. 2.18, the achieved overall IRR increases significantly as the used tap number of h^C becomes sufficient. Thus, a sufficient order of the calibration filter is necessary for good calibration performance.

Fig. 2.19 shows the IRR with the MB UMTS-F signal from Fig. 2.13 [3]. For comparison, the schemes in [2] and [3] are included, which are designated as "Ding" and "Anttila", respectively, and can be regarded as "state-of-the-art" schemes[4]. The additive noise level was -50 dB, which is defined as $10 \log (P_n/P_s)$ with P_n the additive noise power and P_s the power of the feedback signal. The signal block length for each estimation was 64. Furthermore, $L = 16$.

[1] The IRs $h_1 \sim h_4$ will have the same shift.

[2] In practice, the mismatch of the RLPs is especially serious near the cutoff frequency of the LPs.

[3] This signal has very small spectral gaps. Thus, no SIPS is necessary.

[4] The scheme "Ding" applies the same LS-based estimation of $h_1 \sim h_4$ but uses a more complex compensation structure, which requires different calculation of the compensation coefficients. The "Anttila" scheme refers to the WL-LS scheme in [3], which applies a complex-valued LS-based estimation method. In our simulation, the "Anttila" scheme was extended to allow MOD DC-offset estimation.

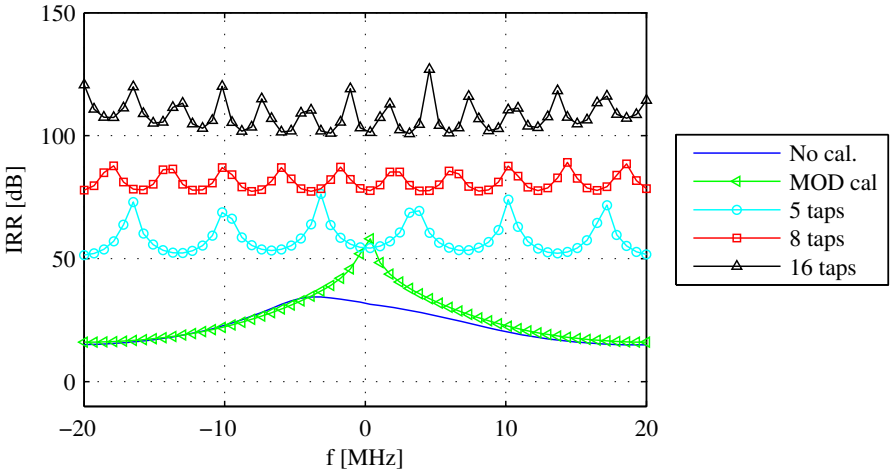

Figure 2.18: Calibration with different filter taps of h^C. No additive noise in the feedback path. Tx signal without spectral gaps.

Both the cases without averaging (i.e. only 1 averaging) and the case with 200 averaging were applied. As shown, for all schemes, the IRR without averaging is already sufficient (about 60 dB), since this signal allows well-conditioned data matrices (both for the proposed- and the reference schemes). However, averaging allows the IRR to be further enhanced (due to better noise mitigation). We can also see that the performance of the proposed scheme is similar to those of the reference schemes. In the case with 200 averaging, the "Ding" scheme has slightly lower achievable IRR than the proposed scheme and the "Anttila" scheme. The reason may be that except for I/Q-imbalance compensation, the "Ding" scheme also tries to compensate for the influence of $h[n]$ and incurs more noise influence. In Sec. 2.7, we will show that the proposed scheme requires lower computational complexity either for the parameter estimation or the pre-equalization.

In the next simulation, the Tx-signal was the LTE signal shown in Sec. 2.5.5.2 (Fig. 2.15). We first apply $N = 64$ and an averaging number of 200. As can be seen from Fig. 2.16, with $N = 64$, this signal leads to large condition numbers of $\boldsymbol{S}_{\mathrm{LS}}$ (due to the relatively large GB). Thus, SIPS should be applied to refill the signal spectrum as described in Sec. 2.5.5. Since the SIPS and the Tx signal have complementary spectral occupations, we compare their power levels in terms of average active PSD, which is defined as $\bar{\Phi} = \frac{1}{\Omega_{\mathrm{in}}} \int_{\omega \in \Omega_{\mathrm{in}}} \Phi(\omega) \mathrm{d}\omega$ with Ω_{in} the frequency set with active spectral contributions. The additive noise level was -50 dB. Fig. 2.20 shows the resulting IRRs. As shown, when no SIPS was applied, the IRR of both the proposed scheme and the reference schemes are insufficient (about 40 dB). Especially within GBs, the IRRs can be even worse than that without calibration. In contrast, when SIPS with a relatively low power level (-40 dB) is applied to the proposed scheme, reasonable IRR (within the signal BW) can be achieved. Actually, the proposed SIPS can also be applied to the reference schemes

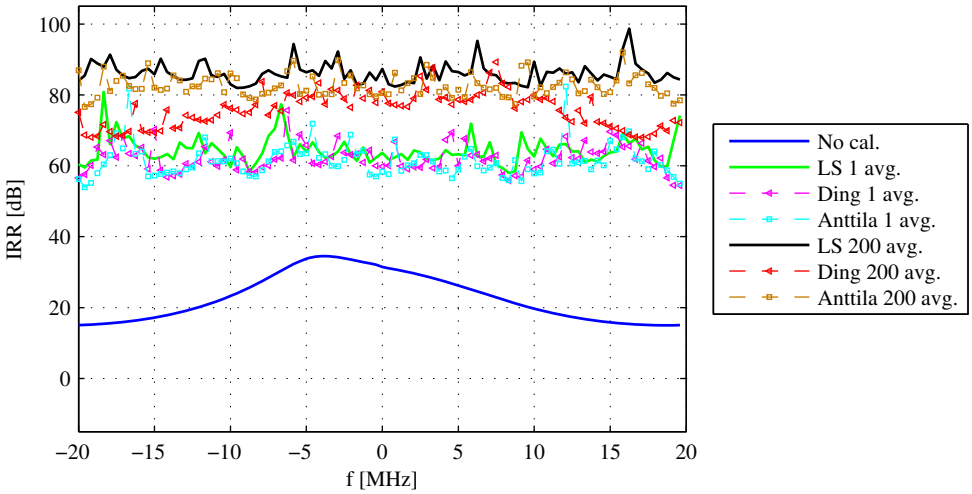

Figure 2.19: Calibration with MB UMTS-F signal; $L = 16$, $10\log(P_n/P_s) = -50dB$, $N = 64$. "LS" indicates the proposed scheme, while "Ding" and "Anttila" indicate the schemes in [2] and [3], respectively.

to enhance their performance.

In Fig. 2.16, we can see that for large N, the condition number with the LTE signal becomes lower. To check the corresponding calibration performance, we carried out the IRR test for the LTE signal with a large block length $N = 64 \times 200 = 12800$. No averaging was applied. The IRR results are shown in Fig. 2.21. As shown, with such a large block length, sufficient IRR (about 60 dB) can be achieved by all schemes without using SIPS. However, we should consider that such a large block length could lead to a more costly implementation.

The same simulation was carried out with the MB UMTS-S signal in Sec. 2.5.5.2 (shown in Fig. 2.12), which has very large spectral gaps. The signal block length and the averaging number were 64 and 200, respectively. From Fig. 2.22, we can see that without SIPS, the IRRs of the proposed scheme and the reference schemes are insufficient (around 40 dB), while a sufficient power level of SIPS (−30 dB) allows high overall IRR (above 60 dB) to be achieved by the proposed scheme. This simulation was also carried out with the large block length $N = 12800$ and without averaging. However, unlike the case with the LTE signal, the IRR results remain similar to those with $N = 64$. The reason was that with this signal, a large block size does not lead to a strongly reduced condition number, as shown in Fig. 2.16.

Now, the MOD I/Q-imbalance and DC-offset error parameters are modeled to be slowly time variant as follows: $g(t) = g_0 + \Delta g e^{-\frac{t}{\tau}}$, $\varphi(t) = \varphi_0 + \Delta\varphi e^{-\frac{t}{\tau}}$ and $d(t) = d_0 + \Delta d e^{-\frac{t}{\tau}}$, where $g_0 = 1.02, \varphi_0 = 2°, d_0 = 0.09 + j0.04, \tau = 20\text{s}$ and $\Delta g = 0.07, \Delta\varphi = 3°, \Delta d = 0.09 + j0.09$. This models the effect of the parameter drift after system cold start. The LPF parameters are modeled as time invariant, since they have much smaller variance than the MOD parameters in practical systems. The following cases are compared via simulation: no calibration, calibration

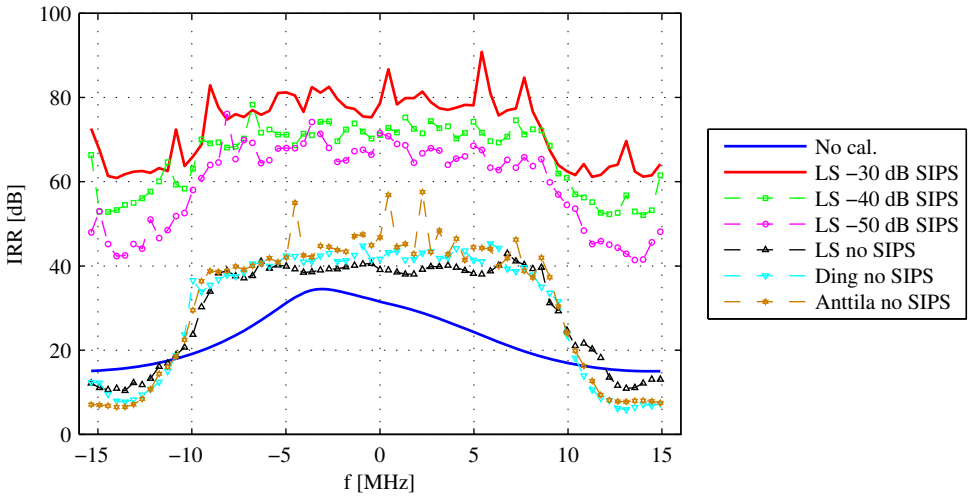

Figure 2.20: Calibration with the LTE signal from Fig. 2.15. SIPS with different power levels were applied. $N = 64$ with the averaging number 200. Furthermore, $L = 16$.

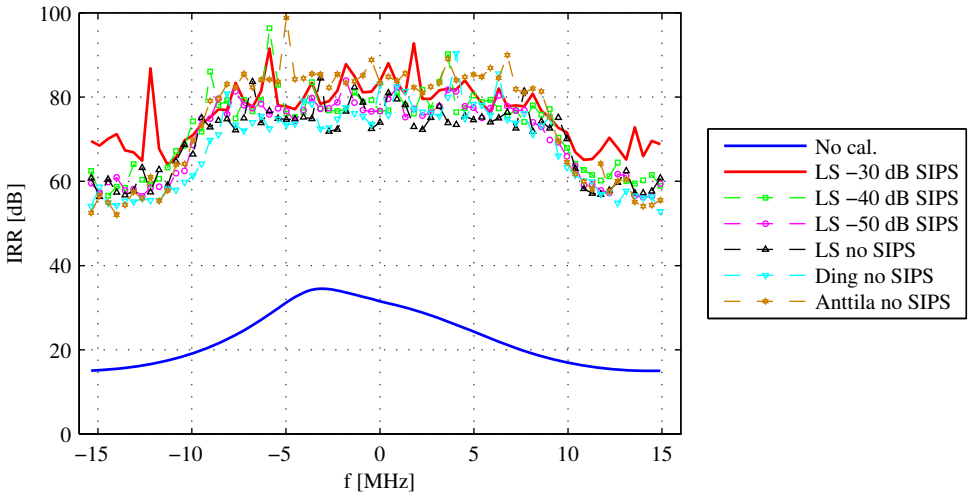

Figure 2.21: Calibration with the LTE signal from Fig. 2.15. SIPS with different power levels were applied. $N = 12800$ without averaging. Furthermore, $L = 16$.

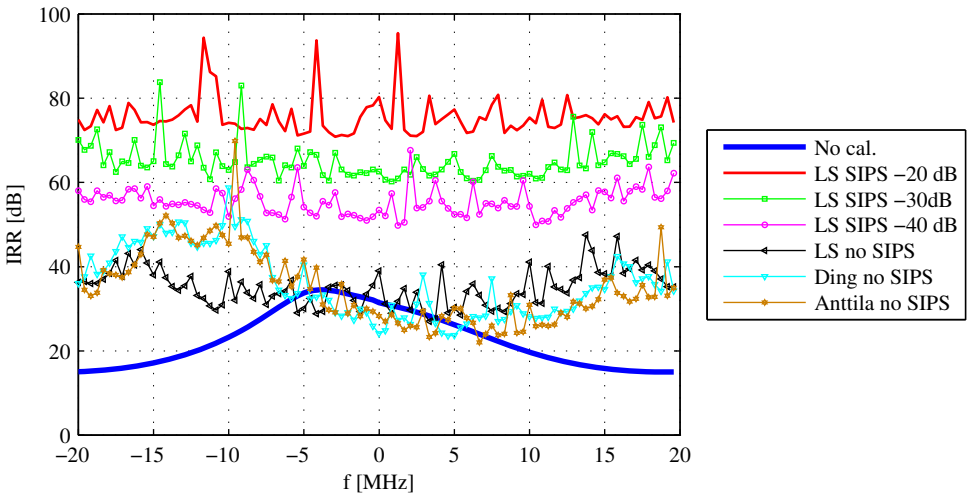

Figure 2.22: Calibration with the MB UMTS signal from Fig. 2.12, SIPS with different power levels were applied. $N = 64$ with the averaging number 200. Furthermore, $L = 16$.

without parameter tracking (the parameters are only estimated at $t = 1$ s) and calibration with tracking (applying the algorithm in Sec. 2.5.3). In the case with tracking, the tracking interval was 0.6 s. The MB UMTS-F signal was used for estimation with $N = 12800$ and without averaging. The additive noise level was -50 dB. Fig. 2.23 shows the simulation results. As shown, when no tracking is applied, high IRR can only be achieved within a short time period close to $t = 1$ s. As the parameter changes, the IRR decreases. In contrast, when tracking is applied, the achievable IRR remains high over the entire observed time.

Finally, in all the simulations mentioned above, as long as the I/Q-imbalance is sufficiently compensated for (indicated by sufficiently high IRR), the MOD DC-offset was found almost completely suppressed. Thus, the proposed scheme is effective both against I/Q-imbalance and MOD DC-offset.

2.6 Simplified Two-Phase Parameter Estimation

In [38], we have proposed an Iterative Frequency Domain Estimation (IFDE) scheme as an alternative to the LS-based scheme in Sec. 2.5. The goal of the IFDE was to avoid the ill-conditioned matrix problem (of LSE) without using SIPS. However, the IFDE scheme requires quite high computational complexity due to iterative processing. Moreover, in some cases, SIPS still has to be applied[1], which can generate interference. In this section, we propose a simplified yet effective calibration scheme that is generally free of both SIPS and ill-conditioned matrix problem.

[1]When the spectral gaps are symmetrical w.r.t. the DC frequency, no SIPS is required. Otherwise, SIPS is needed.

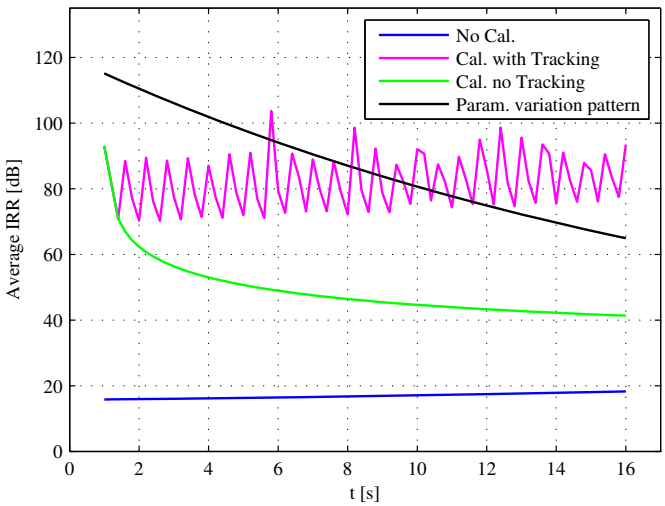

Figure 2.23: Comparison of different cases: 1) No calibration; 2) Calibration and tracking; 3) Calibration without tracking. IRR is averaged in frequency domain.

Both in Sec. 2.5 and [38], it was assumed that all relevant RF parameters can be time-variant. In this section, we assume that the transfer functions of the BB LP filters are time-invariant, which is generally the case in practice. The parameters of MOD I/Q-imbalance and DC-offset as well as the MOD frequency response are assumed to be slowly time variant. Specifically, we assume that the variation of the MOD frequency response within the observed BW can be approximately modeled by a time varying scaling factor. This assumption will be verified by the HIL experiment results in Sec. 2.8. An example of variation of the MOD frequency response due to temperature fluctuation is shown in Fig. 2.24.

Different parameter estimation methods are applied for the initial calibration phase and the parameter tracking phase. In the initial calibration phase, a pilot based frequency domain estimation is applied. In the tracking phase, a semi-blind LS-based time-domain estimation is applied. Under the assumption of time-invariant filter imbalance, only the MOD I/Q-imbalance and DC-offset parameters have to be estimated in the tracking phase.

2.6.1 Pilot-Based Initial Calibration

The initial calibration is based on the BB model in Fig. 2.6. In the initial calibration phase, dedicated pilot sequences can be used to obtain initial estimation of the I/Q-imbalance and MOD DC-offset parameters. Since high SNR can be achieved for the feedback signals, we ignore the additive noise in the following descriptions.

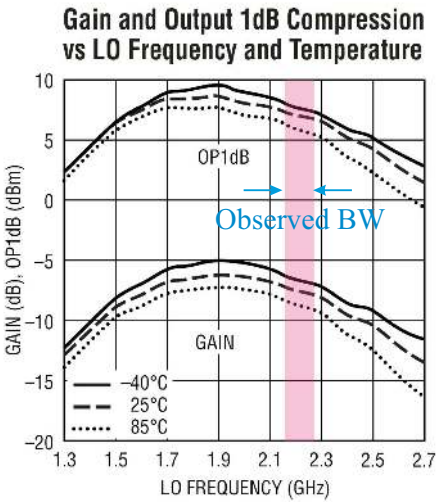

Figure 2.24: Frequency response of a MOD. Cited from the data sheet of LT5528 1.5 GHz to 2.4 GHz high linearity direct quadrature MOD (Linear Technology).

2.6.1.1 Initial Parameter Estimation

First, a length-N real valued sequence $x[n] = \mathcal{F}_N^{-1}\{X[k]\}$ is constructed with $X[k] = X^*[-k], \forall\, |k| < \frac{N}{2} - 1$, $X[-\frac{N}{2}] = 1$ and

$$|X[k]| = \begin{cases} 1, & \forall -\frac{N}{2} \leq k \leq \frac{N}{2} - 1, k \neq 0 \\ 0, & k = 0 \end{cases} \tag{2.63}$$

where N is an even number.

Afterwards, $x[n]$ is extended with a CP and transmitted through the I-branch. No signal is transmitted through the Q-branch. According to Fig. 2.6, the I- and Q-branches of the feedback path will contain the signals $y_{\mathrm{II}}[n] = x[n] \circledast_N h_1[n] + d_{\mathrm{re}}$ and $y_{\mathrm{QI}}[n] = x[n] \circledast_N h_3[n] + d_{\mathrm{im}}$, respectively. The DFT of these two signals are $Y_{\mathrm{II}}[k] = X[k]H_1[k] + Nd_{\mathrm{re}}\delta[k]$ and $Y_{\mathrm{QI}}[k] = X[k]H_3[k] + Nd_{\mathrm{im}}\delta[k]$, where $H_{1;3}[k] = \mathcal{F}_N\{h_{1;3}[n]\}$ and $\delta[k]$ is a unit impulse.

We define $R_{1;3}[k] := Y_{\mathrm{II;IQ}}[k]X^*[k]$ and can obtain the estimates of $H_{1;3}[k]$ as follows:

$$\hat{H}_{1;3}[k] = R_{1;3}[k], \forall -\frac{N}{2} \leq k \leq \frac{N}{2} - 1, k \neq 0. \tag{2.64}$$

Note that since $X[0] = 0$, we have $R_{1;3}[0] = 0$. Thus, $H_{1;3}[0]$ can not be correctly estimated by $R_{1;3}[0]$. We define $r_{1;3}[n] = \mathcal{F}_N^{-1}\{R_{1;3}[k]\}$ and assume the maximum length of $h_{1;3}[n]$ to be

L. Accordingly, the IR $h_{1;3}[n]$ can be estimated by (see also [41]):

$$\hat{h}_{1;3}[n] = r_{1;3}[n] + \frac{1}{N-L}\sum_{l=0}^{L-1} r_{1;3}[l], \forall 0 \leq n \leq L-1. \tag{2.65}$$

Now, the same $x[n]$ is extended with a CP and transmitted through the Q-branch. No signal is transmitted through the I-branch. The I- and Q-branches of the feedback path will contain the signals $y_{\mathrm{IQ}}[n] = x[n] \circledast_N h_2[n] + d_{\mathrm{re}}$ and $y_{\mathrm{QQ}}[n] = x[n] \circledast_N h_4[n] + d_{\mathrm{im}}$, respectively. The IRs $h_{2;4}[n]$ can be estimated similarly to the estimation of $h_{1;3}[n]$.

The MOD DC-offset can be estimated by:

$$\hat{d} = \frac{1}{2N}\left[Y_{\mathrm{II}}[0] + Y_{\mathrm{QI}}[0] + j\left(Y_{\mathrm{QI}}[0] + Y_{\mathrm{QQ}}[0]\right)\right], \tag{2.66}$$

where $Y_{\mathrm{IQ;QQ}}[k] = \mathcal{F}_N\left\{y_{\mathrm{IQ;QQ}}[n]\right\}$.

In practice, due to the limited steepness of the transfer function of the RLP filters (mentioned in Sec. 2.5.2), $H_{1;2;3;4}[k]$ will contain a part of the transition area of the RLPs. This part of $H_{1;2;3;4}[k]$ may suffer strongly from additive noise. Thus, as in Sec. 2.5.2, we select a frequency index set $\mathcal{I}_a$ excluding the DC frequency and this area and construct IRs which have the same frequency response as $\hat{H}_{1;2;3;4}[k]$ within $\mathcal{I}_a$. Such IRs are obtained as follows:

$$\hat{\boldsymbol{h}}_i = \left(\boldsymbol{F}_{(\mathcal{I}_{\mathrm{a}},\mathcal{L})}\right)^{\dagger} \hat{\boldsymbol{H}}_{i,\mathcal{I}_{\mathrm{a}}}, \forall i = 1,2,3,4, \tag{2.67}$$

where $\boldsymbol{h}_i = [h_i[0], \ldots, h_i[L-1]]^T$, $\hat{\boldsymbol{H}}_i = [\hat{H}_i[-\frac{N}{2}], \ldots, \hat{H}_i[\frac{N}{2}-1]]^T$ and $\mathcal{L} = [0, \ldots, L-1]$.

2.6.1.2 Calculation of Pre-Equalization Coefficients

Now, we have the estimates $\hat{d}$, $\hat{h}_{1;2;3;4}[n]$ and $\hat{H}_{1;2;3;4}[k], \forall k \in \mathcal{I}_{\mathrm{a}}$. The MOD offset compensation coefficients ζ can be calculated according to Sec. 2.3 using $\hat{h}_{1;2;3;4}[n]$. For I/Q-imbalance compensation, we first calculate $W[k]$ with

$$\begin{aligned} W[k] &= \hat{H}_\beta[k]/\hat{H}_\alpha[k], \forall k \in \mathcal{I}_{\mathrm{a}}, \\ \hat{H}_\alpha[k] &= \hat{H}_1[k] + j\hat{H}_3[k], \forall k \in \mathcal{I}_{\mathrm{a}}, \\ \hat{H}_\beta[k] &= \hat{H}_4[k] - j\hat{H}_2[k], \forall k \in \mathcal{I}_{\mathrm{a}}. \end{aligned} \tag{2.68}$$

Afterwards, c and $h^C[n]$ can be calculated as described in Sec. 2.5.2.

2.6.2 Semi-Blind Parameter Tracking

2.6.2.1 Tracking Algorithm

For parameter tracking, the time index is divided into intervals. Similar to Sec. 2.5.3, we denote the coefficients from the previous interval with the notation $\tilde{(\cdot)}$. To maintain sufficient IRR of

the system, the parameter tracking should be carried out without interrupting the ongoing pre-equalization. Fig. 2.25 illustrates the system model which includes the pre-equalization with the previous coefficients. Since we assume that the MOD FR only varies with a time varying scaling factor, we denote the IR of the BB equivalent RF block to be $\chi h[n]$, where χ is assumed to be different from interval to interval. For the first tracking interval after the initial calibration, we set $\tilde{\chi} = 1$.

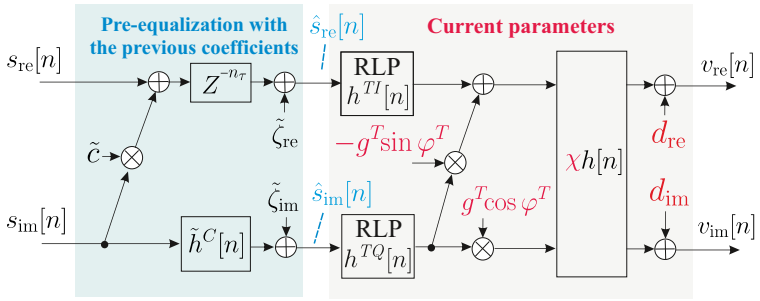

Figure 2.25: Baseband signal model with pre-equalization

By assuming perfect initial parameter estimation and pre-equalization coefficient calculation, we have:

$$h^C[n] = \frac{1}{\tilde{g}^T \cos\tilde{\varphi}^T} \bar{h}^C[n], \tag{2.69}$$

with

$$\bar{h}^C[n] := \mathcal{F}^{-1}\left\{ \frac{H^{TI}(\omega)}{H^{TQ}(\omega)} \right\}\Big|_{n-n_\tau}, \tag{2.70}$$

where n_τ is length of the IR part of (2.69) at negative indices. With (2.69) and (2.70), the signal model of Fig. 2.25 can be transformed into that of Fig. 2.26.

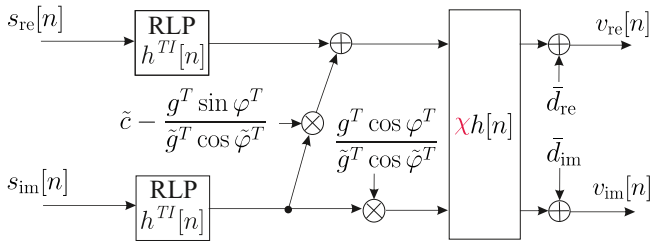

Figure 2.26: Equivalent baseband signal model with pre-equalization

In Fig. 2.26, the following relation exists:

$$\bar{d} = \tilde{\zeta}_{\mathrm{re}} \sum_{n=0}^{L-1} h_\alpha[n] + j\tilde{\zeta}_{\mathrm{im}} \sum_{n=0}^{L-1} h_\beta[n] + d, \tag{2.71}$$

where unlike (2.3),

$$\begin{aligned} h_\alpha[n] &= h^{TI}[n] * h[n]\chi, \\ h_\beta[n] &= g^T e^{j\varphi^T} h^{TQ}[n] * h[n]\chi. \end{aligned} \tag{2.72}$$

Note that at the moment of the parameter tracking, we have the following parameters and coefficients available:

$$\begin{aligned} \tilde{\varphi}^T &= \arctan \tilde{c} \\ \tilde{h}_\alpha[n] &= h^{TI}[n] * h[n]\tilde{\chi}, \\ \tilde{h}_\beta[n] &= \tilde{g}^T e^{j\tilde{\varphi}^T} h^{TQ}[n] * h[n]\tilde{\chi} \end{aligned} \tag{2.73}$$

as well as $\tilde{\chi}, \tilde{c}$ and $\tilde{h}^C[n]$. Our goal is to calculate the following new pre-equalization coefficients

$$\begin{aligned} c &= \tan \varphi^T, \\ h^C[n] &= \frac{1}{g^T \cos \varphi^T} \bar{h}^C[n] \end{aligned} \tag{2.74}$$

from the communication signal $s[n]$, the feedback signal $v[n]$ and the known parameters and coefficients. To achieve this goal, we first express the relation between the input and feedback signals as:

$$\begin{aligned} v[n] &= (s_{\mathrm{re}}[n] + s_{\mathrm{im}}[n]\,(\vartheta_1 + j\vartheta_2)) * \bar{h}[n]\chi + \bar{d} \\ &= s_{\mathrm{re}}[n] * \bar{h}[n]\chi + j s_{\mathrm{im}}[n] * \bar{h}[n]\chi K_1 + \bar{d}, \end{aligned} \tag{2.75}$$

where

$$\begin{aligned} \vartheta_1 &:= \tilde{c} - \frac{g^T \sin \varphi^T}{\tilde{g}^T \cos \tilde{\varphi}^T},\ \vartheta_1 \in \mathbb{R} \\ \vartheta_2 &:= \frac{g^T \cos \varphi^T}{\tilde{g}^T \cos \tilde{\varphi}^T},\ \vartheta_2 \in \mathbb{R} \\ K_1 &:= \frac{g^T e^{j\varphi^T}}{\tilde{g}^T \cos \tilde{\varphi}^T} - j\tilde{c} = \vartheta_2 - j\vartheta_1, \\ \bar{h}[n] &:= h^{TI}[n] * h[n]. \end{aligned} \tag{2.76}$$

Note that $\bar{h}[n]$ can be calculated by $\frac{\tilde{h}_\alpha[n]}{\tilde{\chi}}$. We further define

$$\begin{aligned} \boldsymbol{v}[n] &:= [v[n], \ldots, v[N+n-1]]^T, \\ \bar{s}_1[n] &:= s_{\mathrm{re}}[n] * \bar{h}[n], \\ \bar{s}_2[n] &:= s_{\mathrm{im}}[n] * \bar{h}[n], \\ \bar{\boldsymbol{s}}_{1;2}[n] &:= [\bar{s}_{1;2}[n], \ldots, \bar{s}_{1;2}[N+n-1]]^T. \end{aligned} \tag{2.77}$$

With (2.77), (2.75) can be extended to the following matrix equation:

$$\boldsymbol{v}[n] = \underbrace{[\eta \mathbf{1}_{N\times 1}, \bar{\boldsymbol{s}}_1[n], \bar{\boldsymbol{s}}_2[n]]}_{\bar{\boldsymbol{\Gamma}}} \underbrace{\begin{bmatrix} \frac{\bar{d}}{\eta} \\ \chi \\ j\chi K_1 \end{bmatrix}}_{\boldsymbol{p}}, \tag{2.78}$$

where N is the observation block length and $\eta \in \mathbb{R}^+$ is a scaling factor to improve the condition number of $\bar{\boldsymbol{\Gamma}}$ (see Sec. 2.6.2.2). The vector $\boldsymbol{p}$ can be estimated by:

$$\hat{\boldsymbol{p}} = \left(\bar{\boldsymbol{\Gamma}}\right)^{\dagger} \boldsymbol{v}[n]. \tag{2.79}$$

From $\boldsymbol{p}$, the parameters χ, K_1 and $\bar{d}$ can be easily extracted. Now, we can obtain:

$$\begin{aligned} \vartheta_1 &= \mathcal{I}m\left\{-K_1\right\}, \\ \vartheta_2 &= \mathcal{R}e\left\{K_1\right\}. \end{aligned} \tag{2.80}$$

According to (2.76), we obtain the following desired coefficients:

$$\begin{aligned} c &= \left(\tilde{c} - \vartheta_1\right)\vartheta_2^{-1}, \\ h^C[n] &= \tilde{h}^C[n]\vartheta_2^{-1}. \end{aligned} \tag{2.81}$$

From (2.71), if we can compute $h_\alpha[n]$ and $h_\beta[n]$, we can obtain d and further calculate the new MOD DC-offset compensation parameters ζ. From (2.72), (2.73) and (2.76), we can obtain:

$$\begin{aligned} h_\alpha[n] &= \tilde{h}_\alpha[n]\frac{\chi}{\tilde{\chi}}, \\ h_\beta[n] &= \tilde{h}_\beta[n]\left(\frac{\vartheta_2 + j\left(\tilde{c} - \vartheta_1\right)}{1 + j\tilde{c}}\right)\left(\frac{\chi}{\tilde{\chi}}\right). \end{aligned} \tag{2.82}$$

With (2.71) and (2.82), d can be obtained by:

$$d = \bar{d} - \tilde{\zeta}_{\text{re}} \sum_{n=0}^{L-1} h_\alpha[n] - j\tilde{\zeta}_{\text{im}} \sum_{n=0}^{L-1} h_\beta[n]. \tag{2.83}$$

Afterwards, ζ can be calculated as in Sec. 2.3.

2.6.2.2 Matrix Condition Analysis

The key step of the parameter tracking is the LSE of the parameters with (2.79). In practice, additive noise exists. Thus, similar to the LSE in Sec. 2.5, the condition number of $\bar{\boldsymbol{\Gamma}}$ is crucial for the estimation quality. The lower the condition number, the less the noise amplification in the estimates. In this section, we will analyze the condition number of $\bar{\boldsymbol{\Gamma}}$.

The condition number of $\bar{\mathbf{\Gamma}}$ can be expressed as:

$$\kappa\left(\bar{\mathbf{\Gamma}}\right) = \frac{\sigma_1\left(\bar{\mathbf{\Gamma}}\right)}{\sigma_3\left(\bar{\mathbf{\Gamma}}\right)}, \tag{2.84}$$

where $\sigma_m, m = 1, 2, 3$ is the m^{th} singular value of $\bar{\mathbf{\Gamma}}$ in descending order [1].

Now, we define $\mathbf{\Theta} := \frac{1}{N}\bar{\mathbf{\Gamma}}^H\bar{\mathbf{\Gamma}}$, whose eigenvalues are $\lambda_m\left(\mathbf{\Theta}\right) = \frac{1}{N}\sigma_m^2\left(\bar{\mathbf{\Gamma}}\right), m = 1, 2, 3$. Thus, the condition number of $\mathbf{\Theta}$ is

$$\kappa\left(\mathbf{\Theta}\right) = \frac{\sigma_1^2\left(\bar{\mathbf{\Gamma}}\right)}{\sigma_3^2\left(\bar{\mathbf{\Gamma}}\right)} \tag{2.85}$$

and we have

$$\kappa\left(\bar{\mathbf{\Gamma}}\right) = \sqrt{\kappa\left(\mathbf{\Theta}\right)}. \tag{2.86}$$

This indicates that if we know the condition number of $\mathbf{\Theta}$, we know that of $\bar{\mathbf{\Gamma}}$. The matrix $\mathbf{\Theta}$ can be written as:

$$\mathbf{\Theta} = \frac{1}{N}\begin{bmatrix} N\eta^2 & \eta\sum_{n=0}^{N-1}\bar{s}_1[n] & \eta\sum_{n=0}^{N-1}\bar{s}_2[n] \\ \eta\sum_{n=0}^{N-1}\bar{s}_1^*[n] & \sum_{n=0}^{N-1}|\bar{s}_1[n]|^2 & \sum_{n=0}^{N-1}\bar{s}_1^*[n]\bar{s}_2[n] \\ \eta\sum_{n=0}^{N-1}\bar{s}_2^*[n] & \sum_{n=0}^{N-1}\bar{s}_1[n]\bar{s}_2^*[n] & \sum_{n=0}^{N-1}|\bar{s}_2[n]|^2 \end{bmatrix}, \tag{2.87}$$

When $N \to \infty$, $\mathbf{\Theta}$ can be rewritten as:

$$\mathbf{\Theta} = \begin{bmatrix} \eta^2 & \eta\mu_{\bar{s}_1} & \eta\mu_{\bar{s}_2} \\ \eta\mu_{\bar{s}_1^*} & R_{\bar{s}_1,\bar{s}_1}[0] & R_{\bar{s}_2,\bar{s}_1}[0] \\ \eta\mu_{\bar{s}_2^*} & R_{\bar{s}_1,\bar{s}_2}[0] & R_{\bar{s}_2,\bar{s}_2}[0] \end{bmatrix}, \tag{2.88}$$

where

$$R_{\bar{s}_x,\bar{s}_y}[l] := E\left\{\bar{s}_x[n]\bar{s}_y^*[n+l]\right\}, \forall x, y \in \{1, 2\} \tag{2.89}$$

is a correlation function and μ_x indicates the mean value of x. Now, we recall the proper WSS assumption of $s[n]$ (see Sec. 2.5.5.1 and App. A.1) and the corresponding properties:

$$\begin{aligned} &R_{s_{\text{re}},s_{\text{re}}}[l] = R_{s_{\text{im}},s_{\text{im}}}[l], \\ &R_{s_{\text{re}},s_{\text{im}}}[-l] = -R_{s_{\text{re}},s_{\text{im}}}[l], \\ &R_{s_{\text{re}},s_{\text{im}}}[0] = 0. \end{aligned} \tag{2.90}$$

According to [93], the following relations exist:

$$\begin{aligned} R_{\bar{s}_1,\bar{s}_1}[l] &= \bar{h}[l] * \bar{h}^*[-l] * R_{s_{\text{re}},s_{\text{re}}}[l], \\ R_{\bar{s}_2,\bar{s}_2}[l] &= \bar{h}[l] * \bar{h}^*[-l] * R_{s_{\text{im}},s_{\text{im}}}[l]. \end{aligned} \tag{2.91}$$

[1] $\bar{\mathbf{\Gamma}}$ has rank 3

With (2.90) and (2.91), we can obtain:

$$R_{\bar{s}_1,\bar{s}_1}[l] = R_{\bar{s}_2,\bar{s}_2}[l]. \tag{2.92}$$

We can further show that (see App. A.4):

$$R_{\bar{s}_1,\bar{s}_2}[l] = \bar{h}[l] * \bar{h}^*[-l] * R_{s_{\mathrm{re}},s_{\mathrm{im}}}[l]. \tag{2.93}$$

With (2.93) and (2.90), we can prove that (see App. A.5)

$$R_{\bar{s}_1,\bar{s}_2}[-l] = -R^*_{\bar{s}_1,\bar{s}_2}[l], \tag{2.94}$$

which implies $R_{\bar{s}_1\bar{s}_2}[0] = 0$. Furthermore, according to [97], $R_{\bar{s}_2\bar{s}_1}[0] = R^*_{\bar{s}_1\bar{s}_2}[0] = 0$.

Recalling the zero-mean assumption of $s[n]$, we have:

$$\mu_{\bar{s}_1} = \mu_{\bar{s}_2} = \mu_{\bar{s}_1^*} = \mu_{\bar{s}_2^*} = 0. \tag{2.95}$$

By denoting $P := R_{\bar{s}_1,\bar{s}_1}[0] = R_{\bar{s}_2,\bar{s}_2}[0]$ and assuming that we can choose $\eta^2 = P$, the matrix (2.88) becomes:

$$\boldsymbol{\Theta} = \begin{bmatrix} P & 0 & 0 \\ 0 & P & 0 \\ 0 & 0 & P \end{bmatrix}, \tag{2.96}$$

which has the eigenvalues $\lambda_m = P, m = 1, 2, 3$. Thus, we have

$$\lim_{N\to\infty} \kappa\left(\boldsymbol{\Theta}\right) = 1, \text{ and } \quad \lim_{N\to\infty} \kappa\left(\bar{\boldsymbol{\Gamma}}\right) = 1, \tag{2.97}$$

which means that if the observed signal block for the estimation in (2.79) is long enough, the condition number of $\bar{\boldsymbol{\Gamma}}$ would be close to 1. Thus, the LSE of (2.79) will provide good estimation quality.

2.6.2.3 Performance Analysis Considering Time Synchronization Error

Although the LSE (2.79) is well-conditioned according to Sec. 2.6.2.2, it can be seen from (2.75) and (2.78) that the LSE may be sensitive to misalignment between the signal samples $v[n]$ and $s_{1;2}[n]$. This can probably be caused by time synchronization error. In this section, we will analyze the influence of time synchronization error based on the statistical characteristics of $s[n]$. Let ς be the number of misaligned samples, (2.78) changes to:

$$\boldsymbol{v}[n+\varsigma] = \bar{\boldsymbol{\Gamma}}_\varsigma \boldsymbol{p} \tag{2.98}$$

with

$$\bar{\boldsymbol{\Gamma}}_\varsigma = \left[\eta \mathbf{1}_{N\times 1}, \bar{\boldsymbol{s}}_1[n+\varsigma], \bar{\boldsymbol{s}}_2[n+\varsigma]\right]. \tag{2.99}$$

Accordingly, the estimation of (2.79) changes to:

$$\begin{aligned}\hat{\boldsymbol{p}} &= \left(\bar{\boldsymbol{\Gamma}}\right)^{\dagger} \boldsymbol{v}[n+\varsigma] \\ &= \left(\bar{\boldsymbol{\Gamma}}^{H}\bar{\boldsymbol{\Gamma}}\right)^{-1} \bar{\boldsymbol{\Gamma}}^{H}\bar{\boldsymbol{\Gamma}}_{\varsigma}\boldsymbol{p}.\end{aligned} \tag{2.100}$$

From Sec. 2.6.2.2, we have $\boldsymbol{\Theta} = \frac{1}{N}\bar{\boldsymbol{\Gamma}}^{H}\bar{\boldsymbol{\Gamma}}$. We further define $\mathfrak{Q} := \frac{1}{N}\bar{\boldsymbol{\Gamma}}^{H}\bar{\boldsymbol{\Gamma}}_{\varsigma}$. When $N \to \infty$, we have

$$\mathfrak{Q} = \begin{bmatrix} \eta^2 & \eta\mu_{\bar{s}_1} & \eta\mu_{\bar{s}_2} \\ \eta\mu_{\bar{s}_1^*} & R_{\bar{s}_1,\bar{s}_1}[-\varsigma] & R_{\bar{s}_2,\bar{s}_1}[-\varsigma] \\ \eta\mu_{\bar{s}_2^*} & R_{\bar{s}_1,\bar{s}_2}[-\varsigma] & R_{\bar{s}_2,\bar{s}_2}[-\varsigma] \end{bmatrix}. \tag{2.101}$$

If $s[n]$ is proper, we have

$$R_{\bar{s}_1,\bar{s}_1}[l] = R_{\bar{s}_2,\bar{s}_2}[l] \quad \text{(see (2.92))} \tag{2.102}$$

$$R_{\bar{s}_2,\bar{s}_1}[l] = -R_{\bar{s}_1,\bar{s}_2}[l] \quad \text{(see the proof in App. A.6).} \tag{2.103}$$

With (2.102), (2.103) and the zero mean assumption of $s[n]$, $\mathfrak{Q}$ can be rewritten as:

$$\mathfrak{Q} = \begin{bmatrix} \eta^2 & 0 & 0 \\ 0 & R_{\bar{s}_1,\bar{s}_1}[-\varsigma] & -R_{\bar{s}_1,\bar{s}_2}[-\varsigma] \\ 0 & R_{\bar{s}_1,\bar{s}_2}[-\varsigma] & R_{\bar{s}_1,\bar{s}_1}[-\varsigma] \end{bmatrix}. \tag{2.104}$$

With (2.96), (2.104) and (2.78), the estimation of (2.100) becomes:

$$\begin{aligned}\hat{\boldsymbol{p}} &= \boldsymbol{\Theta}^{-1}\mathfrak{Q}\,\boldsymbol{p} \\ &= \begin{bmatrix} P & 0 & 0 \\ 0 & P & 0 \\ 0 & 0 & P \end{bmatrix}^{-1} \times \begin{bmatrix} P & 0 & 0 \\ 0 & \rho & -\theta \\ 0 & \theta & \rho \end{bmatrix} \times \begin{bmatrix} \frac{\bar{d}}{\eta} \\ \chi \\ j\chi K_1 \end{bmatrix} = \begin{bmatrix} \frac{\bar{d}}{\eta} \\ \frac{\chi(\rho - j\theta K_1)}{P} \\ \frac{\chi(\theta + j\rho K_1)}{P} \end{bmatrix}.\end{aligned} \tag{2.105}$$

where $\rho := R_{\bar{s}_1,\bar{s}_1}[-\varsigma] = R_{\bar{s}_2,\bar{s}_2}[-\varsigma], \theta = R_{\bar{s}_1,\bar{s}_2}[-\varsigma] = -R_{\bar{s}_2,\bar{s}_1}[-\varsigma]$. For simplicity of analysis, we assume $\rho, \theta \in \mathbb{R}$[1]. From (2.105), we can see that time synchronization error only affects the estimation of χ and K_1, which can be written as:

$$\hat{\chi} = \chi\frac{(\rho - j\theta K_1)}{P}, \tag{2.106}$$

$$\hat{K_1} = \frac{(\hat{\boldsymbol{p}})_3}{j\,(\hat{\boldsymbol{p}})_2} = K_1\frac{\left(\frac{\theta}{K_1\rho} + j\right)}{\left(\frac{K_1\theta}{\rho} + j\right)}. \tag{2.107}$$

[1]From (2.91) and (2.93), we can see that $\rho, \theta \in \mathbb{R}$ when $h[l] * h^*[-l] \in \mathbb{R}$. According to (2.76), $\bar{h}[n] := h^{TI}[n] * h[n]$. In practice, the FR of $h[n]$ (can be regarded as a joint effect of the FRs of the MOD and the feedback path) is very flat. Thus, the IR $h[n]$ can be approximated by a one tap filter $h[n] = G_h\delta[n], G_h \in \mathbb{C}$. Accordingly, $h[l] * h^*[-l] \approx |G_h|^2 h^{TI}[l] * h^{TI}[-l] \in \mathbb{R}$.

While χ is important for the compensation of MOD DC-offset, K_1 is crucial for I/Q-imbalance compensation. The estimate of (2.106) is perfect when $\theta \to 0, \rho \to P$, while the estimate of (2.107) is perfect when $\theta \to 0, \rho \neq 0$. Otherwise, scaled versions[1] of the original parameters are obtained. Generally, the closer the values of θ and ρ to 0 and P, respectively, the better the estimation. Interestingly, we notice that the estimation of K_1 may be much less affected by time synchronization error than that of χ. The reason is that with practical I/Q-imbalance parameters, K_1 is very close to one[2]. Thus, the scaling factor of K_1 in (2.107) can also be close to one. For further analysis, we calculate the normalized estimation MSE of χ and K_1 as follows:

$$\begin{aligned} MSE_{\chi} &= \left|\frac{\hat{\chi}-\chi}{\chi}\right|^2 = \left|\left(\frac{\rho}{P}-1\right) - jK_1\frac{\theta}{P}\right|^2, \\ MSE_{K_1} &= \left|\frac{\hat{K_1}-K_1}{K_1}\right|^2 = \left|\frac{(1-K_1^2)\frac{\theta}{\rho}}{K_1\left(\frac{\theta}{\rho}K_1+j\right)}\right|^2. \end{aligned} \tag{2.108}$$

Note that in the reality, no signal is perfectly proper. As will be shown, the tracking performance with time synchronization error is very sensitive to improperness. Thus, improper signals should also be taken into account in our analysis[3]. For improper signals, (2.102), (2.103) can not be fulfilled anymore, which stem from (A.1.3) and (A.1.4). As a result, the Complementary Auto-Correlation Function (CACF) is not zero.

In practice, signals that have no intersection of active frequency bands with their images can be regarded as quasi proper[4]. In contrast, signals that have intersections of active frequency bands with their images are generally improper. For improper signals, we still assume circularity i.e. $R_{s_{\mathrm{re}},s_{\mathrm{re}}}[0] = R_{s_{\mathrm{im}},s_{\mathrm{im}}}[0]$ and $R_{s_{\mathrm{re}},s_{\mathrm{im}}}[0] = R_{s_{\mathrm{im}},s_{\mathrm{re}}}[0] = 0$[5].

Considering improper signals, (2.105) should be rewritten as:

$$\begin{aligned} \hat{\boldsymbol{p}} &= \boldsymbol{\Theta}^{-1}\boldsymbol{\Omega}\,\boldsymbol{p} \\ &= \begin{bmatrix} P & 0 & 0 \\ 0 & P & 0 \\ 0 & 0 & P \end{bmatrix}^{-1} \times \begin{bmatrix} P & 0 & 0 \\ 0 & \rho & -\theta \\ 0 & \theta' & \rho' \end{bmatrix} \times \begin{bmatrix} \frac{\bar{d}}{\eta} \\ \chi \\ j\chi K_1 \end{bmatrix} = \begin{bmatrix} \frac{\bar{d}}{\eta} \\ \frac{\chi(\rho - j\theta K_1)}{P} \\ \frac{\chi(\theta' + j\rho' K_1)}{P} \end{bmatrix}, \end{aligned} \tag{2.109}$$

[1] The scaling factors are generally complex valued.

[2] In practice, g^T is close to 1 while φ^T is close to 0. Moreover, we assume the parameter changes from one tracking interval to another is very small. Thus, according to the definition in (2.76), K_1 is close to 1.

[3] In contrast, the condition number analysis in Sec. 2.5.5.1, Sec. 2.6.2.2 and Sec. 2.6.2.5 are much less sensitive to improperness. While the condition number only affects the noise influence on the estimation, the time synchronization error causes model mismatch.

[4] Let $\mathcal{F}_{\mathrm{D}}$ and $\mathcal{F}_{\mathrm{I}}$ be the sets of active frequency bands of a signal and its image, respectively. Properness can be fulfilled when $\mathcal{F}_{\mathrm{D}} \cap \mathcal{F}_{\mathrm{I}} = \emptyset$. One example is a single side band signal. Another example is an MB UMTS signal with the $+p^{\mathrm{th}}$- and $-q^{\mathrm{th}}$ subbands active, where $p, q > 0$ and $p \neq q$. However, due to effects e.g. spectral leakage, the PSD in the inactive frequency bands can not be exactly zero. Thus, the properness of such signals is not perfect.

[5] Circularity is a subordinate property of properness [48].

where $\rho := R_{\bar{s}_1,\bar{s}_1}[-\varsigma]$, $\rho' = R_{\bar{s}_2,\bar{s}_2}[-\varsigma]$, $\theta := R_{\bar{s}_2,\bar{s}_1}[-\varsigma] = R_{\bar{s}_1,\bar{s}_2}[\varsigma]$, $\theta' = R_{\bar{s}_1,\bar{s}_2}[-\varsigma]$[1]. We assume $\rho, \rho', \theta, \theta' \in \mathbb{R}$. Accordingly, the estimates and the normalized MSE of χ and K_1 become:

$$\begin{aligned}
\hat{\chi}' &= \chi \frac{(\rho - j\theta K_1)}{P}, \\
\hat{K_1}' &= K_1 \frac{\left(\frac{\theta'}{K_1\rho} + j\frac{\rho'}{\rho}\right)}{\left(\frac{K_1\theta}{\rho} + j\right)}, \\
MSE'_{\chi} &= \left|\left(\frac{\rho}{P} - 1\right) - jK_1\frac{\theta}{P}\right|^2, \\
MSE'_{K_1} &= \left|\frac{-j\upsilon + j(1-K_1)\upsilon_{\mathrm{re}} + (1-K_1^2)\theta}{K_1(\theta K_1 + j\rho)}\right|^2 = \left|\frac{\frac{-j\upsilon}{\rho} + j(1-K_1)\frac{\upsilon_{\mathrm{re}}}{\rho} + (1-K_1^2)\frac{\theta}{\rho}}{K_1\left(\frac{\theta}{\rho}K_1 + j\right)}\right|^2,
\end{aligned} \tag{2.110}$$

where $\upsilon = (\rho - \rho') + j(\theta' - \theta) = R_{\bar{s},\bar{s}^*}[-\varsigma]$ with $R_{\bar{s},\bar{s}^*}[l] = \bar{h}[l] * \bar{h}^*[-l] * R_{s,s^*}[l]$ and $R_{s,s^*}[l]$ the CACF of $s[n]$. Note that $MSE'_{\chi} = MSE_{\chi}$. Moreover, $MSE'_{K_1} \to MSE_{K_1}$ when $\upsilon \to 0$.

Eq. (2.108) and (2.110) show that the estimation MSE of χ and K_1 are determined by the values of θ, ρ, θ' as well as υ. These values are mainly dependent on the PSD of $s[n]$[2]. Generally, the larger amount of spectral gaps a signal has, the larger $|\rho|$ tends to be. With the same amount of spectral gaps, the stronger the symmetric part of the PSD[3], the larger $|\rho|$ becomes. Since improper signals probably have stronger symmetric PSD parts than proper signals, they tend to have larger $|\rho|$. Furthermore, signals with stronger symmetric PSD parts tend to have smaller $|\theta|$ and $|\theta'|$ values. But the $|\upsilon|$ value of such signals tend to be larger.

Fig. 2.27 illustrates the MSE of χ (for both proper and improper signals) as a function of both $\frac{\rho}{P}$ and $\frac{\theta}{P}$. The applied value $K_1 = 0.9999 - 0.0001j$ stems from the parameters $\tilde{g}^T = 1.02, \tilde{\varphi}^T = 2°, g^T = 1.0199$ and $\varphi^T = 1.9945°$, which are extracted from the tracking simulation in Sec. 2.5.7. As shown, except for $\frac{\rho}{P}$ close to 1 and $\frac{\theta}{P}$ close to zero (both simultaneously), the MSE is quite high. Thus, the estimation of χ is quite sensitive to time synchronization error.

Fig. 2.28 illustrates the MSE of K_1 as a function of $\frac{\theta}{\rho}$ for both proper and improper signals. As shown, the MSE of proper signals is generally very small. The reason is that the value $\frac{1-K_1^2}{K_1}$ is very small, which dominates the MSE value (see (2.108)). In contrast, the MSE of improper signals is much higher. The reason is that with realistic improper signals, we have $|\upsilon| \gg |(1-K_1)\upsilon_{\mathrm{re}}|$ and $|\upsilon| \gg |(1-K_1^2)\theta|$. Thus, υ is the dominating factor of the MSE (see

[1] Note that $\boldsymbol{\Theta} = \mathrm{diag}\{[P, P, P]\}$ is only true when $s[n]$ is proper or $\bar{h}[n]$ is a single tap filter. Anyway, with realistic circular signals, $\boldsymbol{\Theta}$ can still be approximated by $\mathrm{diag}\{[P, P, P]\}$. This approximation is used here for simplicity.

[2] Actually, they also depend on the FR of $\bar{h}[n]$. However, since this FR is generally quite flat, we ignore its influence.

[3] The PSD can generally be decomposed into a symmetric part and an anti-symmetric part. While the symmetric part is the DTFT of $R_{s_{\mathrm{re}},s_{\mathrm{re}}}[l] + R_{s_{\mathrm{im}},s_{\mathrm{im}}}[l]$, the anti-symmetric part is the DTFT of $j\left(R_{s_{\mathrm{re}},s_{\mathrm{im}}}[l] - R_{s_{\mathrm{im}},s_{\mathrm{re}}}[l]\right)$. For the quasi-proper signals mentioned before, the symmetric- and anti-symmetric PSD parts are almost equally strong.

(2.110)). It can be seen that another dominant factor is ρ[1]. Moreover, in the region $\frac{\theta}{\rho} < 1$, the MSE of K_1 is almost independent from $\frac{\theta}{\rho}$. Note that for the results in Fig. 2.28 and the following two figures, we have assumed $\frac{\theta}{\rho} > 0$ (for improper signals also $\theta > 0, \rho > 0$) for simplicity. However, App. A.7 shows that the signs of θ and ρ has only negligible influence on the MSE of K_1.

Fig. 2.29 further shows the MSE of K_1 as a function of $\left|\frac{\upsilon}{2P}\right|$, which is the magnitude of the normalized CACF $\frac{R_{s,s^*}[-\varsigma]}{jR_{s,s}[0]}$. This figure shows that for very small $|\upsilon|$ ($|\upsilon| < 0.0025$), all variables $\frac{\theta}{\rho}$, ρ and $|\upsilon|$ have strong influence on the MSE of K_1. However, for larger $|\upsilon|$ ($|\upsilon| > 0.0025$), the MSE of K_1 is mainly determined by ρ and $|\upsilon|$, while $\frac{\theta}{\rho}$ has almost no influence. Note that for simplicity of illustration, we have assumed $\upsilon_{\text{re}} = \upsilon_{\text{im}}$. However, App. A.7 will show that for a fixed $|\upsilon|$, the variation of υ_{re} and υ_{im} has only negligible effect on the MSE of K_1.

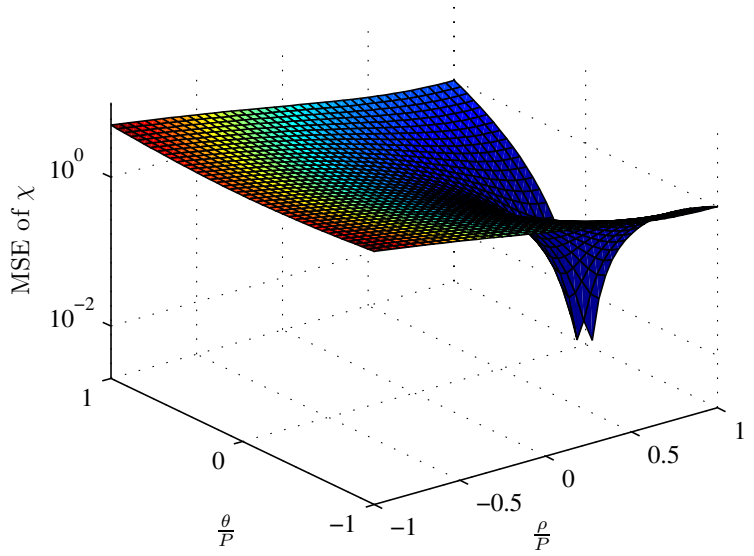

Figure 2.27: Theoretical normalized estimation MSE of χ as functions of $\frac{\theta}{P}$ and $\frac{\rho}{P}$ for both proper and improper signals. $K_1 = 0.9999 - 0.0001j$.

The illustrations above assume that K_1 is very close to 1. Now, we investigate the influence of different K_1 values on the estimation MSE of K_1. Fig. 2.30 illustrates the MSE as a function of $|K_1|$ for both proper and improper signals. As shown, for proper signals, minimums of MSE can be observed when K_1 is close to 1. The larger the deviation of K_1 from 1, the higher the MSE. In contrast, for improper signals, the MSE is much less sensitive to K_1 except for the case with both large θ and large ρ. Note that for improper signals, large θ is of low probability.

The dependence of MSE of K_1 on the value of K_1 helps to analyze the error propagation across successive tracking intervals. Generally, if no time synchronization error is present, the proposed tracking algorithm is free of error propagation[2]. In the case with time synchronization

[1]The value of ρ affects the denominator of the expression of MSE'_{K_1} in (2.110).
[2]This will be verified in Sec. 2.6.3.

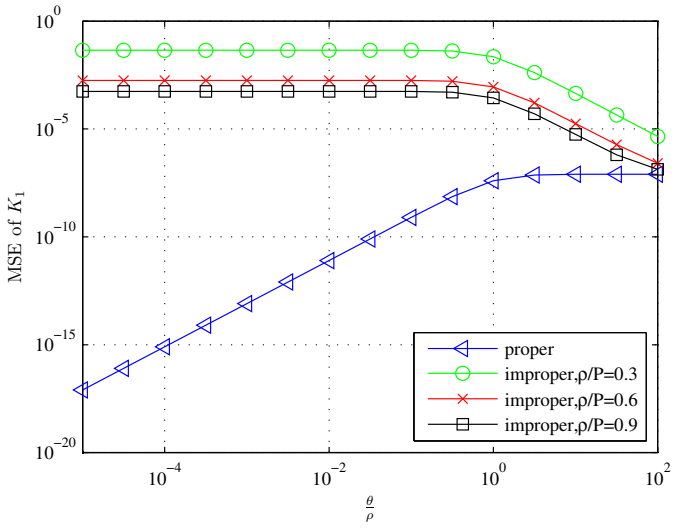

Figure 2.28: Theoretical normalized estimation MSE of K_1 as a function of $\frac{\theta}{\rho}$ for both proper and improper signals. $K_1 = 0.9999 - 0.0001j$, $\frac{\upsilon}{2P} = 0.0075 + 0.0075j$.

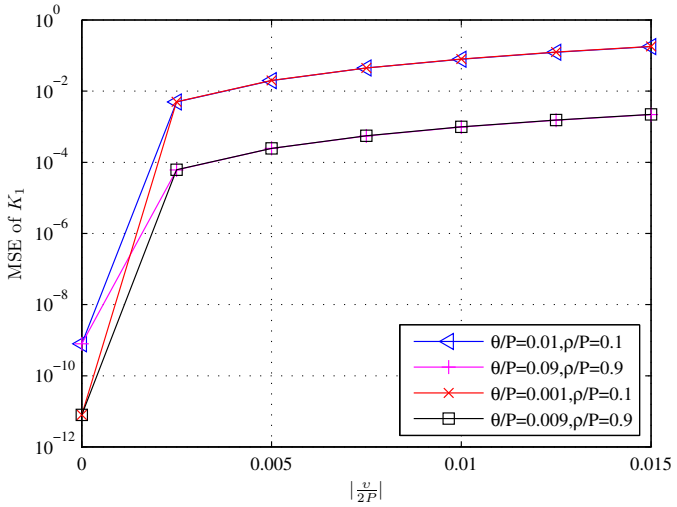

Figure 2.29: Theoretical normalized estimation MSE of K_1 as a function of $\left|\frac{\upsilon}{2P}\right|$ i.e. $\left|\frac{R_{s,s^*}[-\varsigma]}{R_{s,s}[0]}\right|$ for improper signals. For simplicity, we assume $\upsilon_{\mathrm{re}} = \upsilon_{\mathrm{im}}$. $K_1 = 0.9999 - 0.0001j$

error, the estimation error of K_1 causes estimation error of c. From (2.76), estimation errors of c can probably increase the deviation of $|K_1|$ from 1. For proper signals, such deviation of $|K_1|$ will in turn, deteriorate the estimation of c of the next tracking interval. This forms an error propagation cycle. Thus, as long as time synchronization is present, the tracking performance (i.e. IRR) can degrade from one tracking interval to another. According to Fig. 2.28, the higher the value of $\frac{\theta}{\rho}$, the stronger the performance degradation[1]. In contrast, for improper signals, the MSE of K_1 is insensitive to the value of K_1. Thus, the effect of error propagation is much weaker.

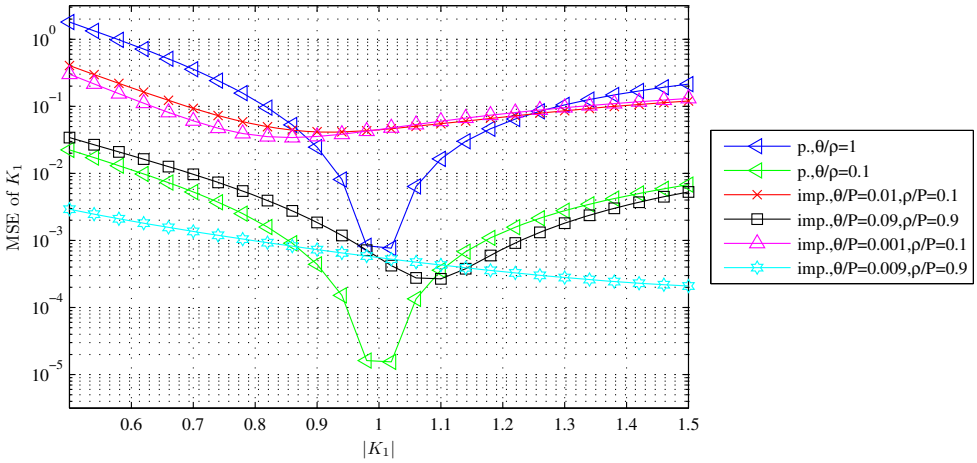

Figure 2.30: Theoretical normalized estimation MSE of K_1 as a function of $|K_1|$ for both proper and improper signals. $\Im m\{K_1\}$ was fixed to 0.0001. $\frac{v}{2P} = 0.0075 + 0.0075j$

2.6.2.4 Extension for Tolerance of Time Synchronization Error

In this section, we extend the proposed tracking algorithm for the toleration of time synchronization errors within a certain range. First, the multiplications with χ and χK_1 in the second line of Eq. (2.75) can be equivalently written as convolutions in the following equation:

$$v[n - n_{\mathrm{w}}] = \bar{s}_1[n] * (\chi\delta[n - n_{\mathrm{w}}]) + \bar{s}_2[n] * (j\chi K_1\delta[n - n_{\mathrm{w}}]) + d, \tag{2.111}$$

where $\delta[n]$ is the unit-impulse function and n_{w} is a time index shift, which should be chosen according to the desired tolerable range of the time synchronization error (will be shown later). We further define $J := 2n_{\mathrm{w}} - 1$. By applying the definitions in (2.77) and considering a

[1]Note that the MSE in Fig. 2.28 assumes that no timing synchronization was present in the previous tracking interval, allowing perfect estimation of $\tilde{c}$.

misalignment of ς in $v[n]$, Eq. (2.111) can be rewritten into the following matrix form:

$$\boldsymbol{v}[n+\varsigma] = \underbrace{\left[\eta \mathbf{1}_{N\times 1}, \bar{\boldsymbol{S}}^{\mathrm{Ext}}_{1,J}[n], \bar{\boldsymbol{S}}^{\mathrm{Ext}}_{2,J}[n]\right]}_{\bar{\boldsymbol{\Gamma}}^{\mathrm{Ext}}_{J}} \underbrace{\begin{bmatrix} \frac{d}{\eta} \\ \chi \boldsymbol{\Xi}_{J,\varsigma} \\ j\chi K_1 \boldsymbol{\Xi}_{J,\varsigma} \end{bmatrix}}_{\boldsymbol{p}^{\mathrm{Ext}}}, \tag{2.112}$$

where

$$\begin{aligned} \bar{\boldsymbol{S}}^{\mathrm{Ext}}_{1;2,J}[n] &= \underbrace{[\bar{\boldsymbol{s}}_{1;2}[n+n_{\mathrm{w}}-1], \ldots, \bar{\boldsymbol{s}}_{1;2}[n], \ldots, \bar{\boldsymbol{s}}_{1;2}[n-n_{\mathrm{w}}+1]]}_{N\times J \text{ Toeplitz matrix}} \\ \boldsymbol{\Xi}_{J,\varsigma} &= \underbrace{\left[\mathbf{0}_{1\times(n_{\mathrm{w}}-\varsigma-1)}, 1, \mathbf{0}_{1\times(n_{\mathrm{w}}+\varsigma-1)}\right]^T}_{J\times 1 \text{ column vector with the} (n_{\mathrm{w}}-\varsigma)^{\mathrm{th}} \text{ element equal to } 1} . \end{aligned} \tag{2.113}$$

Now, $\boldsymbol{p}^{\mathrm{Ext}}$ can be estimated by

$$\hat{\boldsymbol{p}}^{\mathrm{Ext}} = \left(\bar{\boldsymbol{\Gamma}}^{\mathrm{Ext}}_{J}\right)^{\dagger} \boldsymbol{v}[n+\varsigma]. \tag{2.114}$$

The estimates of the desired parameters χ, $j\chi K_1$ and d can be obtained by extracting the three elements of $\hat{\boldsymbol{p}}^{\mathrm{Ext}}$ with the largest magnitudes. By applying such an estimation, time synchronization errors up to $\varsigma = \pm(n_{\mathrm{w}}-1) = \pm\frac{J-1}{2}$ can be tolerated, which just result in position variation of the parameters χ and $j\chi K_1$ within $\hat{\boldsymbol{p}}^{\mathrm{Ext}}$.

2.6.2.5 Matrix Condition Analysis After Extension

Now, we analyze the condition number of $\bar{\boldsymbol{\Gamma}}^{\mathrm{Ext}}_{J}$. Similar to the analysis in Sec. 2.5.5 and 2.6.2.2, we first define

$$\begin{aligned} \boldsymbol{\Theta}^{\mathrm{Ext}} &:= \frac{1}{N}\left(\bar{\boldsymbol{\Gamma}}^{\mathrm{Ext}}_{J}\right)^{H} \bar{\boldsymbol{\Gamma}}^{\mathrm{Ext}}_{J}, \\ &= \begin{bmatrix} \eta^2 & \eta\boldsymbol{\mu}^{H}_{\bar{s}_1} & \eta\boldsymbol{\mu}^{H}_{\bar{s}_2} \\ \eta\boldsymbol{\mu}_{\bar{s}_1} & \boldsymbol{\Theta}_{\bar{s}_1,\bar{s}_1} & \boldsymbol{\Theta}_{\bar{s}_1,\bar{s}_2} \\ \eta\boldsymbol{\mu}_{\bar{s}_2} & \boldsymbol{\Theta}_{\bar{s}_2,\bar{s}_1} & \boldsymbol{\Theta}_{\bar{s}_2,\bar{s}_2} \end{bmatrix}, \end{aligned} \tag{2.115}$$

where

$$\boldsymbol{\mu}_{\bar{s}_{1;2}} := \frac{\eta}{N}\left(\bar{\boldsymbol{S}}^{\mathrm{Ext}}_{1;2,J}[n]\right)^{H} \mathbf{1}_{N\times 1}, \tag{2.116}$$

$$\boldsymbol{\Theta}_{\bar{s}_x,\bar{s}_y} := \frac{1}{N}\left(\bar{\boldsymbol{S}}^{\mathrm{Ext}}_{x,J}[n]\right)^{H} \bar{\boldsymbol{S}}^{\mathrm{Ext}}_{y,J}[n], \forall x, y \in \{1,2\}. \tag{2.117}$$

According to Sec. 2.5.5 and 2.6.2.2, we have the following relation of condition numbers:

$$\kappa\left(\boldsymbol{\Theta}^{\mathrm{Ext}}\right) = \kappa^2\left(\bar{\boldsymbol{\Gamma}}^{\mathrm{Ext}}_{J}\right). \tag{2.118}$$

When $N \to \infty$, the assumption on zero-mean WSS $s[n]$ yields

$$\begin{aligned} \boldsymbol{\mu}_{\bar{s}_{1;2}} &= \mathbf{0}_{J\times 1}, \\ \left(\boldsymbol{\Theta}_{\bar{s}_x,\bar{s}_y}\right)_{k,l} &= R_{\bar{s}_x,\bar{s}_y}[k-l], \forall k,l \in [0,J-1], \forall x,y \in \{1,2\}. \end{aligned} \tag{2.119}$$

Moreover, η should be chosen as

$$\eta = \frac{1}{\sqrt{2NJ}} \left|\left|\left[\bar{\boldsymbol{S}}^{\text{Ext}}_{1,J}[n], \bar{\boldsymbol{S}}^{\text{Ext}}_{2,J}[n]\right]\right|\right|_F, \tag{2.120}$$

so that the condition number of $\boldsymbol{\Theta}^{\text{Ext}}$ can be determined by[1]

$$\begin{bmatrix} \boldsymbol{\Theta}_{\bar{s}_1,\bar{s}_1} & \boldsymbol{\Theta}_{\bar{s}_1,\bar{s}_2} \\ \boldsymbol{\Theta}_{\bar{s}_2,\bar{s}_1} & \boldsymbol{\Theta}_{\bar{s}_2,\bar{s}_2} \end{bmatrix}. \tag{2.121}$$

We further define

$$\acute{\Phi}_{\bar{s}_x,\bar{s}_y}(\omega, J) := \sum_{l=-J+1}^{J-1} R_{\bar{s}_x,\bar{s}_y}[l] e^{-j\omega n}, \forall x,y \in \{1,2\}. \tag{2.122}$$

From (2.51), (2.91) and (2.93), we can see that

$$\begin{aligned} \acute{\Phi}_{\bar{s}_1,\bar{s}_1}(\omega, J) &= \left|\bar{H}(\omega)\right|^2 \acute{\Phi}_{s_{\text{re}},s_{\text{re}}}(\omega, J), \\ \acute{\Phi}_{\bar{s}_2,\bar{s}_2}(\omega, J) &= \left|\bar{H}(\omega)\right|^2 \acute{\Phi}_{s_{\text{im}},s_{\text{im}}}(\omega, J), \\ \acute{\Phi}_{\bar{s}_1,\bar{s}_2}(\omega, J) &= \left|\bar{H}(\omega)\right|^2 \acute{\Phi}_{s_{\text{re}},s_{\text{im}}}(\omega, J). \end{aligned} \tag{2.123}$$

Following the derivation procedure from (2.55) to (2.61), we can obtain the following eigenvalue bounds:

$$\min_{\omega} \acute{\Phi}_{\bar{s},\bar{s}}(\omega, J) \le \lambda_m\left(\boldsymbol{\Theta}^{\text{Ext}}\right) \le \max_{\omega} \acute{\Phi}_{\bar{s},\bar{s}}(\omega, J),\ \forall 1 \le m \le 2J, \tag{2.124}$$

where

$$\acute{\Phi}_{\bar{s},\bar{s}}(\omega, J) := \acute{\Phi}_{\bar{s}_1,\bar{s}_1}(\omega, J) + \Im m\left\{\acute{\Phi}_{\bar{s}_1,\bar{s}_2}(\omega, J)\right\}. \tag{2.125}$$

Moreover, the condition numbers of $\boldsymbol{\Theta}^{\text{Ext}}$ and $\bar{\boldsymbol{\Gamma}}^{\text{Ext}}_J$ are bounded by

$$\kappa\left(\boldsymbol{\Theta}^{\text{Ext}}\right) \le \frac{\max_{\omega} \acute{\Phi}_{\bar{s},\bar{s}}(\omega, J)}{\min_{\omega} \acute{\Phi}_{\bar{s},\bar{s}}(\omega, J)}, \quad \text{and} \quad \kappa\left(\bar{\boldsymbol{\Gamma}}^{\text{Ext}}_J\right) \le \sqrt{\frac{\max_{\omega} \acute{\Phi}_{\bar{s},\bar{s}}(\omega, J)}{\min_{\omega} \acute{\Phi}_{\bar{s},\bar{s}}(\omega, J)}}, \tag{2.126}$$

respectively.

[1] Please refer to App. A.3 for explanation.

With (2.122), (2.123), (2.125) and (2.52), we obtain

$$\acute{\Phi}_{\bar{s},\bar{s}}(\omega, J) = \left|\bar{H}(\omega)\right|^2 \acute{\Phi}_{s,s}(\omega, J). \tag{2.127}$$

Considering that $\left|\bar{H}(\omega)\right|^2$ has a relatively flat shape, the condition number bounds are mainly determined by $\acute{\Phi}_{s,s}(\omega, J)$ i.e. the spectral characteristics of $s[n]$ and the Toeplitz extension size J. This is similar to the case in Sec. 2.5.5.

Similar to Fig. 2.11, Fig. 2.31 shows the condition number as a function of the number of active subbands in an MB UMTS signal, where different J values were applied[1]. As shown, the condition number remains very low with $J = 1$. In the case with relatively small number of active subbands (e.g. $1 \sim 4$), a small increase in J can already lead to a strong increase of the condition number. Compared to Fig. 2.11, as the number of active subbands increases, the condition number decrease (with $J = 3$ or $J = 5$) is much faster. The reason is that the J values are small.

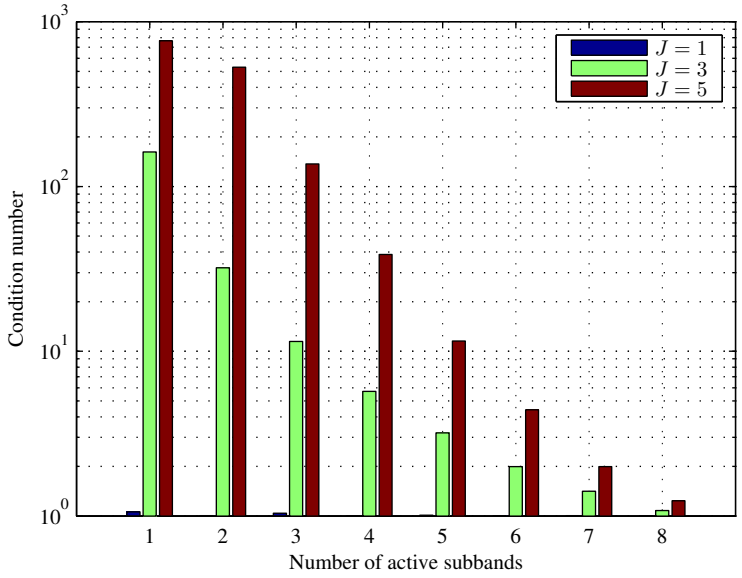

Figure 2.31: Condition number as a function of the number of active subbands in an MB UMTS signal. Different Toeplitz extension sizes are compared. $N = 4096$.

Fig. 2.32 shows the condition number as a function of J for different signal types. As shown, the larger the value of J, the higher the condition number. The increase rate of the condition number differs from signal to signal.

[1]The maximum time synchronization errors that can be tolerated with $J = 1, 3, 5$ are $\pm 0, \pm 1, \pm 2$, respectively.

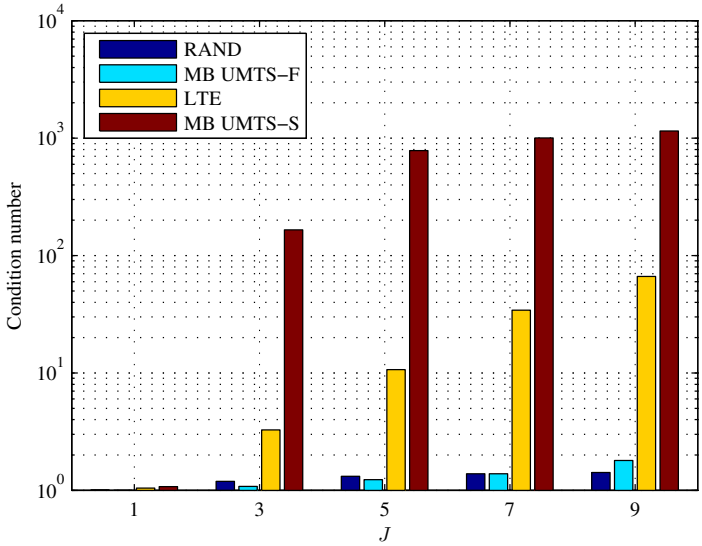

Figure 2.32: Condition number as a function of the Toeplitz extension. Different signals are compared. $N = 4096$.

2.6.3 Numerical Simulation Results

In the simulation, the I/Q-imbalance and DC offset error parameters are modeled as time variant. The parameter values and the variation pattern are the same as in the tracking test of Sec. 2.5.7. A similar variation pattern is applied for χ. In all following simulations, the additive noise level $10\log(P_n/P_s) = -50$ dB was applied. For the initial calibration, pilot sequences of length 256 were applied. The averaging number was 200. For the tracking, we first use the three signal types in Sec. 2.5.7, i.e. LTE, MB UMTS-F and MB UMTS-S, for parameter estimation. More signal types will be used, when time synchronization error is encountered. The used number of samples for tracking will be specified in the description of each result. For simplicity, no averaging was applied.

First, we investigate the calibration performance with perfect time synchronization. Fig. 2.33 shows the IRR of the simplified scheme with the MB UMTS-S signal, which has the largest spectral gap and can cause severe ill-conditioned matrix problem in the LSE. The used signal block length was 2048. The tracking interval was 0.2 s. As shown, in spite of the large spectral gaps of the MB UMTS-S signal, relatively high IRR can be achieved by the simplified scheme both at the initial calibration phase and at the tracking phase. For performance comparison, we recall the results in Sec. 2.5.7 (see Fig. 2.22). As reported in Sec. 2.5.7, with such a transmit signal, the LS-based scheme and the schemes in [2] and [3] have bad performance even when a very large signal block (12800 samples) is applied.

Fig. 2.34 and 2.35 show the IRR as a function of time. The following cases are compared: no calibration, calibration without parameter tracking (the parameters are only estimated at

$t = 1$ s with the scheme in Sec. 2.6.1.), calibration with tracking applying LSE, calibration with tracking applying IFDE [38] and calibration with tracking applying the simplified scheme. While the LTE signal is applied in Fig. 2.34, the MB UMTS-S signal is applied in Fig. 2.35. In all cases, no SIPS is applied. The number of samples used was 12800. The tracking interval was 0.6 s. As shown in Fig. 2.34, the simplified scheme, the LS scheme and the IFDE scheme can achieve sufficient IRR over the entire observed time. However, with the same number of samples used, the IRR achieved by the simplified scheme is much higher than those by the LSE- and the IFDE schemes. In Fig. 2.35, only the simplified scheme can achieve high IRR. Both LSE and IFDE show poor performance. Especially, the performance of the IFDE was much worse than that without calibration. While the LSE suffers from ill-conditioned matrix problem, the IFDE suffers from divergence, which is caused by the strong correlation between the real- and imaginary parts of the MB UMTS-S signal[1].

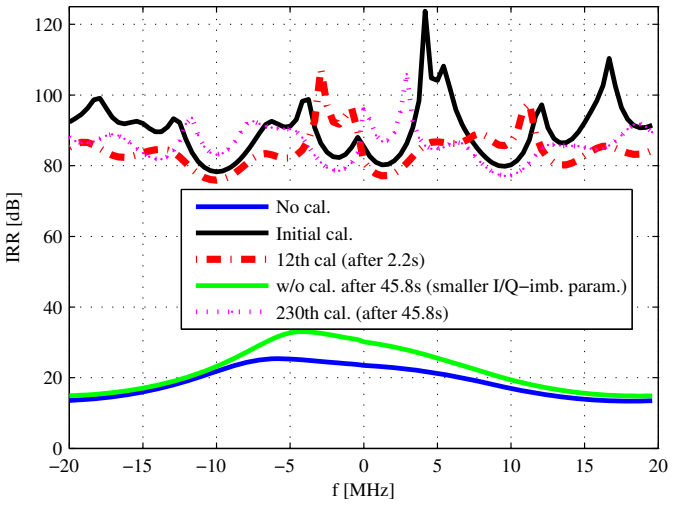

Figure 2.33: IRR with the simplified two-phase method at different tracking times. $10\log(P_n/P_s) = -50\text{dB}, N = 2048$.

Now, we investigate the influence of time synchronization error in the tracking phase. According to the analysis in Sec. 2.6.2.3, the tracking performance under time synchronization error mainly depends on the characteristics of the signal PSD. For a detailed verification, we extend the used signal types in the following simulations. The extended signal types are listed below:

- **MB UMTS-S,3**: The MB UMTS signal of Fig. 2.12, which can adopt maximum 8 subbands (this also applies to the following MB UMTS signals). However, only one subband is active. The number "3" indicates that the only active subband is the 3$^{\text{rd}}$

[1]Due to divergence, the IFDE yields $h^C[n]$ with very large values, which strongly amplifies the Q-branch signal. As a result, the IRR becomes very low.

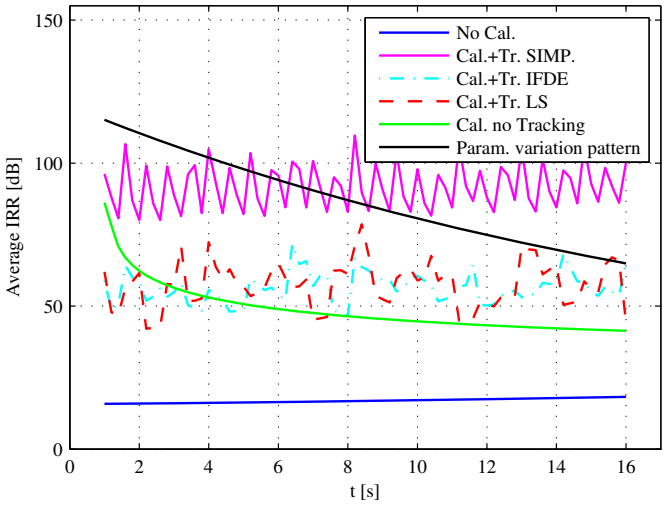

Figure 2.34: Tracking with LTE signal. Different schemes are compared. $10\log(P_n/P_s) = -50$ dB. No SIPS was applied. $N = 12800$.

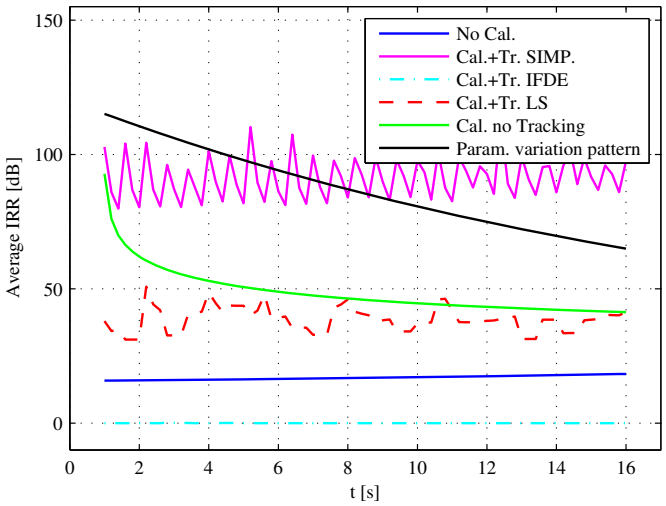

Figure 2.35: Tracking with MB UMTS-S signal. Different schemes are compared. $10\log(P_n/P_s) = -50$ dB. No SIPS was applied. $N = 12800$.

subband[1];

- **MB UMTS-S,0**: An MB UMTS signal with only one subband active, which has a zero IF;
- **MB UMTS-M,-3 3**: An MB UMTS signal with two subband active, i.e. the -3^{rd}- and the 3^{rd} subbands. The notation "-M" indicates that multiple subbands are active;
- **MB UMTS-M,1 2 3 4**: An MB UMTS signal with all four subbands on the right spectrum side[2] active, i.e. the $1^{\text{st}} \sim 4^{\text{th}}$ subbands;
- **LTE**: The LTE signal of Fig. 2.15;
- **MB UMTS-F**: The MB UMTS signal of Fig. 2.13 with all subbands active.

The ACF $R_{s,s}[l]$ and the CACF $R_{s,s*}[l]$, the correlation functions $R_{s_{\text{re}},s_{\text{re}}}[l]$ and $R_{s_{\text{re}},s_{\text{im}}}[l]$ as well as the function $\left|\frac{R_{s_{\text{re}},s_{\text{im}}}[l]}{R_{s_{\text{re}},s_{\text{re}}}[l]}\right|$ of the signals above are illustrated in Fig. 2.36, Fig. 2.37 and Fig. 2.38, respectively[3]. While "MB UMTS-S,3" and "MB UMTS-S,1 2 3 4" are quasi proper signals (see Sec. 2.6.2.3), "MB UMTS-S,0", "MB UMTS-S,-3 3", "LTE" and "MB UMTS-F" are improper signals. From Fig. 2.36 and Fig. 2.37, we can see that the improper signals have much stronger CACF but much weaker $|R_{s_{\text{re}},s_{\text{im}}}[l]|$ than the quasi proper signals (we mainly observe the range $-7 < l < 7$). Fig. 2.38 further shows that the quasi proper signals have much higher values of $\left|\frac{R_{s_{\text{re}},s_{\text{im}}}[l]}{R_{s_{\text{re}},s_{\text{re}}}[l]}\right|$ than the improper signals. Moreover, we can also see that the more spectral gap a signal has, the larger the ACF magnitude as well as $|R_{s_{\text{re}},s_{\text{re}}}[l]|$ tend to be[4]. Note that since $\bar{h}[n]$ has only minor influence on the characteristics of $\left|R_{\bar{s}_x,\bar{s}_y}[l]\right|, \forall x, y \in \{1,2\}$ (see Sec. 2.6.2.2), we can generally use $|R_{s,s}[l]|$, $|R_{s,s*}[l]|$, $|R_{s_{\text{re}},s_{\text{re}}}[l]|$ and $|R_{s_{\text{re}},s_{\text{im}}}[l]|$ to represent $|R_{\bar{s},\bar{s}}[l]|$, $|R_{\bar{s},\bar{s}*}[l]|$, $|R_{\bar{s}_1,\bar{s}_1}[l]|$ and $|R_{\bar{s}_1,\bar{s}_2}[l]|$, respectively, for performance analysis. Applying the values of the correlation functions in Fig. 2.36 and Fig. 2.37 to (2.110), the theoretical estimation MSE of K_1 with different signal types can be obtained, which is shown in Fig. 2.39.

Fig. 2.40 and 2.41 show the tracking IRRs with the extended signal types as functions of the time synchronization error. While Fig. 2.40 shows the IRRs of the first tracking interval after the occurrence of a time synchronization error, Fig. 2.41 shows those of the sixth tracking interval. Here, for simplicity of illustration, we assume that the time synchronization error remains constant after its occurrence. Moreover, no Toeplitz extension was applied. As shown, the IRR results in Fig. 2.40 are generally consistent with the theoretical MSEs in Fig. 2.39. While the IRRs with quasi proper signals are quite high[5] in spite of time synchronization error, the IRRs with improper signals degrade strongly as the time synchronization error becomes larger. This can be explained by the stronger CACF of the improper signals shown in Fig. 2.36. Among the quasi proper signals, the "MB UMTS-S,3" signal has higher IRR than the "MB

[1] The whole subband index set is $\{-4,-3,-2,-1,1,2,3,4\}$.
[2] W.r.t. the DC frequency.
[3] The correlation functions are calculated with a correlation block length of 12800.
[4] Strictly speaking, the more spectral gaps the symmetric PSD part has, the higher the value of $|R_{s_{\text{re}},s_{\text{re}}}[l]|$.
[5] Above 60 dB for time synchronization errors within ± 9 samples.

UMTS-M,1 2 3 4" signal. Actually, if both signals are perfectly proper, the IRR relation of both signals should follow the relation of the corresponding $\left|\frac{R_{s_{\mathrm{re}},s_{\mathrm{im}}}[l]}{R_{s_{\mathrm{re}},s_{\mathrm{re}}}[l]}\right|$ values (which represents $\frac{\theta}{\rho}$) in Fig. 2.38. However, the results in Fig. 2.40 and Fig. 2.38 regarding the quasi proper signals do not match. The reason is that both signals are not perfectly proper. Although not obviously shown in Fig. 2.36, the CACF of the "MB UMTS-M,1 2 3 4" signal (about 1×10^{-4}) is much higher than that of the "MB UMTS-S,3" signal (about 3×10^{-5}), resulting in higher estimation MSE of K_1. Among the improper signals, the best performance is achieved with the "MB UMTS-S,0" signal. The reason is that the large amount of spectral gaps as well as the strong symmetric PSD part lead to large values of $|R_{s_{\mathrm{re}},s_{\mathrm{re}}}[l]|$ and thus, ρ (see Fig. 2.37), which dominates the MSE of K_1 for improper signals[1]

As shown in Fig. 2.41, the IRRs with improper signals in the sixth tracking interval have not changed too much from those in the first tracking interval. In contrast, depending on the value of the time synchronization error, the IRRs with quasi proper signals can continuously degrade from one tracking interval to the next[2]. This verifies that proper signals are more sensitive to error propagation[3]. Especially, the IRR with the "MB UMTS-S,3" signal shows strong periodical fluctuation (for time synchronization errors within ± 10 samples). Such fluctuation can be explained by the fluctuation of the value $\left|\frac{R_{s_{\mathrm{re}},s_{\mathrm{im}}}[l]}{R_{s_{\mathrm{re}},s_{\mathrm{re}}}[l]}\right|$ in Fig. 2.38, which is determined by the PSD characteristic of this signal[4]. For proper signals, the MSE of K_1 is mainly determined by $\frac{\theta}{\rho}$ i.e. $\left|\frac{R_{s_{\mathrm{re}},s_{\mathrm{im}}}[l]}{R_{s_{\mathrm{re}},s_{\mathrm{re}}}[l]}\right|$ (see Fig. 2.28). Thus, the fluctuation of $\left|\frac{R_{s_{\mathrm{re}},s_{\mathrm{im}}}[l]}{R_{s_{\mathrm{re}},s_{\mathrm{re}}}[l]}\right|$ causes fluctuation in the MSE of K_1 (as shown in Fig. 2.39), which leads to fluctuation of the error propagation influence.

Fig. 2.42 shows the IRR as a function of time with sporadic time synchronization error. As an example, the LTE signal was used for estimation. Moreover, $N = 2048$ was applied. The tracking interval was 0.4 s. The three marked areas (in red) in this figure correspond to one, two and three consecutive tracking procedures with time synchronization errors, respectively. For simplicity, the value of the time synchronization error was fixed to two (samples). As shown again, time synchronization causes severe IRR drop. However, as soon as the time synchronization error disappears, the IRR gets back to high values. This verifies that in the case without time synchronization error, the proposed tracking algorithm is free of error propagation.

Now, in order to cope with time synchronization error, the Toeplitz extension in Sec. 2.6.2.4 is applied. Fig. 2.43 and 2.44 show the IRRs (as functions of the time syncrhonization error) with the Toeplitz extension sizes $J = 3$ and $J = 5$, respectively, in the first tracking interval after the occurrence of time synchronization error. The IRRs in the sixth tracking interval are similar, when the time synchronization error is within $\frac{J-1}{2}$ samples. As shown, the Toeplitz extension technique makes the tracking scheme robust against time synchronization error. In

[1] Considering the CACF values of the improper signals shown in Fig. 2.36. Please refer to Fig. 2.28 and Fig. 2.29.

[2] Only when time synchronization does not disappear.

[3] Please refer to the result in Fig. 2.30 and the corresponding interpretation.

[4] For MB UMTS-S signals, the further the active subband is away from the DC frequency, the smaller the fluctuation period.

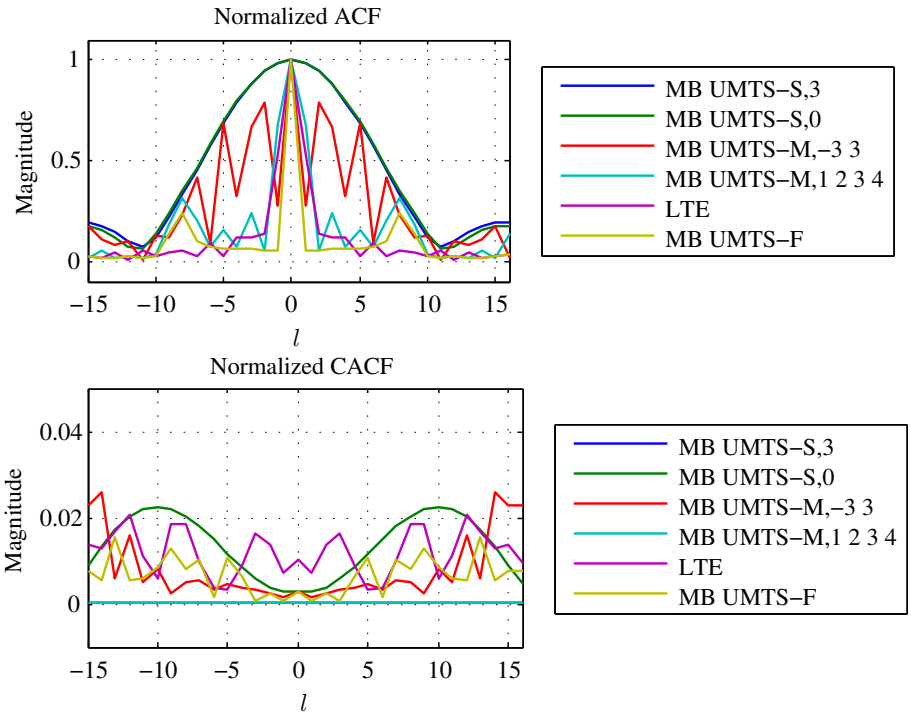

Figure 2.36: ACF and CACF of different signals (both are normalized by $2P$ i.e. $R_{s,s}[0]$).

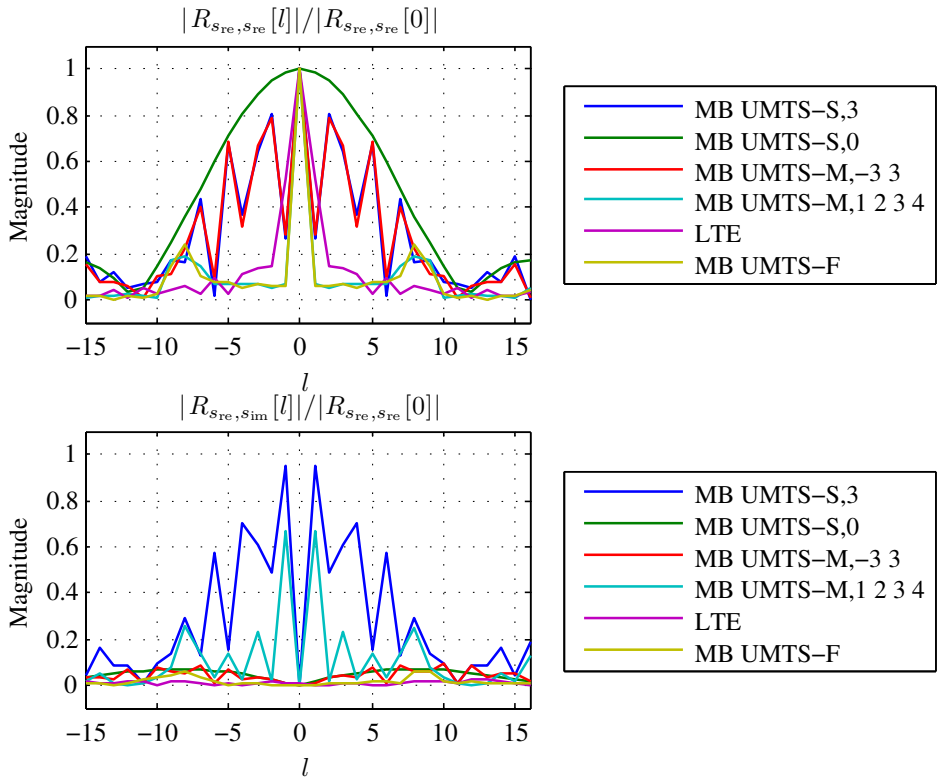

Figure 2.37: The correlation functions $R_{s_{\mathrm{re}},s_{\mathrm{re}}}[l]$ and $R_{s_{\mathrm{re}},s_{\mathrm{im}}}[l]$ of different signals. Both are normalized by P i.e. $R_{s_{\mathrm{re}},s_{\mathrm{re}}}[0]$.

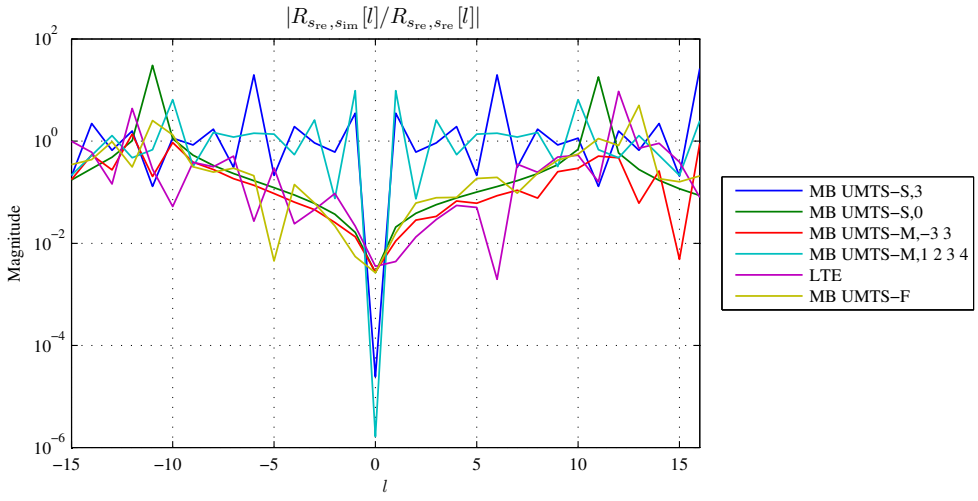

Figure 2.38: The function $\left|\frac{R_{s_{\mathrm{re}},s_{\mathrm{im}}}[l]}{R_{s_{\mathrm{re}},s_{\mathrm{re}}}[l]}\right|$ of different signals.

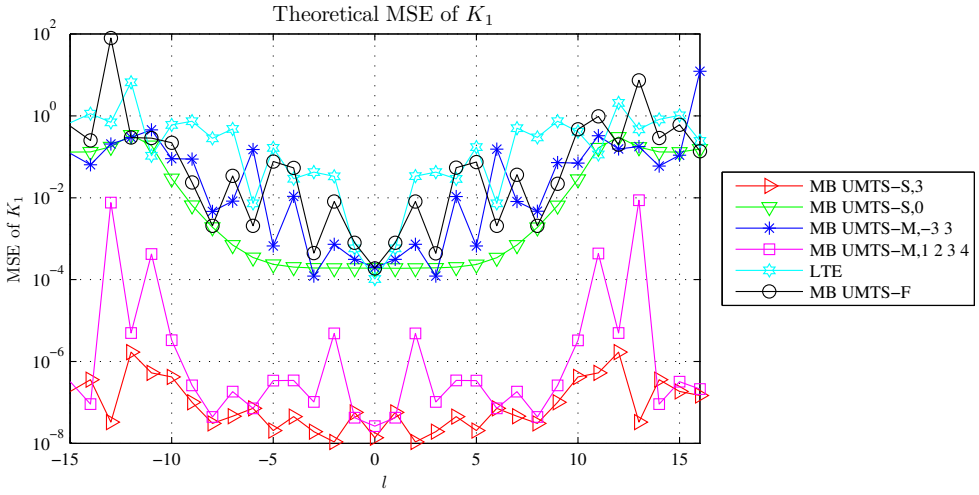

Figure 2.39: The theoretical MSE of K_1 calculated from the correlation functions of different signals. The noise influence was ignored.

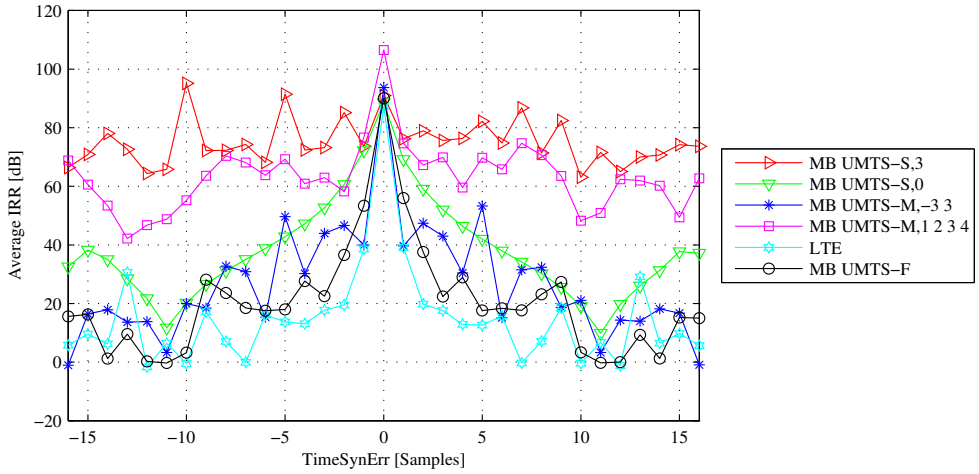

Figure 2.40: IRR in the first tracking interval after the occurrence of a time synchronization error. Different signals are compared. $10\log(P_n/P_s) = -50$ dB. $N = 12800$.

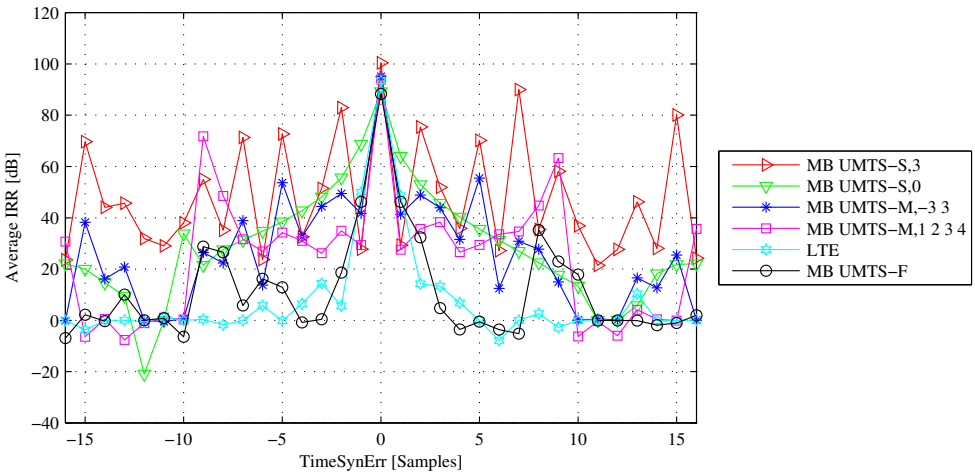

Figure 2.41: IRR in the sixth tracking interval after the occurrence of a time synchronization error. Different signals are compared. $10\log(P_n/P_s) = -50$ dB. $N = 12800$.

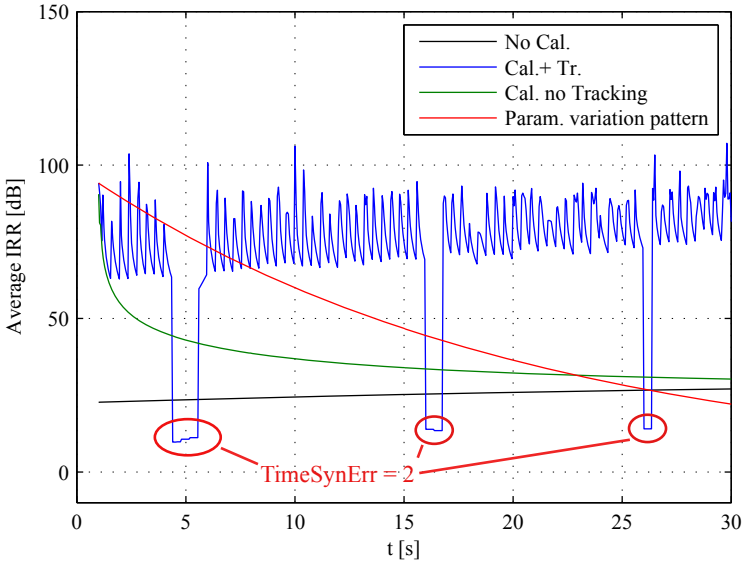

Figure 2.42: IRR as a function of time with sporadic time synchronization error. LTE signal was used for estimation. Time synchronization error was 2 samples. The tracking interval was 0.4 s. $10\log(P_n/P_s) = -50$ dB. $N = 2048$.

Fig. 2.43 and Fig. 2.44, time synchronization errors up to ±1 and ±2, respectively, can be tolerated. However, we can also see that due to the condition number increase caused by Toeplitz extension, the achievable IRR with the "MB UMTS-S,3" and "MB UMTS-S,0" signals (within the tolerable time synchronization error range) is decreased considerably (compared to the case without Toeplitz extension and without time synchronization error). In contrast, the IRRs of the other signals remain quite high, since the corresponding condition numbers do not increase too much due to the Toeplitz extension (see Fig. 2.32).

Fig. 2.45 shows the number of required samples to achieve $IRR \geq 60$ as a function of J for the three main signal types: MB UMTS-F, LTE and MB UMTS-S (i.e. the "MB UMTS-S,3"). As shown, the required numbers of samples for both the LTE signal and the MB UMTS-F signal are generally quite small [1]. In contrast, when the MB UMTS-S signal is used, much larger numbers of samples are required.

Finally, considering the results in Fig. 2.40, Fig. 2.41, Fig. 2.43 and Fig. 2.44, we can conclude that the application of Toeplitz extension should depend on PSD characteristics of the signal as well as the statistical characteristic of the time synchronization error (which depends on the applied time synchronization mechanism). For quasi proper signals (e.g. "MB UMTS-S,3" and "MB UMTS-M,1 2 3 4"), Toeplitz extension is unnecessary, since the tracking with such signals can inherently tolerate certain range of time synchronization error, as long as this error does not last for a long time[2]. For improper signals, Toeplitz extension should be applied, since such signals are sensitive to time synchronization error. The Toeplitz extension size J should be chosen according to the statistics of the time synchronization error. The number of signal samples used for estimation depends on the amount of spectral gaps of the signal. Generally, the larger the amount of spectral gaps, the larger the number of signal samples required to achieve a reasonable IRR.

In the results above, we mainly focused on the I/Q-imbalance compensation performance. It should be remarked that in all the simulations above (except for those with time synchronization error in Fig. 2.40 and Fig. 2.41), as long as the I/Q-imbalance is sufficiently compensated for, the MOD DC-offset was found to be almost completely suppressed.

2.7 Complexity Issues and Discussion

Tab. 2.1 shows the complexity of the different pre-equalization circuits. As shown, the proposed pre-equalization circuit (Fig. 2.7) requires the lowest complexity, while the circuit complexities of "Ding" and "Anttila" are similar[3].

Tab. 2.2 shows the computational complexity expressions for the parameter estimation[4]

[1] Except for the case with the LTE signal applying $J = 7$.

[2] But the MOD DC-offset compensation can be affected considerably, which needs further investigation.

[3] For I/Q-imbalance compensation, "Ding" applies four real FIR filters of length L, while "Anttila" applies one length-L complex FIR filter. Moreover, for fair comparison, the "Anttila" scheme was extended to include MOD DC-offset compensation.

[4] This also includes the pre-equalization coefficient calculation. Moreover, it is assumed that the inverse of

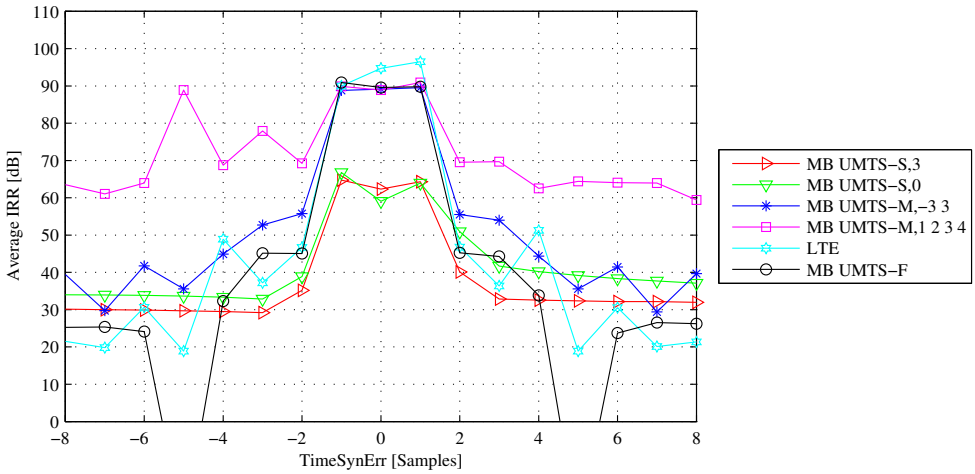

Figure 2.43: IRR as a function of time synchronization error after Toeplitz extension with $J = 3$. Different signals are compared. $10 \log (P_n/P_s) = -50$ dB. $N = 12800$.

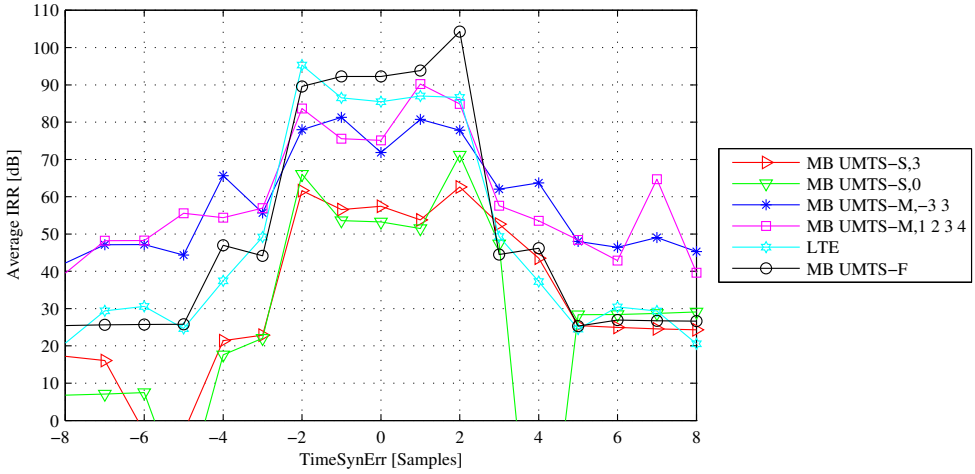

Figure 2.44: IRR as a function of time synchronization error after Toeplitz extension with $J = 5$. Different signals are compared. $10 \log (P_n/P_s) = -50$ dB. $N = 12800$.

Table 2.1: Complexity of Different Pre-Equalization Circuits

Scheme	**Real MULs**	**Real ADDs**
Proposed	$L + 1$	$L + 2$
Ding	$4L$	$4L$
Anttila	$4L$	$2L + 2$

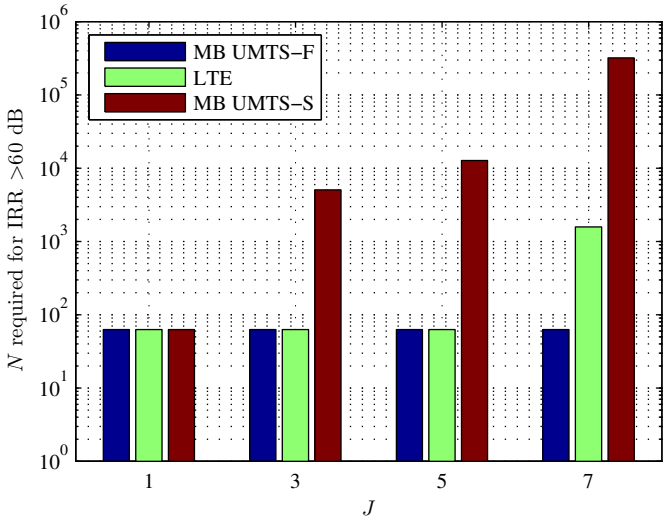

Figure 2.45: Number of required samples to achieve $IRR > 60$ as a function of the Toeplitz extension. Different signals are compared. $10\log(P_n/P_s) = -50$ dB.

of different schemes. We assume that the reference schemes also use the DFT-length L_F for the calculation of pre-equalization coefficients. For the initial estimation of the SIMP scheme, averaging[1] is applied with the averaging number $B_A = \left\lceil \frac{N}{L_F} \right\rceil$. For the IFDE scheme in [38], N_I is the number of iterations. Moreover, N_F is the DFT-length for iterative processing and B is the number of signal blocks for averaging. For fair comparison, we should have $N = BN_F$, so that the number of used signal samples is the same as the other schemes. Note that both for the LS-based scheme and the IFDE scheme, the computational complexity for the spectral analysis and the generation and deployment of SIPS is not included, which may require extra DFT and IDFT operations and increase the total computational complexity slightly. Recalling that spectral analysis and SIPS can be applied to the LS-based scheme and the "Ding"- and "Anttila" schemes to solve ill-conditioned matrix problems, the resulting increase in computational complexity of all these three schemes will be the same.

By substituting the simulation parameters $L = 16$ as well as $L_F = 64, N_F = 256, N_I = 10$ into the expressions in Tab. 2.2, the computational complexity can be shown in Fig. 2.46 as a function of N. Generally, the lowest and the highest computational complexity are required by the proposed "SIMP" scheme[2] and the IFDE scheme, respectively. We can also see that the "Anttila" scheme has higher complexity than the "SIMP" tracking scheme, the LS-based

a $N \times N$ (real/complex) matrix requires $\frac{N^3-N}{3}$ MULs (real/complex). The pseudo inverse of a matrix $\boldsymbol{X}$ is computed by $\left(\boldsymbol{X}^H\boldsymbol{X}\right)^{-1}\boldsymbol{X}^H$. In practice, different implementations can be used to calculate the pseudo inverse and thus, can lead to different computational complexities. Finally, we approximate the complexity of a real division with a real MUL, although the latter is less complex.

[1] Note that division operation for averaging can be efficiently implemented by using barrel shifters.

[2] Except for the case of $N = 64$. Even if we add the complexity of both the initial estimation and tracking of the "SIMP" scheme, it is still the lowest one (except for $N = 64$).

scheme (initial estimation/tracking) and the "Ding" scheme. The reason is that the "Anttila" scheme requires pseudo-inverse calculation of a $N \times (2L+1)$ complex valued matrix[1], while the other three schemes just requires similar calculations with real-valued inputs[2]. Furthermore, it should be remarked that according to Sec. 2.5.7 and Sec. 2.6.3, when signals with large spectral gaps e.g. MB-UMTS-S are applied, the SIMP scheme requires much less signal samples than the other schemes to achieve comparable performance[3]. Thus, in such cases, the SIMP scheme requires significant lower computational complexity than the other schemes.

Based on the comparison above, the proposed schemes can have lower complexity in the pre-equalization circuit and/or the parameter estimation than the reference schemes. Moreover, except for initial estimation, the proposed schemes also consider parameter tracking, which is a very practical issue. Compared to the proposed LS-based scheme, the proposed "SIMP" scheme has lower computational complexity for parameter estimation and does not require SIPS, which may generate ItCI and increase Tx power. Thus, the "SIMP" scheme is actually the most efficient, effective, flexible and practical scheme.

Table 2.2: Computational Complexity of Different Estimation Schemes

Scheme	**Number of real MULs**
LS,init.	$10L_F(2+\log_2 L_F)+4(2+N)+\frac{4}{3}L\,(1+9N+L(3+2L+6N))$
LS,track.	$\frac{2}{3}\,(3(8+11L_F+6L_F\log_2 L_F+2N)+L(5+18N+2L(3+2L+6N))$
SIMP,init.	$B_A(8+L_F(36+26\log_2 L_F))$
SIMP,track.,$J=0$	$52+72N+L(13+4L+4N)$
SIMP,track.,$J\neq 0$	$20+13L+4L(L+N)+\frac{8}{3}(1+2J)(3N+2J(1+J+3N))$
Ding	$\frac{4}{3}(3(2+L_F(2+4\log_2 L_F)+N)+L(1+9N+L(3+2L+6N)))$
Anttila	$\frac{4}{3}(6+6L_F+9L_F\log_2 L_F+6N+4L(1+L)(1+2L+6N))$
IFDE	$8+10L_F(2+\log_2 L_F)+\frac{16}{3}B(L(-1+3L'+L(6+L+6L'))N_I$ $+3N_F(\log_2 N_F+4N_I))$

2.8 Hardware-In-the-Loop (HIL) Experiment

Hardware-In-the-Loop (HIL) experiment is a very efficient and effective way to provide proof-of-concept of algorithms. It is also an important step towards prototype development. In this section, the HIL verification of the proposed Smart-RF schemes are described.

2.8.1 Structure of the Experimental Device

The HIL experiments are performed with a broadband wireless experimental device, which has been developed and fabricated at Fraunhofer Institute for Telecommunication (Heinrich-Hertz-Institute). Fig. 2.47 shows the structure of the experimental device, which is hosted in

[1]Note that the "Anttila" scheme is extended to include MOD DC-offset estimation.

[2]Both the LS-based scheme and the "Ding" scheme require pseudo-inverse of a $N \times (2L+1)$ real-valued matrix. The "SIMP" tracking requires pseudo-inverse of a real-valued $N \times (2J+1)$ matrix.

[3]Assuming $J \leq 3$.

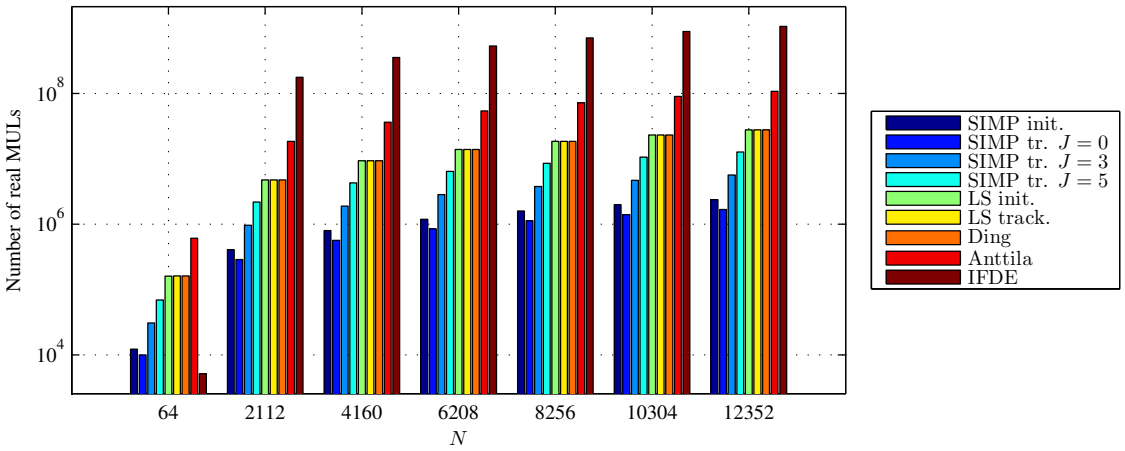

Figure 2.46: Computational complexity for parameter estimation as a function of N i.e. number of reference signal samples.

a high performance Personal Computer (PC) and consists of digital components, analog BB components and RF components. The digital platform is a commercial ProcStarII FPGA board (Gidel Ltd.), where high performance FPGA devices (ALTERA Stratix II) and large sample-memories (64 MB DDR II) are located. This FPGA board exchanges configuration-, control- and transmission data with software applications (e.g. MatLab) in the host PC via PCI-X bus. A high speed signal converter board has been developed to connect the analog BB- and RF-parts with the digital platform. This converter board contains two 16bit IQ-DACs and two 8bit IQ-ADCs as well as power supply devices and control logic. The sampling rate of the DAC and ADC can be up to 250 MHz and 500 MHz, respectively. The analog BB- and RF-components are designed as small form-factor modules that can be plugged onto the converter board. Thus, they are interchangeable to adapt the device to different RF architectures and RF frequencies. Currently, frontend components for both the 1.975 $\sim$ 2.525 GHz band and the 60 GHz band are available. Moreover, this device can be equipped with two Tx- and two Rx antennas.

2.8.2 HIL Experimental Setup for Smart-RF Test

Fig. 2.48 shows the HIL experimental setup for Smart-RF test. As shown, the BB sampling rate of the Tx is 40 MHz. Correspondingly, the Tx signal BW is below 40 MHz. Recall from Fig. 2.47 that the experimental system has two Tx- and two Rx paths[1]. For the Smart-RF test, only one Tx path of the experimental device is utilized. The DACs have internal rate-doubler with interpolation filter. The pass-band of the RLPs is 20 MHz. Different MOD modules are available[2], which can convert the Tx BB signal on to the 2.4 GHz or 2.6 GHz bands. Both the

[1]Each path has an I/Q-modulator/demodulator.

[2]Including an ATMEL 700 MHz - 2700 MHz Direct Quadrature Modulator T0790 and an LT5528 1.5 GHz to 2.4 GHz high linearity direct quadrature MOD (Linear Technology).

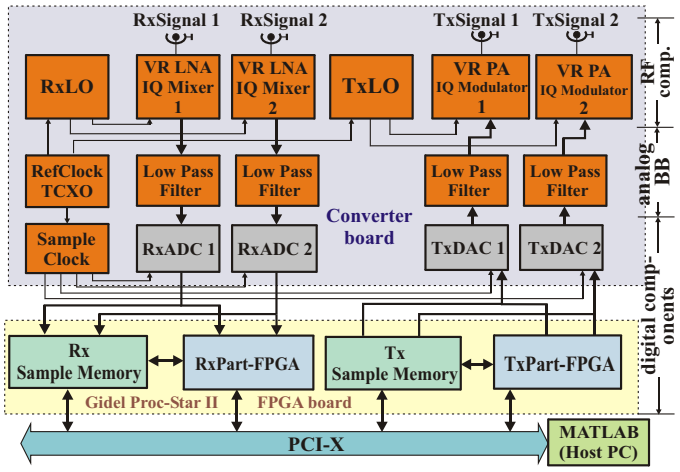

Figure 2.47: Structure of the experimental device (VR: Variable Gain; PA: Power Amplifier).

output signals of the MOD and the PA are coupled with feedback paths, which are mapped to both Rx paths of the experimental device[1]. In each feedback path, the RF signal is filtered and down converted to an IF signal with the IF frequency 40 MHz. Afterwards, each IF signal is sampled by an ADC with the sampling rate 160 MHz. In the digital BB, the IF signal is perfectly I/Q-demodulated to a zero-IF signal, filtered and down-sampled to $f_s = 40$ MHz. The interfacing between the real time signal processing in FPGA and the off-line signal processing (in MATLAB) is realized by up-/downloading signal samples to/from the sample-memories of the FPGA board (see Fig. 2.47).

The parameter estimation for I/Q-imbalance and DC-offset as well as for the PA pre-distortion is carried out in MATLAB (offline processing). While the schemes described in this chapter are used for I/Q-imbalance and DC-offset estimation, the schemes in [51, 60] are applied for the calculation of the PA-predistortion coefficients[2]. In contrast, the pre-equalizer for I/Q-imbalance compensation (Fig. 2.7) as well as the PA pre-distorter ([60]) are implemented in FPGA and operate in real time. However, unlike in the theoretical model, the MOD DC-offset compensation is not carried out by adding DC-terms to the Tx signal digitally. The reason was that in the experimental system, a capacitor at the DAC output will remove the DC-components of the Tx signal. Thus, the MOD DC-offset compensation is carried out by adjusting the MOD input DC voltage[3].

[1] the RF switch in Fig. 2.48 just illustrates a way to reduce hardware complexity

[2] Both the calculation of the PA-predistortion coefficients and the realtime FPGA implementation of the pre-distortion were implemented by Jacek Liszewski.

[3] Via an auxiliary control register of the DAC.

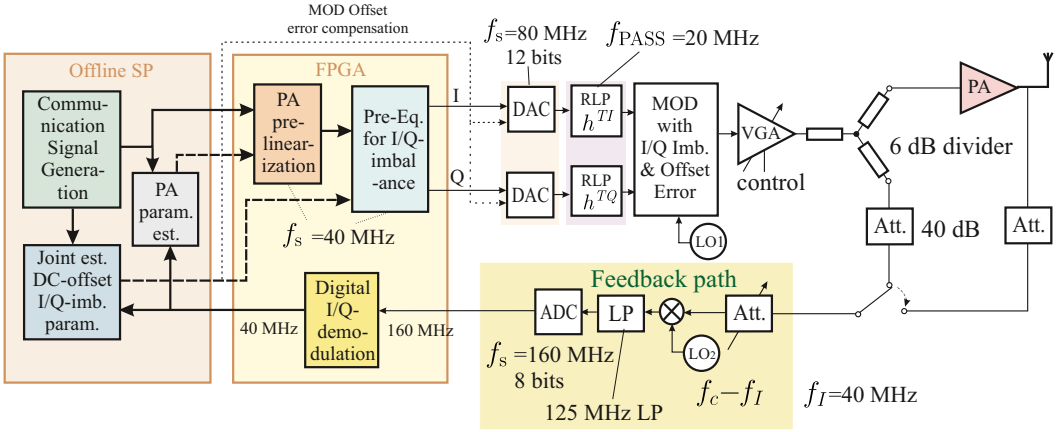

Figure 2.48: HIL experimental setup for Smart-RF test.

2.8.3 HIL Experiment Results

In this section, we mainly focus on the compensation of I/Q-imbalance and MOD DC-offset. Nevertheless, some results of the combination of I/Q-imbalance compensation and PA pre-distortion will also be shown. For simplicity, pilot based time synchronization was applied, which allows near-perfect time synchronization.

Fig. 2.49 and 2.50 show the measured IRR with the LS-based scheme in Sec. 2.5. Both results with an LTE signal and an MB UMTS-S signal are shown. About 51200 signal samples were applied for estimation (with signal blocks of length 256 and averaging number of 200). After parameter estimation and coefficient upload (to the realtime pre-equalizer to activate the pre-equalization), a reference sequence was transmitted and then captured from the feedback path for IRR measurement, which was done in MATLAB using a similar method as in [48]. As shown, when the SIPS power was high enough ($40 \sim 50$ dB), average IRR above 50 dB can be achieved[1].

The effectiveness of I/Q-imbalance compensation was also investigated by spectrum measurement. First, a Single-Side-Band (SSB) signal was generated, which has constant spectral power in the active band. Afterwards, this signal was uploaded to a Random-Access-Memory (RAM) in the FPGA and was transmitted repeatedly. The spectrum of the MOD output was measured by a R&S spectrum analyzer. Fig. 2.51 shows the measurement result of the following difference cases: No calibration, frequency-independent calibration (see 2.5.7) and frequency selective calibration (with the pilot based estimation of the simplified scheme in Sec. 2.6.1). As shown, when no calibration is applied, relatively high image power is present. Moreover, the image power shows strong frequency selectivity. When frequency-independent calibration is applied, only the image power near the DC-frequency is suppressed. The image power at other

[1]Note that the low IRR at the spectrum edge is caused by the transition area of the decimation filter. In practice, such spectral areas are usually reserved as GB. Thus, the IRR in these areas are actually out of interest

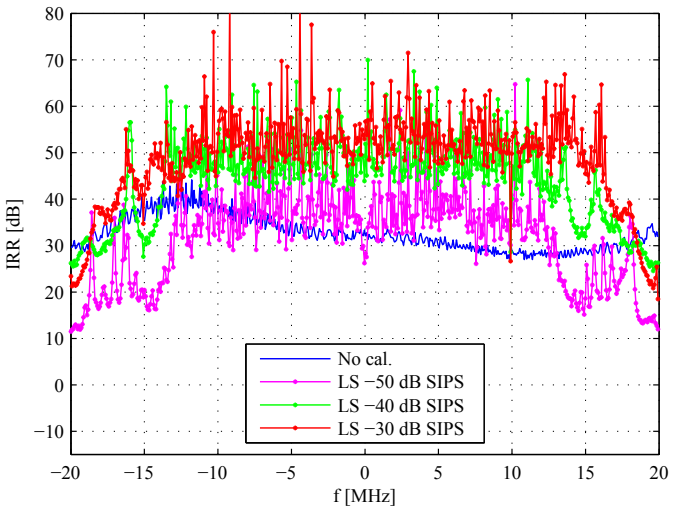

Figure 2.49: HIL result: IRR as a function of frequency applying LSE with an LTE signal. Different SIPS power levels were applied. $N = 256$ with 200 averaging.

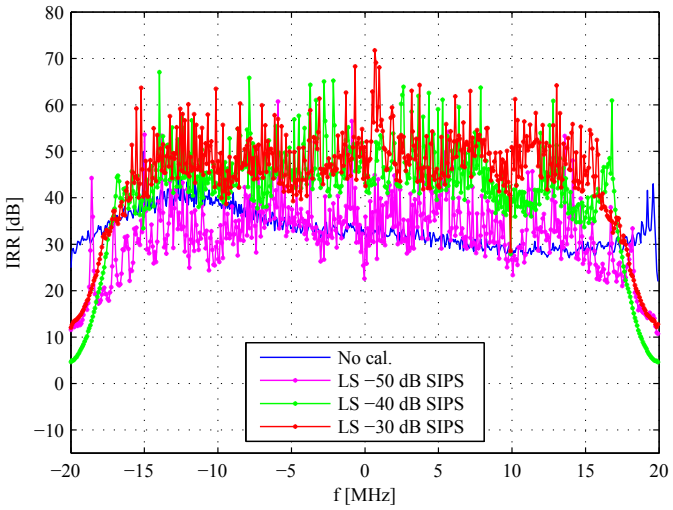

Figure 2.50: HIL result: IRR as a function of frequency applying LSE with an MB UMTS-S signal. Different SIPS power levels were applied. $N = 256$ with 200 averaging.

frequencies is still quite high. When frequency selective calibration is applied, the image power within the whole image band is sufficiently removed.

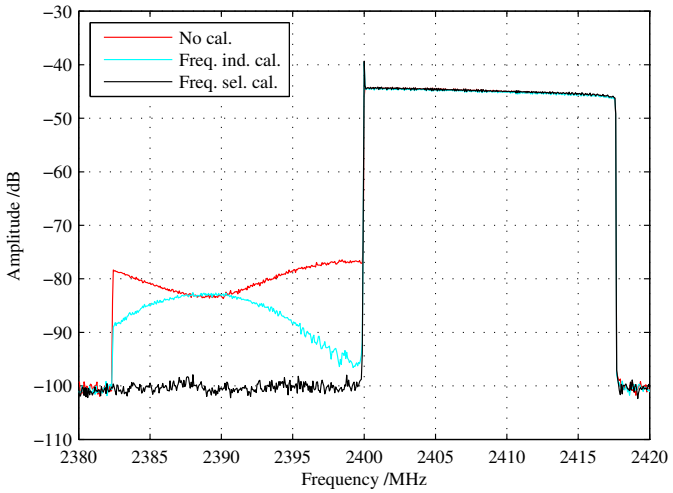

Figure 2.51: HIL result: Measured spectrum of the MOD output when an SSB signal was transmitted. Different schemes are compared: No calibration, frequency independent calibration and frequency selective calibration.

Now, the semi-blind tracking scheme in Sec. 2.6.2 is investigated. To achieve variation of the MOD parameters, the temperature of the MOD chip (on the MOD module) was changed by applying an aerator. Furthermore, a temperature measurement device is connected to the MOD chip to control and record the temperature. The investigated temperature values were 25°,45°,65°,85° and 30°. For each temperature value, different IRR measurements were carried out: 1) Without calibration; 2) With the pilot based calibration in Sec. 2.6.1 for each temperature value; 3) With the pilot based calibration in Sec. 2.6.1 only for 25°, afterwards the semi-blind tracking scheme in Sec. 2.6.2 was applied; 4) With the pilot based calibration in Sec. 2.6.1 only for 25°, afterwards these initial parameters were used for the following calibration; 5) No calibration. The measured IRR values are the average values over the signal bandwidth.

Fig. 2.52 shows the measurement results with an MB UMTS-S signal[1]. The results with other signal types were found to be similar. As shown, when no calibration is applied, the IRR is low (around 40 dB) and changes with temperature. When no tracking is applied, high IRR (above 55 dB) is only achieved with the initial temperature. Afterwards, the IRR drops down as the temperature changes. The larger the temperature variation (from the initial temperature of 25°), the stronger the IRR degradation. In contrast, the IRR of the semi-blind tracking scheme

[1]It was interesting to note that the parameter change of the Linear Technology LT5528 MOD due to temperature variation is much stronger than that of the ATMEL T0790 MOD. Thus, we show the results with the Linear Technology LT5528 MOD. Since the results in Fig. 2.49 ∼ Fig. 2.51 were obtained with the ATMEL T0790 MOD, different IRR values (without calibration) can be observed.

remains sufficiently high in spite of temperature change. With each temperature value, the achieved IRR of the semi-blind tracking scheme is as high as that with the pilot based scheme. With this result, the simplified assumption about the MOD frequency response variation in Sec. 2.6 can be verified. As a reference, Fig. 2.53 shows the measured amplitude- and phase imbalance parameters of the MOD for different temperatures[1].

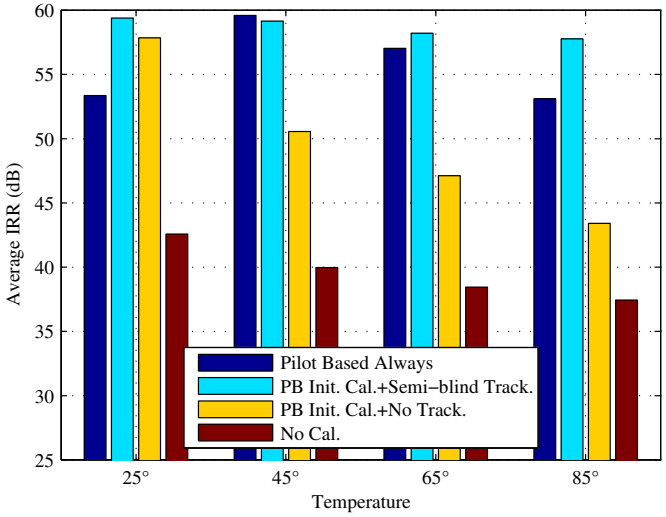

Figure 2.52: HIL result: Measured IRR of different temperatures. Different schemes are compared. **Pilot Based Always:** Pilot based calibration in Sec. 2.6.1 for each temperature value; **PB Init. Cal.+Semi-blind Track.:** Pilot based calibration in Sec. 2.6.1 only for 25°, afterwards the semi-blind tracking scheme in Sec. 2.6.2; **PB Init. Cal.+No Track.:** Pilot based calibration in Sec. 2.6.1 only for 25°, afterwards apply these parameters for the following calibration; **No Cal.:** No calibration at all.

Finally, the combination of I/Q-imbalance compensation and PA pre-distortion was demonstrated[2]. A multi-band IF signal of 20 MHz bandwidth was generated, which should have 4 subbands of 5 MHz in total. However, only two subbands left to the carrier frequency were active. To facilitate spectrum measurement, this signal was stored in a RAM of the FPGA and was be transmitted repeatedly. With the software interfaces to the FPGA[3], the pre-equalization for I/Q-imbalance compensation as well as the pre-distortion for PA linearization (see [60]) can be switched on and off. The spectrum of the PA output was measured by a spectrum analyzer. As shown in Fig. 2.54, four different cases are compared: No compensation of I/Q-imbalance and PA non-linearity was applied; I/Q-imbalance compensation only; PA pre-distortion only; Compensation of both effects. As shown, as no compensation was applied, strong image signal can be observed. Moreover, the out-of-band radiation of the signal was also strong. While

[1] It is to remark that both temperature- and time values are just roughly measured values

[2] The corresponding result was produced jointly with Jacek Liszewski and Benjamin Schubert in the SmartRF project [23].

[3] Via controlling-registers.

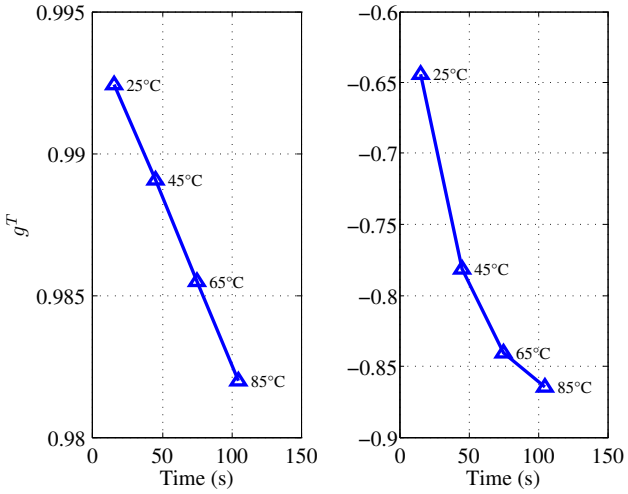

Figure 2.53: HIL result: Measured MOD I/Q-imbalance parameter with different temperatures.

I/Q-imbalance compensation could only suppress the image signal, the PA pre-distortion can only suppress the out-of-band radiation. As both I/Q-imbalance compensation and PA pre-distortion were switched on, both the image signal and the out-of-band radiation were strongly suppressed. Anyway, even after compensation of both effects, residual interference can be observed. Further study of such interference as well as further performance improvement remain future work.

In the results above, we mainly focused on the I/Q-imbalance compensation performance. In most of the cases, sufficient I/Q-imbalance compensation is accompanied with sufficient MOD DC-offset suppression. However, due to cross-talk effects and other imperfections, the MOD DC-offset suppression is still unstable. Further improvements are required in the future.

2.9 Chapter Summary

In this chapter, the Smart-RF concept for cellular mobile systems was investigated with the emphasis on flexible and robust joint compensation of frequency selective I/Q-imbalance and MOD DC-offset at the Tx of BSs. To allow multi-band multi-standard BSs, the compensation scheme should be standard independent. Moreover, the scheme should be able to track the parameter variations in time.

We assume that an I/Q-imbalance free feedback path is available, so that parameter estimation is allowed at the Tx. Based on the realistic BB- and RF frontend structure, we first derived an equivalent baseband signal model. Afterwards, a low complexity compensation circuit was proposed, which requires only one real FIR filter and some minor operations.

Considering the standard independence requirement of the compensation scheme, the pa-

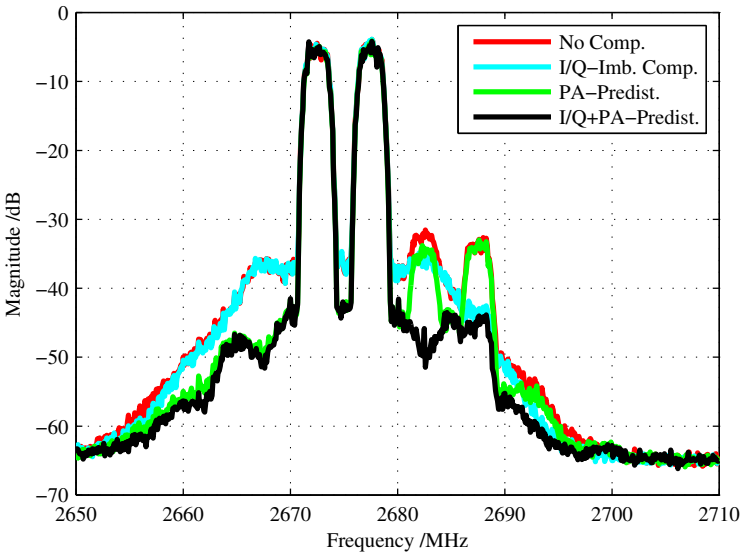

Figure 2.54: HIL result: Measured spectrum of a two-carrier signal. Different schemes are compared: No calibration; Only I/Q-imbalance compensation; Only PA pre-distortion; Both I/Q-imbalance compensation and PA pre-distortion.

rameter estimation should work both with dedicated pilot signals and the regular communication signals. The latter case is more challenging. To achieve this goal, we first proposed a LS-based method. Both the cases of initial estimation and parameter tracking were considered. However, the estimation accuracy of the LS method depends strongly on the condition number of the data matrix. After carrying out mathematical analysis, we identified that spectral gaps in communication signals are the main cause of the ill-conditioned matrix problem, which results in significant performance degradation. To solve this problem, we proposed a spectral refilling technique, which adds SIPS to the communication signals.

Since adding SIPS can cause interference to the communication signal as well as the neighbor channels, we proposed a more advanced scheme (indicated by "SIMP"). This scheme is based on a simplified assumption of the parameter variation: the MOD I/Q-imbalance and the DC-offset can be time variant, while the filter I/Q-imbalance remains unchanged. Two different estimation methods are used for the initial estimation and parameter tracking. For the initial estimation, a pilot-based frequency domain method was proposed. After the initial compensation, we assumed that the filter I/Q-imbalance was perfectly compensated for. Thus, for the parameter tracking, only the MOD I/Q-imbalance and the DC-offset have to be estimated. For the tracking, we proposed a semi-blind time domain method. With this advanced scheme, the ill-conditioned matrix problem is avoided without applying SIPS. Good estimation quality can be achieved with communication signals of different characteristics. However, unlike the LSE, the SIMP scheme can be sensitive to time synchronization errors. To avoid this problem, we have proposed

a "Toeplitz extension" based solution and have analyzed the corresponding performance.

The effectiveness of all proposed schemes were verified both by numerical simulations and HIL experiments. Simulation results also show that the proposed schemes outperform the state-of-the-art schemes. For the HIL experiment, the proposed compensation circuit was implemented in realtime in FPGA. The achievable IRR in the experimental platform was as high as 55 dB. Finally, the HIL result of the combination of I/Q-imbalance compensation and PA pre-distortion was also shown. Furthermore, complexity analysis was conducted, which shows that the proposed schemes have lower complexity in the pre-equalization circuit and/or the parameter estimation than the state-of-the art schemes. Among the proposed schemes, the simplified two phase scheme is much less complex than the LS-based scheme.

Based on the simulation- and HIL results as well as the complexity analysis, we can conclude that the simplified two phase scheme is most practical. Compared to the LS-based scheme, it has the advantages of higher flexibility, better performance, lower computational complexity and less implementation effort.

Chapter 3

Design Concept for 60 GHz WLAN

3.1 Introduction

Future WLAN systems are expected to provide data rates of up to 10 Gbps, which can only be achieved by increasing the spectral efficiency of the transmission scheme and by exploiting the frequency resources that have not been used so far. Recently, 60 GHz millimeter-waves have attracted great interest for future WLAN systems. The specific advantages of this frequency band are the large unlicensed available bandwidth and the short wavelength, allowing very high data rates and small antenna dimensions, respectively. Furthermore, there is no interference to todays wireless systems. Since these waves have a comparatively high free space attenuation[1] and strong penetration loss in common materials, the system coverage is small. This implies less Inter-Channel Interference (ItCI) and Co-Channel Interference (CoCI) in cellular systems, which allows a better frequency reuse.

In this chapter, we investigate the design of a future 60 GHz WLAN system which can serve both high data rate and high user density at the same time at reasonable cost. A typical application of such system is the IFE system of aircrafts, which requires a sum data rate in the order of several Gbps with user densities of up to thousand passengers per system. Currently, IFE systems are based on wired connections with all their disadvantages in terms of low flexibility, weight and high installation cost. In order to improve IFE systems, wireless techniques such as IEEE 802.11n and infrared systems have been considered. However, an IEEE 802.11n system cannot provide the required data rate and the high user density at the same time. The drawback of infrared systems is that LOS connection is always required. If it is absent, the signal bandwidth is strongly limited due to the low-pass characteristic of the channel response function [100]. Currently, IEEE 802.11n is being extended to two VHT

[1] LOS path loss of 68 dB at 1 meter distance.

variants, including the IEEE 802.11ac and IEEE 802.11ad, which operate in the 5 GHz band and the 60 GHz band, respectively. Although these two standards are supposed to proved data rates beyond 1 Gbps[31, 101], respectively, they may not be able to support the high user density[1]. Based on the considerations above, a well designed 60 GHz WLAN system for IFE is strongly motivated. In this chapter, the technical descriptions are mainly based on this typical example.

In this chapter, we will first present the overall system design including system configuration, frame structure, diversity scheme for the DL and power control. A first simulative evaluation of the system performance is also included. Afterwards, the following specific aspects are investigated in detail: optimization of time domain windowing and GB size for cellular OFDM systems, joint estimation and compensation of RF-impairments and the MIMO channel in the DL, efficient MUD schemes for the UL. An overview of all these aspects is given as follows:

1. **Optimization of Time Domain Windowing and Guardband Size for Cellular OFDM Systems:** In the proposed 60 GHz WLAN design, OFDM is applied to achieve high spectral efficiency, robustness against multipath propagation and low complexity implementation. It is well known that OFDM signals have sidelobes in the spectrum, causing ItCI to the neighboring frequency channels in a cellular system. The sidelobes can be suppressed by RC windowing in time domain, while the ItCI can be reduced by reserving a GB between neighboring frequency channels. A higher ROF of the RC window leads to better sidelobe suppression and allows a smaller GB size to increase the spectral efficiency. However, higher ROF implies longer symbol duration, which reduces the data rate. Therefore, there exist a tradeoff between the ROF and the GB size. In this thesis, a joint optimization technique for the ROF and GB size is presented, which maximizes the data rate.

2. **Joint Estimation and Compensation of RF-Impairments and the MIMO Channels:** To allow low-cost, low-power and fully integrated implementation of the 60 GHz WLAN system, Direct (up/down) Conversion Architecture (DCA) is applied. However, DCA is sensitive to the RF-impairment I/Q-imbalance, which exists both at the Tx and the Rx. Due to I/Q-imbalance, the achievable data rate can be severely limited. Thus, I/Q-imbalance compensation is desired. With the transmission BW of 250 MHz, the I/Q-imbalance effect is frequency-selective, giving more challenge to the compensation. In this chapter, we assume that the I/Q-imbalance free feedback path described in Ch. 2 is unavailable. Therefore, both Tx- and Rx I/Q-imbalance have to be compensated at the Rx. Furthermore, we also consider the presence of CFO. Two concepts of impairment compensation are studied: 1) Joint digital compensation of I/Q-imbalance and the MIMO

[1] Although IEEE 802.11ac has adopted OFDMA and Multi-User (MU) MIMO to enhance multi-user performance, the small available BW at the 5 GHz band can be a limiting factor for this standard to be applied in a high-user-density network. In contrast, despite the large available BW at 60 GHz, the multi-user performance of IEEE 802.11ad can be limited by the lack of advanced multiple access mechanism.

channel assuming analog CFO compensation (via oscillator adjustment); 2) Joint digital compensation of CFO, I/Q-imbalance and the MIMO channel. For each concept, effective schemes are proposed, which are based on low-overhead preambles and require relatively low computational complexity.

3. **Efficient Multi-User Detection Schemes for the Uplink:** In the UL, CP-assisted DS-CDMA transmission scheme is applied to allow low CF of the Tx signals and low signal processing effort at the User Terminals (UT). With such a transmission scheme, frequency domain MUD can be applied, which has much lower computational complexity than the conventional time domain MUD. In this thesis, different antenna diversity schemes are proposed for the frequency domain MUD, including SIMO, MISO and MIMO. After comparison of these schemes, the most practical scheme is identified by considering hardware- and computational complexity as well as performance.

3.2 Overall System Design

3.2.1 System Configuration

The proposed system has a cellular structure with a number of Access Points (AP). Fig. 3.1 shows the cell plan in an aircraft, with frequency reuse factor 8. In each cell, an AP serves up to 32 UT at the seats. The antennas of the APs are mounted inside the sidewall, primarily radiating into the half space towards the inside of the cabin with a low gain. The antennas at the UTs have omnidirectional radiation characteristics. The carrier frequencies of adjacent cells should have maximal possible separation, so that ItCI is minimized.

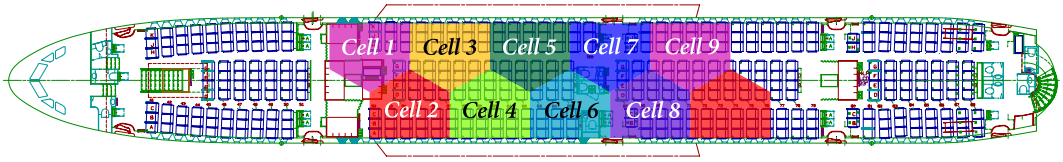

Figure 3.1: Radio cells with frequency reuse factor 8, different colors of the cells represent different operation frequencies

Fig. 3.2 shows the cellular system architecture. The APs have access to the data of the content server by a gigabit ethernet backbone network and communicate with the UTs by using a 60 GHz air-interface. The UL and DL of the air-interface operate in Frequency Division Duplex (FDD) mode. The user links to the APs are assigned dynamically, depending on the momentary channel state. As shown in Fig. 3.2, for UTs on the border of two neighboring cells, the UL and DL channels can even be assigned to different APs. In the case of very poor

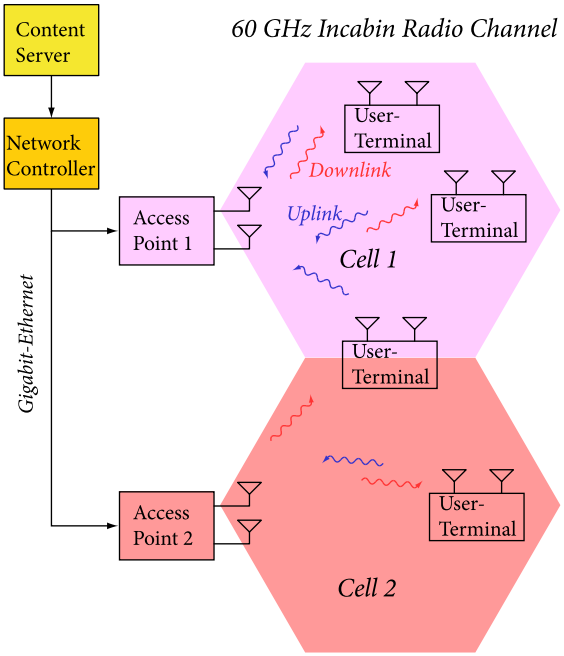

Figure 3.2: Cellular system architecture for wireless IFE system

channel quality or AP failure, handover of UTs to other APs are possible. Fig. 3.2 also shows that MIMO is applied to achieve diversity gain, which will be described later.

Fig. 3.3 shows the frequency allocation. There are in total 8 UL channels in the range of 58.5 GHz to 59 GHz with a channel spacing of 62.5 MHz. For the DL, there are 8 channels in the range of 60.5 GHz to 62 GHz with a spacing of 250 MHz. The difference between UL- and DL channel spacing results from the different effective data rates per user in UL and DL, which are 1 Mbit/s and 10 Mbit/s, respectively. The resulting sum raw data rate per AP is 1 Gbit/s in the DL and 250 Mbit/s in the UL. For achieving these data rates, 16-QAM is used for the DL, while QPSK is used for the UL. It should be noted that if the channel quality is bad, the system should be capable of switching to more robust modulation schemes via mechanisms which are similar to the burst-profile management in WiMAX [102].

For the UL, FDMA/CDMA is used as multiple access scheme. Each UL channel is divided into 5 FDMA subbands, which are separated by Raised-Cosine (RC) filters. The roll-off-factor of the RC filters is 0.81, which was optimized to achieve a low crest-factor of the UL signal while maintaining the required data rate of 1 Mbit/s. In each subband, CDMA with code length 8 is applied. Furthermore, the CDMA is transmitted in blocks with CPs, allowing frequency domain MUD.

For the DL, OFDMA/TDMA broadcast scheme is used. In each DL channel, OFDM signals with 256 subcarriers are transmitted. The consecutive OFDM symbols are grouped into time

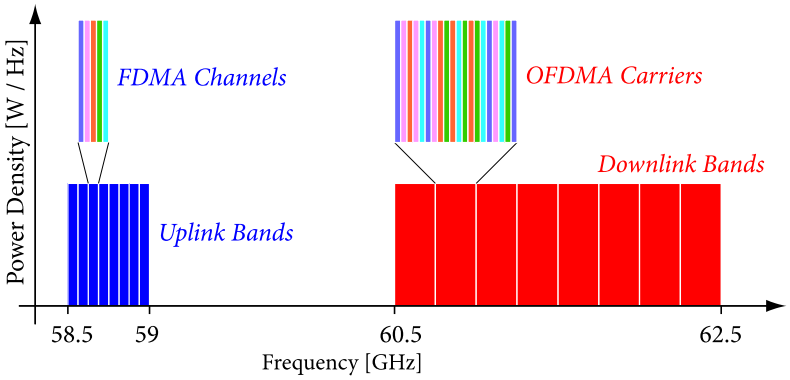

Figure 3.3: Frequency allocation for the wireless IFE system

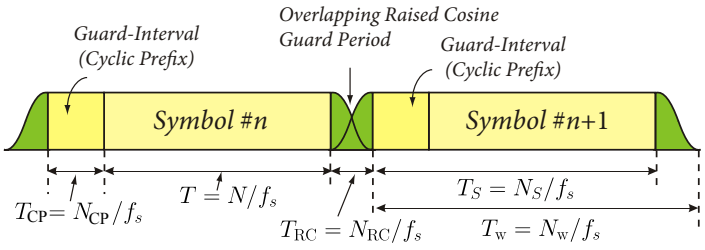

Figure 3.4: RC windowed OFDM symbols in time domain

slots, each of them dedicated to different groups of UTs. To suppress the side-lobes in the spectrum of the OFDM signal, RC windowing is used in the time domain, i.e. each block of the OFDM time domain signal is extended with RC guard periods T_{RC} as shown in Fig. 3.4. It will be shown in Sec. 3.3 that the ROF of the RC-window, defined as $r := \frac{T_{\mathrm{RC}}}{T_S}$, and the GB size can be optimized to maximize the achievable data rate. According to the results in Sec. 3.3, we can either have $f_s = 250$ MHz with $r = 5.2\%$ and 17 NULL subcarriers or have $f_s = 238.6$ MHz with $r = 5.6\%$ and no NULL subcarriers. These parameter sets lead to the maximized data rates of 336.4 Mbit/s and 339.6 Mbit/s, respectively.

The main reason of using FDMA/CDMA in the UL and OFDMA/TDMA in the DL is to realize low cost UTs, since OFDM enables low complexity receivers while the crest-factor of CDMA signals can be kept relatively low (compared to that of OFDM), reducing the cost of power amplifiers at the UTs significantly. An additional advantage of CDMA is that very simple Tx signal generation is allowed, reducing the signal processing complexity of the UTs. In contrast, SC-FDMA (used in LTE uplink) requires both DFT and IDFT at the UTs. Furthermore, using TDMA provides more time slots for a UT to process a frame, relaxing the signal processing demand. Another advantage of TDMA is that power control across time slots is possible, which can be used for CoCI mitigation (see Sec. 3.2.4). The use of FDMA in the UL reduces the bandwidth of the UL CDMA signals and thus results in a shorter code length, which reduces the complexity of the multi-user detection at AP significantly [103]. FDMA also enables adaptive subband allocation in the UL.

3.2.2 Frame Structure

The DL frame structure is adopted from the WiMAX OFDMA PHY [102] as shown in Fig. 3.5. A frame is extended both in time and frequency, in terms of OFDM symbol number and subchannels, respectively, where a subchannel is a group of permutated subcarriers. The frame is divided into preamble, broadcast control field and data bursts. The preamble is used for time and frequency synchronization, channel estimation, AGC (Automatic Gain Control) etc. The broadcast control field contains the important control messages including FCH (Frame Control Header), DL-/UL-MAP (Media Access Protocol), DCD and UCD (DL and UL Channel Descriptor) [102]. A data burst can be assigned all the subchannels (Full Usage of Subchannels, FUSC) or only a subset of them (Partial Usage of Subchannels, PUSC). Each data burst contains one or more MAC PDUs (Packet Data Unit) for one or more UTs and uses specified modulation and coding schemes represented by the burst-profile [104]. The burst-profile of each burst as well as the burst location and size (in terms of used subchannels and burst length) are specified in the DL-MAP messages.

The UL frame structure is defined according to the FDMA/CDMA scheme, as shown in Fig. 3.6. Each registered UT transmits data in the allocated frequency code channel. The transmission is performed in blocks with CPs. The frequency and time synchronization of the UL is derived from that of the DL and information in the UCD and UL-MAP messages [102].

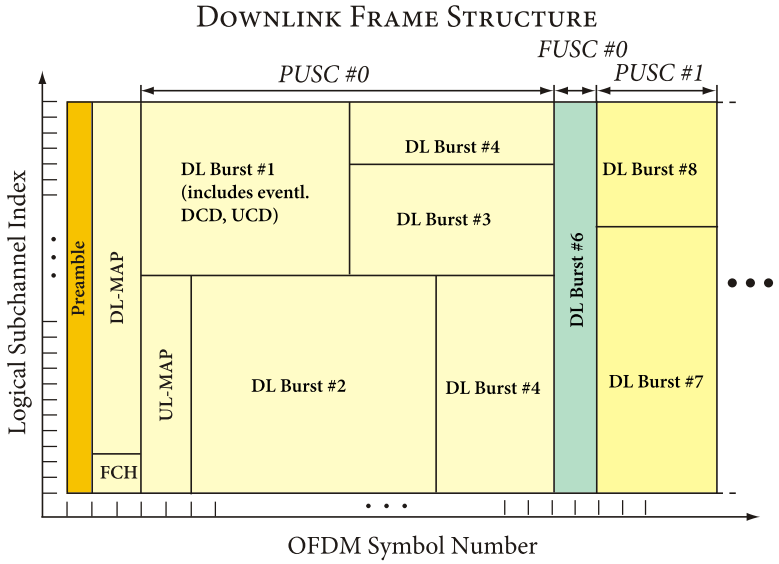

Figure 3.5: Frame structure of the DL using OFDMA

The UCD message specifies the UL channel frequency and the subband frequency. The UL-MAP specifies the time offset between the start time of a DL-frame and that of an UL-frame. Due to the CP and the comparatively low chip rate, time synchronization errors within a certain range can be tolerated.

Except for the regular data transmission, the AP reserves intervals in the UL for two kinds of channel estimations. The first one is the channel estimate in an FDMA subband, which is necessary for the multi-user detection at the AP [103]. All the UTs using this subband transmit pilot sequences simultaneously, which are circularly shifted CAZAC sequences with different shifts that are larger than the maximal channel length. At the AP, the periodic cross-correlation between the received sequence and the original sequence is calculated. The correlation result contains the time shifted channel IRs of all the involved UTs.

The other one is the channel quality estimation of the whole UL frequency band, which is needed for the adaptive FDMA subband allocation. This estimation is obtained in a similar way. All active UTs transmit differently shifted CAZAC sequences simultaneously, which are longer than that for the subband channel estimation and have a higher chip rate. According to the estimated channel quality, the AP optimizes the subband assignment for all the UTs.

Moreover, the AP also reserves intervals for initial ranging requests for network entry. They may cover several FDMA subbands or the whole UL bandwidth. The access to these intervals is contention based. It is to remark that all the aforementioned allocations are specified in the UL-MAP message in the DL frame.

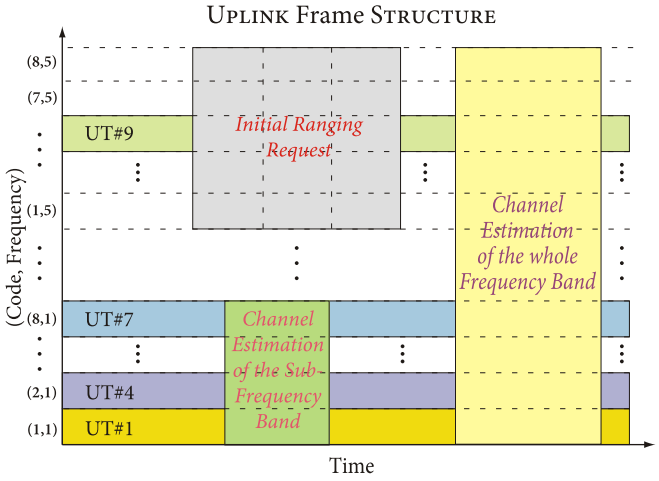

Figure 3.6: Frame structure of the UL using FDMA/CDMA

3.2.3 DL Antenna Diversity Scheme

Multiple Tx- and Rx antennas can be applied to improve the capacity and reliability of communication links. Since 60 GHz waves allow small antenna dimensions, the application of antenna diversity technique is very suitable. In this section, we concentrate on the DL. In Sec. 3.6, antenna diversity schemes for the UL will be described. Furthermore, for simplicity, we don't consider any RF impairment here. DL antenna diversity schemes considering RF impairments will be presented in Sec. 3.4 and 3.5.

3.2.3.1 Space-Time Code (STC) and Maximal-Ratio Combining (MRC)

The IFE system is designed to have 2 Tx antennas at the AP and 2 Rx antennas at each UT. Thus, the DL corresponds to a 2×2 MIMO OFDM transmission. To achieve diversity gain, an Alamouti-based Space-Time Code (STC) [105] and Maximal-Ratio Combining (MRC) are used at the Tx and the Rx side, respectively. Let

$$\boldsymbol{S}_b = \left[S_b[-\frac{N}{2}], \ldots, S_b[-1], S_b[1], \ldots, S_b[\frac{N}{2} - 1] \right]^T$$

denote the data symbols at the subcarriers, which are transmitted in the b^{th} block. N is the number of subcarriers. Note that the DC subcarrier is not used. Moreover, for simplicity, we do not consider the NULL subcarriers. The STC encoder combines two consecutive blocks according to the following equations:

$$\begin{aligned} \boldsymbol{S}^{(1)} &= \left[\boldsymbol{S}_b, -\boldsymbol{S}_{b+1}^* \right] \\ \boldsymbol{S}^{(2)} &= \left[\boldsymbol{S}_{b+1}, \boldsymbol{S}_b^* \right], \end{aligned} \tag{3.1}$$

where $\boldsymbol{S}^{(1)}$ and $\boldsymbol{S}^{(2)}$ are the inputs of the IDFTs corresponding to the 1st and the 2nd Tx antenna, respectively. In the in-cabin scenario, the channels are assumed to be quasi-static. The received symbols at the r^{th} Rx antenna can be written as:

$$\begin{aligned}\left[\boldsymbol{Y}_b^{\langle r\rangle}, \boldsymbol{Y}_{b+1}^{\langle r\rangle}\right] &= \operatorname{diag}\left\{\boldsymbol{H}^{\langle r,1\rangle}\right\}\boldsymbol{S}^{(1)} + \operatorname{diag}\left\{\boldsymbol{H}^{\langle r,2\rangle}\right\}\boldsymbol{S}^{(2)} \\ &= \Big[\operatorname{diag}\left\{\boldsymbol{H}^{\langle r,1\rangle}\right\}\boldsymbol{S}_b \ + \operatorname{diag}\left\{\boldsymbol{H}^{\langle r,2\rangle}\right\}\boldsymbol{S}_{b+1}, \\ &\qquad -\operatorname{diag}\left\{\boldsymbol{H}^{\langle r,1\rangle}\right\}\boldsymbol{S}_{b+1}^{*} + \operatorname{diag}\left\{\boldsymbol{H}^{\langle r,2\rangle}\right\}\boldsymbol{S}_b^{*}\Big],\end{aligned} \tag{3.2}$$

where $\boldsymbol{H}^{\langle r,i\rangle} = \left[H^{\langle r,i\rangle}[-\frac{N}{2}], \ldots, H^{\langle r,i\rangle}[-1], H^{\langle r,i\rangle}[1], \ldots, H^{\langle r,i\rangle}[\frac{N}{2}-1]\right]^T$ and $H^{\langle r,i\rangle}[k]$ is the coefficient of the channel between the i^{th} Tx antenna and the r^{th} Rx antenna at the k^{th} subcarrier. The STC decoder of each Rx antenna decodes the received signals as follows:

$$\begin{aligned}\hat{\boldsymbol{S}}_b^{\langle r\rangle} &= \operatorname{diag}\left\{\boldsymbol{H}^{\langle r,1\rangle *}\right\}\boldsymbol{Y}_b^{\langle r\rangle} + \operatorname{diag}\left\{\boldsymbol{H}^{\langle r,2\rangle}\right\}\boldsymbol{Y}_{b+1}^{\langle r\rangle *} \\ \hat{\boldsymbol{S}}_{b+1}^{\langle r\rangle} &= \operatorname{diag}\left\{\boldsymbol{H}^{\langle r,2\rangle *}\right\}\boldsymbol{Y}_b^{\langle r\rangle} - \operatorname{diag}\left\{\boldsymbol{H}^{\langle r,1\rangle}\right\}\boldsymbol{Y}_{b+1}^{\langle r\rangle *}.\end{aligned} \tag{3.3}$$

The MRC combined signal at each subcarrier is just the sum of the STC decoded signals from each Rx antenna [105]. Since the channel coefficients at different subcarriers generally have different magnitudes, the power of the MRC combined signal at each subcarrier should be normalized. Thus, the estimations of the k^{th} element of transmitted blocks are:

$$\left(\hat{\boldsymbol{S}}_b\right)_k = \frac{\sum_{r=1}^{2}\left(\hat{\boldsymbol{S}}_b^{\langle r\rangle}\right)_k}{\sum_{i=1}^{2}\sum_{r=1}^{2}\left|\left(\boldsymbol{H}^{\langle r,i\rangle}\right)_k\right|^2}, \quad \left(\hat{\boldsymbol{S}}_{b+1}\right)_k = \frac{\sum_{r=1}^{2}\left(\hat{\boldsymbol{S}}_{b+1}^{\langle r\rangle}\right)_k}{\sum_{i=1}^{2}\sum_{r=1}^{2}\left|\left(\boldsymbol{H}^{\langle r,i\rangle}\right)_k\right|^2}. \tag{3.4}$$

3.2.3.2 Simulation Results

The system performance with different antenna configurations (SISO, SIMO, MISO and MIMO)[1] was simulated with the measured 60 GHz channels from [106]. The scenario of the in-cabin channel measurements and the locations of the AP and the UTs are shown in Fig. 3.7. The IR and FR of a measured 60 GHz channel realization are shown in Fig. 3.8 as an example. According to [106], an open-ended waveguide was used as Tx antenna. All antennas were vertically polarized. Since the AP-UT separation varies over the UT locations, a different Path Loss (PL) occurs for each UT. However, the noise power at each UT and the transmit power of the AP are assumed to be constant. Thus, each transmit power level of the AP results in different SNR values at the UTs. In order to evaluate the performance of the whole system, the transmit power of the AP is varied between −3 and 12 dBm. The test signals are transmitted in blocks with different Tx powers. At each UT, the SNR as well as the BER of each block are

[1] For MISO, STC is applied at Tx; For SIMO, MRC is applied at Rx; For MIMO, both STC and MRC are applied as described in Sec. 3.2.3.1.

calculated and stored in pairs. The whole SNR range is divided into a number of SNR bins. The BER values of all UTs corresponding to the SNR values in a certain bin are averaged to obtain a point for the BER-SNR curve. For the simulation, we assumed an ideal LNA (Low Noise Amplifier) with noise figure $N_F = 0$ dB. However, taking a realistic N_F of the LNA into account is just equivalent to subtracting N_F from the Tx power. Separate simulations were done for LOS channels and OLOS (Obstructed-LOS) channels. It is to remark that for MISO and MIMO, the Tx power of each Tx antenna is half of that in the case of SISO and SIMO, so that the total Tx power of each scheme is the same and the comparison is fair. Moreover, perfect channel knowledge is assumed and no channel coding was applied. The obtained BER-SNR curves are shown in Fig. 3.9 and 3.10 for LOS and OLOS channels, respectively. In the SIMO and MIMO case, the SNR is the averaged value at each Rx antenna.

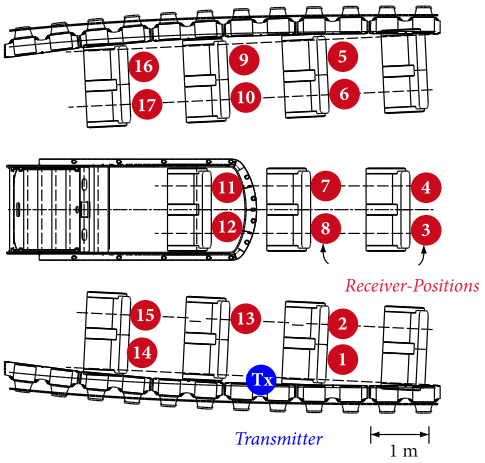

Figure 3.7: Scenario in the cabin for channel measurement

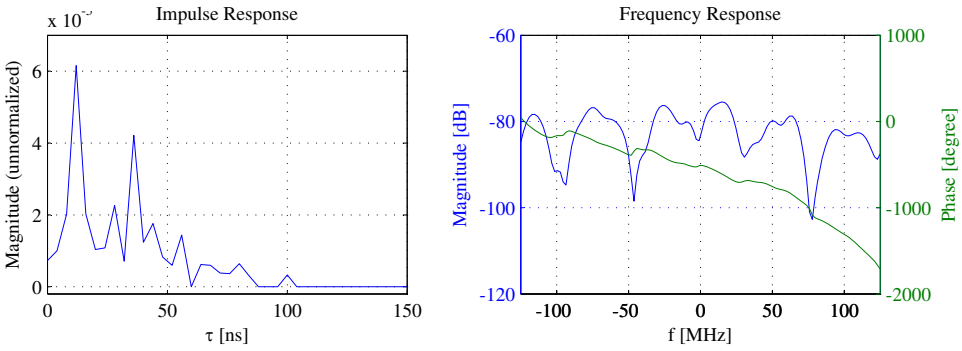

Figure 3.8: IR and FR of a 60 GHz channel realization at position 8, OLOS.

As shown in Fig. 3.9 and 3.10, the MIMO configuration achieves the largest diversity gain of 11.7 dB for LOS and 13.13 dB for OLOS, respectively, at a BER of 10^{-3}. The performance in an AWGN channel is also given for comparison. We can see that the performance with MIMO is close to that of a SISO transmission over an AWGN channel.

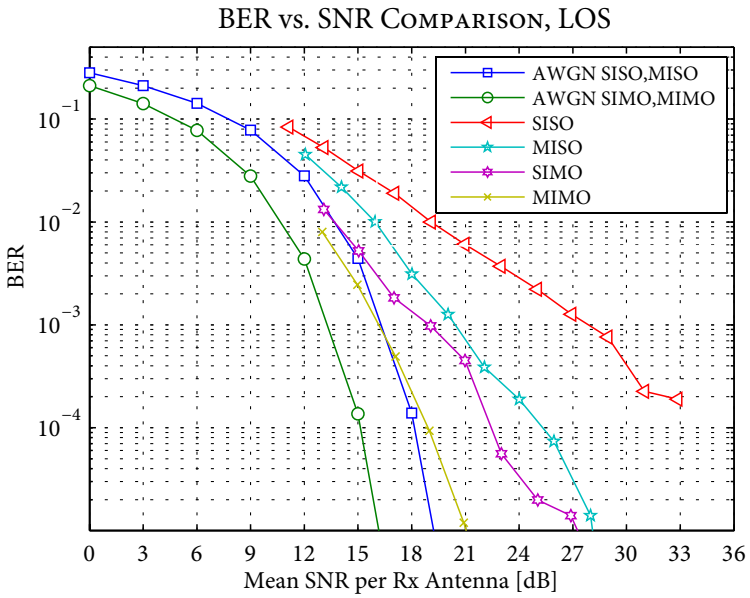

Figure 3.9: BER performance vs SNR, 16 QAM, LOS channels

3.2.4 Power Control Considerations

In order to find the required Tx power value which enables the desired system performance, the simulation results in Sec. 3.2.3.2 are further evaluated. We only consider the MIMO case. For each Tx power level, the average BER at each UT is calculated. These BER values are compared and the highest one is taken as the upper bound at this Tx power level. Fig. 3.11 shows the BER upper bound as a function of the Tx power. As can be seen, the required Tx power for a BER of 10^{-3} is 1.54 dBm for LOS and 9.54 dBm for OLOS. Since OLOS is the dominant case in an indoor scenario, a Tx power of about 10 dBm is necessary to ensure the system performance. It is to remark that this value is associated with the gains of the Tx and Rx antennas used for the channel measurements in [106], which are 5 dBi and 2 dBi, respectively. This matches the antenna properties described in Sec. 3.2.1.

Since OFDMA/TDMA is used as multiple access scheme, power control can be applied to optimize the power consumption. The UTs with similar channel qualities can be grouped together, assigned to the same time slot and supplied with an appropriate Tx power level.

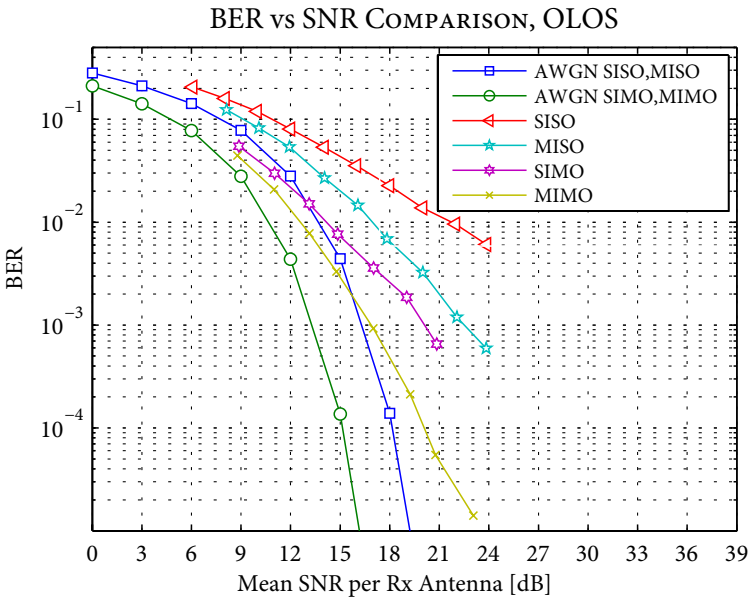

Figure 3.10: BER performance vs SNR, 16 QAM, OLOS

In this way, the Tx power levels are different in consecutive time slots and the overall power consumption can be minimized.

Furthermore, since the content server can act as a central resource controller, the APs which use the same DL channel can be coordinated to mitigate CoCI.

Fig. 3.12 (a) shows the case without coordination. Both APs in the figure operate at the same carrier frequency. Within a cell, the UTs at the cell edges which are closest to the interfering APs can be regarded as the worst case UTs. Compared to other UTs in the cell, they are farthest away from the own AP and closest to the interfering AP. Without coordination, both APs may transmit signals to these UTs at the same time. Since the PL increases with the distance between the Tx and Rx [106], the Tx power has to be comparatively high, so that the Rx power of these UTs is sufficiently high for signal detection. On the other hand, this causes a high CoCI level.

Fig. 3.12(b) shows the CoCI mitigation scheme in principle. The transmission of the APs can be coordinated as follows: AP_1 transmits a high power signal to UT_1, because it is a worst case UT. At the same time, AP_2 transmits a low power signal to UT_4, which is closer to it. In this way, the interference at UT_1 is reduced. On the other hand, if the Tx power levels of the APs are properly adjusted, the SIR of UT_4 is still sufficient for signal detection. If we define high power and low power time slots for the system, this coordination can be regarded as applying a reuse factor larger than one for high power time slots[1].

[1]In other words, the high power time slots can not be used at the same time by two interfering APs with

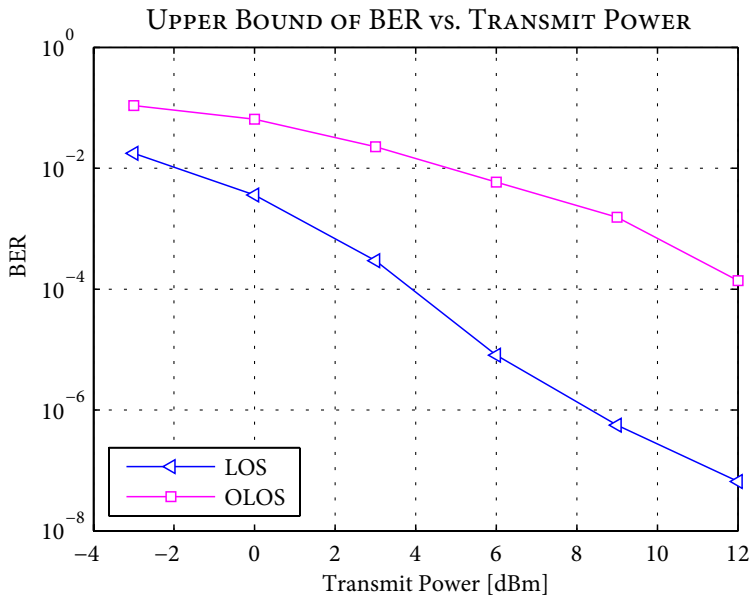

Figure 3.11: Upper bound of BER performance vs Tx power

3.3 Optimization of Time Domain Windowing and Guard-band Size for Cellular OFDM Systems

3.3.1 Background and Overview

An important issue for the design of a cellular OFDM system is the band-limitation to meet spectral mask constraints. In time domain, an OFDM signal can be regarded as the sum of many sinusoidal carriers modulated by data symbols and windowed by a rectangular function [107]. Rectangular windowing is equivalent to spectral shaping by the sinc pulse. This results in spectrum spreading, degrades the spectral efficiency [107] and causes interference to neighboring channels.

There are two common techniques for the spectral sidelobe suppression of OFDM BB signals: LP filtering and RC windowing. Applying LP filter can effectively reduce the sidelobes, but requires up-sampling of the transmitted BB signal and very high order digital filter, resulting in high computational overhead. Furthermore, filtering chops off significant energy from the outer subcarriers, causing ICI and reduced effective SNR [107].

Further sidelobe suppression techniques were developed in the context of cognitive radio, including the insertion of Cancellation Carriers (CC) [108], subcarrier weighting [109], Multiple Choice Sequence (MCS) [110] and Adaptive Symbol Transition (AST) [111]. Although these

the smallest distance.

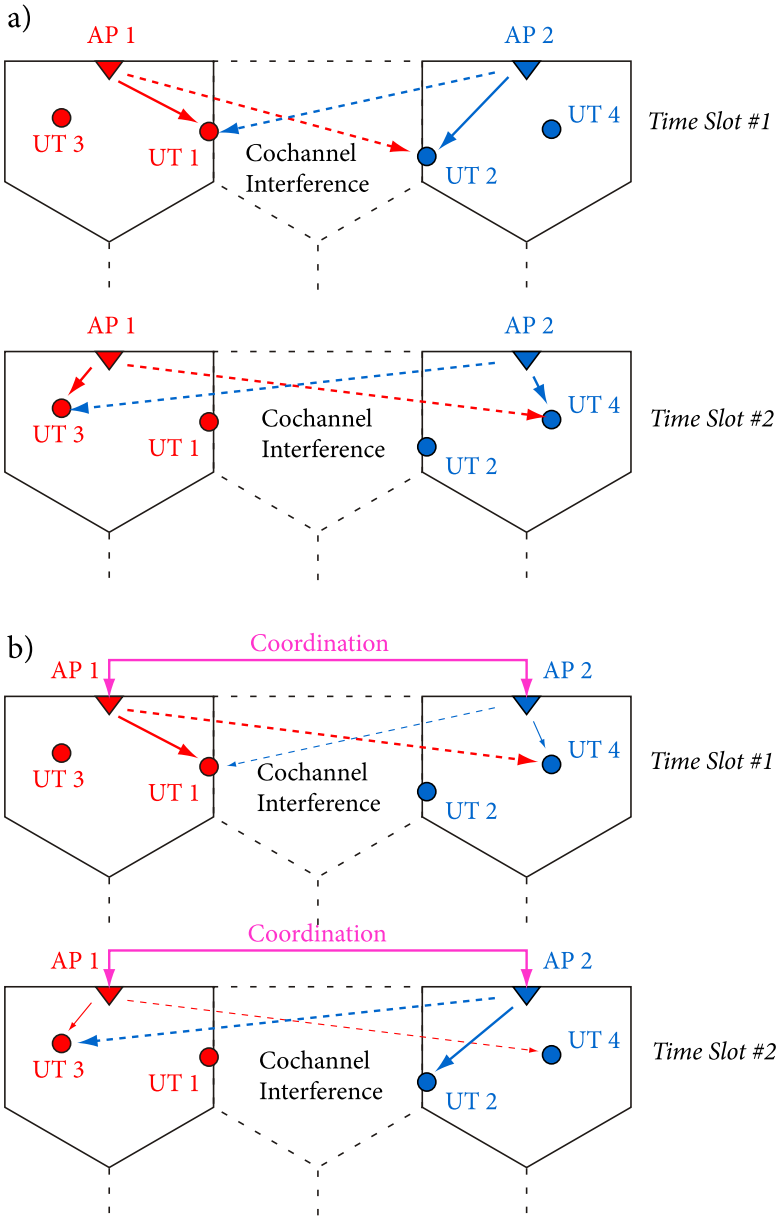

Figure 3.12: Power control for CoCI mitigation

techniques can reduce the sidelobes significantly, they require relatively high computational complexity. Moreover, CC results in increased PAPR, while subcarrier weighting increases the BER [111]. For MCS, an extra signaling channel and side information are necessary, which reduces the system throughput.

In contrast, RC windowing is much simpler, although the sidelobe suppression is not as significant as with the other techniques. As shown in Fig. 3.4, only an RC guard period needs to be added to the OFDM signal. RC guard periods of consecutive OFDM symbols can overlap with each other and are omitted at the receiver [107]. In Fig. 3.4, T_{RC}, T_{CP} and T are the durations of the RC guard period, the CP (also called Guard-Interval, i.e. GI, for combating multipath propagation) and the FFT section, respectively. Moreover, we define the symbol duration $T_{\mathrm{S}} := T_{\mathrm{CP}} + T$ and the windowed symbol duration $T_{\mathrm{w}} := T_{\mathrm{S}} + T_{\mathrm{RC}}$. The notations N_{CP}, N, N_{RC}, N_{w} and N_{S} designate the sample number of the corresponding sections. Finally, the ROF is defined as $r := \frac{T_{\mathrm{RC}}}{T_{\mathrm{S}}} = \frac{N_{\mathrm{RC}}}{N_{\mathrm{S}}}$.

The RC period smoothes the signal transition between consecutive symbols and thus reduces the sidelobe level. However, it can not completely remove the sidelobes. In order to suppress the ItCI caused by the remaining sidelobes, it's necessary to introduce a GB between adjacent channels. This can be done either by reserving NULL subcarriers at the spectrum edges or reducing the signal BW while maintaining the channel raster. Furthermore, we assume no BB up-sampling at the Tx. Thus, reducing the signal bandwidth is equivalent to reducing the sampling frequency f_s.

A higher ROF r leads to faster decay of the side lobes [107] and thus requires a smaller GB, which increases the spectral efficiency. On the other hand, higher r implies longer symbol duration, which in turn reduces the data rate. Thus, a trade-off between the value of r and the GB size must be found to obtain the maximal achievable data rate, so that the radio resource is exploited most efficiently. This optimization problem is studied in following.

The work in this section is based on our previous work [40].

3.3.2 Signal Model

The (periodical) continuous time BB OFDM signal before windowing as well as the corresponding spectrum can be written as:

$$\begin{aligned} s(t) &= \sum_{k=-\frac{N}{2}}^{\frac{N}{2}-1} S[k] e^{j2\pi k \Delta f t} \\ \circ\!\!-\!\!\bullet \quad S(f) &= \sum_{k=-\frac{N}{2}}^{\frac{N}{2}-1} S[k] \delta(f - k\Delta f), \end{aligned} \tag{3.5}$$

where N is the number of subcarriers, $S[k]$ is the data symbol modulating the k-th subcarrier, $\Delta f = \frac{f_s}{N}$ is the subcarrier spacing and $\delta(f)$ is the dirac delta distribution. The data symbols

are drawn from a constellation Ω, which can be BPSK, QPSK or M^2-QAM ($M > 2$).

The signal in Fig. 3.4 is obtained by windowing $s(t)$ with an RC window of duration $2T_{\mathrm{RC}} + T_{\mathrm{S}}$, whose time and frequency domain expressions are given by:

$$w(t,r) = \begin{cases} \frac{1}{T_{\mathrm{w}}}, & |t| \leq \frac{(1-r)T_{\mathrm{w}}}{2} \\ \frac{1}{2T_{\mathrm{w}}}\left[1+\cos\left(\frac{\pi}{2r}\left[\frac{2|t|}{T_{\mathrm{w}}}+r-1\right]\right)\right], & \frac{(1-r)T_{\mathrm{w}}}{2} < |t| \leq \frac{(1+r)T_{\mathrm{w}}}{2} \\ 0, & \text{otherwise} \end{cases} \tag{3.6}$$

$$\circ\!\!-\!\!\bullet \quad W(f,r) = \mathrm{sinc}(fT_{\mathrm{w}})\left[\frac{\cos(r\pi T_{\mathrm{S}} f)}{1-4r^2T_{\mathrm{S}}^2 f^2}\right]. \tag{3.7}$$

Note that if $r = 0$, the RC window turns into a rectangular window. Thus, the following analysis also includes the special case of rectangular windowing. The windowed OFDM signal in time- and frequency domains can be written as:

$$\acute{s}(t,r) = s(t)w(t,r) \circ\!\!-\!\!\bullet \acute{S}(f,r) = \sum_{k=-\frac{N}{2}}^{\frac{N}{2}-1} S[k]W(f-k\Delta f, r). \tag{3.8}$$

It should be stated that a time shift of the window function only causes a linear phase shift in the spectrum, which has no influence on the decay of the sidelobes. Thus, the usage of non-causal representation of the RC window in (3.8) is reasonable. Furthermore, the modulation of the BB OFDM signal to the RF band does not change the sidelobe level. Therefore, the ItCI is calculated from the equivalent BB signal in the following.

3.3.3 Sidelobe Reduction to Meet Spectral Mask

In cellular systems, the cells using adjacent frequency channels may generate ItCI to each other, which degrades the transmission quality. This problem is especially severe for the UTs locating at the cell edges. As shown in Fig. 3.13, these UTs are nearest to the interfering AP and farthest away from its own AP[1]. To mitigate this problem, two measures should be taken. The first measure is to allocate the frequency channels properly, so that the distance between the cells using adjacent channels is maximized (as depicted in Fig. 3.13). With such channel allocation, the interference signals will be transmitted over a longer distance than the dedicated signals. As a result, the interference signal is more attenuated than the dedicated signal. The second measure is to restrict the power of the out-of-band radiation i.e. the sidelobe of the transmitted signal. Usually, a spectral mask is predefined, which specifies the maximum allowable sidelobe level.

Now, we concentrate our analysis on the second measure. As mentioned in Sec. 3.3.1, we

[1]Since the PL increases with the distance between Tx and Rx [112], such UTs receive relatively strong interference signal and relatively weak dedicated signal.

apply RC windowing to reduce the sidelobes of OFDM signals. For simplicity, we assume that there is only one significant interfering AP (as in Fig. 3.13). Anyhow, the generalization to the case of more significant interference sources is straightforward [1].

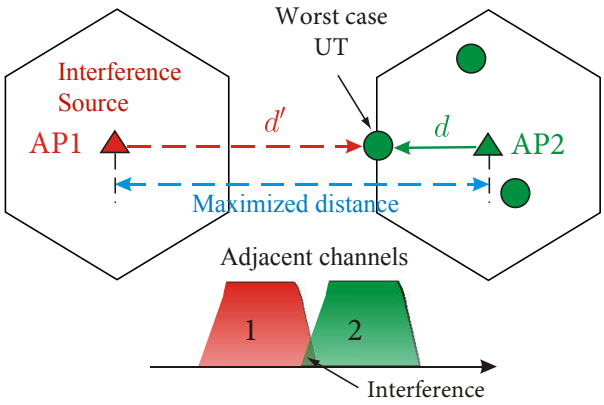

Figure 3.13: Interference from neighboring cells

Based on (3.8), the sidelobe generated by a RC windowed OFDM signal is illustrated in Fig. 3.14. As shown in Fig. 3.14, when r increases, the oscillation magnitude of $W(f,r)$ decreases, resulting in reduced sidelobe level of the OFDM signal. Note that for simplicity, the sidelobe generated by a single OFDM symbol is observed. As will be shown in App. B.1, the power spectrum (incl. the sidelobes) of multiple OFDM symbols just scales with the square of the number of OFDM symbols. Thus, the analysis with a single OFDM symbol is representative.

Without loss of generality, we consider the sidelobes on the right spectrum edge of the interference signal, which is shown on the left hand side of Fig. 3.14. In the adjacent channel, we can observe that the closer the frequency to the left spectrum edge, the stronger the interference. Thus, we can use the sidelobe level (of the interference signal) at the left-most subcarrier of the adjacent channel as reference for interference suppression. We first assume that no NULL subcarrier is reserved at the spectrum edges for GB construction. In this case, the frequency of the left-most subcarrier of the adjacent channel is $f_\nu = B - \frac{N}{2}\Delta f$, where B is the channel spacing. The extension of the analysis to the case of NULL subcarriers reservation will be given later.

We denote the constellation points with the largest magnitude as $S_{\max}$. From (3.8) and $|S[k]| \leq |S_{\max}|, \forall k$, the sidelobe power at f_ν is bounded by:

$$\left|\acute{S}(f_\nu, r)\right|^2 \leq |S_{\max}|^2 \left(\sum_{k=-\frac{N}{2}}^{\frac{N}{2}-1} |W(f_\nu - k\Delta f, r)| \right)^2 , \tag{3.9}$$

[1] When the network parameters are known.

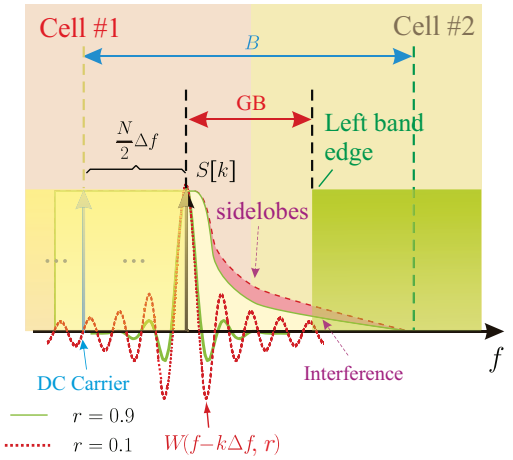

Figure 3.14: RC windowed OFDM signals in frequency domain

where a non-zero DC carrier is considered to simplify the analysis. Let P_{S} be the average spectral power of the interference signal within its bandwidth. From the predefined spectral mask, the ratio between P_{S} and the maximum allowable sidelobe power at f_ν can be derived. This ratio is denoted as ρ_{SM} and is used as interference suppression criterion. For simplicity, we approximate P_{S} with the mean square magnitude of the constellation points, which is denoted as $\bar{P}_{\mathcal{Q}}$[1]. From the constellation $\mathcal{Q}$, the following ratio is known: $\lambda_{\mathcal{Q}} := \frac{|S_{\max}|^2}{\bar{P}_{\mathcal{Q}}}$. Accordingly, to meet the spectral mask, the following inequality can be applied:

$$\frac{1}{\lambda_{\mathcal{Q}} \left(\sum_{k=-\frac{N}{2}}^{\frac{N}{2}-1} |W(f_\nu - k\Delta f, r)| \right)^2} \geq \rho_{\mathrm{SM}}. \tag{3.10}$$

We further assume that the transmit power levels of all APs are equal and the interfering signal is attenuated by $A_I^{\mathrm{dB}} = 10 \log A_I$ [dB] more than the dedicated signal (due to a larger transmission distance). To ensure the transmission quality at the cell edge, the A_I^{dB} of the worst case UT in Fig. 3.13 should be used. The value of A_I^{dB} can be calculated from the network parameters i.e. cell size, propagation environment and the PL model [112]. The influence of the multipath channel is considered by taking the corresponding PL model into account. Accordingly, when (3.10) is fulfilled, the SIR at the left spectrum edge of the adjacent channel, ρ_{AC}, should suffice:

$$\rho_{\mathrm{AC}} \geq \rho_{\mathrm{SM}} A_I. \tag{3.11}$$

[1]Recall that we consider the spectrum of a single OFDM symbol. In practice, P_{S} is usually larger than $\bar{P}_{\mathcal{Q}}$ due to the spectral convolution in (3.8). Thus, using $\bar{P}_{\mathcal{Q}}$ to approximate P_{S} leads to even stronger interference suppression.

For further analysis, Eq. (3.10) is rewritten as follows:

$$20\log\left(\sum_{k=-\frac{N}{2}}^{\frac{N}{2}-1}|W(f_\nu - k\Delta f, r)|\right) \leq \Gamma^{\mathrm{dB}}, \tag{3.12}$$

where $\Gamma^{\mathrm{dB}} := -10\log\lambda_{\mathrm{Q}} - 10\log\rho_{\mathrm{SM}}$. Eq. (3.12) provides the requirement on the windowing function to meet the spectral mask. This requirement will serve as the basis for the optimization of the RC window and the GB size.

Now, we extend our analysis to the case of reserving N_0 NULL subcarriers at the spectrum edges to construct a GB, where N_0 is an odd number. In this case, Eq. (3.12) changes to:

$$20\log\left(\sum_{k=-\frac{N}{2}+\frac{N_0+1}{2}}^{\frac{N}{2}-\frac{N_0+1}{2}}|W(f'_\nu - k\Delta f, r)|\right) \leq \Gamma^{\mathrm{dB}}, \tag{3.13}$$

where $f'_\nu = B - \frac{N-N_0-1}{2}\Delta f$.

3.3.4 Optimal RC Guard Period and Guardband Size

The optimal RC guard period and GB size are characterized by maximizing the data rate per OFDM symbol while satisfying the sidelobe reduction constraint in Sec. 3.3.3.

To simplify the analysis, we normalize the frequency in (3.7) to the subcarrier spacing and substitute $\kappa = \frac{f}{\Delta f}$. Now, we rewrite the window spectrum (3.7) as a function of κ and r for fixed N_S and N:

$$\acute{W}(\kappa, r) = \mathrm{sinc}\left(\frac{\kappa N_{\mathrm{S}}(1+r))}{N}\right)\left[\frac{\cos(\frac{r\pi N_{\mathrm{S}}\kappa}{N})}{1-\frac{4r^2N_{\mathrm{S}}^2\kappa^2}{N^2}}\right]. \tag{3.14}$$

By substituting (3.14) and $\kappa_{\mathrm{N}} = \frac{f_\nu}{\Delta f} - \frac{N}{2} + 1$ and $k' = k - \frac{N}{2} + 1$ into (3.12), we obtain the following inequality:

$$20\log\left(\sum_{k'=-N+1}^{0}\left|\acute{W}(\kappa_{\mathrm{N}} - k', r)\right|\right) \leq \Gamma^{\mathrm{dB}}. \tag{3.15}$$

Note that for the function $\sum_{k'=-N+1}^{0}\left|\acute{W}(\kappa - k', r)\right|$, $\kappa = 0$ and $\kappa = \kappa_{\mathrm{N}}$ correspond to the right-most subcarrier frequency of the interference signal and the left-most subcarrier frequency of the interfered signal, respectively. This simplifies the calculation of the GB size.

In a similar way, the following inequality can be derived from (3.13) for the case with NULL subcarrier reservation:

$$20\log\left(\sum_{\substack{k''=-N\\+N_0+1}}^{0}\left|\acute{W}(\kappa'_{\mathrm{N}} - k'', r)\right|\right) \leq \Gamma^{\mathrm{dB}}, \tag{3.16}$$

with $\kappa'_{\mathrm{N}} = \frac{f'_\nu}{\Delta f} - \frac{N-N_0-1}{2}$ and $k'' = k - \frac{N-N_0-1}{2}$. Actually, since

$$\sum_{k''=-N+1}^{0} \left|\acute{W}(\kappa'_{\mathrm{N}} - k'', r)\right| \geq \sum_{k''=-N+N_0+1}^{0} \left|\acute{W}(\kappa'_{\mathrm{N}} - k'', r)\right|, \tag{3.17}$$

we just need to observe the function $20\log\left(\sum_{k''=-N+1}^{0}\left|\acute{W}(\kappa - k'', r)\right|\right)$ with $\kappa = \kappa_{\mathrm{N}}$ and $\kappa = \kappa'_{\mathrm{N}}$ for the two interference criteria above, respectively. Actually, the difference between both sides of (3.17) is very small, because the contributions which are dropped on the right hand side of (3.17) come from the left-most subcarriers which have frequency distance of at least $\Delta f(N - N_0)$ away from the right-most subcarrier. Their influence on the sidelobe level is negligible.

Because of the decay property of the spectral pulse $\acute{W}(\kappa, r)$, it is possible to reduce the number of summation terms on the left hand side of (3.17) to $M < N - 1$ with sufficient accuracy (e.g. for $N = 256$, $M = 64$ is sufficient). Thus, we approximate the left sum of (3.17) with $\sum_{k''=-M}^{0}\left|\acute{W}(\kappa'_{\mathrm{N}} - k'', r)\right|$ and define the following function:

$$G(\kappa, r) := \sum_{k'=-M}^{0} \left|\acute{W}(\kappa - k', r)\right|. \tag{3.18}$$

For each possible r, i.e. N_{RC}, we search for the optimal location of the left-most subcarrier in the neighboring channel, $\tilde{\kappa}(r)$, according to the following requirement, which corresponds to (3.15):

$$\tilde{\kappa}(r) = \min\left\{\acute{\kappa}\,|\forall\kappa \geq \acute{\kappa} : 20\log G(\kappa, r) \leq \Gamma^{\mathrm{dB}}\right\}. \tag{3.19}$$

This search can be easily done by standard numeric tools. Finally, the denormalized GB size is $\tilde{\kappa}(r)\Delta f$.

There are 3 different cases of GB construction:

1. Only NULL subcarriers are reserved and $f_s = B$. The number of NULL subcarriers needed to construct the GB is:

$$N_0(r) = \lceil\tilde{\kappa}(r)\rceil + ((\lceil\tilde{\kappa}(r)\rceil))_2, \tag{3.20}$$

where the $((\cdot))_2$ operator ensures that N_0 is an odd number.

The data rate per OFDM symbol can be calculated by:

$$R_{\mathrm{d}}^{(\mathrm{I})}(r) = \frac{(N - N_0(r) - N_{\mathrm{p}})N_b R_C}{(N + N_{\mathrm{CP}} + rN_{\mathrm{S}})f_s} \quad \text{bits/s}, \tag{3.21}$$

where N_{p} is the number of pilot subcarriers, N_b is the number of bits per data symbol and R_C is the code rate of the channel code.

2. Only the sampling frequency f_s is reduced, no NULL subcarriers are reserved ($N_0 = 0$) and B is fixed. For a given r, the following relations exist: $\tilde{\kappa} = \frac{f_\nu}{\Delta f} - \frac{N}{2} + 1$, $f_\nu = B - \frac{N}{2}\Delta f$ and $f_s = N\Delta f$. Thus, we have

$$f_s(r) = \frac{NB}{\tilde{\kappa}(r) + N - 1}. \tag{3.22}$$

In this case, $R_\mathrm{d}(r)$ becomes:

$$R_\mathrm{d}^{(\mathrm{II})}(r) = \frac{(N - N_\mathrm{p})N_b R_C}{(N + N_\mathrm{CP} + rN_\mathrm{S})f_s(r)} \quad \text{bits/s}. \tag{3.23}$$

3. Both NULL subcarriers and f_s reduction are used. For a given N_0,

$$\begin{aligned} f_\nu(r) &= B - \left(\frac{N}{2} - \frac{N_0 + 1}{2}\right)\Delta f(r) \\ &= \left[\tilde{\kappa}(r) + \left(\frac{N}{2} - \frac{N_0 + 1}{2}\right)\right]\Delta f(r). \end{aligned} \tag{3.24}$$

Thus, we have

$$f_s(r) = \frac{NB}{\tilde{\kappa}(r) + N - N_0 - 1}. \tag{3.25}$$

In this case, $R_\mathrm{d}(r)$ is expressed as:

$$R_\mathrm{d}^{(\mathrm{III})}(r) = \frac{(N - N_0 - N_\mathrm{p})N_b r_C}{(N + N_\mathrm{CP} + N_\mathrm{RC})f_s(r)} \quad \text{bits/s}. \tag{3.26}$$

For all three cases, $R_\mathrm{d}(r)$ can be maximized with respect to r:

$$\tilde{r} = \arg\max_r \quad R_\mathrm{d}(r). \tag{3.27}$$

The search for $\tilde{r}$ can be done by standard numeric tools. It should be stated that since the GB size is determined by r, the joint optimization of ROF and the GB size becomes a one dimensional optimization.

3.3.5 Numerical Illustration of the Parameter Optimization

The parameters of the IFE system described in Sec. 3.2 were used to illustrate the optimization technique. Recall that there are totally eight downlink channels in the range of 60.5 GHz to 62 GHz, with channel spacing $B = 250$ MHz. The OFDM signals in each channel have $N = 256$ subcarriers. According to the measured 60 GHz channel length [106], the CP- i.e. the GI length

is chosen to be $N_{\mathrm{CP}} = 32$. Adjacent frequency channels are not allocated to neighbor cells but with an additional distance of at least one cell. For a worst case UT at the edge of a cell, only one interfering AP was considered. With a cell diameter of 5 m, the interfering signal is attenuated by $A_I^{\mathrm{dB}} = 7.9$ dB more than the dedicated signal according to the path-loss model in [106]. The modulation scheme is 16-QAM, corresponding to $N_b = 4$ bits/symbol, $S_{\max} = \sqrt{18}$ and $10 \log \lambda_{\mathrm{Q}} = 2.55$ dB. Furthermore, we set $\rho_{\mathrm{SM}}^{\mathrm{dB}} = 10 \log \rho_{\mathrm{SM}} = 32\,\mathrm{dB}$, which corresponds to SIR of $\rho_{\mathrm{AC}}^{\mathrm{dB}} = 10 \log \rho_{\mathrm{AC}} \geq 39.9$ dB at the left spectrum edge of the adjacent channel. Such SIR values should be sufficient for most of the modulation schemes. Based on the above parameters, $\tilde{\kappa}(r)$ in (3.19) is searched for as follows:

$$\tilde{\kappa}(r) = \min \left\{ \acute{\kappa} \,|\forall \kappa \geq \acute{\kappa} : 20 \log G(\kappa, r) \ \leq -34.55\,\mathrm{d}B \right\}. \tag{3.28}$$

The ROF values used for the search are: $\left\{ r = \frac{N_{\mathrm{RC}}}{N_S}, N_{\mathrm{RC}} = 1, \ldots, 64 \right\}$. The function $20 \log G(\kappa, r)$ is depicted in Fig. 3.15. The corresponding $\tilde{\kappa}(r)$'s are marked.

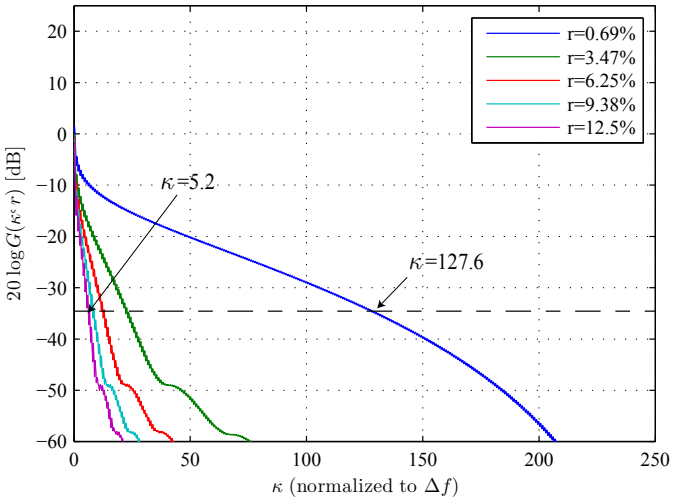

Figure 3.15: Sidelobes of $20 \log G(\kappa, r)$, N=256

The first two GB construction cases have been considered. Fig. 3.16 shows that in both cases, the required GB decreases with increasing r. The decrease is particularly fast in the low ROF region. Fig. 3.17 shows the data rate per OFDM symbol as a function of r (see (3.21) and (3.23)). As coding scheme, an inner convolution code with code rate $\frac{1}{2}$ and an outer Reed-Solomon-Code with code rate $\frac{7}{8}$ were used. Thus, the overall code rate is $R_C = \frac{7}{16}$. In both cases, the data rate functions have convex shapes, which enables simple maximization of R_d and thus the optimization of r. In the first case, the maximal achievable data rate is 336.4 Mbit/s with $N_0 = 17$ and $r = 5.2\%$, corresponding to $N_{\mathrm{RC}} = 15$. In the second case, the maximal data rate is 339.6 Mbit/s with a reduced sampling frequency of $f_s = 238.6$ MHz

and $r = 5.6\%$, corresponding to $N_{\mathrm{RC}} = 16$. A slightly higher maximal data rate is achieved by reducing f_s to construct the GB. The reason is that for the calculation of N_0 in (3.20), $\tilde{\kappa}(r)$ is rounded to the nearest greater integer, which increases the actual GB slightly.

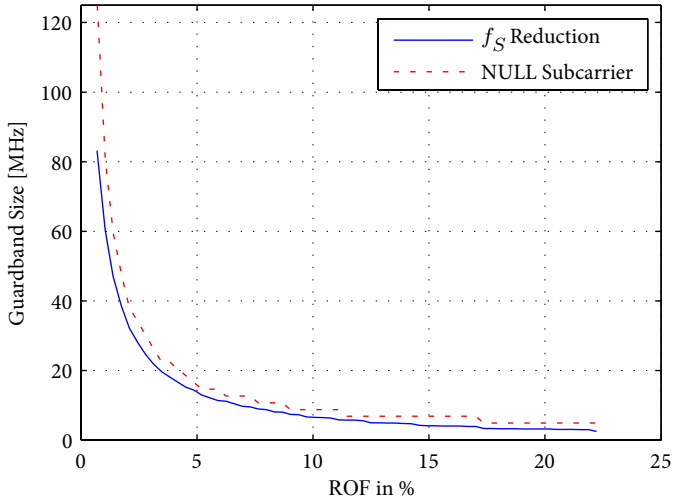

Figure 3.16: Guardband size as a function of r

To verify the sidelobe reduction, OFDM signals are generated with the optimized parameters. Fig. 3.18 shows the corresponding OFDM signal spectrum with NULL subcarrier reservation. For comparison, an OFDM signal without RC windowing is also included. As shown, significant sidelobe reduction is achieved by RC windowing, which is consistent with the predefined value of $\rho_{\mathrm{SM}}^{\mathrm{dB}}$ [1]. Similar results can be observed in the case of sampling frequency reduction.

3.3.6 Analysis of Instantaneous Interference per OFDM Symbol

For the interference analysis in Sec. 3.3.3, we have observed the OFDM signal spectrum in a general sense. In other words, the observed spectrum corresponds to the signal of (3.8) over infinite time. This analysis can be used to reduce the sidelobe and to meet the spectral mask.

In this section, we investigate the behavior of the instantaneous interference in each OFDM symbol as well as the influence of RC windowing on such interference. As shown in Fig. 3.19, for each OFDM symbol in the interfered channel, only a section of the interference signal with duration T (the FFT-block duration) is relevant. We call this section as "interference section". There are generally two cases of interference sections: A) The interference section does not contain the RC guard period; B) The interference section contains the RC guard period (the whole period or only parts of it).

[1] Note that $\rho_{\mathrm{AC}}^{\mathrm{dB}}$ is higher since the influence of A_I^{dB} is included.

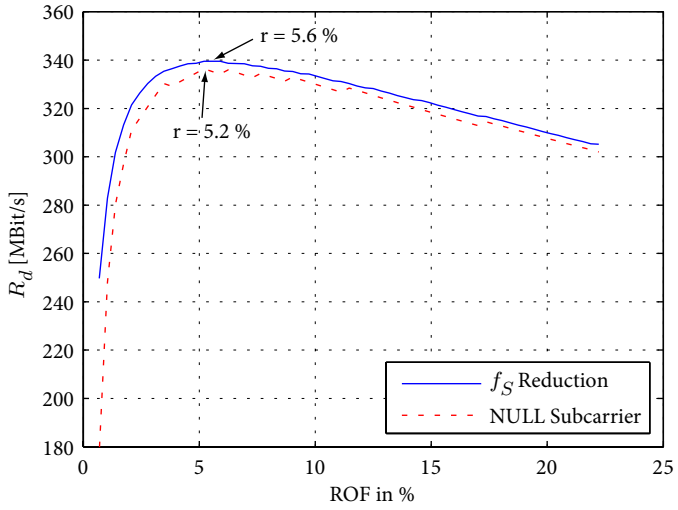

Figure 3.17: Data rate per OFDM symbol as a function of r

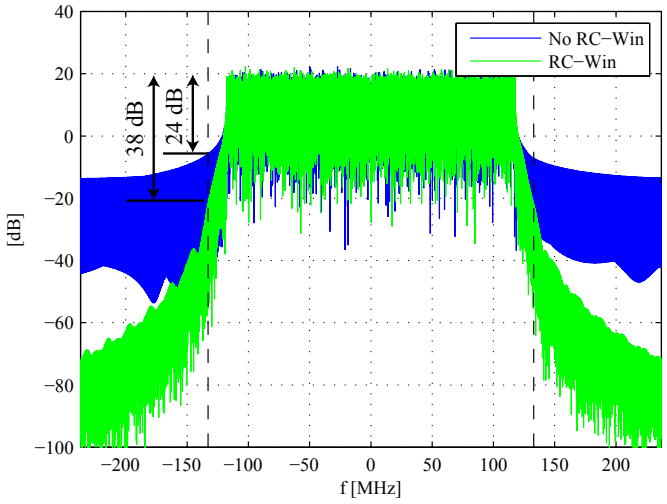

Figure 3.18: Spectra of OFDM signals with- and without RC windowing.

The interference behavior in the two cases above was investigated via simulation. In the simulation, the optimized parameters in Sec. 3.3.5 were used to generate OFDM signal frames in two adjacent channels (with $B = 250$ MHz). Each signal frame contains 256 OFDM symbols, which are generated from randomly chosen 16-QAM symbols. The spectral relation between these two signal frames was as depicted in Fig. 3.13, where the interference signal has $A_I^{\text{dB}} = 7.9$ dB less power than the interfered signal. For both case A and case B, 1000 OFDM signal frames per channel were generated. The instantaneous SIR at the left-most subcarrier of each interfered OFDM symbol is evaluated. Note that in case B, the position of the RC guard period was random. For comparison, the same simulation was carried out with OFDM signals without RC windowing.

In case A, the RC windowing has no influence on the interference level. In this case, if perfect frequency synchronization is achieved between the APs of adjacent channels and NULL subcarriers are used to construct GBs[1], no ItCI is present. The reason is that the subcarriers of the OFDM signals in adjacent channels reside in the zeros of each other's sidelobes. This is verified by Fig. 3.20, which shows the CDF of the instantaneous SIR at the left most subcarrier of the interfered OFDM symbols. As shown, all SIR values lie above 210 dB. However, if CFO is present or f_s reduction is applied to construct GB, the corresponding SIR will become much lower. This is shown in Fig. 3.21, where the corresponding CFO value was 90 kHz. We can also see that the SIR with NULL subcarrier reservation and CFO is still much higher than that with f_s reduction.

In case B, if no RC windowing is applied, the interference section will contain hard transitions of the modulated data symbols on each subcarrier. As a result, the interference will be stronger than case A. When RC windowing is applied, the corresponding data symbol transitions are smoothed, resulting in interference reduction. According to Fig. 3.21, when no RC windowing is applied, 99.9% of the SIR values lie above 14.6 dB for f_s reduction and 15.6 dB for NULL subcarrier reservation, respectively. When RC windowing is applied, the corresponding SIR values lie above 17.4 dB and 18.7 dB, respectively. Thus, the SIR gain by RC windowing is about 3 dB. We can also see that the SIR with RC windowing in case B is similar to that in case A with f_s reduction.

Generally, the instantaneous SIR at the left-most subcarrier of each interfered OFDM symbol can be much lower than the desired value of $\rho_{\text{AC}}^{\text{dB}} \geq 39.9$ dB (in Sec. 3.3.5). Moreover, the improvement by RC windowing is relatively small. The reason is that taking an interference section out of the interference signal is equivalent to an extra rectangular windowing on this signal. This windowing results in considerable sidelobe regrowth.

If higher instantaneous SIR per OFDM symbol is desired, larger GB should be reserved[2]. However, further investigation is still needed to find the optimal GB size and the optimal ROF which allows high instantaneous SIR per OFDM symbol. To achieve this goal, the sectioning of the interference signal (i.e. the additional rectangular windowing) should be taken into account

[1] In other words, if $f_s = B$.

[2] Further simulations show that reserving more GB is much more effective than increasing r.

in the signal model, the interference analysis and the optimization procedure. This remains future work.

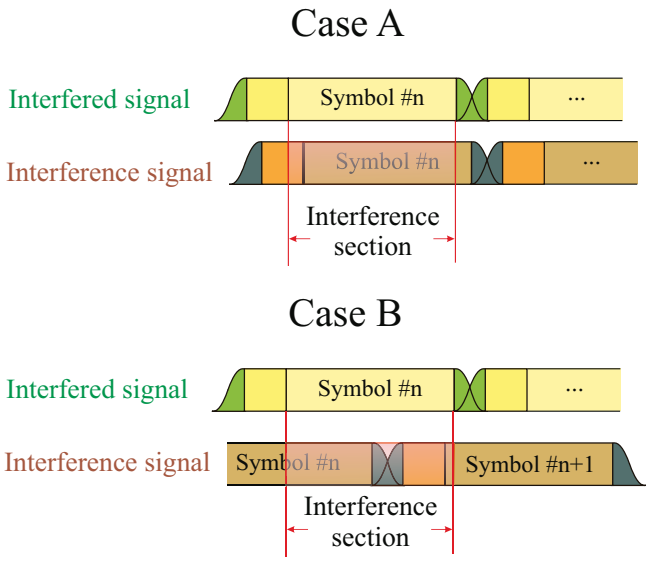

Figure 3.19: Different cases of interference sections.

3.4 Efficient Joint Estimation and Compensation of I/Q-Imbalance and the MIMO Channel

3.4.1 Background and Overview

Except for high data rate, the 60 GHz WLAN system is expected to have low-cost, low-power, small size and flexible implementation, which leads to the application of DCA both at the Tx and Rx. Since MIMO technique is applied, multiple RF front-ends and BB analog component chains are required, which put further restriction on the size and cost of the individual RF and BB analog components. As a result, hardware impairments, i.e. the "dirty RF effects", become more severe. The typical impairments include CFO, DC-Offset and I/Q-imbalance. Since DC-offset can be easily suppressed by AC-coupling [113], it is not considered in our investigation. While CFO causes Common Phase Error (CPE) and Inter-Carrier-Interference (ICI), I/Q-imbalance causes MFI. As a result, the application of high-order modulation (e.g. 16-QAM, 64-QAM) is limited, corresponding to insufficient spectral efficiency. In our investigation, we consider both the MOD- and DMOD I/Q-imbalance and the I/Q-imbalance of the BB analog components (typically the LPFs). The overall effect of both I/Q-imbalance effects is referred to as "frequency selective I/Q-imbalance".

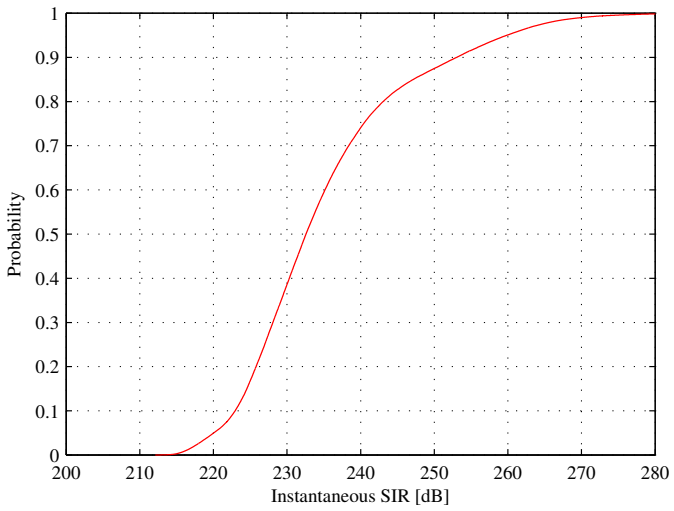

Figure 3.20: CDF of instantaneous SIR at the left most subcarrier of the interfered signal in case A with NULL subcarrier reservation.

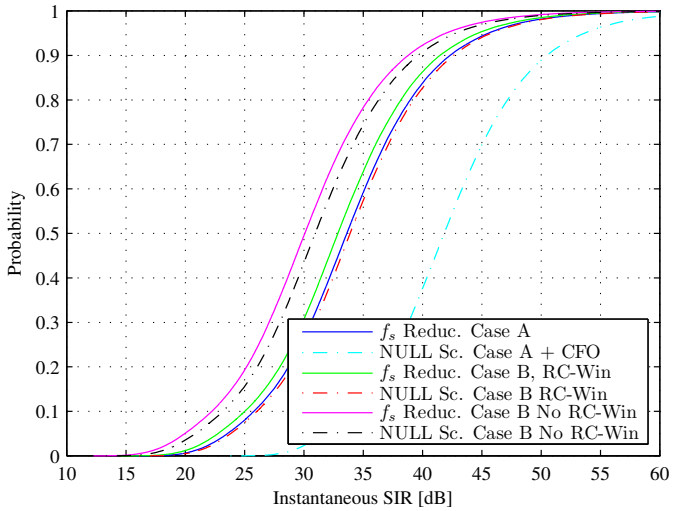

Figure 3.21: CDF of the instantaneous SIR at the left most subcarrier of the interfered signal in different cases.

As mentioned in Sec. 2.1.5, there are generally two different ways of Tx/Rx-I/Q-imbalance compensation. The first way is to compensate the Tx-I/Q-imbalance at the Tx and the Rx-I/Q-imbalance at the Rx, respectively[1]. The advantages of this way were already given in Sec. 2.1.5. After Tx-I/Q-imbalance has been compensated for (e.g. using the scheme in Sec. 2), a number of existing schemes, e.g. [48, 114, 115, 116, 117, 118, 119, 120], can be applied to estimate/compensate for the CFO and/or Rx-I/Q-imbalance at the Rx. However, this way is only feasible when feedback paths are available at the Tx[2]. The second way is to compensate both Tx- and Rx-I/Q-imbalance at the Rx. If the feedback paths mentioned above are unavailable, e.g. due to cost constraints[3], this way should be chosen. Actually, if the PA can be assumed to be operating within the linear region, this is also a very effective way. Except for allowing lower hardware complexity at the Tx, this way has an interesting advantage that extra diversity gain due to Tx-I/Q-imbalance can be exploited [83, 84, 121]. However, such diversity gain can only be achieved by advanced detection schemes e.g. V-BLAST, which generally requires high computational complexity. In this thesis, we focus on the second way.

There are also two ways of CFO compensation. The first way is the analog compensation, where the Rx LO frequency is adjusted according to the estimated CFO value [122]. For the CFO estimation in the presence of I/Q-imbalance, a lot of methods e.g. [115, 116, 117, 123] can be applied. Since the CFO varies very slowly in time (mainly due to temperature change), the corresponding estimation only needs to be carried out with a relatively long period (instead of for each communication frame). After analog CFO compensation, the CFO can be excluded from the system model. The second way is the digital compensation. The most common digital CFO compensation is the time domain sample-wise phase derotation. In this thesis, both ways of CFO compensation are considered. In this section, perfect analog CFO compensation is assumed[4]. Thus, we concentrate our investigation on the digital compensation of Tx- and Rx-I/Q-imbalance. In the next section (Sec. 3.5), digital CFO compensation is considered jointly with the digital Tx- and Rx-I/Q-imbalance compensation, which requires more complicated signal modeling, parameter estimation and impairment compensation.

Assuming Rx-side compensation of Tx-I/Q-imbalance, a further issue would be whether to estimate and compensate Tx-, Rx-I/Q-imbalance and the radio channel (SISO/MIMO) jointly or separately. First, we discuss the combination possibilities of Tx- and Rx-I/Q-imbalance compensation according to the following two cases (which correspond to the two CFO compensation ways mentioned above):

1. **No CFO is present** (i.e. perfect analog CFO compensation): In this case, the effects of Tx- and Rx-I/Q-imbalance are generally hard to separate. Thus, most of the existing

[1] In MIMO systems with Tx-side pre-compensation, the Tx-I/Q-imbalance of different Tx antennas is compensated separately.

[2] The work in [88] can be regarded as a special case where the Rx of the same device is used as the feedback path during calibration.

[3] This is especially true in MIMO systems or peer-to-peer communication (although it is not the target use case in this thesis).

[4] This assumption can also be found in a lot of works e.g. [79, 124, 125, 126, 127].

works estimate/compensate Tx- and Rx-I/Q-imbalance jointly with the radio channel in one step [42, 79, 83, 84, 121, 125, 126, 127, 128, 129, 130]. In [82, 124], a two-step estimation method was proposed. While the channel estimates in the first step contains I/Q-imbalance influence, the estimates in the second step are mixtures of I/Q-imbalance- and channel coefficients. In [76, 131], a separate estimation scheme was proposed for the Tx- and Rx- frequency-independent I/Q-imbalance. However, this scheme is based on approximate assumptions on the I/Q-imbalance parameter values[1] and requires large amount of pilot data, imposing high overhead. Moreover, after the estimation, Tx-,Rx-I/Q-imbalance and the channel are still compensated jointly. In MIMO systems of this case, I/Q-imbalance of different Tx-/Rx antennas is generally compensated for jointly.

2. **CFO is present**: In this case, the most efficient way is to estimate and compensate Tx- and Rx-I/Q-imbalance separately. The reason is that the CFO effect lies between both I/Q-imbalance effects (see Sec. 3.5) and allows to decouple Tx- and Rx-I/Q-imbalance. Examples can be found in the hybrid domain compensation of [44, 81, 90, 123, 132], where Rx-I/Q-imbalance and CFO are compensated in time domain, while Tx-I/Q-imbalance and the radio channel are compensated in frequency domain. However, exceptions can also be found, i.e. in the works [133, 134, 135], where Tx-, Rx-I/Q-imbalance and the channel are jointly estimated. Moreover, CFO is compensated in time domain, while Tx- and Rx-I/Q-imbalance as well as the channel are compensated two dimensionally in time- and frequency domains using Per-Tone-EQualization (PTEQ). The main drawbacks of this scheme are high computational complexity and slow convergence. Generally, in MIMO systems of this case, Rx-I/Q-imbalance of different Rx antennas can either be jointly [133, 134, 135] or separately [44, 90, 123] compensated for. However, the separate version is more efficient. In contrast, Tx-I/Q-imbalance of different Tx antennas has to be compensated for jointly[2].

In both cases above, I/Q-imbalance[3] can be compensated jointly with the radio channels (SISO or MIMO) [42, 44, 81, 83, 84, 128, 129, 130, 131, 133, 134, 135] or separately from them [48, 90, 123, 132]. The compensation in [82, 124] is a special case which conducts separate STC-decoding but still applies partially joint compensation of Tx-, Rx-I/Q-imbalance and the channel[4]. Generally, the joint compensation will increase the signal detection dimension. For MIMO systems with N_T and N_R Tx- and Rx- antennas, respectively, the separate and joint compensation correspond to signal detection dimensions of $N_T \times N_R$ and $2N_T \times 2N_R$, respectively[129]. In the scheme of [82, 124], due to partially joint compensation, the signal detection dimension is $2N_T \times 2N_T$[5]. However, let N_D be the total number of data subcarriers, the

[1] Assuming very small Tx I/Q-imbalance values.
[2] Since the Rx signal at each Rx antenna contains the I/Q-imbalance effects of all Tx antennas.
[3] Only Tx-I/Q-imbalance or both Tx- and Rx-I/Q-imbalance in the case of Rx-side compensation only; Only Rx-I/Q-imbalance in the case of Tx side Tx-I/Q-imbalance compensation i.e. when perfect Tx is assumed.
[4] The coefficients $a[k], b[k], c[k], d[k]$ in [82, 124] include the influence of both Tx/Rx-I/Q-imbalance and the MIMO channel.
[5] Assuming N_T consecutive OFDM data symbols are encoded to N_T consecutive OFDM symbol slots and

joint compensation only requires signal detection on $\frac{N_D}{2}$ subcarriers[1], which is half the number required by the separate compensation. Furthermore, the separate compensation requires extra complexity[2] for the calculation of separate compensation coefficients (for Tx-I/Q-imbalance and the radio channels) as well as for the actual compensation of I/Q-imbalance (see [90]). Thus, for small N_T and N_R and simple equalization schemes (e.g. ZF), the complexity of both joint- and separate compensation may be similar. For large N_T, N_R and the cases where complex equalization/detection schemes are applied (e.g. V-BLAST), the separate compensation generally has lower complexity. An additional advantage of the separate compensation is that signal detection algorithms can be designed without considering these RF impairments [3]. In contrast, with adequate algorithms that consider I/Q-imbalance e.g. those in [83, 84, 121], the joint scheme can profit from extra diversity gain introduced by Tx-I/Q-imbalance. In Sec. 3.4.9 and Sec. 3.5.7, some complexity analysis will be given based on the parameters of the 60 GHz IFE system.

To give a general view, the possible combinations of the compensation of Tx-, Rx-I/Q-imbalance and the radio Channel are summarized in the two tables in App. B.3.

In this section, we focus on the joint estimation and compensation of Tx-, Rx-I/Q-imbalance and the MIMO channel in OFDM systems. Since indoor 60 GHz channels can be regarded as quasi static within each communication signal frame (i.e. block-fading), the most efficient and practical way for the joint parameter estimation is to apply preambles. In MIMO systems, different Tx/Rx-branches have different I/Q-imbalance parameters. As a result, the dimension of parameters to be estimated is much higher than SISO systems. Thus, it is necessary to design overhead-efficient and optimal preambles.

Regarding our focus, there are a number of related works, which have been mentioned above. While [129, 136, 137, 138] only investigate frequency independent I/Q-imbalance, [79, 82, 85, 86, 88, 121, 124, 125, 126, 127, 128, 131] consider frequency-selective I/Q-imbalance. The latter are much more relevant for broadband high data rate wireless communication. Most of the existing works have some drawbacks. The schemes in [128, 131] require recursive algorithms due to the absence or incompleteness of parameter estimation. As a result, high computational complexity and large latency can be expected. The semi-blind based scheme in [121] is only suitable for QPSK and Spatial Multiplexing (SM). The two-step scheme in [82, 124] is an effective and efficient scheme for STC coded MIMO OFDM systems. However, it is more suitable for pilot-data-multiplexed type[4] parameter estimation, i.e. in the case of fast fading channels. If the pilot design in [82, 124] is used as preamble, at least four OFDM symbols are required. Thus, it is not overhead efficient as preamble[5]. The pilot design and parameter estimation scheme in

across all N_T Tx antennas.

[1] The joint compensation is done on mirroring subcarrier pairs

[2] W.r.t. the signal detection.

[3] In other words, algorithms that have been designed without considering these RF impairments can be applied.

[4] Also called "comb-type" in [139].

[5] More comparison between the proposed schemes and the scheme in [82, 124] can be found in Sec. 3.4.8 and Sec. 3.4.9.

[79][1] is overhead efficient but not suitable for OFDM systems with GB. As will be shown, this scheme will suffer from significant performance degradation due to the presence of OFDM GB. The most advanced state-of-the-art preamble design and parameter estimation were presented by [125, 126, 127] and our previous work [42][2]. With these schemes, estimation Mean Square Error (MSE) close to the Cramer-Rao Lower Bound (CRLB) can be achieved. Especially, [127] provides a large variety of pilot designs for both preambles and pilot-data-multiplexed symbols. However, most of these designs, except for the [CDM-F;Null] and [FDM;Null] designs, require multiple OFDM symbols and are not overhead efficient enough as preambles. Moreover, the estimators in [127] require relatively high computational complexity than our schemes.

The work in this section is an extension of our previous work [42]. First, joint channel and I/Q-imbalance compensation schemes are derived for different antenna diversity configurations. Afterwards, optimal preamble design rules are derived. Based on these design rules, three preamble designs are proposed, which allow low preamble overhead (i.e. of about one OFDM symbol length) and low CF. Based on these preambles, efficient joint estimation schemes are proposed. Finally, numerical simulation results as well as complexity analysis are presented to verify the advantages of the proposed schemes. The novelties of our schemes can be summarized as follows:

- The proposed preamble designs also consider OFDM systems with large GB, where the equidistant pilot subcarrier allocation in [125, 126, 127] can not be applied. In this case, we apply partially equidistant pilot subcarrier allocation. Practical subcarrier index selection schemes are proposed[3] (see Sec. 3.4.6.1 and Sec. 3.4.7.1);
- Edge subcarrier inclusion is proposed to improve estimation accuracy (see Sec. 3.4.6.1);
- Methods for achieving low Crest Factor (CF) of the preambles are proposed, which allows "preamble power boosting"[4];
- The estimation schemes are developed for the individual preamble designs with minimized computational complexity. In contrast, a common high complexity estimator is applied for all preamble designs in [125, 126, 127];
- The estimation schemes apply Linear Minimum Mean Square Estimation (LMMSE), which allows better performance than Maximum Likelihood Estimation (MLE)[5] used in [125, 126, 127] but without increasing computational complexity[6];

[1] Although this scheme was designed for SISO systems, it can be extended to MIMO.
[2] Our preamble designs and estimation schemes have been developed in parallel to those of [125, 126, 127]. Although they are similar, there are quite a few technical details.
[3] Only for the Frequency Domain Separation (FDS) scheme and the multi-functional preamble based scheme.
[4] When the CF of the preamble is much lower than the communication signals, the preamble can be transmitted with much higher power than the communication signal.
[5] This definition follows those in [140, 141]. However, such estimation is called Least-Square Estimation (LSE) in [127]. The fact is that, for linear models with Gaussian white noise, the MLE is equivalent to the LSE [142].
[6] Only when applying fixed assumed SNR values in the LMMSE estimation.

- The proposed multi-functional preamble in Sec. 3.4.7 is only slightly longer than one OFDM symbol but can be used both for frame detection/time synchronization and joint I/Q-imbalance- and channel estimation, allowing further reduction of the preamble overhead.

3.4.2 Signal- and System Model

Fig. 3.22 shows the MIMO OFDM system model, where N_T and N_R are the numbers of Tx- and Rx antennas, respectively. The samples of the Tx- and Rx time domain OFDM symbols are indicated as $s[n]$ and $y[n], \forall n \in \mathcal{N}$, respectively. Their DFTs are denoted as $S[k]$ and $Y[k]$, respectively, where k is the OFDM subcarrier index[1]. Furthermore, we assume that a sufficient CP is attached to each OFDM symbol at the Tx and will be eliminated at the Rx. In Fig. 3.22, all individual LPF are modeled to have different IRs. The discrete IRs of the Tx- or Rx LPFs in the I- and Q-branches are indicated as $h^{TI;RI}[n]$ and $h^{TQ;RQ}[n]$, respectively. The difference between $h^{TI;RI}[n]$ and $h^{TQ;RQ}[n]$ is the source of frequency selective I/Q-imbalance. The MOD- or DMOD amplitude- and phase imbalance are indicated by $g^{T;R}$ and $\varphi^{T;R}$, respectively. Furthermore, $h_{\mathrm{RF}}^{\langle r,i\rangle}$ indicates the radio channel between the i^{th} Tx and the r^{th} Rx. These radio channels are assumed to be quasi constant within a communication signal frame (i.e. block fading channels).

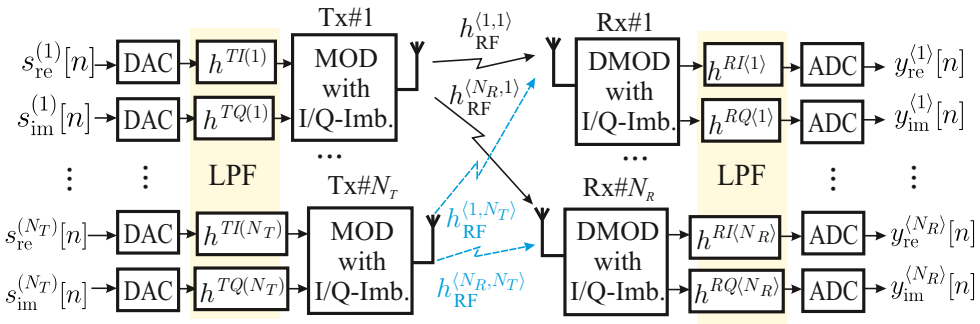

Figure 3.22: MIMO system model with Tx- and Rx- I/Q-imbalance

For further analysis, a BB model should be derived. For simplicity, we use $h^{\langle r,i\rangle}[n]$ to indicate an equivalent BB discrete IR, which includes the cascading effect of $h_{\mathrm{RF}}^{\langle r,i\rangle}$ and the RF chain. Furthermore, we denote the equivalent BB version of the i^{th} MOD output and the r^{th} DMOD input as $u^{(i)}[n]$ and $x^{\langle r\rangle}[n]$, respectively. Due to Tx I/Q-imbalance, $u^{(i)}[n]$ can be expressed in terms of $s^{(i)}[n]$ (direct part) and $s^{(i)*}[n]$ (image part) as follows (see e.g. [45, 86, 124]):

$$u^{(i)}[n] = s^{(i)}[n] * h_{\mathrm{D}}^{T(i)}[n] + s^{(i)*}[n] * h_{\mathrm{I}}^{T(i)}[n], \tag{3.29}$$

[1]Note that the Tx- and Rx antenna indexes are omitted for simplicity.

with

$$h_{\mathrm{D;I}}^{T(i)}[n] := \left(h^{TI(i)}[n] \pm g^{T(i)} e^{j\varphi^{T(i)}} h^{TQ(i)}[n]\right)/2. \tag{3.30}$$

At the Rx, we define $\acute{x}^{\langle r\rangle}[n] := x^{\langle r\rangle}[n] + \eta^{\langle r\rangle}[n]$, where $\eta^{\langle r\rangle}[n]$ is the AWGN at the r^{th} Rx. Due to Rx I/Q-imbalance, $y^{\langle r\rangle}[n]$ can be expressed in terms of $\acute{x}^{\langle r\rangle}[n]$ and $\acute{x}^{\langle r\rangle *}[n]$ ((see e.g. [86, 114, 124])):

$$y^{\langle r\rangle}[n] = \acute{x}^{\langle r\rangle}[n] * h_{\mathrm{D}}^{R\langle r\rangle}[n] + \acute{x}^{\langle r\rangle *}[n] * h_{\mathrm{I}}^{R\langle r\rangle}[k], \tag{3.31}$$

with

$$h_{\mathrm{D;I}}^{R\langle r\rangle}[n] := \left(h^{RI\langle r\rangle}[n] \pm g^{R\langle r\rangle} e^{\mp j\varphi^{R\langle r\rangle}} h^{RQ\langle r\rangle}[n]\right)/2. \tag{3.32}$$

Based on (3.29), (3.31) and $x^{\langle r\rangle}[n] = \sum_{i=1}^{N_T} u^{(i)}[n] * h^{\langle r,i\rangle}[n]$, the relation between $y^{\langle r\rangle}[n]$ and $s^{(i)}[n]$ can be obtained:

$$y^{\langle r\rangle}[n] = \sum_{i=1}^{N_T} \left(s^{(i)}[n] * h_{\mathrm{D}}^{\langle r,i\rangle}[n] + s^{(i)*}[n] * h_{\mathrm{I}}^{\langle r,i\rangle}[n]\right) + \tilde{\eta}^{\langle r\rangle}[n], \tag{3.33}$$

where

$$\begin{aligned}
h_{\mathrm{D}}^{\langle r,i\rangle}[n] &= h_{\mathrm{D}}^{T(i)}[n] * h^{\langle r,i\rangle}[n] * h_{\mathrm{D}}^{R\langle r\rangle}[n] + h_{\mathrm{I}}^{T(i)*}[n] * h^{\langle r,i\rangle *}[n] * h_{\mathrm{I}}^{R\langle r\rangle}[n], \\
h_{\mathrm{I}}^{\langle r,i\rangle}[n] &= h_{\mathrm{I}}^{T(i)}[n] * h^{\langle r,i\rangle}[n] * h_{\mathrm{D}}^{R\langle r\rangle}[n] + h_{\mathrm{D}}^{T(i)*}[n] * h^{\langle r,i\rangle *}[n] * h_{\mathrm{I}}^{R\langle r\rangle}[n], \\
\tilde{\eta}^{\langle r\rangle}[n] &= \eta^{\langle r\rangle}[n] * h_{\mathrm{D}}^{R\langle r\rangle}[n] + \eta^{\langle r\rangle *}[n] h_{\mathrm{I}}^{R\langle r\rangle}[n].
\end{aligned} \tag{3.34}$$

We call $h_{\mathrm{D}}^{\langle r,i\rangle}[n]$ and $h_{\mathrm{I}}^{\langle r,i\rangle}[n]$ the "direct-" and "image" channels, respectively. Moreover, we assume a maximum length L for $h_{\mathrm{D;I}}^{\langle r,i\rangle}[n]$ i.e. $h_{\mathrm{D;I}}^{\langle r,i\rangle}[n] = 0, \forall n > L$. Considering the CP-assisted structure of OFDM signals, Eq. (3.33) can be equivalently written in frequency domain (for each OFDM symbol) as

$$Y^{\langle r\rangle}[k] = \sum_{i=1}^{N_T} \left(S^{(i)}[k] H_{\mathrm{D}}^{\langle r,i\rangle}[k] + S^{(i)*}[-k] H_{\mathrm{I}}^{\langle r,i\rangle}[k]\right) + \tilde{N}^{\langle r\rangle}[k], \tag{3.35}$$

where $Y^{\langle r\rangle}[k] = \mathcal{F}_N\left\{y^{\langle r\rangle}[n]\right\}$, $S^{(i)}[k] = \mathcal{F}_N\left\{s^{(i)}[n]\right\}$, $H_{\mathrm{D;I}}^{\langle r,i\rangle}[k] = \mathcal{F}_N\left\{h_{\mathrm{D;I}}^{\langle r,i\rangle}[n]\right\}$ and $\tilde{N}^{\langle r\rangle}[k]$ is the AWGN noise spectrum.

Note that the used signal model complies with that in [125, 126, 127].

3.4.3 Joint Channel and Frequency-Selective I/Q-Imbalance Compensation

Based on the signal model (3.35), joint channel and I/Q-imbalance compensation schemes can be derived. For simplicity, we consider $N_T \leq 2$ and $N_R \leq 2$. The extension to more Tx/Rx antennas is straightforward. In the following, we will derive the input-output equation systems for all possible antenna diversity schemes, including STC and SM. Signal detection can be done

according to these equation systems. Note that the derivation in this section complies with the theoretical framework in [129], which was derived considering only frequency-independent Rx-I/Q-imbalance.

3.4.3.1 SISO Case

In SISO case, $N_T = N_R = 1$. Both the Tx and the Rx indexes in (3.35) can be omitted. From (3.35), we can express $Y[k]$ and $Y^*[-k]$ in the following matrix notation:

$$\begin{bmatrix} Y[k] \\ Y^*[-k] \end{bmatrix} = \begin{bmatrix} H_{\mathrm{D}}[k] & H_{\mathrm{I}}[k] \\ H_{\mathrm{I}}^*[-k] & H_{\mathrm{D}}^*[-k] \end{bmatrix} \begin{bmatrix} S[k] \\ S^*[-k] \end{bmatrix} + \begin{bmatrix} \tilde{N}[k] \\ \tilde{N}^*[-k] \end{bmatrix}. \tag{3.36}$$

3.4.3.2 MISO Case

We consider a 2×1 MISO system which applies subcarrier-wise Alamouti STC [124]. The consecutive OFDM symbol pairs to be transmitted from the 1st and 2nd Tx antennas are $\left\{S_{b_1}[k], -S_{b_2}^*[k]\right\}$ and $\left\{S_{b_2}[k], S_{b_1}^*[k]\right\}$, respectively, where b_1 and b_2 are consecutive symbol indexes with $b_2 = b_1 + 1$. According to (3.35), the two consecutive received OFDM symbols can be expressed as:

$$\begin{aligned} Y_{b_1}[k] &= S_{b_1}[k]H_{\mathrm{D}}^{(1)}[k] + S_{b_1}^*[-k]H_{\mathrm{I}}^{(1)}[k] + \\ &\quad S_{b_2}[k]H_{\mathrm{D}}^{(2)}[k] + S_{b_2}^*[-k]H_{\mathrm{I}}^{(2)}[k] + \tilde{N}_{b_1}[k], \\ Y_{b_2}[k] &= -S_{b_2}^*[k]H_{\mathrm{D}}^{(1)}[k] - S_{b_2}[-k]H_{\mathrm{I}}^{(1)}[k] + \\ &\quad S_{b_1}^*[k]H_{\mathrm{D}}^{(2)}[k] + S_{b_1}[-k]H_{\mathrm{I}}^{(2)}[k] + \tilde{N}_{b_2}[k]. \end{aligned} \tag{3.37}$$

From (3.37), the received symbols $Y_{b_1}[k]$, $Y_{b_2}[k]$ and their images $Y_{b_1}^*[-k]$, $Y_{b_2}^*[-k]$ can be expressed in the following matrix equation:

$$\boldsymbol{Y}_{\mathrm{STC},k} = \boldsymbol{H}_{\mathrm{STC},k}\boldsymbol{S}_{\mathrm{STC},k} + \tilde{\boldsymbol{N}}_{\mathrm{STC},k}, \tag{3.38}$$

where $\boldsymbol{Y}_{\mathrm{STC},k} = \left[Y_{b_1}[k], Y_{b_1}^*[-k], Y_{b_2}^*[k], Y_{b_2}[-k]\right]^T$, $\boldsymbol{S}_{\mathrm{STC},k} = \left[S_{b_1}[k], S_{b_1}^*[-k], S_{b_2}[k], S_{b_2}^*[-k]\right]^T$, $\tilde{\boldsymbol{N}}_{\mathrm{STC},k} = \left[\tilde{N}_{b_1}[k], \tilde{N}_{b_1}^*[-k], \tilde{N}_{b_2}[k], \tilde{N}_{b_2}^*[-k]\right]^T$ and $\boldsymbol{H}_{\mathrm{STC},k}$ is given by

$$\begin{bmatrix} H_{\mathrm{D}}^{(1)}[k] & H_{\mathrm{I}}^{(1)}[k] & H_{\mathrm{D}}^{(2)}[k] & H_{\mathrm{I}}^{(2)}[k] \\ H_{\mathrm{I}}^{(1)*}[-k] & H_{\mathrm{D}}^{(1)*}[-k] & H_{\mathrm{I}}^{(2)*}[-k] & H_{\mathrm{D}}^{(2)*}[-k] \\ H_{\mathrm{D}}^{(2)*}[k] & H_{\mathrm{I}}^{(2)*}[k] & -H_{\mathrm{D}}^{(1)*}[k] & -H_{\mathrm{I}}^{(1)*}[k] \\ H_{\mathrm{I}}^{(2)}[-k] & H_{\mathrm{D}}^{(2)}[-k] & -H_{\mathrm{I}}^{(1)}[-k] & -H_{\mathrm{D}}^{(1)}[-k] \end{bmatrix}.$$

3.4.3.3 SIMO Case

We consider a 1×2 SIMO system. According to (3.35), the received OFDM symbols and their images are expressed as:

$$\begin{bmatrix} Y^{\langle 1 \rangle}[k] \\ Y^{\langle 1 \rangle *}[-k] \\ Y^{\langle 2 \rangle}[k] \\ Y^{\langle 2 \rangle *}[-k] \end{bmatrix} = \begin{bmatrix} H_{\mathrm{D}}^{\langle 1 \rangle}[k] & H_{\mathrm{I}}^{\langle 1 \rangle}[k] \\ H_{\mathrm{I}}^{\langle 1 \rangle *}[-k] & H_{\mathrm{D}}^{\langle 1 \rangle *}[-k] \\ H_{\mathrm{D}}^{\langle 2 \rangle}[k] & H_{\mathrm{I}}^{\langle 2 \rangle}[k] \\ H_{\mathrm{I}}^{\langle 2 \rangle *}[-k] & H_{\mathrm{D}}^{\langle 2 \rangle *}[-k] \end{bmatrix} \begin{bmatrix} S[k] \\ S^{*}[-k] \end{bmatrix} + \tilde{\boldsymbol{N}}'_k, \tag{3.39}$$

where $\tilde{\boldsymbol{N}}'_k = \left[\tilde{N}^{\langle 1 \rangle}[k], \tilde{N}^{\langle 1 \rangle *}[-k], \tilde{N}^{\langle 2 \rangle}[k], \tilde{N}^{\langle 2 \rangle *}[-k]\right]^T$.

3.4.3.4 MIMO Case

First, we consider the 2×2 MIMO case with STC. By extending the expressions of (3.37) with an Rx index r, we obtain the following relation between the transmitted and the received symbols:

$$\begin{bmatrix} \boldsymbol{Y}_{\mathrm{STC},k}^{\langle 1 \rangle} \\ \boldsymbol{Y}_{\mathrm{STC},k}^{\langle 2 \rangle} \end{bmatrix} = \begin{bmatrix} \boldsymbol{H}_{\mathrm{STC},k}^{\langle 1 \rangle} \\ \boldsymbol{H}_{\mathrm{STC},k}^{\langle 2 \rangle} \end{bmatrix} \boldsymbol{S}_{\mathrm{STC},k} + \begin{bmatrix} \tilde{\boldsymbol{N}}_{\mathrm{STC},k}^{\langle 1 \rangle} \\ \tilde{\boldsymbol{N}}_{\mathrm{STC},k}^{\langle 2 \rangle} \end{bmatrix}, \tag{3.40}$$

where

$$\boldsymbol{Y}_{\mathrm{STC},k}^{\langle r \rangle} = \left[Y_{b_1}^{\langle r \rangle}[k], Y_{b_1}^{\langle r \rangle *}[-k], Y_{b_2}^{\langle r \rangle *}[k], Y_{b_2}^{\langle r \rangle}[-k]\right]^T,$$

$$\tilde{\boldsymbol{N}}_{\mathrm{STC},k}^{\langle r \rangle} = \left[\tilde{N}_{b_1}^{\langle r \rangle}[k], \tilde{N}_{b_1}^{\langle r \rangle *}[-k], \tilde{N}_{b_2}^{\langle r \rangle *}[k], \tilde{N}_{b_2}^{\langle r \rangle *}[-k]\right]^T$$

and $\boldsymbol{H}_{\mathrm{STC},k}^{\langle r \rangle}$ is constructed by $\boldsymbol{H}_{\mathrm{STC},k}$, whose components are extended with an Rx index r.

Now, we consider the case of 2×2 MIMO SM, where two parallel data streams, $S^{(1)}[k]$ and $S^{(2)}[k]$, are transmitted from the two Tx antennas, respectively. According to (3.35), the following matrix equation can be obtained:

$$\boldsymbol{Y}_{\mathrm{SM},k} = \begin{bmatrix} \boldsymbol{H}_{\mathrm{SM},k}^{\langle 1 \rangle} \\ \boldsymbol{H}_{\mathrm{SM},k}^{\langle 2 \rangle} \end{bmatrix} \boldsymbol{S}_{\mathrm{SM},k} + \tilde{\boldsymbol{N}}'_k, \tag{3.41}$$

where

$$\boldsymbol{Y}_{\mathrm{SM},k} = \left[Y^{\langle 1 \rangle}[k], Y^{\langle 1 \rangle *}[-k], Y^{\langle 2 \rangle}[k], Y^{\langle 2 \rangle *}[-k]\right]^T,$$

$$\boldsymbol{S}_{\mathrm{SM},k} = \left[S^{(1)}[k], S^{(1)*}[-k], S^{(2)}[k], S^{(2)*}[-k]\right]^T$$

and

$$\boldsymbol{H}_{\mathrm{SM},k}^{\langle r \rangle} = \begin{bmatrix} H_{\mathrm{D}}^{\langle r,1 \rangle}[k] & H_{\mathrm{I}}^{\langle r,1 \rangle}[k] & H_{\mathrm{D}}^{\langle r,2 \rangle}[k] & H_{\mathrm{I}}^{\langle r,2 \rangle}[k] \\ H_{\mathrm{I}}^{\langle r,1 \rangle *}[-k] & H_{\mathrm{D}}^{\langle r,1 \rangle *}[-k] & H_{\mathrm{I}}^{\langle r,2 \rangle *}[-k] & H_{\mathrm{D}}^{\langle r,2 \rangle *}[-k] \end{bmatrix}.$$

Based on (3.36), (3.38), (3.39), (3.40) and (3.41), the transmitted data symbols can be detected e.g. with ZF or MMSE equalization. In the SM case, more advanced equalization

techniques can be applied e.g. V-BLAST [143].

3.4.4 Preamble Design Rules for Joint Channel and Frequency-Selective I/Q-Imbalance Estimation

The design rules presented in this section is based on the a similar principle as those described in [125, 126, 127]. However, we have included practical considerations.

3.4.4.1 Maximum Likelihood Estimation (MLE)

Let us consider the general case of using B OFDM symbols as preamble. Since the joint estimation scheme is the same for all Rx antennas, the Rx index will be omitted in our analysis. By extending Eq. (3.33) with an OFDM symbol index b, we can write the received B OFDM symbols in the following matrix form

$$\boldsymbol{y} = \boldsymbol{\Gamma}\boldsymbol{h} + \tilde{\boldsymbol{\eta}}, \tag{3.42}$$

with the following definitions

$$\begin{aligned}
\boldsymbol{y} &:= \left[\boldsymbol{y}_1^T, \ldots, \boldsymbol{y}_B^T\right]^T, \\
&\quad \text{with } \boldsymbol{y}_b := \left[y_b[0], \ldots, y_b[N-1]\right]^T, \\
\boldsymbol{h} &:= \left[\boldsymbol{h}_{\mathrm{D}}^{(1)^T}, \boldsymbol{h}_{\mathrm{I}}^{(1)^T}, \ldots, \boldsymbol{h}_{\mathrm{D}}^{(N_T)^T}, \boldsymbol{h}_{\mathrm{I}}^{(N_T)^T}\right]^T, \\
&\quad \text{with } \boldsymbol{h}_{\mathrm{D;I}}^{(i)} := \left[h_{\mathrm{D;I}}^{(i)}[0], \ldots, h_{\mathrm{D;I}}^{(i)}[L-1]\right]^T, \\
\tilde{\boldsymbol{\eta}} &:= \left[\tilde{\eta}_1^T, \ldots, \tilde{\eta}_B^T\right]^T, \\
&\quad \text{with } \tilde{\boldsymbol{\eta}}_b := \left[\tilde{\eta}_b[0], \ldots, \tilde{\eta}_b[N-1]\right]^T,
\end{aligned} \tag{3.43}$$

$$\boldsymbol{\Gamma} := \begin{bmatrix} \boldsymbol{\Gamma}_1^{(1)} & \boldsymbol{\Gamma}_1^{(1)*} & \cdots & \boldsymbol{\Gamma}_1^{(N_T)} & \boldsymbol{\Gamma}_1^{(N_T)*} \\ \vdots & \vdots & \ddots & \vdots & \vdots \\ \boldsymbol{\Gamma}_B^{(1)} & \boldsymbol{\Gamma}_B^{(1)*} & \cdots & \boldsymbol{\Gamma}_B^{(N_T)} & \boldsymbol{\Gamma}_B^{(N_T)*} \end{bmatrix}, \tag{3.44}$$

$$\boldsymbol{\Gamma}_b^{(i)} := \begin{bmatrix} s_b^{(i)}[0] & s_b^{(i)}[N-1] & \cdots & s_b^{(i)}[N-L+1] \\ s_b^{(i)}[1] & s_b^{(i)}[0] & \cdots & s_b^{(i)}[N-L+2] \\ \vdots & \vdots & \ddots & \vdots \\ s_b^{(i)}[N-1] & s_b^{(i)}[N-2] & \cdots & s_b^{(i)}[N-L] \end{bmatrix}. \tag{3.45}$$

Note that the $N \times L$ matrix $\boldsymbol{\Gamma}_b^{(i)}$ contains circularly shifted versions of the column vector $\boldsymbol{s}_b^{(i)} := \left[s_b^{(i)}[0], \ldots, s_b^{(i)}[N-1]\right]^T$. Moreover, we assume that $\tilde{\eta}_b[n]$ is approximately white noise[1].

[1] Due to the filtering of the Rx LPFs, $\tilde{\eta}_b[n]$ is not exactly white. However, the FR of practical Rx LPFs is relatively flat within the signal bandwidth. Thus, the deviation of $\tilde{\eta}[n]$ from white noise is generally negligible

According to [140, 141], the MLE of $\boldsymbol{h}$ is obtained by[1].

$$\hat{\boldsymbol{h}} = \left(\boldsymbol{\Gamma}^H \boldsymbol{\Gamma}\right)^{-1} \boldsymbol{\Gamma}^H \boldsymbol{y}. \tag{3.46}$$

3.4.4.2 Cramer-Rao Lower Bound (CRLB)

According to [142, 144], the MLE in (3.46) attains the CRLB (of MSE)

$$CRLB = \frac{1}{N_T} \mathrm{Tr}\left(\sigma_\eta^2 \left(\boldsymbol{\Gamma}^H \boldsymbol{\Gamma}\right)^{-1}\right) \tag{3.47}$$

with $\sigma_\eta^2 = E\left\{\left|\tilde{\eta}[n]\right|^2\right\}$. Assuming constant Tx power for all Tx antennas, i.e.

$$P_s = \frac{1}{N} \sum_{n=0}^{N-1} \left|s_b^{(i)}[n]\right|^2, \forall i, b,$$

the CRLB has the minimum value (see [127, 141, 144, 145])

$$\breve{CRLB} = \frac{2L\sigma_\eta^2}{BNP_s}, \tag{3.48}$$

when

$$\boldsymbol{\Gamma}^H \boldsymbol{\Gamma} = BNP_s \boldsymbol{I}_{2N_T L}. \tag{3.49}$$

3.4.4.3 Optimal Preamble Design Rules

The condition in (3.49) yields the following optimal preamble design rules:

1. $\sum_{b=1}^{B} {\boldsymbol{\Gamma}_b^{(i)}}^H \boldsymbol{\Gamma}_b^{(i)} = BNP_s \boldsymbol{I}_L, \forall i$. This condition corresponds to the separability of different channel taps within each individual $\boldsymbol{h}_{\mathrm{D;I}}^{(i)}$ and is called "white noise optimality" in [125, 126, 127];

2. $\sum_{b=1}^{B} {\boldsymbol{\Gamma}_b^{(i_0)}}^H \boldsymbol{\Gamma}_b^{(i_1)} = \boldsymbol{0}_L, \forall i_0 \neq i_1$. This condition corresponds to the separability of the channels of different Tx antennas, i.e. $\boldsymbol{h}_{\mathrm{D;I}}^{(i_0)}$ and $\boldsymbol{h}_{\mathrm{D;I}}^{(i_1)}, \forall i_0 \neq i_1$;

3. $\sum_{b=1}^{B} {\boldsymbol{\Gamma}_b^{(i_0)}}^H \boldsymbol{\Gamma}_b^{(i_1)*} = \boldsymbol{0}_L, \forall i_0, i_1$. This condition corresponds to the separability between each direct channel and each image channel, i.e. between $\boldsymbol{h}_{\mathrm{D}}^{(i_0)}$ and $\boldsymbol{h}_{\mathrm{I}}^{(i_1)}, \forall i_0, i_1$;

4. $BN \geq 2N_T L$, so that $\boldsymbol{\Gamma}^H \boldsymbol{\Gamma}$ has full rank[2]. This implies that the preamble can be applied to systems with $N_T \leq \left\lfloor \frac{BN}{2L} \right\rfloor$ Tx antennas.

(see also [125, 126, 127]).

[1] This MLE estimator is only used for the derivation of the preamble design rules. Actually, this estimator requires very high computational complexity. In the following, we will present simplified and improved estimators for each proposed preamble design.

[2] Assuming the rules 1),2),3) are fulfilled.

Note that both design rules 2) and 3) are called "zero cross channel interference conditions" in [125, 126, 127].

3.4.4.4 Practical Considerations

Following the way of analysis in [141], we found out that rule 1) requires the preamble power to be evenly distributed (averaged across B OFDM symbols) to cyclically equidistant subcarriers with a distance $0 \leq d \leq \left\lfloor \frac{N}{L} \right\rfloor$. This requirement can be expressed as

$$\frac{1}{B}\sum_{b=1}^{B}\left|S_b^{(i)}[k]\right|^2 = \begin{cases} A, & k = md + k_0,\ \forall m = 0,\ldots,L' \\ & \forall -\frac{N}{2} \leq k_0 \leq -\frac{N}{2} + d - 1 \\ 0, & \text{otherwise} \end{cases} \tag{3.50}$$

for all i, where $A = \frac{N^2 P_s}{L'} > 0$ and $L' = \frac{N}{d}$, $L' \in \mathbb{N}$.

In practical OFDM systems, NULL subcarriers are usually reserved for GB construction[1]. Considering that at least L pilot subcarriers are required for the estimation of a single channel IR of length L[2], rule 1) can not be fulfilled when $N_0 > \frac{N}{L}$. In this case, only partially equidistant subcarriers can be allocated [146]. As a result, the minimum CRLB can not be achieved with the MLE (3.46)[3]. Fortunately, as we will show, the degradation is relatively small with the proposed improved estimators.

3.4.5 Preamble with Time Domain Separation (TDS)

3.4.5.1 Preamble Design

This design just requires one OFDM symbol as preamble. For simplicity, we first consider the case without NULL subcarriers (GB- and DC subcarriers). The preamble for the 1st Tx antenna is constructed to be a length-N preamble sequence, $s[n]$, with its DFT satisfying

$$|S[k]| = 1, \forall k \quad \text{and} \quad S[k] = e^{jk\pi} S^*[-k], \forall k. \tag{3.51}$$

The first property implies perfect PACF, which fulfills the first design rule. Furthermore, these two properties correspond to the optimality conditions in [79], which fulfill the second design rule. Since a sequence with perfect PACF is orthogonal to all circularly shifted versions of itself, we can assign $s[((n-n_0))_N]$ to the 2nd Tx antenna with $L \leq n_0 \leq \frac{N}{2} - L$, so that the third design rule is fulfilled. Preambles for further Tx antennas can be constructed following the same principle.

In the case with NULL subcarriers, we have to set $|S[k]| = 0, \forall k \notin \mathcal{I}_D$ and the design rules

[1] Corresponds to the 1st case in Sec. 3.3.4.

[2] This can also be derived from $\sum_{b=1}^{B} \mathbf{\Gamma}_b^{(i)H} \mathbf{\Gamma}_b^{(i)} = BNP_s \boldsymbol{I}_L, \forall i$.

[3] In this case, the schemes in [125, 126, 127] will also suffer from degradation

are not perfectly fulfilled. As mentioned, we will compensate this imperfectness with a proper estimation scheme.

Finally, for preamble designs, the CF (of the corresponding analog signal) is also a crucial factor. If the preamble CF is much lower than the CF of the communication signals, "preamble boosting" is allowed [41] to enhance estimation performance. By adapting proper phasing schemes e.g. [147] on $S[k], \forall k = 1, \ldots, \frac{N_D}{2}$, low preamble CF can be achieved.

3.4.5.2 Estimation Scheme

Let the preambles $s[n]$ and $s[((n-n_0))_N]$ be transmitted from the 1st and 2nd Tx antennas, respectively. According to (3.35), the received frequency domain OFDM symbol is:

$$Y[k] = \left(H_{\mathrm{D}}^{(1)}[k] + H_{\mathrm{D}}^{(2)}[k]e^{j\frac{2\pi k n_0}{N}}\right) S[k] + \left(H_{\mathrm{I}}^{(1)}[k] + H_{\mathrm{I}}^{(2)}[k]e^{j\frac{2\pi k n_0}{N}}\right) S^*[-k] + \tilde{N}[k]. \quad (3.52)$$

Afterwards, we multiply $Y[k]$ by $S^*[k]$. With $R[k] := S^*[k]Y[k]$ and $S^*[k]S^*[-k] = e^{jk\pi}\left|S[k]\right|^2$, we have:

$$R[k] = \left(H_{\mathrm{D}}^{(1)}[k] + H_{\mathrm{D}}^{(2)}[k]e^{j\frac{2\pi k n_0}{N}}\right) \left|S[k]\right|^2 + \left(H_{\mathrm{I}}^{(1)}[k] + H_{\mathrm{I}}^{(2)}[k]e^{j\frac{2\pi k n_0}{N}}\right) e^{jk\pi}\left|S[k]\right|^2 + \breve{N}[k], \quad (3.53)$$

where $\breve{N}[k] = S^*[k]\tilde{N}[k]$. In the case without NULL subcarriers, $\left|S[k]\right|^2 = 1, \forall k$. After performing the IDFT $\gamma[n] := \mathcal{F}_N^{-1}\{R[k]\}$, we obtain:

$$\gamma[n] = h_{\mathrm{D}}^{(1)}[n] + h_{\mathrm{D}}^{(2)}[((n-n_0))_N] + h_{\mathrm{I}}^{(1)}[((n-\frac{N}{2}))_N] + h_{\mathrm{I}}^{(2)}[((n-\frac{N}{2}-n_0))_N] + \breve{\eta}[n] \quad (3.54)$$

with $\breve{\eta}[n]$ denoting the IDFT of $\breve{N}[k]$. Fig. 3.23 illustrates $\gamma[n]$. Note that with practical I/Q-imbalance parameters, $\left|h_{\mathrm{I}}^{(i)}\right|, \forall i$ is relatively small. As shown, the individual length-L IR can be easily separated in time domain and then transformed back to frequency domain. This is actually the MLE which minimizes noise influence by exploiting the channel length information.

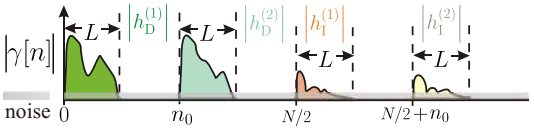

Figure 3.23: Illustration of $\gamma[n]$

However, in the presence of NULL subcarriers, we have $|S[k]| = 1, \forall k \in \mathcal{I}_D$ and $|S[k]| = 0, \forall k \notin \mathcal{I}_D$, which can be regarded as a window function. We define $W[k] := \left|S[k]\right|^2$, whose N-point IDFT is:

$$w[n] = \frac{1}{N}\left[\frac{\sin\left(\frac{\pi n(N-N_0)}{N}\right)}{\sin\left(\frac{\pi n}{N}\right)} - 1\right]. \quad (3.55)$$

From (3.53), the IDFT of $R[k]$ becomes:

$$\begin{aligned}\gamma'[n] &= \Big(h_{\mathrm{D}}^{(1)}[n] + h_{\mathrm{D}}^{(2)}[((n-n_0))_N] + h_{\mathrm{I}}^{(1)}[((n-\frac{N}{2}))_N] \\ &\quad + h_{\mathrm{I}}^{(2)}[((n-\frac{N}{2}-n_0))_N] + \breve{\eta}[n]\Big) \circledast_N w[n] \\ &= \gamma[n] \circledast_N w[n].\end{aligned} \tag{3.56}$$

The circular convolution in (3.56) results in interference between different IR taps and between the individual IRs, which will increase estimation error. To solve this problem, we first rewrite Eq. (3.56) in matrix notation:

$$\boldsymbol{\gamma}' = \boldsymbol{w}_{(:,\mathcal{L})}\boldsymbol{h} + \boldsymbol{\eta}', \tag{3.57}$$

where

$$\begin{aligned}\boldsymbol{\gamma}' &:= [\gamma'[0], \ldots, \gamma'[N-1]]^T, \\ \boldsymbol{h} &:= \Big[h_{\mathrm{D}}^{(1)}[0], \ldots, h_{\mathrm{D}}^{(1)}[L-1], h_{\mathrm{D}}^{(2)}[0], \ldots, h_{\mathrm{D}}^{(2)}[L-1], h_{\mathrm{I}}^{(1)}[0], \ldots, \\ &\quad h_{\mathrm{I}}^{(1)}[L-1], h_{\mathrm{I}}^{(2)}[0], \ldots, h_{\mathrm{I}}^{(2)}[L-1]\Big]^T,\end{aligned} \tag{3.58}$$

and $\boldsymbol{w}$ is an $N \times N$ convolution matrix with its i,j^{th} element $(\boldsymbol{w})_{i,j} = w[((i-j))_N]$. Moreover, the noise term is $\boldsymbol{\eta}' = [\eta'[0], \ldots, \eta'[N-1]]$ with $\eta'[n] = \breve{\eta}[n] \circledast_N w[n]$. The index set $\mathcal{L}$ is

$$\left\{0, \ldots, L-1, n_0, \ldots, n_0+L-1, \frac{N}{2}, \ldots, \frac{N}{2}+L-1, \frac{N}{2}+n_0, \ldots, \frac{N}{2}+n_0+L-1\right\}.$$

Considering that the power of $\gamma'[n]$ is concentrated in the samples with indexes in $\mathcal{L}$, we can apply the following two estimators for $\boldsymbol{h}$:

1. MLE (see also [41]):
$$\hat{\boldsymbol{h}} = \left(\boldsymbol{w}_{(\mathcal{L},\mathcal{L})}\right)^{-1} \boldsymbol{\gamma}'_{(\mathcal{L},:)}. \tag{3.59}$$

2. LMMSE:
$$\hat{\boldsymbol{h}} = \underbrace{\left(\boldsymbol{w}_{(\mathcal{L},\mathcal{L})} + \frac{2N_T L}{\rho}\boldsymbol{I}_{2N_T L}\right)^{-1}}_{\mathfrak{w}} \boldsymbol{\gamma}'_{(\mathcal{L},:)}, \tag{3.60}$$

   where ρ is the Rx SNR at each Rx antenna.

The condition number of $\boldsymbol{w}_{(\mathcal{L},\mathcal{L})}$ depends on N, L and N_0. Generally, the LMMSE is more robust against ill-conditioned $\boldsymbol{w}_{(\mathcal{L},\mathcal{L})}$. Note that for the MLE in (3.59), $\left(\boldsymbol{w}_{(\mathcal{L},\mathcal{L})}\right)^{-1}$ can be pre-computed from the system parameters and stored in the Rx device. Moreover, it has only real valued elements. Thus, the computational complexity is relaxed. For the LMMSE in (3.60), if $\mathfrak{w}$ is recalculated for each signal frame (due to an updated ρ value), the computational

complexity will be much higher. However, in practice, a fixed ρ can be assumed and used for the calculation of $\mathfrak{w}$. With a properly chosen fixed value, this assumption has only negligible influence on the estimation quality[1]. In this way, the LMMSE has the same computational complexity as the MLE.

The desired coefficients $H_{\mathrm{D;I}}^{\langle r,i\rangle}[k]$ can be estimated by extracting the individual IRs from $\hat{\boldsymbol{h}}$ and transform them back to frequency domain:

$$\hat{H}_{\mathrm{D;I}}^{(i)}[k] = \sum_{n=0}^{L-1} \hat{h}_{\mathrm{D;I}}^{(i)}[n] e^{-j\frac{2\pi kn}{N}}, \forall k \in \mathfrak{I}_D. \tag{3.61}$$

Generally, this estimation scheme requires $4(N - N_0 - 1) + 8N_T^2L^2 + 2(2N_T + 1)N\log_2 N$ real multiplications (MULs), where $4N\log_2 N$ real MULs are required for IDFT/DFT. However, when there are no NULL subcarriers reserved[2], the deconvolutions in (3.59) and (3.60) can be omitted. The required number of real MULs reduces to about $4(N - N_0 - 1) + 2(2N_T + 1)N\log_2 N$, which is relatively low.

Finally, this scheme can be regarded as the extension of the first one in [41] to include the I/Q-imbalance effect. This preamble can also be regarded as the MIMO extension of that in [79] with improved estimation scheme to cope with the GB problem.

3.4.6 Preamble with Frequency Domain Separation (FDS)

3.4.6.1 Preamble Design

3.4.6.1.1 Preamble Construction

This preamble is constructed in frequency domain and requires also just one OFDM symbol. First, each Tx antenna (i) is assigned a subcarrier set $\mathfrak{I}_i$ with $|\mathfrak{I}_i| = L', \forall i$. The preamble of each Tx antenna should fulfill:

$$\left|S^{(i)}[k]\right| = \begin{cases} 1, & k \in \mathfrak{I}_i \\ 0, & \text{otherwise} \end{cases}. \tag{3.62}$$

Furthermore, the subcarrier sets $\mathfrak{I}_i, \forall i$ should have the following properties:

1. $L' \geq L$, so that this subcarrier set can be used to estimate an IR with L taps (e.g. $h_{\mathrm{D}}^{(i)}[n]$).
2. $\mathfrak{I}_i, \forall i$ is an equidistant subcarrier set, so that the 1st design rule is fulfilled[3].
3. $\mathfrak{I}_{i_0} \cap \mathfrak{I}_{i_1} = \emptyset, \forall i_0 \neq i_1$, so that the 2nd design rule is fulfilled.
4. $\mathfrak{I}_{i_0} \cap (-\mathfrak{I}_{i_1}) = \emptyset, \forall i_0, i_1$, so that the 3rd design rule is fulfilled.

[1] Within the realistic SNR range.
[2] Corresponding to the second case of Sec. 3.3.4.
[3] In the ideal case, $\mathfrak{I}_i$ should be a circularly equidistant subcarrier set. However, in the practice, especially in the presence of large GBs, $\mathfrak{I}_i$ can also be a partially equi-distant subcarrier set (see Sec. 3.4.4.4).

Considering the properties above, this preamble can only be applied to the cases with $N_T \leq \left\lfloor \frac{N_D}{2L'} \right\rfloor$ Tx antennas.

To obtain low CF preambles, the non-zero subcarriers of $S^{(i)}[k]$ of each Tx antenna can be assigned values of a length-L' CAZAC sequence $T^{(i)}(\kappa)$ with $\left|T^{(i)}(\kappa)\right| = 1$, i.e. $S^{(i)}[(\mathcal{I}_i)_\kappa] = T^{(i)}(\kappa), \forall \kappa = 0, \ldots, L'-1$. In this way, the analog signal of the preamble possesses a CF as low as that of the analog signal of the original CAZAC sequence [1].

3.4.6.1.2 Subcarrier Index Selection

Here, we present a subcarrier index selection scheme for $\mathcal{I}_i, \forall i$, so that the desired properties above can be matched.

First, the distance d is computed as $d = \left\lfloor \frac{N_D}{L'} \right\rfloor - \Delta d$, where the integer $\Delta d \geq 0$ is an adjustment factor. Increasing Δd leads to increase of the number of subcarriers used for estimation. This will result in an increase in computational complexity. Note that $d \geq 2N_T$ should hold.

For each Tx, we choose two equidistant positive index sets $\mathcal{I}_{i,1} = \left\{k_{i,1} : d : \frac{N_D}{2}\right\}$ and $\mathcal{I}_{i,2} = \left\{k_{i,2} : d : \frac{N_D}{2}\right\}$, where $k_{i,1} \neq k_{i,2}, \forall i$; $k_{i_0,1;2} \neq k_{i_1,1;2}, \forall i_0 \neq i_1$ and $1 \leq k_{i,1;2} \leq d, \forall i$. The desired index set is obtained by $\mathcal{I}_i = (-\mathcal{I}_{i,2}) \cup \mathcal{I}_{i,1}$. If possible, $k_{i,1}$ and $k_{i,2}$ should be chosen to meet $k_{i,1} + k_{i,2} = d$ so that the equi-distance requirement is perfectly fulfilled. However, if $d = 2N_T$, one of the index sets can not suffice $k_{i,1} + k_{i,2} = d$. Fortunately, this has only negligible influence on the CF and the estimation performance.

In the proposed estimation schemes (Sec. 3.4.6.2), the noise influence on estimation is mainly suppressed by exploiting the correlation between neighboring subcarriers. Due to the GB (especially when the GB size exceeds the distance between the pilot subcarriers), the edge subcarriers (the subcarriers that are very close to the NULL subcarrers) may have less neighboring subcarriers within the allocated pilot subcarrers set. In other words, less correlation can be exploited for the edge subcarriers. As a result, the estimation error on the edge subcarriers may be larger than the other subcarriers. To avoid this problem, the subcarriers closest to the NULL subcarriers may be allocated to the preambles. Thus, if the equi-distant subcarrier sets do not include these subcarriers, they should be additionally included. The inclusion should be properly done, so that the desired properties in Sec. 3.4.6.1.1 are still matched. Although the inclusion of such subcarriers could slightly impair the equi-distance requirement, we will show in Sec. 3.4.8 that both performance enhancement and complexity reduction can be achieved.

Tab. 3.1 illustrates the proposed subcarrier selection with- and without additional edge subcarriers. Note that with the parameters in Tab. 3.1, only one of the subcarrier sets can have additional edge subcarrier: Either $\mathcal{I}_1$ includes -117 or $\mathcal{I}_2$ includes 117.

[1] For a CAZAC sequence, the CF remains constant after DFT or IDFT. Assigning the values of a CAZAC sequence to partially equidistant subcarriers can be interpreted as a d-fold repetition, phase rotation (constant phase difference between neighboring samples) and fractional oversampling (due to GB reservation) of the IDFT of the original CAZAC sequence. All these operations have negligible effect on the CF. Note that not the CF of the discrete sequence but of the corresponding analog BB signal is used as criterion.

Table 3.1: Illustration of Subcarrier Index Selection, $N = 256, N_0 = 17, L = 32, N_T = 2, d = 6, k_{1,1} = 1, k_{1,2} = 5, k_{2,1} = 2, k_{2,2} = 4$

Parameters	**Index Sets**
Without additional edge subcarriers	$\mathcal{I}_1 = \{-115, \ldots, -11, -5, 1, 7, \ldots, 119\}$ $\mathcal{I}_2 = \{-118, \ldots, -10, -4, 2, 8, \ldots, 116\}$
With additional edge subcarriers	$\mathcal{I}_1 = \{-117, -115, \ldots, -11, -5, 1, 7, \ldots, 119\}$ $\mathcal{I}_2 = \{-118, \ldots, -10, -4, 2, 8, \ldots, 116\}$

3.4.6.2 Estimation Scheme

From (3.35) and the properties in Sec. 3.4.6.1.1, we can express the received OFDM symbol as

$$Y[k] = \begin{cases} S^{(i)}[k] H_{\mathrm{D}}^{(i)}[k] + \tilde{N}[k], & k \in \mathcal{I}_i \\ S^{(i)*}[-k] H_{\mathrm{I}}^{(i)}[k] + \tilde{N}[k], & k \in -\mathcal{I}_i \end{cases}. \tag{3.63}$$

Eq. (3.63) can be rewritten into the following matrix notations:

$$\begin{aligned} \boldsymbol{Y}_{(\mathcal{I}_i,:)} &= \boldsymbol{T}^{(i)} \boldsymbol{F}_{(\mathcal{I}_i,\mathcal{L})} \boldsymbol{h}_{\mathrm{D}}^{(i)} + \tilde{\boldsymbol{N}}_{(\mathcal{I}_i,:)}, \\ \boldsymbol{Y}_{(-\mathcal{I}_i,:)} &= \acute{\boldsymbol{T}}^{(i)*} \boldsymbol{F}_{(-\mathcal{I}_i,\mathcal{L})} \boldsymbol{h}_{\mathrm{I}}^{(i)} + \tilde{\boldsymbol{N}}_{(-\mathcal{I}_i,:)}, \end{aligned} \tag{3.64}$$

where

$$\begin{aligned} \boldsymbol{Y} &= [Y(-N_D/2), \ldots, Y(N_D/2)]^T, \\ \boldsymbol{T}^{(i)} &= \mathrm{diag}\left\{ \left[T^{(i)}[0], \ldots, T^{(i)}[L'-1] \right] \right\}, \\ \acute{\boldsymbol{T}}^{(i)} &= \mathrm{diag}\left\{ \left[T^{(i)}[L'-1], \ldots, T^{(i)}[0] \right] \right\}, \\ \mathcal{L} &= \{0, \ldots, L-1\}, \\ \boldsymbol{h}_{\mathrm{D;I}}^{(i)} &= \left[h_{\mathrm{D;I}}^{(i)}[0], \ldots, h_{\mathrm{D;I}}^{(i)}[L-1] \right], \\ \tilde{\boldsymbol{N}} &= \left[\tilde{N}(-N_D/2), \ldots, \tilde{N}(N_D/2) \right]^T. \end{aligned} \tag{3.65}$$

Two different estimators of $\boldsymbol{h}_{\mathrm{D;I}}^{(i)}$ can be obtained:

1. The MLE:

$$\begin{aligned} \hat{\boldsymbol{h}}_{\mathrm{D}}^{(i)} &= \mathfrak{T}_{\mathrm{D}}^{(i)} \boldsymbol{T}^{(i)*} \boldsymbol{Y}_{(\mathcal{I}_i,:)}, \\ \hat{\boldsymbol{h}}_{\mathrm{I}}^{(i)} &= \mathfrak{T}_{\mathrm{I}}^{(i)} \acute{\boldsymbol{T}}^{(i)} \boldsymbol{Y}_{(-\mathcal{I}_i,:)}, \end{aligned} \tag{3.66}$$

with

$$\begin{aligned} \mathfrak{T}_{\mathrm{D}}^{(i)} &:= \left(\boldsymbol{F}_{(\mathcal{I}_i,\mathcal{L})} \right)^{\dagger}, \\ \mathfrak{T}_{\mathrm{I}}^{(i)} &:= \left(\boldsymbol{F}_{(-\mathcal{I}_i,\mathcal{L})} \right)^{\dagger}. \end{aligned} \tag{3.67}$$

2. The LMMSE:

$$\begin{aligned}\hat{\boldsymbol{h}}_{\mathrm{D}}^{(i)} &= \mathfrak{Q}_{\mathrm{D}}^{(i)}\boldsymbol{T}^{(i)*}\boldsymbol{Y}_{(\mathcal{I}_i,:)},\\ \hat{\boldsymbol{h}}_{\mathrm{I}}^{(i)} &= \mathfrak{Q}_{\mathrm{I}}^{(i)}\acute{\boldsymbol{T}}^{(i)*}\boldsymbol{Y}_{(-\mathcal{I}_i,:)}\end{aligned} \tag{3.68}$$

with

$$\begin{aligned}\mathfrak{Q}_{\mathrm{D}}^{(i)} &:= \left(\boldsymbol{F}_{(\mathcal{I}_i,\mathcal{L})}^H\boldsymbol{F}_{(\mathcal{I}_i,\mathcal{L})} + \frac{L}{\rho}\boldsymbol{I}_L\right)^{-1}\boldsymbol{F}_{(\mathcal{I}_i,\mathcal{L})}^H,\\ \mathfrak{Q}_{\mathrm{I}}^{(i)} &:= \left(\boldsymbol{F}_{(-\mathcal{I}_i,\mathcal{L})}^H\boldsymbol{F}_{(-\mathcal{I}_i,\mathcal{L})} + \frac{L}{\rho}\boldsymbol{I}_L\right)^{-1}\boldsymbol{F}_{(-\mathcal{I}_i,\mathcal{L})}^H.\end{aligned} \tag{3.69}$$

Note that the condition numbers of $\boldsymbol{F}_{(\mathcal{I}_i,\mathcal{L})}$ and $\boldsymbol{F}_{(-\mathcal{I}_i,\mathcal{L})}$ depend on the parameters N, N_0, L and L'. Similar to the TDS scheme, the LMMSE is more robust against ill-conditioned problem of $\boldsymbol{F}_{(\mathcal{I}_i,\mathcal{L})}$ and $\boldsymbol{F}_{(-\mathcal{I}_i,\mathcal{L})}$ than the MLE. Afterwards, the desired frequency domain coefficients can be obtained with (3.61).

Similar to the TDS-based scheme, the LMMSE is more robust against ill-conditioned problem of $\boldsymbol{F}_{(\mathcal{I}_i,\mathcal{L})}$. Moreover, the matrices $\mathfrak{T}_{\mathrm{D}}^{(i)}\boldsymbol{Y}_{(\mathcal{I}_i,:)}$ and $\mathfrak{T}_{\mathrm{I}}^{(i)}\acute{\boldsymbol{T}}^{(i)}$ in the MLE as well as $\mathfrak{Q}_{\mathrm{D}}^{(i)}\boldsymbol{T}^{(i)*}$ and $\mathfrak{Q}_{\mathrm{I}}^{(i)}\acute{\boldsymbol{T}}^{(i)}$ in the LMMSE can be regarded as known and pre-computed (assuming that a fixed ρ is used for LMMSE). Based on the considerations above, this scheme requires $8N_TL'L + 4N_TN\log_2 N$ real MULs.

Finally, this preamble can be regarded as the extension of frequency domain sequence in [41] to include I/Q-imbalance effect. It can also be regarded as MIMO extension of [86] and is optimized for block fading channels.

3.4.7 Design and Application of a Multi-Functional Preamble

Although the TDS- and the FDS preambles only require one OFDM symbol as preamble, they can only be used for the estimation of I/Q-imbalance and the MIMO channel. Extra preamble may be needed for frame detection and time synchronization, increasing the preamble overhead. To further reduce the preamble overhead, we propose a new preamble, which is slightly longer than an OFDM symbol but can be used both for frame detection/time synchronization and joint MIMO channel and I/Q-imbalance estimation. In other words, this preamble is multi-functional.

3.4.7.1 Preamble Design

3.4.7.1.1 Preamble Structure

Instead of applying a single- or multiple OFDM symbols as preamble, we construct a preamble which consists of two OFDM symbol halves. The structure of the preamble is shown in Fig. 3.24,

with

$$\begin{aligned}\boldsymbol{s}_{b,\text{half}}^{(i)} &= \left[s_b^{(i)}[0],\ldots,s_b^{(i)}[\frac{N}{2}-1]\right],\forall b=1,2\\ \boldsymbol{s}_{b,\text{CP}}^{(i)} &= \left[s_b^{(i)}[N-L],\ldots,s_b^{(i)}[N-1]\right],\forall b=1,2,\end{aligned} \tag{3.70}$$

where $s_b^{(i)}[n],\forall n\in\mathcal{N},\forall b=1,2,\forall i$ are two different OFDM symbols. As will be shown, when all even subcarriers are nulled, all information of the OFDM symbol $s_b^{(i)}[n],\forall n\in\mathcal{N}$ is contained in $\boldsymbol{s}_{b,\text{half}}^{(i)}$[1]. Moreover, we restrict

$$s_2^{(i)}[n]=s_1^{(i)}[n]e^{j\phi},\forall n\in\mathcal{N}_1, \tag{3.71}$$

so that this preamble can be used for frame detection and time synchronization (e.g. applying the methods in [148, 149]). Under the restriction of (3.71), the OFDM symbols $s_b^{(i)}[n],\forall b=1,2$ are constructed according to the optimal design rules in Sec. 3.4.4, so that this preamble can be used for joint MIMO channel- and I/Q-imbalance estimation. Note that with such structure, the preamble length is just slightly over one OFDM symbol

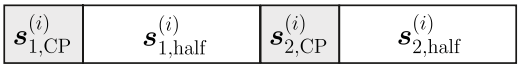

Figure 3.24: The structure of the multi-functional preamble

3.4.7.1.2 Subcarrier Allocation

Let $S_b^{(i)}[k],-\frac{N}{2}\le k\le\frac{N}{2}-1$ be the DFT of $s_b^{(i)}[n],\forall n\in\mathcal{N}$. As mentioned before, all even subcarriers are nulled. In this case, we have

$$s_b^{(i)}[n+\frac{N}{2}]=-s_b^{(i)}[n],\forall n\in\mathcal{N}_1, \tag{3.72}$$

which implies that all information of the OFDM symbol is contained in the first half of its time domain sequence. The proof for (3.72) is given in App. B.2. Note that (3.72) implies that $\boldsymbol{s}_{b,\text{CP}}^{(i)}=\left[-s_b^{(i)}[\frac{N}{2}-L],\ldots,-s_b^{(i)}[\frac{N}{2}-1]\right]$.

Let $\mathcal{I}_{\text{odd}}=\left\{-\frac{N}{2}+1:2:\frac{N}{2}-1\right\}$ be the index set of the odd subcarriers, while $\mathcal{I}_{\text{NULL}}$ is the index set of the NULL subcarriers for GB reservation. To fulfill the requirement in (3.71), the two OFDM symbols of the same Tx antenna should have the same active pilot subcarrier sets. To approximately fulfill the 1st design rule (see Sec. 3.4.4.4), we allocate partially equi-distant

[1]Generally, this is fulfilled when either the even- or the odd subcarriers are nulled. However, since the even subcarriers contains the DC subcarrier, which is already nulled, they are chosen instead of the odd subcarriers.

subcarriers to each Tx antenna with the following index set

$$\mathcal{I}_i = \left\{ k_0^{(i)} : d : k_0^{(i)} + (L'-1)d \right\}, \forall i, \tag{3.73}$$

with $-\frac{N_D}{2} + 1 \leq k_0^{(i)} \leq -\frac{N_D}{2} + d$ and $d \leq \left\lfloor \frac{N_D}{L} \right\rfloor$. Note that $|\mathcal{I}_i| = L'$ and $L' \geq L$[1]. Moreover, the following relation can be observed:

$$\begin{aligned} &\mathcal{I}_i \subset \mathcal{I}_{\text{odd}}, \forall i \\ &\mathcal{I}_i \cap \mathcal{I}_{\text{NULL}} = \emptyset, \forall i. \end{aligned} \tag{3.74}$$

To fulfill the 2nd design rule, we set $k_0^{(i_0)} \neq k_0^{(i_1)}, \forall i_0 \neq i_1$ so that

$$\mathcal{I}_{i_0} \cap \mathcal{I}_{i_1} = \emptyset, \forall i_0 \neq i_1. \tag{3.75}$$

To fulfill the 3rd design rule i.e. the separability between each direct channel and each image channel, the relation between $\mathcal{I}_{i_0}$ and $-\mathcal{I}_{i_1}, \forall i_0, i_1$ has to be investigated. With the subcarrier allocation in (3.73), there are generally three possible relations between $\mathcal{I}_{i_0}$ and $-\mathcal{I}_{i_1}, \forall i_0, i_1$, which are listed as follows:

1. $\mathcal{I}_{i_0} = -\mathcal{I}_{i_1}$, for a certain Tx pair (i_0, i_1) with $i_0 \neq i_1$. Considering (3.75), we have $\pm\mathcal{I}_{i_0;i_1} \cap \pm\mathcal{I}_{i_2} = \emptyset, \pm\mathcal{I}_{i_0;i_1} \cap \mp\mathcal{I}_{i_2} = \emptyset \forall i_2 \neq i_0$ and $i_2 \neq i_1$.
2. $\mathcal{I}_i = -\mathcal{I}_i$ for a certain i. Considering (3.75), we have $\pm\mathcal{I}_i \cap \pm\mathcal{I}_{i'} = \emptyset, \pm\mathcal{I}_i \cap \mp\mathcal{I}_{i'} = \emptyset, \forall i' \neq i$.
3. For a certain Tx i_0, $\mathcal{I}_{i_0} \cap -\mathcal{I}_{i_0} = \emptyset, -\mathcal{I}_{i_0} \cap \mathcal{I}_{i_1} = \emptyset, \forall i_1 \neq i_0$. Considering (3.75), we have $\pm\mathcal{I}_{i_0} \cap \pm\mathcal{I}_{i_1} = \emptyset, \pm\mathcal{I}_{i_0} \cap \mp\mathcal{I}_{i_1} = \emptyset, \forall i_1 \neq i_0$.

Tab. 3.2 illustrates the above relations with several examples. As shown, depending on the design parameters, the selected subcarrier index sets may have one or more relations listed above. In Sec. 3.4.7.1.3 and 3.4.7.2.2, we will show that the 3rd design rule can be fulfilled by applying an adequate pilot symbol assignment scheme according to the relations above.

Similar to Sec. 3.4.6.1, certain edge subcarriers may be properly included to avoid large estimation error on the edge subcarriers. This inclusion should be properly done so that the requirements of case 1), 2) and 3) are still fulfilled.

3.4.7.1.3 Pilot Symbol Assignment

To achieve low CF, the allocated subcarriers for each antenna are assigned the values of a length-L' CAZAC sequence, $T_b^{(i)}[\kappa]$, with $\left|T_b^{(i)}[\kappa]\right| = 1, \forall \kappa = 0, \ldots, L'-1$. This assignment can be expressed as:

$$S_b^{(i)}[\mathcal{I}_i(\kappa)] = T_b^{(i)}[\kappa], \forall \kappa = 0, \ldots, L'-1, \forall i, b, \tag{3.76}$$

[1] This means that the proposed preamble can be applied to systems with $N_T \leq \frac{N_D}{2L}$ Tx antennas

Table 3.2: Illustration of Possible Relations Between $\mathcal{I}_{i_0}$ and $-\mathcal{I}_{i_1}, \forall i_0, i_1$, $N = 256, N_0 = 17$

Parameters	**Index Sets**	**Relations**
$N_T = 3$ $L = 32$ $d = 6$	$\mathcal{I}_1 = \{\ldots, -7, -1, 5, 11, \ldots\}$ $\mathcal{I}_2 = \{\ldots, -11, -5, 1, 7, \ldots\}$ $\mathcal{I}_3 = \{\ldots, -9, -3, 3, 9, \ldots\}$	1) $\mathcal{I}_1 = -\mathcal{I}_2$ 2) $\mathcal{I}_3 = -\mathcal{I}_3$ $\pm\mathcal{I}_{1;2} \cap \pm\mathcal{I}_3 = \emptyset$ $\pm\mathcal{I}_{1;2} \cap \mp\mathcal{I}_3 = \emptyset$
$N_T = 2$ $L = 32$ $d = 6$	$\mathcal{I}_1 = \{\ldots, -9, -3, 3, 9, \ldots\}$ $\mathcal{I}_2 = \{\ldots, -7, -1, 5, 11, \ldots\}$	2) $\mathcal{I}_1 = -\mathcal{I}_1$ 3) $\mathcal{I}_2 \cap -\mathcal{I}_2 = \emptyset$ $\pm\mathcal{I}_1 \cap \pm\mathcal{I}_2 = \emptyset$ $\pm\mathcal{I}_1 \cap \mp\mathcal{I}_2 = \emptyset$
$N_T = 2$ $L = 18$	$\mathcal{I}_1 = \{\ldots, -19, -7, 5, 17, \ldots\}$ $\mathcal{I}_2 = \{\ldots, -13, -1, 11, 23, \ldots\}$	3) $\mathcal{I}_{1;2} \cap -\mathcal{I}_{1;2} = \emptyset$ $\pm\mathcal{I}_1 \cap \pm\mathcal{I}_2 = \emptyset$ $\pm\mathcal{I}_1 \cap \mp\mathcal{I}_2 = \emptyset$

which implies

$$\left|S_b^{(i)}[k]\right| = \begin{cases} 1, & k \in \mathcal{I}_i \\ 0, & \text{otherwise} \end{cases}. \tag{3.77}$$

In this way, the analog signal of the preamble possesses a CF as low as that of the analog signal of the original CAZAC sequence (similar to the FDS design). Furthermore, to fulfill (3.71), we restrict:

$$T_2^{(i)}[\kappa] = T_1^{(i)}[\kappa] e^{j\phi}, \forall i, \kappa. \tag{3.78}$$

In Sec. 3.4.7.3, we will show how to adjust ϕ to fulfill the 3$^{\text{rd}}$ design rule.

3.4.7.1.4 Spatial Diversity for Time Synchronization

In [149], it was shown that by exploiting spatial diversity, the performance of time synchronization can be enhanced. Moreover, the preamble structure in (3.71) was also investigated in [149]. According to [149], the short sequences $\boldsymbol{s}_{b,\text{half}}^{(i)}$ between different Tx antennas should be shift-orthogonal to each other (with a maximum shift of L), so that spatial diversity can be exploited effectively. It can be proved that this requirement is fulfilled by the proposed preamble (see App. B.4). However, I/Q-imbalance was not investigated in [149]. When applying the correlation method in [149], the correlation peak power will be reduced due to I/Q-imbalance[1]. Fortunately, since the mirror interference usually has relatively low power, the degradation of the time synchronization performance is minor.

[1]Due to I/Q-imbalance, the received signal of the second short preamble will contain a term with a $e^{-j\phi}$ phase shift. Moreover, the correlation output will contain terms with $\boldsymbol{s}_{b,\text{half}}^{(i_0)}$ and $\boldsymbol{s}_{b,\text{half}}^{(i_1)*}, \forall i_0, i_1$, which are not always shift orthogonal to each other.

3.4.7.2 Estimation Scheme

First, the received preamble is extended to reconstruct the two OFDM symbols. Afterwards, LSE [1] is performed on the pilot subcarriers (both $\mathcal{I}_i$ and $-\mathcal{I}_i$). Finally, MLE or LMMSE of $H_{\mathrm{D;I}}^{\langle r,i\rangle}[k]$ can be obtained.

3.4.7.2.1 Extension of the Received Preamble

We first define

$$\begin{aligned}\bar{Y}_b[k] &:= \sum_{i=1}^{N_T}\left(S_b^{(i)}[k]H_{\mathrm{D}}^{(i)}[k] + S_b^{(i)*}[-k]H_{\mathrm{I}}^{(i)}[k]\right),\\ \bar{y}_b[n] &:= \mathcal{F}_N^{-1}\left\{\bar{Y}_b[k]\right\}, \forall n \in \mathcal{N},\end{aligned} \tag{3.79}$$

which is the received signal (after CP removal) without noise influence, when $s_b^{(i)}[n], n \in \mathcal{N}$ (the complete OFDM symbol) was transmitted. Based on (3.72)and (3.79), we can easily prove that (see App. B.5)

$$\bar{y}_b[n + \frac{N}{2}] = -\bar{y}_b[n], \forall n \in \mathcal{N}_1. \tag{3.80}$$

For the joint estimation, $\bar{Y}_b[k]$ is desired. However, from the received preamble, we only have the following signal which contains just a half of $\{\bar{y}_b[n], n \in \mathcal{N}\}$:

$$y_b[n] = \bar{y}_b[n] + \tilde{\eta}_b[n], n \in \mathcal{N}_1, \tag{3.81}$$

where $\tilde{\eta}_b[n]$ is the corresponding noise term. To reconstruct $\bar{Y}_b[k]$, $\{y_b[n], n \in \mathcal{N}_1\}$ can be extended to the following length-N sequence

$$y_b^E[n] = \begin{cases} y_b[n], & n \in \mathcal{N}_1 \\ -y_b[n - \frac{N}{2}], & n \in \mathcal{N}_2 \end{cases}. \tag{3.82}$$

Eq. (3.80), (3.81) and (3.82) yield the following relation:

$$y_b^E[n] = -y_b[n - \frac{N}{2}] = \bar{y}_b[n] - \tilde{\eta}_b[n - \frac{N}{2}], \forall n \in \mathcal{N}_2. \tag{3.83}$$

From (3.81), (3.82) and (3.83), we have

$$y_b^E[n] = \bar{y}_b[n] + \acute{\eta}_b[n], \forall n \in \mathcal{N} \tag{3.84}$$

[1] According to the definition in [139].

where $\acute{\eta}_b[n] = \tilde{\eta}_b[n], \forall n \in \mathcal{N}_1$ and $\acute{\eta}_b[n] = -\tilde{\eta}_b[n - \frac{N}{2}], \forall n \in \mathcal{N}_2$. Finally, the DFT of $y_b^E[n]$ is[1]

$$\begin{aligned} Y_b^E[k] &= \bar{Y}_b[k] + \acute{N}_b[k] \\ &= \sum_{i=1}^{N_T} \left(S_b^{(i)}[k] H_{\mathrm{D}}^{(i)}[k] + S_b^{(i)*}[-k] H_{\mathrm{I}}^{(i)}[k] \right) + \acute{N}_b[k], \end{aligned} \tag{3.85}$$

where $\acute{N}_b[k] = \mathcal{F}_N \{\acute{\eta}_b[n]\}$. Based on (3.85), the estimation of $H_{\mathrm{D;I}}^{(i)}[k], \forall k \in \mathcal{I}_{\mathrm{D}}$ can be carried out.

3.4.7.2.2 LSE of Coefficient Subsets

Now, we apply LSE to estimate the coefficient subsets $H_{\mathrm{D}}^{(i)}[k], \forall k \in \mathcal{I}_i$ and $H_{\mathrm{I}}^{(i)}[k], \forall k \in -\mathcal{I}_i$. The LSE is derived according to the subcarrier relations described in Sec. 3.4.7.1.2 as follows:

Case 1)

In case 1), $\mathcal{I}_{i_0} = -\mathcal{I}_{i_1}$ with $i_0 \neq i_1$. From (3.77) and (3.85), we obtain:

$$\begin{aligned} Y_b^E[k] &= S_b^{(i_0)}[k] H_{\mathrm{D}}^{(i_0)}[k] + S_b^{(i_1)*}[-k] H_{\mathrm{I}}^{(i_1)}[k] + \acute{N}_b[k], \ \forall k \in \mathcal{I}_{i_0} \text{ with } i_0 \neq i_1, \\ Y_b^E[k] &= S_b^{(i_1)}[k] H_{\mathrm{D}}^{(i_1)}[k] + S_b^{(i_0)*}[-k] H_{\mathrm{I}}^{(i_0)}[k] + \acute{N}_b[k], \ \forall k \in \mathcal{I}_{i_1} \text{ with } i_0 \neq i_1. \end{aligned} \tag{3.86}$$

Substituting $b = 1, 2$ into the first Eq. of (3.86), we can obtain the following matrix Eq. for $k \in \mathcal{I}_{i_0}$:

$$\underbrace{\begin{bmatrix} Y_1^E[k] \\ Y_2^E[k] \end{bmatrix}}_{\mathbb{Y}_k} = \underbrace{\begin{bmatrix} S_1^{(i_0)}[k] & S_1^{(i_1)*}[-k] \\ S_2^{(i_0)}[k] & S_2^{(i_1)*}[-k] \end{bmatrix}}_{\mathbb{S}_k} \underbrace{\begin{bmatrix} H_{\mathrm{D}}^{(i_0)}[k] \\ H_{\mathrm{I}}^{(i_1)}[k] \end{bmatrix}}_{\mathbb{H}_k} + \underbrace{\begin{bmatrix} \acute{N}_1[k] \\ \acute{N}_2[k] \end{bmatrix}}_{\acute{\mathbb{N}}_k}. \tag{3.87}$$

With (3.87), the LSE of $H_{\mathrm{D}}^{(i_0)}[k]$ and $H_{\mathrm{I}}^{(i_1)}[k], \forall k \in \mathcal{I}_{i_0}$ can be obtained by:

$$\check{\mathbb{H}}_k = (\mathbb{S}_k)^{-1} \mathbb{Y}_k + \acute{\mathbb{N}}_k. \tag{3.88}$$

With the second Eq. of (3.86), the LSE of $H_{\mathrm{D}}^{(i_1)}[k]$ and $H_{\mathrm{I}}^{(i_0)}[k], \forall k \in \mathcal{I}_{i_1}$ can be obtained in a similar way.

Case 2)

In case 2), $\mathcal{I}_i = -\mathcal{I}_i$. From (3.85), we obtain the following matrix equation for $k \in \mathcal{I}_i$:

$$\underbrace{\begin{bmatrix} Y_1^E[k] \\ Y_2^E[k] \end{bmatrix}}_{\mathbb{Y}_k} = \underbrace{\begin{bmatrix} S_1^{(i)}[k] & S_1^{(i)*}[-k] \\ S_2^{(i)}[k] & S_2^{(i)*}[-k] \end{bmatrix}}_{\mathbb{S}_k} \underbrace{\begin{bmatrix} H_{\mathrm{D}}^{(i)}[k] \\ H_{\mathrm{I}}^{(i)}[k] \end{bmatrix}}_{\mathbb{H}_k} + \underbrace{\begin{bmatrix} \acute{N}_1[k] \\ \acute{N}_2[k] \end{bmatrix}}_{\acute{\mathbb{N}}_k}. \tag{3.89}$$

[1] Actually, $\bar{Y}_b[k]$ can also be reconstructed from the $\frac{N}{2}$-point DFT of $y_b[n], n \in \mathcal{N}_1$, i.e. $\bar{Y}_b[2k+1] + \acute{N}_b[2k+1] = \mathcal{F}_{\frac{N}{2}} \left\{ y_b[n] e^{-j\frac{2\pi n}{N}} \right\} = \sum_{n=0}^{\frac{N}{2}-1} y_b[n] e^{-j\frac{2\pi n}{N}} e^{-j\frac{4\pi kn}{N}}, \forall -\frac{N}{4} \leq k \leq \frac{N}{4} - 1$. However, in practical implementation, this method will require extra multiplication (with $e^{-j\frac{2\pi n}{N}}$) and an extra DFT block of length-$\frac{N}{2}$. In contrast, the operations (3.83) requires negligible computation effort. Moreover, the output of (3.83) can be fed to the DFT block that is used for the OFDM data symbols. In this way, the computational complexity is kept low.

Thus, the LSE of $H_{\mathrm{D}}^{(i)}[k]$ and $H_{\mathrm{I}}^{(i)}[k], \forall k \in \mathcal{I}_i$ can be obtained with (3.88).

Case 3)

In case 3), $\mathcal{I}_{i_0} \cap (-\mathcal{I}_{i_0}) = \emptyset, (-\mathcal{I}_{i_0}) \cap \mathcal{I}_{i_1} = \emptyset, \forall i_1 \neq i_0$. From (3.77) and (3.85), we obtain for $k \in \mathcal{I}_{i_0}$:

$$\begin{aligned} Y_b^E[k] &= S_b^{(i_0)}[k] H_{\mathrm{D}}^{(i_0)}[k] + \acute{N}_b[k], \\ Y_b^E[-k] &= S_b^{(i_0)*}[k] H_{\mathrm{I}}^{(i_0)}[-k] + \acute{N}_b[-k], \end{aligned} \tag{3.90}$$

With (3.77), the LSE is simply:

$$\begin{aligned} \check{H}_{\mathrm{D}}^{(i_0)}[k] &= \frac{1}{2} \sum_{b=1}^{2} S_b^{(i_0)*}[k] Y_b^E[k], \forall k \in \mathcal{I}_{i_0} \\ \check{H}_{\mathrm{I}}^{(i_0)}[-k] &= \frac{1}{2} \sum_{b=1}^{2} S_b^{(i_0)}[k] Y_b^E[-k], \forall k \in \mathcal{I}_{i_0} \end{aligned} \tag{3.91}$$

3.4.7.2.3 MLE and LMMSE

Now, for each Tx, we have obtained the LSEs $\check{H}_{\mathrm{D}}^{(i)}[k], \forall k \in \mathcal{I}_i$ and $\check{H}_{\mathrm{I}}^{(i)}[k], \forall k \in -\mathcal{I}_i$. Similar to the FDS preamble based scheme, $\boldsymbol{h}_{\mathrm{D;I}}^{(i)}$ can be estimated with the following two methods:

1. The MLE:

$$\begin{aligned} \hat{\boldsymbol{h}}_{\mathrm{D}}^{(i)} &= \mathfrak{T}_{\mathrm{D}}^{(i)} \check{\boldsymbol{H}}_{\mathrm{D},\mathcal{I}_i}^{(i)}, \\ \hat{\boldsymbol{h}}_{\mathrm{I}}^{(i)} &= \mathfrak{T}_{\mathrm{I}}^{(i)} \check{\boldsymbol{H}}_{\mathrm{I},-\mathcal{I}_i}^{(i)}, \end{aligned} \tag{3.92}$$

   with $\mathfrak{T}_{\mathrm{D;I}}^{(i)}$ defined as in (3.67).

2. The LMMSE:

$$\begin{aligned} \hat{\boldsymbol{h}}_{\mathrm{D}}^{(i)} &= \mathfrak{Q}_{\mathrm{D}}^{(i)} \check{\boldsymbol{H}}_{\mathrm{D},\mathcal{I}_i}^{(i)}, \\ \hat{\boldsymbol{h}}_{\mathrm{I}}^{(i)} &= \mathfrak{Q}_{\mathrm{I}}^{(i)} \check{\boldsymbol{H}}_{\mathrm{I},-\mathcal{I}_i}^{(i)}. \end{aligned} \tag{3.93}$$

   with $\mathfrak{Q}_{\mathrm{D;I}}^{(i)}$ defined as in (3.69).

Afterwards, estimates of $H_{\mathrm{D;I}}^{(i)}[k]$ can be obtained with (3.61). The overall estimation scheme requires $16N_T L' + 8N_T L' L + 4N_T N \log_2 N$ real MULs.

3.4.7.3 Pilot Symbol Optimization

In this section, we will show how to adjust the pilot symbols to minimize estimation error and meanwhile, to fulfill (3.78) so that the preamble can be used for frame detection and time synchronization. Similar to Sec. 3.4.7.2.2, we investigate the different cases of subcarrier relation in Sec. 3.4.7.1.2.

In case 1), since $\mathcal{I}_{i_0} = -\mathcal{I}_{i_1}$ with $i_0 \neq i_1$, we have

$$S_b^{(i_1)*}[-\mathcal{I}_{i_0}(\kappa)] = S_b^{(i_1)*}[\mathcal{I}_{i_1}(\kappa')] = T_b^{(i_1)*}[\kappa'], \tag{3.94}$$

where $\kappa' = L' - \kappa - 1$. Substituting (3.94) into the definition of $\mathbb{S}_k$ in (3.87), the following expression can be obtained

$$\mathbb{S}_{\mathcal{I}_{i_0}(\kappa)} = \begin{bmatrix} T_1^{(i_0)}[\kappa] & T_1^{(i_1)*}[\kappa'] \\ T_2^{(i_0)}[\kappa] & T_2^{(i_1)*}[\kappa'] \end{bmatrix}. \tag{3.95}$$

To eliminate noise amplification in (3.88), the condition number of $\mathbb{S}_{\mathcal{I}_{i_0}(\kappa)}$ has to be 1, which implies the following conditions:

$$\left|T_1^{(i_0)}[\kappa]\right|^2 + \left|T_2^{(i_0)}[\kappa]\right|^2 = \left|T_1^{(i_1)*}[\kappa']\right|^2 + \left|T_2^{(i_1)*}[\kappa']\right|^2 \tag{3.96}$$

$$T_1^{(i_0)*}[\kappa]T_1^{(i_1)*}[\kappa'] + T_2^{(i_0)*}[\kappa]T_2^{(i_1)*}[\kappa'] = 0. \tag{3.97}$$

Since $\left|T_b^{(i)}[\kappa]\right| = 1, \forall\kappa$, the condition (3.96) is automatically fulfilled. Actually, this condition complies with the 1$^{\text{st}}$ design rule. By substituting (3.78) into (3.97), we found out that (3.97) is fulfilled when $\phi = \frac{\pi}{2} + m\pi, \forall m \in \mathcal{Z}$, while $T_1^{(i)}[\kappa], \forall i$ can be an arbitrary length-L' CAZAC sequence.

In case 2), since $\mathcal{I}_i = -\mathcal{I}_i$, we have

$$S_b^{(i)*}[-\mathcal{I}_i(\kappa)] = S_b^{(i)*}[\mathcal{I}_i(\kappa')] = T_b^{(i)*}[\kappa']. \tag{3.98}$$

Substituting (3.98) into the definition of $\mathbb{S}_k$ in (3.89), we obtain:

$$\mathbb{S}_{\mathcal{I}_i(\kappa)} = \begin{bmatrix} T_1^{(i)}[\kappa] & T_1^{(i)*}[\kappa'] \\ T_2^{(i)}[\kappa] & T_2^{(i)*}[\kappa'] \end{bmatrix}. \tag{3.99}$$

To force the condition number of $\mathbb{S}_{\mathcal{I}_i(\kappa)}$ to 1, the following condition is required:

$$T_1^{(i)*}[\kappa]T_1^{(i)*}[\kappa'] + T_2^{(i)*}[\kappa]T_2^{(i)*}[\kappa'] = 0. \tag{3.100}$$

Similarly to case 1), we found out that when $\phi = \frac{\pi}{2} + m\pi, \forall m \in \mathcal{Z}$, (3.100) is fulfilled.

In case 3), the estimation (3.91) implies that the noise influence on the LSE is independent of ϕ. Moreover, according to (3.77), (3.85) and (3.91), there is no noise amplification in the LSE. Thus, in this case, ϕ can be arbitrary.

Interestingly, it can be shown that the pilot symbol adjustment above leads to the fulfillment of the 3$^{\text{rd}}$ design rule. In summary, both the optimal preamble design rules and (3.71) can be fulfilled (see the proof in App. B.6). For all cases of subcarrier relation, $T_1^{(i)}[\kappa], \forall i$ can be an arbitrary length-L' CAZAC sequence. Especially, if the pilot subcarrier allocation only

contains the 3rd case of subcarrier relation (e.g. the last example in Tab. 3.2), ϕ can be arbitrary. Otherwise, $\phi = \frac{\pi}{2} + m\pi, \forall m \in \mathcal{Z}$[1].

3.4.8 Simulation Results

In our simulations, we observe the case of of $N_T = 2$. The amplitude and phase imbalance of the MOD/DMOD are about 5% and 5°, respectively. The LPFs in the I- and Q-branches (in all Tx-/Rx branches) have relative amplitude mismatch and phase differences of up to 10% and 10°, respectively. All different Tx- and Rx branches have different I/Q-imbalance parameters. Furthermore, all imbalance parameters are assumed to be time invariant. The measured 60 GHz channels in [150] with Obstructed-Line-Of-Sight (OLOS) were used[2], which are severely frequency selective and are typical for broadband indoor short range transmission. Accordingly, we set $L = 32$. Among the three GB-reservation cases in Sec. 3.3.4, we only observe the first case, i.e. only NULL subcarriers are used. The Nyquist rate of 250 MHz was applied. Two different OFDM parameter sets are investigated: $N = 256, N_0 = 17$ (designed for the IFE system) and $N = 512, N_0 = 91$ (WiMAX for comparison). Note that in both cases, we have $N_0 > \frac{N}{L}$. Thus, the circularly equi-distant subcarrier allocation of [125, 126] can not be applied. Thus, no comparison was conducted with the schemes in [125, 126].

Fig. 3.25 and Fig. 3.26 show the estimation MSE[3] of the proposed preamble based joint channel and I/Q-imbalance estimation schemes[4]. While Fig. 3.25 shows the case of $N = 256, N_0 = 17$ (relatively small N_0 i.e. GB), Fig. 3.26 shows the case of $N = 512, N_0 = 91$ (relatively large N_0 i.e. GB). Except for the proposed schemes, the direct MIMO extension of the scheme in [79] (designated as "Lopez")[5] and the CRLB in Sec. 3.4.4 were included for comparison. For the FDS- and 2SP schemes, L' was chosen as small as possible to reduce computational complexity. Moreover, both results with MLE and LMMSE are presented[6]. For LMMSE, a fixed ρ was applied with $10\log_{10}\rho = 30$ dB (see Sec. 3.4.5.2, 3.4.6.2 and 3.4.7.2). Furthermore, the cases with and without including the edge subcarriers are compared.

As shown, the scheme in [79] has a relatively high error floor due to influence of the NULL subcarriers. This error floor is removed by the proposed schemes. We can see that when the GB is relatively small (Fig. 3.25), all the proposed schemes can achieve performance that is quite close to the CRLB. The performance difference between MLE and LMMSE as well as between the cases with and without including edge subcarriers (for FDS and 2SP) is negligible. When the GB is relatively large (Fig. 3.26), more performance difference can be observed. While TDS

[1] With $\phi = \frac{\pi}{2} + m\pi, \forall m \in \mathcal{Z}$, the proposed preamble can be seen as an extension of the [FDM;C-T] design in [127]

[2] Unlike the channel realizations used in Sec. 3.2.3.2, the channel realizations used here have normalized gain. SNR variation was achieved by scaling the Rx signal power.

[3] This MSE has normalized value and is defined as $MSE_{\mathrm{n}} = E\left\{\frac{\sum_i \sum_k \sum_{\Pi=\{D,I\}} \left|\hat{H}_{\Pi}^{(i)}[k] - H_{\Pi}^{(i)}[k]\right|^2}{\sum_i \sum_k \sum_{\Lambda=\{D,I\}} \left|H_{\Lambda}^{(i)}[k]\right|^2}\right\}$.

[4] Since the multi-functional preamble consists of two short preambles, it is indicated by "2SP".

[5] Using the TDS preamble but omitting the deconvolution part in the corresponding estimation.

[6] With TDS, the performance of MLE and LMMSE have just negligible difference. Thus, only the MLE result is shown. Moreover, the scheme in [79] is neither MLE nor LMMSE estimation.

with MLE can still achieve near-CRLB performance, FDS and 2SP with MLE and without edge subcarrier inclusion have extremely high MSE. The reason was that the channel coefficients at the edge subcarriers have been estimated with very high estimation error. Both LMMSE and edge subcarrier inclusion can significantly reduce the MSE of FDS and 2SP. However, the best performance was achieved by combining LMMSE with edge subcarrier inclusion. By comparing Fig. 3.25 and Fig. 3.26, we will see that for the same SNR, the MSE in Fig. 3.26 is lower than that in Fig. 3.25. The reason is that longer preambles ($N = 512$) corresponding to Fig. 3.26 leads to more energy used for the parameter estimation.

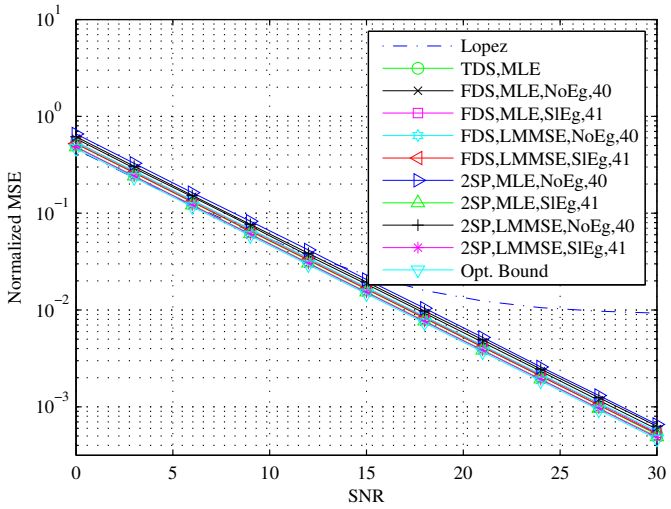

Figure 3.25: MSE as a function of SNR for different schemes, $N = 256, N_0 = 17$. "2SP": the scheme with the multi-functional preamble; "NoEg": the edge subcarriers are not included in the pilot subcarrier sets; "SlEg": the edge subcarriers are included in the pilot subcarrier sets.

Fig. 3.27 and Fig. 3.28 show the BER performance of the proposed schemes as well as several reference cases. For the BER simulation, a 2×2 MIMO OFDM system with 16-QAM modulation was considered, which applies STC at the Tx and ZF equalization at the Rx according to the compensation scheme in Sec. 3.4.3. The following reference cases were included in the simulation: 1) Application of the MIMO extension of the scheme in [79] ("Lopez"); 2) Application of the scheme in [82, 124] ("Zou"). To apply this scheme in our context, four OFDM symbols are used as preamble, which is the lowest allowable number [1]. Moreover, all subcarriers are allocated pilot symbols[2]; 3) BER without I/Q-imbalance compensation ("No Comp."); 4) BER with perfect joint channel and I/Q-imbalance estimation ("Perf. Est."); 5) BER without I/Q-imbalance influence ("No Imb."). Note that the cases 1)∼4) are under I/Q-imbalance influence. In the cases 3) and 5) (both are without I/Q-imbalance compensation),

[1] Corresponding to two pilot slots defined in [82, 124]. Each pilot slot contains a STC-coded block, including two consecutive OFDM symbols. Note that this scheme can also be used for the case that pilot subcarriers and data subcarriers are multiplexed (mainly for the case of fast-fading channels).

[2] In the simulation, we have allocated QPSK symbols following the design in [82, 124].

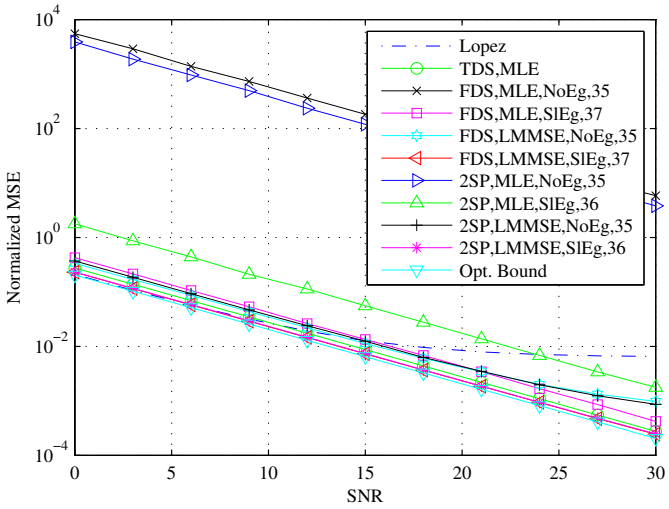

Figure 3.26: MSE as a function of SNR for different schemes, $N = 512, N_0 = 91$

the MIMO channel estimation scheme in [41], the ordinary STC-decoder and the MRC (see Sec. 3.2.3.1) were applied. Simulation shew that all proposed preambles have low CFs (about 2.5 dB), allowing "preamble boosting"[1]. For simplicity, we assume that the "preamble boosting" of all schemes requiring preamble (including the reference schemes) is 8 dB. Moreover, the SNR values shown in Fig. 3.27 and Fig. 3.28 are the average SNR values per Rx antenna.

As shown in Fig. 3.27 and Fig. 3.28, both the scheme without I/Q-imbalance compensation and the "Lopez" scheme have error-floors, where the error-floor of the the "Lopez" scheme is even higher. In contrast, the scheme with perfect joint estimation can achieve almost the same performance as the case without I/Q-imbalance. Furthermore, the proposed schemes can achieve performance quite close to that with perfect joint estimation. The SNR losses of the proposed schemes (due to estimation error) can be quite low (except those with "NoEg"), i.e. between 0.4 dB and 0.9 dB in Fig. 3.27 and about 0.25 dB in Fig. 3.28, respectively, at the BER of 10^{-5}. The reason for the slightly smaller SNR losses in Fig. 3.28 (considering only "SlEg") is the lower estimation MSE due to a longer preamble (as mentioned above). We can also see that in the case of relatively large GB (Fig. 3.28), if no edge subcarriers are included, both FDS and 2SP scheme will have error floors. According to both Fig. 3.27 and Fig. 3.28, the lowest SNR losses can be achieved by TDS (with either MLE or LMMSE) or by FDS/2SP applying both LMMSE and edge subcarrier inclusion. As another reference, the "Zou" scheme has SNR losses of about 1.3 dB in both Fig. 3.27 and Fig. 3.28. Despite the use of four OFDM symbols as preamble[2], the "Zou" scheme is outperformed by the proposed schemes by about 0.8 dB in Fig. 3.27 and about 1.15 dB in Fig. 3.28, respectively. The reason is that the correlation between channel coefficients at neighboring subcarriers (in other word, the channel IR length

[1]The 16-QAM OFDM signal has CF of about 10.5 dB. Thus, we apply preamble boosting of 8 dB.
[2]In contrast, the proposed schemes just require about one OFDM symbol as preamble.

information) is explored better by the proposed scheme for noise mitigation[1].

From Fig. 3.27 and Fig. 3.28, we can see that with the same SNR, the BER of $N = 512$ is generally lower than that of $N = 256$. The reason is that the GB for $N = 512$ is much larger. Thus, for the same time domain SNR, the SNR per subcarrier is higher.

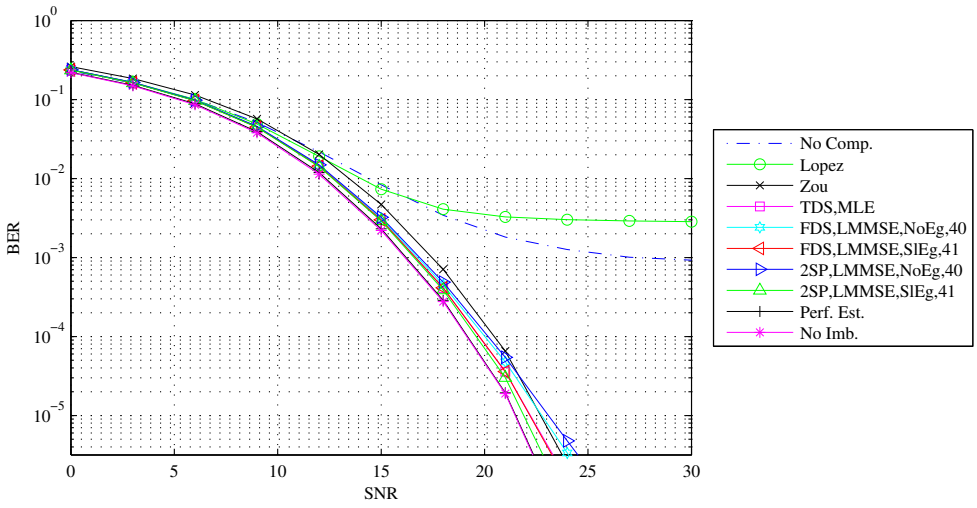

Figure 3.27: BER performance as a function of SNR for different schemes with $N = 256, N_0 = 17$ and 8 dB preamble boosting.

Fig. 3.29 and Fig. 3.30 show the BER results with lower preamble boosting i.e. 4 dB. As seen, compared to the results with 8 dB preamble boosting, slightly higher SNR losses can be observed. For the proposed schemes, the additional SNR losses (due to lower preamble boosting) are about $0.6 \sim 1$ dB and 0.25 dB in the cases of $N = 256$ and $N = 512$, respectively. For the "Zou" scheme, the corresponding additional SNR losses are 1.1 dB and 1.8 dB, respectively, which are higher than those of the proposed schemes.

Now, we examine the suitability of the multi-functional preamble for frame detection/time synchronization. Fig. 3.31 shows the output of the Schmidl-Cox correlator [148], which takes the received multi-functional preamble as input and applies a correlation length of $L + \frac{N}{2}$ (we applied $N = 256, N_0 = 17$). The SNR of the preamble was 25 dB. As shown, a relatively strong peak can be produced by the correlator, which can be used for frame detection/time synchronization. Further investigation on the time synchronization mechanism and performance is beyond the scope of this thesis.

[1]In the original papers of Zou i.e. [82, 124], such correlation was explored to reduce the number of pilot subcarriers (e.g. via interpolation) but not for noise mitigation. Thus, the estimation accuracy of the "Zou" scheme is comparable to the LS scheme defined in [139]. As a result, despite the increased preamble length, the SNR loss in Fig. 3.28 remains almost the same as in Fig. 3.27, since the influence of increase preamble length (i.e. increased pilot energy) is compensated for by the same increase in the number of coefficients to be estimated.

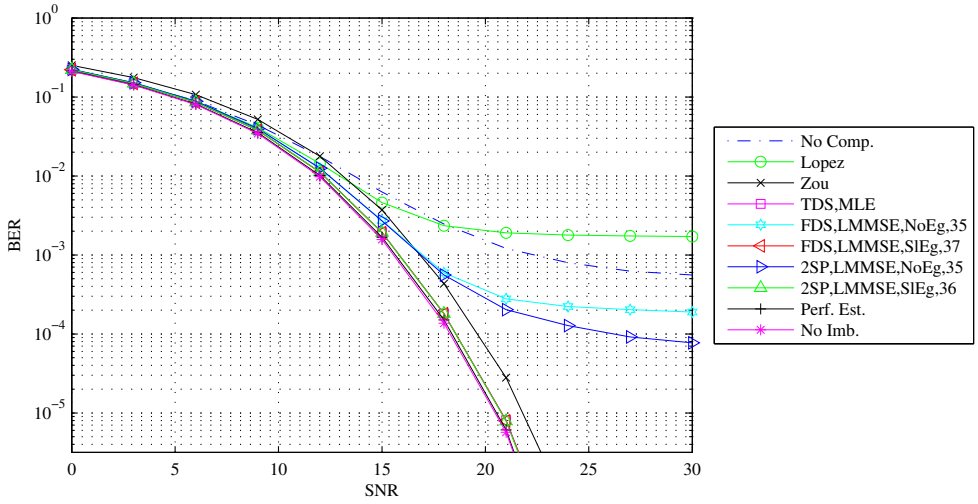

Figure 3.28: BER performance as a function of SNR for different schemes with $N = 512, N_0 = 91$ and 8 dB preamble boosting.

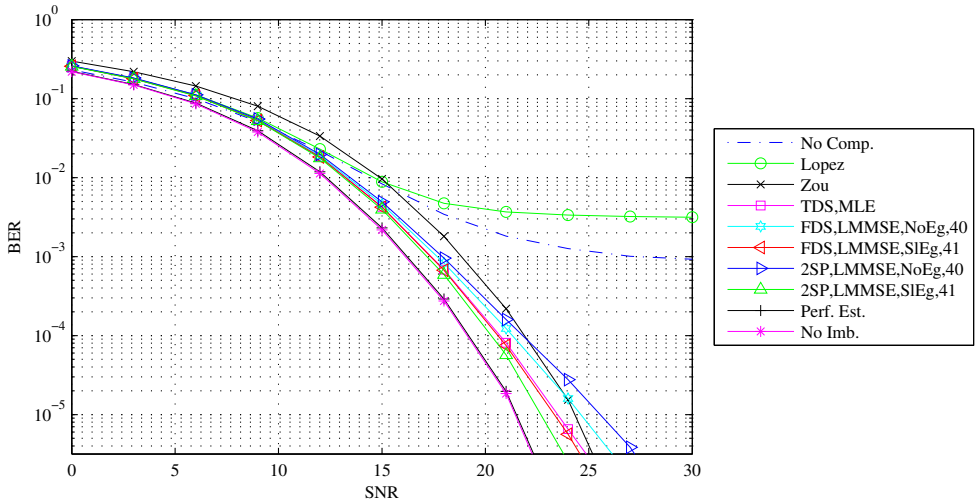

Figure 3.29: BER performance as a function of SNR for different schemes with $N = 256, N_0 = 17$ and 4 dB preamble boosting.

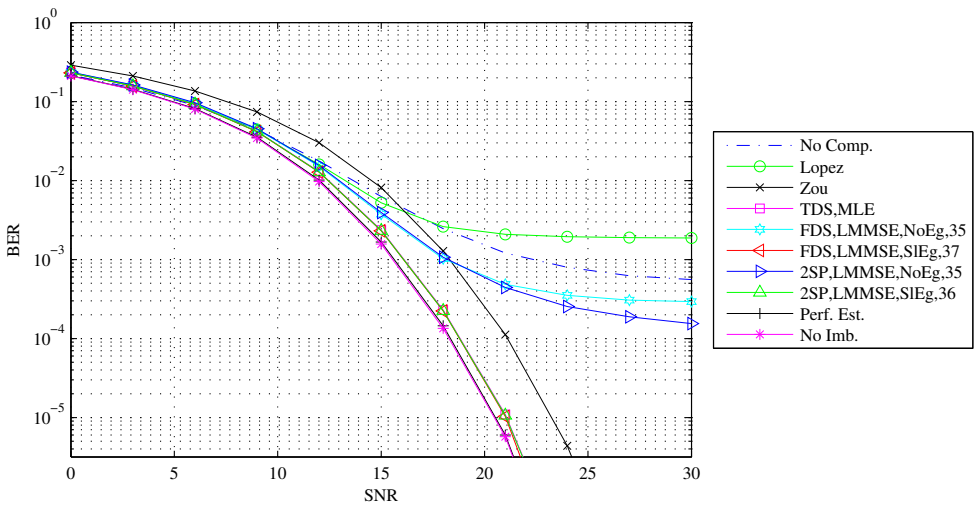

Figure 3.30: BER performance as a function of SNR for different schemes with $N = 512, N_0 = 91$ and 4 dB preamble boosting.

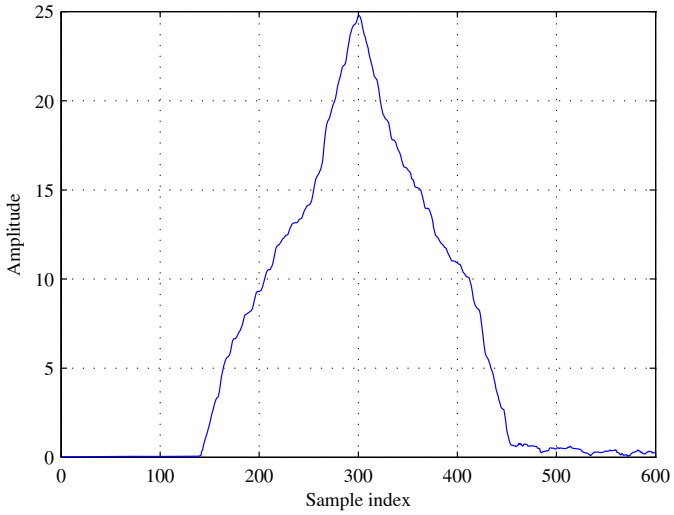

Figure 3.31: Correlator output for frame detection/time synchronization, $N = 256, N_0 = 17$,SNR is 25 dB.

3.4.9 Computational Complexity Issues and Discussion

We divide the computational complexity into three parts. The first part is dedicated to the parameter estimation, e.g. estimation of $H_{\mathrm{D;I}}$ (for all subcarriers and antennas) of the proposed schemes. The second part is dedicated to the calculation of the equalization matrices (or just coefficients) from the parameter estimates. For the proposed schemes, such calculations are carried out based on the matrix equations in Sec. 3.4.3 [1]. For the reference schemes, similar matrix equations can be found in the corresponding literatures. The third part is dedicated to the actual compensation i.e. the equalization of the received signal symbols. While the first- and the second parts are only required once per signal frame, the third part is needed for each received OFDM symbol. Note that in the computational complexity analysis, the regular operations required for OFDM signal reception[2] is not taken into account. Moreover, the analysis in this section just provides a rough estimation of the required computational complexity. The actual numbers would depend on the actual implementation.

3.4.9.1 Computational Complexity of Parameter Estimation

Tab. 3.3 summarizes the computational complexity expressions (for each Rx antenna) of the different schemes for parameter estimation[3]. For the "Zou" scheme, N_P indicates the number of pilot slots [82, 124]. Note that the TDS scheme in the case without NULL subcarrier can be regarded as the MIMO extension of the "Lopez" scheme.

Applying the simulation parameters, the required number of real MULs of the different schemes can be shown in Fig. 3.32. As shown, the MLE in [125, 126, 127] requires much higher computational complexity than the proposed schemes and the "Zou" scheme. Among the proposed schemes in the case with NULL subcarriers, the highest- and lowest computational complexities are required by TDS and FDS, respectively. To achieve comparable performance, the 2SP scheme has only slightly higher computational complexity than the FDS scheme (about $1 \sim 3\%$). Compared to the propsed schemes, the "Zou" scheme has even slightly lower computational complexity. However, we should recall that estimation of the "Zou" scheme is just LSE (defined in [139]). If MLE or LMMSE should be applied to this scheme to enhance estimation accuracy (which would be comparable to that of the proposed schemes), the computational complexity of the "Zou" scheme will be considerably increased[4].

In the case without NULL subcarriers, the proposed TDS scheme has the lowest computational complexity. The reason is that the deconvolution in (3.59) or (3.60) can be omitted

[1] Different signal detection schemes e.g. ZF, MMSE etc., can lead to different complexity.

[2] E.g. transforming the received OFDM symbols to the frequency domain via DFT.

[3] For STC, we assumed N_T consecutive OFDM data symbols are encoded to N_T consecutive OFDM symbol slots and across all N_T Tx antennas. For SM, we assumed that N_T OFDM data symbols are transmitted simultaneously via one OFDM symbol slot.

[4] A part of such complexity increase can be compensated for by decreasing the number of pilot subcarriers. However, since the mixed I/Q-imbalance- and channel coefficients a, b, c, d in [82, 124] involve convolution between more than two channel IRs, the required number of pilot subcarriers is more than doubled compared to that of the proposed schemes.

(see Sec. 3.4.5.2), which allows significant computational complexity reduction. In contrast, the computational complexity of the other schemes remains almost unchanged[1].

Table 3.3: Computational Complexity Expressions

Schemes	**Computational complexity (per Rx antenna)**
TDS (with NULL subc.)	$4(N-N_0-1)+8N_T^2L^2+2(2N_T+1)N\log_2 N$
TDS (no NULL subc.)	$4(N-N_0-1)+2(2N_T+1)N\log_2 N$
FDS	$8N_TL'L+4N_TN\log_2 N$
2SP	$16N_TL'+8N_TL'L+4N_TN\log_2 N$
Zou	$8N_D(1+N_R)N_T^2N_P$
MLE in (3.46) Est. in [125, 126, 127]	$8N_TNLB+4N_TN\log_2 N$

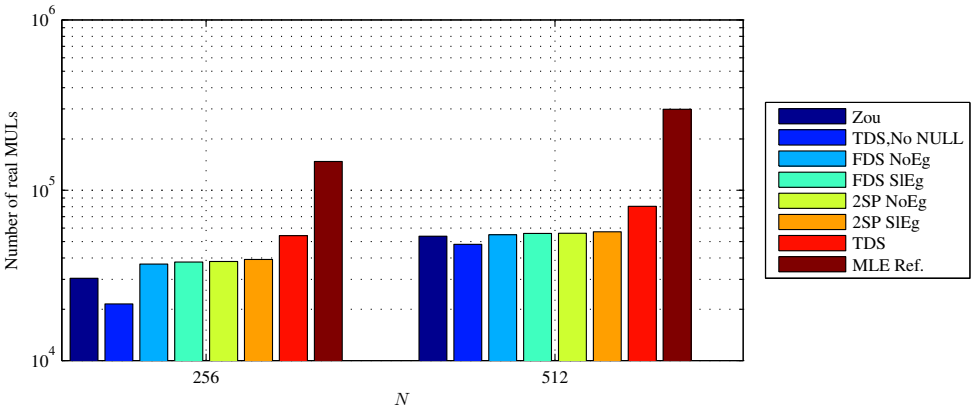

Figure 3.32: Computational complexity (per Rx antenna) of different schemes for parameter estimation.

3.4.9.2 Computational Complexity of Equalization Matrix Calculation and the Actual Compensation

Tab. 3.4 and Tab. 3.5 summarize the computational complexity expressions of the different schemes for the calculation of equalization matrices and for the actual compensation, respectively. Except for the applied joint compensation scheme in Sec. 3.4.3 (indicated by "Joint" or "Jnt Tx/Rx IQ+Ch."), two reference schemes are included: 1) The "Zou" scheme [82, 124], which first conducts STC-decoding and then joint channel and I/Q-imbalance compensation; 2) A scheme assuming perfect Tx (i.e. no Tx I/Q-imbalance) and conducts first Rx-I/Q-imbalance compensation in time domain using real- or complex valued FIR filters (see Sec. 3.4.3 and Sec. B.8, respectively) and then STC/SM-decoding in the frequency domain. This scheme is indicated by "Sep." or "Perf. Tx, Sep. Rx IQ+Ch.". Furthermore, the use of real- or complex

[1]For simplicity, they are not shown in Tab. 3.3 or Fig. 3.32.

valued FIR filters is indicated by "R" or "C", respectively[1]. For all schemes, ZF-equalization is assumed. Note that for simplicity, the equalization matrices are just calculated by simple pseudo-inverse or inverse of the coefficient matrices in Sec. 3.4.3. However, further computational complexity reduction could be achieved by exploiting the structures of the coefficient matrices (see [129]). This is not considered in the analysis here.

Table 3.4: Computational Complexity Expressions for Equalization Matrix Calculation

Scheme	Number of real MULs
Joint, STC	$\frac{4}{3}N_D N_T(-1+4(1+6N_R)N_T^2)$
Joint, SM, $N_T \neq N_R$	$\frac{4}{3}N_D N_T(-1+4N_T(6N_R+N_T))$
Joint, SM, $N_T = N_R$	$\frac{4}{3}N_D N_T(-1+4N_T^2)$
Zou, STC	$\frac{4}{3}N_D N_T(-1+3N_R N_T+4N_T^2)$
Sep., STC	$\frac{4}{3}N_D N_T(-1+(1+6N_R)N_T^2)$
Sep., SM, $N_T \neq N_R$	$\frac{4}{3}N_D N_T(-1+(1+6N_R)N_T^2)$
Sep., SM, $N_T = N_R$	$\frac{4}{3}N_D N_T(-1+N_T^2)$

Table 3.5: Computational Complexity Expressions for the Actual Compensation

Scheme	Number of real MULs (per data symbol)
Joint, STC	$8N_T N_R$
Joint, SM	$8N_R$
Zou, STC	$4N_T(N_R+2)$
Sep., STC,R	$\frac{(1+L_c)N_R(N_{CP}+N)}{N_D}+4N_T N_R$
Sep., STC,C	$4N_R\left(\frac{L_c(N_{CP}+N)}{N_D}+N_T\right)$
Sep., SM,R	$N_R\left(4+\frac{(1+L_c)(N_{CP}+N)}{N_D}\right)$
Sep., SM,C	$\frac{4N_R N_D+L_c(N_{CP}+N)}{N_D}$

By applying the simulation parameters on the expressions in Tab. 3.4 and Tab. 3.5, Fig. 3.33 and Fig. 3.34 can be obtained. Note that in Fig. 3.34, N_T was fixed to 2 while N_R is variable. From Fig. 3.33, we can see that both for STC and SM, the "Joint" scheme requires considerably higher computational complexity for the equalization matrix calculation than the reference schemes. The main reason is the increased matrix dimension.

Fig. 3.34 shows that in the actual compensation phase, the highest computational complexity is required by the "Sep." scheme. The reason is that an FIR filter (real- or complex valued) has to be used in each Rx path to compensate for the Rx-I/Q-imbalance, which consumes considerable complexity. It is also shown that except for $N_R = 1, 2$, the "Zou" scheme requires less computational complexity than the "Joint"- and the "Sep." schemes (when STC is applied).

[1]Note that the used FIR filters have no influence on the computational complexity of the equalization matrix calculation. Thus, "R" and "C" are not used in Tab. 3.4.

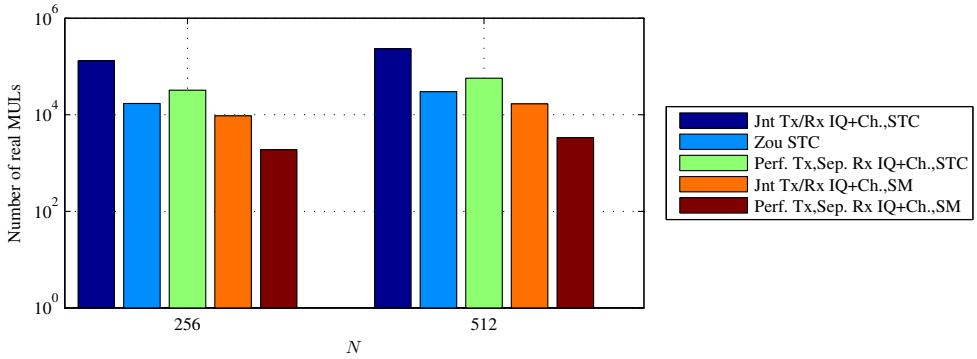

Figure 3.33: Computational complexity of different schemes for the calculation of the equalization matrices.

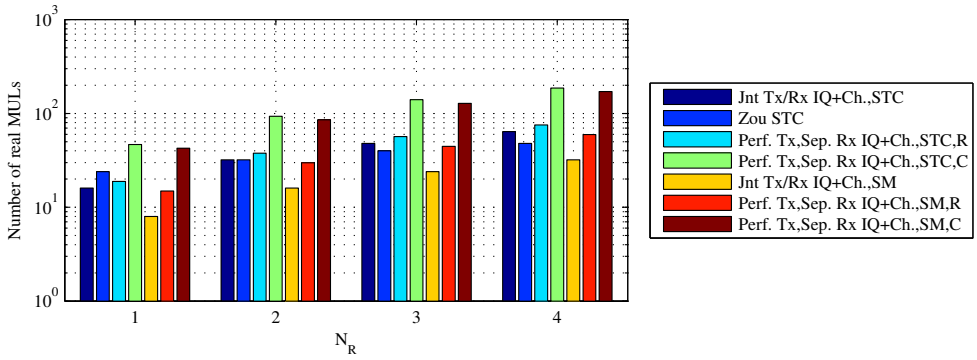

Figure 3.34: Computational complexity per received data symbol (e.g. 16-QAM) for the compensation of I/Q-imbalance and the MIMO channel. $N_T = 2$. For the "Perf. Tx, Sep. Rx IQ+Ch." scheme, we assumed that the Rx-I/Q-imbalance compensation filters are of length $L_c = 8$.

3.4.9.3 Discussion

According to the analysis and the results in Sec. 3.4.9.1 and Sec. 3.4.9.2, the computational complexity of the proposed schemes for parameter estimation is much lower than that of the schemes in [125, 126, 127] but comparable with that of the "Zou" scheme. However, the computational complexity of the applied joint compensation scheme, which includes both equalization matrix calculation and the actual compensation, is generally higher than that of the "Zou" scheme.

Except for computational complexity, we should also consider preamble overhead and performance. On the one hand, compared to the "Zou" scheme, the proposed schemes allow much lower preamble overhead i.e. about one OFDM symbol length. On the other hand, Sec. 3.4.8 has shown that the performance of the proposed schemes is considerably better than that of the "Zou" scheme, despite the fact that the "Zou" scheme has applied much longer preambles for estimation. Note that the performance of the "Zou" scheme can be further enhanced by applying more pilot slots. Thus, as mentioned in Sec. 3.4.1, the "Zou" scheme is more suitable for outdoor scenarios (where pilot-data-multiplexed type estimation should be used), while the proposed schemes are more suitable for indoor scenarios (where preamble-based estimation is more advantageous).

Based on the discussion above, the proposed schemes can achieve quite a good trade-off between performance, overhead and computational complexity. Thus, they are very suitable for indoor broadband wireless communications. Among the proposed schemes, the 2SP scheme may be the most practical one, since multi-functional preamble is applied to further reduce preamble overhead. However, the choice on the scheme should be made based on the context and constraints of the system design as well as the advantages and disadvantages of the candidate schemes.

3.5 Efficient Joint Estimation and Compensation of CFO, I/Q-Imbalance and the MIMO Channel

3.5.1 Background and Overview

In this section, we investigate the joint estimation and compensation of CFO, Tx- and Rx frequency selective I/Q-imbalance and the MIMO channel. Compared to Sec. 3.4, CFO is included in the system model and should be compensated digitally.

A lot of related background information was already given in Sec. 3.4.1. Here, we give a brief overview of the related works. The compensation of CFO and I/Q-imbalance in SISO- and MIMO OFDM systems has been studied in a number of works e.g. [81, 115, 116, 117, 119, 132, 151, 152] and [44, 90, 118, 120, 123, 130, 135], respectively. Among them, [116, 118, 119, 120, 151, 152] only considered frequency-independent I/Q-imbalance, which is not suitable in broadband wireless communication systems. In contrast, the other works considered frequency-

selective I/Q-imbalance. The work [115] has proposed a Non-linear Least-Square (NLS) based scheme for CFO estimation and Rx-I/Q-imbalance compensation. This scheme requires exhaustive numerical search and thus, results in high computational complexity. Improvements have been made by [81, 117] and [90, 123], which have proposed a closed-form Linear Least Square (LLS) estimator and a suboptimal iterative estimator, respectively. Both schemes have lower computational complexity than that in [115]. In [135], perfect CFO estimation was assumed and a PTEQ scheme was proposed for impairment compensation. As mentioned in Sec. 3.4.1, the PTEQ scheme suffers from slow convergence and high computational complexity. In [130], Kalman filter is applied for compensation, which can cope with fast fading MIMO channels. However, this scheme requires high pilot overhead (e.g. ten OFDM symbols as preamble). Many of the works above, including [115, 116, 117, 118, 119, 120, 130], have the additional drawback that only Rx impairments were considered in the system model. Thus, if Tx-I/Q-imbalance is present, the schemes of these works may suffer from severe performance degradation[1]. In [48], blind Rx-I/Q-imbalance estimation and compensation scheme was proposed. When the CFO is sufficiently large, this scheme can provide good Rx-I/Q-imbalance estimation even in low SNR region. The reason is that the Rx noise (which is influenced by Rx-I/Q-imbalance) is also exploited for estimation. For the estimation of CFO, Tx-I/Q-imbalance and the MIMO channel, this scheme needs to be extended.

The most advance state-of-art schemes considering CFO and both Tx- and Rx- frequency-selective I/Q-imbalance in MIMO OFDM systems are those in [90, 123] as well as in our previous work [44]. The drawback of the schemes in [90, 123] is that the used preambles are not overhead- and interference optimal. Moreover, the estimation schemes in[90, 123] require quite hight computational complexity.

This section presents our previous work [44] and a lot of extension, including a new scheme and more detailed simulation results and analysis. First, a novel preamble design is proposed. Afterwards, two efficient estimation schemes are developed based on the preambles and a hybrid domain compensation structure. Both numerical simulation results and complexity analysis are presented to show the advantages of the proposed schemes. The novelties of the proposed schemes can be summarized as follows:

- The proposed preamble is used both for the estimation of CFO and Rx-I/Q-imbalance as well as that of the joint coefficients of Tx-I/Q-imbalance and the MIMO channel. In contrast, most existing schemes apply different preambles for these two estimation procedures (e.g. [81, 90, 117, 123]). Thus, compared to the preambles used in the reference works, our preamble is much more overhead efficient;

- When designing the preamble, the orthogonality between different Tx antennas as well as between direct- and image channels (see Sec. 3.4.4) are taken into account, allowing better estimation accuracy than [90, 123];

[1]Some performance comparison has been shown in [81].

- The proposed preambles have low CF, which enables "preamble power boosting"[1].
- The proposed estimation schemes require much lower computational complexity than those in [90, 123];
- As most of the existing schemes, the CFO estimation and Rx-I/Q-imbalance estimation/compensation of proposed schemes rely on the negative phase-rotation[2] in the mirror interference signal caused by Rx-I/Q-imbalance. As a result, small CFOs can cause difficulties for both estimation and compensation. Conventionally e.g. in [81, 117], "hard switching" is applied, i.e. CFO values smaller than a threshold are regarded as zero [3]. However, an improperly chosen threshold can cause performance degradation. To solve this problem, we have proposed soft metrics which change adaptively with the SNR and allow "soft switching".

3.5.2 Signal- and System Model

Fig. 3.35 shows the MIMO system model considering both CFO and frequency selective I/Q-imbalance. Like in Sec. 3.4, the numbers of Tx- and Rx antennas are N_T and N_R, respectively. The amplitude- and phase imbalance at the i^{th} MOD or at the r^{th} DMOD are indicated by $g^{T(i);R\langle r\rangle}$ and $\varphi^{T(i);R\langle r\rangle}$, respectively. The IR of Tx- or Rx LPFs in the I- and Q-branches are indicated by $h^{TI(i);RI\langle r\rangle}(t)$ and $h^{TQ(i);RQ\langle r\rangle}(t)$, respectively. All different Tx-/Rx branches have different I/Q-imbalance parameters as well as different LPF-IRs. The ordinary carrier frequency is f_c, while a CFO, Δf, is assumed at all Rx DMODs. The IRs of the RF components at the i^{th} Tx or the r^{th} Rx are modeled as $h^{(i);\langle r\rangle}_{\text{RF,Tx;Rx}}(t)$. The radio channel between the i^{th} Tx and the r^{th} Rx is modeled by $h^{\langle r,i\rangle}_{\text{RF}}(t)$ and is assumed to be quasi-static (block-fading).

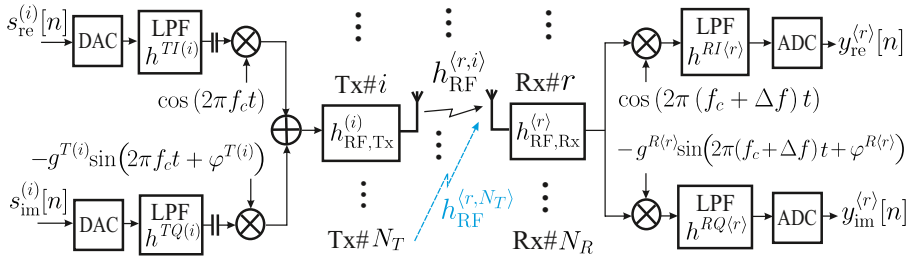

Figure 3.35: System model with CFO and frequency selective I/Q-imbalance

For further analysis, an equivalent BB model should be derived. From Fig. 3.35, the relation between the RLP inputs, $s^{(i)}_{\text{re}}(t)$ and $s^{(i)}_{\text{im}}(t)$, and the modulated signal $u^{\text{RF}(i)}(t)$ (before $h^{(i)}_{\text{RF,Tx}}$

[1] See also Sec. 3.4.
[2] Compared to the direction of the phase-rotation (caused by CFO) without Rx-I/Q-imbalance.
[3] Correspondingly, another I/Q-imbalance- and channel estimation scheme will be applied, which is suitable for the cases without CFO.

can be expressed as

$$\begin{aligned} u^{\mathrm{RF}}(t) &= \left(s_{\mathrm{re}}(t) * h^{TI}(t)\right)\cos\left(2\pi f_c t\right) - \left(s_{\mathrm{im}}(t) * h^{TQ}(t)\right) g^T \sin\left(2\pi f_c t + \varphi^T\right) \\ &= \mathcal{R}e\left\{u(t)e^{j2\pi f_c t}\right\} \end{aligned} \tag{3.101}$$

with $u(t) := s(t) * h_{\mathrm{D}}^T(t) + s^*(t) * h_{\mathrm{I}}^T(t)$ and $h_{\mathrm{D;I}}^T(t) := \left(h^{TI}(t) \pm g^T e^{j\varphi^T} h^{TQ}(t)\right)/2$ [1]. Note that $u(t)$ is the complex envelope of $u^{\mathrm{RF}}(t)$. Let the DMOD input signal be expressed as $v^{\mathrm{RF}}(t) = \mathcal{R}e\left\{v(t)e^{j2\pi f_c t}\right\}$ [2]. The relation between $v(t)$ and the ADC input $y(t)$ can be expressed as (see App. B.7):

$$y(t) = \left(v(t)e^{-j2\pi\Delta f t}\right) * h_{\mathrm{D}}^R(t) + \left(v(t)e^{-j2\pi\Delta f t}\right)^* * h_{\mathrm{I}}^R(t), \tag{3.102}$$

with $h_{\mathrm{D;I}}^R(t) := \left(h^{RI}(t) \pm g^R e^{\mp j\varphi^R} h^{RQ}(t)\right)/2$. Based on (3.101) and (3.102), the equivalent discrete time BB model in Fig. 3.36 can be obtained, where $h_{\mathrm{D;I}}^{T(i)}[n]$ and $h_{\mathrm{D;I}}^{R\langle r\rangle}[n]$ are defined as in (3.30) and (3.32), respectively. Moreover, $h^{\langle r,i\rangle}[n]$ is the equivalent BB channel between the i^{th} Tx and the r^{th} Rx and includes the effects of $h_{\mathrm{RF}}^{\langle r,i\rangle}(t)$, $h_{\mathrm{RF,Tx}}^{(i)}(t)$ and $h_{\mathrm{RF,Rx}}^{\langle r\rangle}(t)$ in Fig. 3.35. The CFO influence is modeled by the multiplication with $e^{j\frac{2\pi\epsilon n}{N}}$, where $\epsilon = -\frac{\Delta f N}{f_s}$ and f_s is the sampling frequency. Finally, $\eta^{\langle r\rangle}[n]$ is the AWGN at the r^{th} Rx branch with $E\left\{\left|\eta^{\langle r\rangle}[n]\right|^2\right\} = \sigma_{\mathrm{n}}^2$.

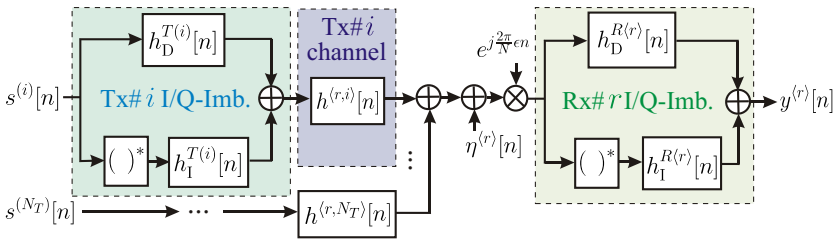

Figure 3.36: Equivalent BB model with CFO and I/Q-imbalance

To further simplify the BB model, the following relation is observed:

$$\begin{aligned} \left(s[n]e^{j\frac{2\pi}{N}\epsilon n}\right) * h[n] &= \sum_{m=-\infty}^{\infty} h[m]\left(s[n-m]e^{j\frac{2\pi}{N}\epsilon(n-m)}\right) \\ &= \left(\sum_{m=-\infty}^{\infty} h[m]e^{-j\frac{2\pi}{N}\epsilon m} s[n-m]\right) e^{j\frac{2\pi}{N}\epsilon n} \\ &= \left[s[n] * \left(h[n]e^{-j\frac{2\pi}{N}\epsilon n}\right)\right] e^{j\frac{2\pi}{N}\epsilon n}, \end{aligned} \tag{3.103}$$

where $s[n]$ and $h[n]$ represent an arbitrary input sequence and an FIR filter, respectively. Eq. (3.103) implies the equivalent system structures in Fig. 3.37, where the following nota-

[1] The Tx index i is omitted for simplicity.
[2] The Rx index r is omitted for simplicity.

tion is used throughout this section (similar to [117]):

$$\begin{aligned}\overrightarrow{(\bullet)} &:= (\bullet)e^{-j\frac{2\pi}{N}\epsilon n}\\ \overleftarrow{(\bullet)} &:= (\bullet)e^{j\frac{2\pi}{N}\epsilon n}.\end{aligned} \tag{3.104}$$

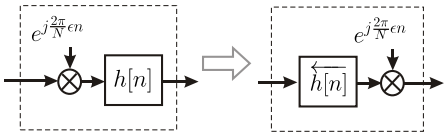

Figure 3.37: Exchanging the positions of a phase rotator and an FIR filter

Based on the equivalent structure in Fig. 3.37, the input-output relation of the BB model in Fig. 3.36 can be rewritten as:

$$\begin{aligned}y^{\langle r\rangle}[n] &= x_{\mathrm{D}}^{\langle r\rangle}[n]e^{j\frac{2\pi\epsilon n}{N}} + x_{\mathrm{I}}^{\langle r\rangle}[n]e^{-j\frac{2\pi\epsilon n}{N}} + \tilde{\eta}^{\langle r\rangle}[n],\\ x_{\mathrm{D}}^{\langle r\rangle}[n] &:= \sum_{i=1}^{N_T} s^{(i)}[n] * h_1^{\langle r,i\rangle}[n] + s^{(i)*}[n] * h_2^{\langle r,i\rangle}[n],\\ x_{\mathrm{I}}^{\langle r\rangle}[n] &:= \sum_{i=1}^{N_T} s^{(i)}[n] * h_3^{\langle r,i\rangle}[n] + s^{(i)*}[n] * h_4^{\langle r,i\rangle}[n],\\ \tilde{\eta}^{\langle r\rangle}[n] &:= \eta^{\langle r\rangle}[n]e^{j\frac{2\pi\epsilon n}{N}} h_{\mathrm{D}}^{R\langle r\rangle}[n] + \eta^{\langle r\rangle *}[n]e^{-j\frac{2\pi\epsilon n}{N}} h_{\mathrm{I}}^{R\langle r\rangle}[n],\end{aligned} \tag{3.105}$$

with

$$\begin{aligned}h_{1;2}^{\langle r,i\rangle}[n] &:= h_{\mathrm{D;I}}^{T(i)}[n] * h^{\langle r,i\rangle}[n] * \overrightarrow{h_{\mathrm{D}}^{R\langle r\rangle}}[n],\\ h_{3;4}^{\langle r,i\rangle}[n] &:= h_{\mathrm{I;D}}^{T(i)*}[n] * h^{\langle r,i\rangle *}[n] * \overleftarrow{h_{\mathrm{I}}^{R\langle r\rangle}}[n],\end{aligned} \tag{3.106}$$

where $h_1^{\langle r,i\rangle} \sim h_4^{\langle r,i\rangle}$ are assumed to be length-L_{h} FIR filters. Eq. (3.105) yields the simplified BB model in Fig. 3.38.

Finally, we remark that although the model of Fig. 3.36 can be found in similar mathematical expression in the literature e.g. [90, 123], the model of Fig. 3.38 is novel (to the best of the authors knowledge).

3.5.3 Compensation of CFO, Frequency-Selective I/Q-Imbalance and the MIMO Channel

For the compensation of CFO, frequency-selective I/Q-imbalance and the MIMO channel, an extended version of the hybrid domain compensation structure in [81] is applied (similar to [90, 123]), which is shown in Fig. 3.39. Within each Rx branch, Rx I/Q-imbalance and CFO

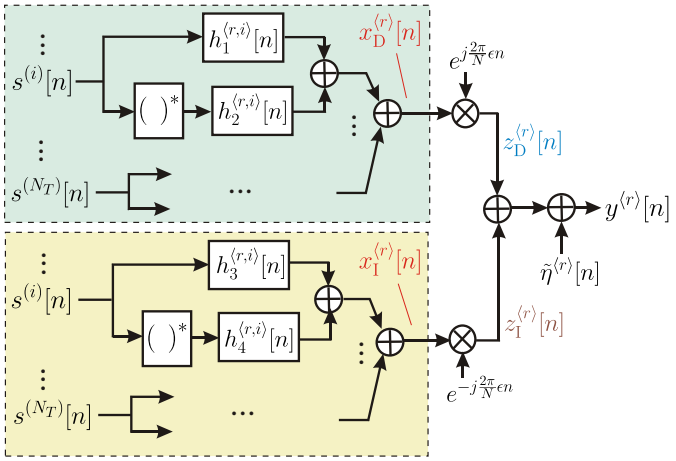

Figure 3.38: Simplified baseband model with CFO and frequency selective I/Q-imbalance

are compensated in time domain. Afterwards, Tx I/Q-imbalance and MIMO channels are compensated in frequency domain.

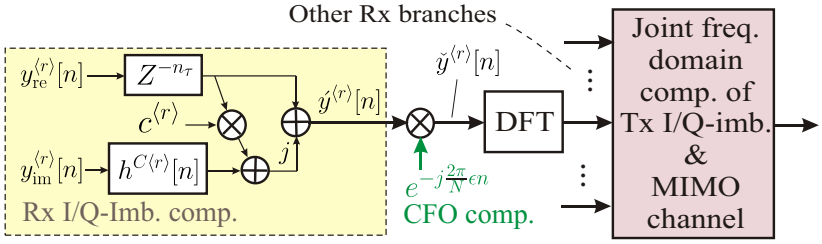

Figure 3.39: Hybrid domain compensation structure

From Fig. 3.39, the Rx signal after Rx I/Q-imbalance compensation can be expressed as:

$$\acute{y}^{\langle r\rangle}[n] = y_{\mathrm{re}}^{\langle r\rangle}[n-n_\tau] + j\left(c y_{\mathrm{re}}^{\langle r\rangle}[n-n_\tau] + h^{C\langle r\rangle}[n] * y_{\mathrm{im}}^{\langle r\rangle}[n]\right), \tag{3.107}$$

where n_τ is the dominant-tap index[1] of the FIR filter $h^{C\langle r\rangle}[n]$, which is of length L_{c}. Eq. (3.107) can be equivalently written as:

$$\acute{y}^{\langle r\rangle}[n] = w_{\mathrm{D}}^{\langle r\rangle}[n] * y^{\langle r\rangle}[n] + w_{\mathrm{I}}^{\langle r\rangle}[n] * y^{\langle r\rangle *}[n] \tag{3.108}$$

with

$$w_{\mathrm{D;I}}^{\langle r\rangle}[n] = \frac{1}{2}\left(\delta[n-n_\tau]\left(1 + jc^{\langle r\rangle}\right) \pm h^{C\langle r\rangle}[n]\right), \tag{3.109}$$

[1] We assume the index starts from 0.

where $\delta[n]$ is the discrete time impulse function. By substituting (3.105) into (3.108), we have

$$\begin{aligned}
&\acute{y}^{\langle r\rangle}[n] = e^{j\frac{2\pi\epsilon n}{N}} \sum_{i=1}^{N_T} \left[s^{(i)}[n] * h_{\mathrm{D}}^{E\langle r,i\rangle}[n] + s^{(i)*}[n] * h_{\mathrm{I}}^{E\langle r,i\rangle}[n] \right] \\
&+ e^{-j\frac{2\pi\epsilon n}{N}} \sum_{i=1}^{N_T} \left[s^{(i)}[n] * \vartheta_{\mathrm{D}}^{E\langle r,i\rangle}[n] + s^{(i)*}[n] * \vartheta_{\mathrm{I}}^{E\langle r,i\rangle}[n] \right] \\
&+ \acute{\eta}^{\langle r\rangle}[n], \\
&h_{\mathrm{D;I}}^{E\langle r,i\rangle}[n] := h_{1;2}^{\langle r,i\rangle}[n] * \overrightarrow{w_{\mathrm{D}}^{\langle r\rangle}}[n] + h_{4;3}^{\langle r,i\rangle *}[n] * \overrightarrow{w_{\mathrm{I}}^{\langle r\rangle}}[n], \\
&\vartheta_{\mathrm{D;I}}^{E\langle r,i\rangle}[n] := h_{3;4}^{\langle r,i\rangle}[n] * \overleftarrow{w_{\mathrm{D}}^{\langle r\rangle}}[n] + h_{2;1}^{\langle r,i\rangle *}[n] * \overleftarrow{w_{\mathrm{I}}^{\langle r\rangle}}[n],
\end{aligned} \tag{3.110}$$

where $\acute{\eta}^{\langle r\rangle}[n]$ is the noise after Rx I/Q-imbalance compensation. From Fig. 3.36, we can see that the phase rotation $e^{-j\frac{2\pi\epsilon n}{N}}$ in (3.105) and (3.110) is caused by the Rx I/Q-imbalance. Thus, after Rx I/Q-imbalance compensation, all signal components in (3.110) having the $e^{-j\frac{2\pi\epsilon n}{N}}$ phase rotation should be eliminated i.e.,

$$\vartheta_{\mathrm{D}}^{E\langle r,i\rangle}[n] = 0,\ \vartheta_{\mathrm{I}}^{E\langle r,i\rangle}[n] = 0,\ \forall i. \tag{3.111}$$

With (3.106) and (3.109), it can be proved that the two equations in (3.111) are equivalent. After successful compensation of Rx I/Q-imbalance and CFO, the signal $\check{y}^{\langle r\rangle}[n]$ in Fig. 3.39 can be expressed as

$$\check{y}^{\langle r\rangle}[n] = \sum_{i=1}^{N_T} \left(s^{(i)}[n] * h_{\mathrm{D}}^{E\langle r,i\rangle}[n] + s^{(i)*}[n] * h_{\mathrm{I}}^{E\langle r,i\rangle}[n] \right) + \check{\eta}^{\langle r\rangle}[n], \tag{3.112}$$

where $\check{\eta}^{\langle r\rangle}[n]$ is the corresponding noise term.

Let $s_b^{(i)}[n], \forall n \in [0, N-1]$ be the b^{th} transmitted OFDM symbol at the i^{th} Tx antenna and $\check{y}_b^{\langle r\rangle}[n], \forall n \in [0, N-1]$ be the corresponding received OFDM symbol after Rx I/Q-imbalance and CFO compensation. Their DFTs are indicated by $S_b^{(i)}[k]$ and $\check{Y}_b^{\langle r\rangle}[k]$, respectively. Assuming sufficient CP length N_{CP}, (3.112) yields

$$\check{Y}_b^{\langle r\rangle}[k] = \sum_{i=1}^{N_T} \left(S_b^{(i)}[k] H_{\mathrm{D}}^{E\langle r,i\rangle}[k] + S_b^{(i)*}[-k] H_{\mathrm{I}}^{E\langle r,i\rangle}[k] \right) + \check{N}^{\langle r\rangle}[k], \tag{3.113}$$

where $H_{\mathrm{D;I}}^{E\langle r,i\rangle}[k] = \mathcal{F}_N \left\{ h_{\mathrm{D;I}}^{E\langle r,i\rangle}[n] \right\}$. Eq. (3.113) can be rewritten in different matrix equations for all possible antenna diversity or spatial multiplexing schemes according to Sec. 3.4.3. Based on these matrix equations, various equalization techniques e.g. ZF and MMSE can be used to recover the original data symbols. In the following, we will show how to obtain the compensation coefficients based on novel preamble designs.

3.5.4 Joint Estimation Scheme Based on Closed-Form CFO Estimation

This scheme is developed based on the BB model of Fig. 3.38. First, a special preamble is applied to estimate ϵ and $h_1^{\langle r,i\rangle}[n] \sim h_4^{\langle r,i\rangle}[n]$. Based on the estimates of ϵ and $h_1^{\langle r,i\rangle}[n] \sim h_4^{\langle r,i\rangle}[n]$, all required coefficients for the compensation of CFO and I/Q-imbalance can be calculated.

3.5.4.1 Preamble Design

Inspired by [116], the proposed preamble consists of a 3 fold repetition of a basic sequence $\dot{s}^{(i)}[n], n = 0, \ldots, N_P - 1$, which is constructed according to FDS design in Sec. 3.4.6 and varies for different Tx antennas. To illustrate the transmission of the preamble, all signals in Fig. 3.38 are extended with the notation $(\dot{\bullet})$. The 3 fold repetition structure is used to estimate ϵ, $\dot{x}_{\mathrm{D}}^{\langle r\rangle}[n]$ and $\dot{x}_{\mathrm{I}}^{\langle r\rangle}[n]$ in Fig. 3.38. Based on $\dot{x}_{\mathrm{D}}^{\langle r\rangle}[n]$ and $\dot{s}^{(i)}[n]$, $h_1^{\langle r,i\rangle}[n]$ and $h_2^{\langle r,i\rangle}[n]$ can be estimated, while based on $\dot{x}_{\mathrm{I}}^{\langle r\rangle}[n]$ and $\dot{s}^{(i)}[n]$, $h_3^{\langle r,i\rangle}[n]$ and $h_4^{\langle r,i\rangle}[n]$ can be estimated.

Since 3 fold repetition is applied, we should minimize the length of the basic sequence, N_P, to minimize the preamble overhead. To apply the FDS design in Sec. 3.4.6, $\dot{s}^{(i)}[n]$ is constructed as an OFDM symbol with N_P subcarriers, where N_P could be different from N [1]. Let $\dot{S}^{(i)}[k] = \mathcal{F}_{N_P}\left\{\dot{s}^{(i)}[n]\right\}$. As mentioned above, $\dot{s}^{(i)}[n]$ is used to estimate $2N_T$ equivalent channel IRs of length L_{h} (i.e. $h_{1;3}^{\langle r,i\rangle}[n]$ and $h_{2;4}^{\langle r,i\rangle}[n]$). Thus, at least $2N_T L_{\mathrm{h}}$ subcarriers should be active within $\dot{S}^{(i)}[k]$. In order to reserve the same GB as the OFDM data symbols, we should have $N_P \geq \frac{2N_T L_{\mathrm{h}} N}{N_D}$. To facilitate the FFT implementation, we choose $N_P = 2^{\left\lceil \log_2\left(\frac{2N_T L_{\mathrm{h}} N}{N_D} + N_{\mathrm{a}}\right)\right\rceil}$, where N_{a} is a number to adjust N_P. The number of NULL subcarriers in the basic sequence is $N_{0,P} = \left\lceil \frac{N_P N}{N_D} \right\rceil$, while the number of active subcarriers is $N_{D,P} = N_P - N_{0,P}$. Now, the active subcarriers can be allocated to different Tx antennas according to the FDS design in Sec. 3.4.6. Let $\mathcal{I}_i$ with $|\mathcal{I}_i| = L'$ be the index set of the allocated subcarriers for the i^{th} Tx, which fulfills the requirements in Sec. 3.4.6.1.1. By assigning values of a length-L' CAZAC sequence $T^{(i)}(\kappa)$ with $\left|T^{(i)}(\kappa)\right| = 1$ to the allocated subcarriers of each basic sequence, i.e.

$$\dot{S}^{(i)}[(\mathcal{I}_i)_\kappa] = T^{(i)}(\kappa), \forall \kappa = 0, \ldots, L' - 1, \quad \text{and} \quad \dot{S}^{(i)}[k] = 0, \forall k \notin \mathcal{I}_i, \tag{3.114}$$

low CF of the basic sequence can be achieved. Finally, the total length of the preamble is $N_{\mathrm{CP}} + 3N_P$.

Note that using a different DFT-length (N_P) in the preamble from that in the data signals (N) will require extra[2] DFT-blocks or reconfigurable DFT-blocks (w.r.t. the block length) in the signal processing implementation (e.g. in FPGA). As a result, the implementation complexity will be higher[3]. In contrast, the preambles in Sec. 3.4 use the same DFT-length as the data OFDM symbols and allows lower implementation complexity.

[1] N is the number of subcarriers in the data OFDM symbols.
[2] W.r.t. the DFT-blocks for the ordinary OFDM data symbols.
[3] The corresponding increase in computational complexity will be included in the computational complexity expressions of Sec. 3.5.7

3.5.4.2 Estimation Scheme

Let $\dot{y}_b^{\langle r\rangle}[n]$ be the received signal of the b^{th} repetition of the basic sequence. Eq. (3.105) yields the following expression:

$$\begin{aligned}&\dot{y}_b^{\langle r\rangle}[n] = \dot{z}_{\mathrm{D}}^{\langle r\rangle}[n]e^{j\frac{2\pi\epsilon N_P(b-1)}{N}} + \dot{z}_{\mathrm{I}}^{\langle r\rangle}[n]e^{-j\frac{2\pi\epsilon N_P(b-1)}{N}} + \dot{\tilde{\eta}}_b^{\langle r\rangle}[n], \forall n = 0,\ldots,N_P-1,\\ &\text{with}\quad \dot{z}_{\mathrm{D}}^{\langle r\rangle}[n] := \dot{x}_{\mathrm{D}}^{\langle r\rangle}[n]e^{j\frac{2\pi\epsilon n}{N}},\ \dot{z}_{\mathrm{I}}^{\langle r\rangle}[n] := \dot{x}_{\mathrm{I}}^{\langle r\rangle}[n]e^{-j\frac{2\pi\epsilon n}{N}}.\end{aligned} \tag{3.115}$$

With $b = 1, 2, 3$, (3.115) yields 3 equations. According to [116], if we ignore the noise term, the following matrix equation can be obtained:

$$\dot{\boldsymbol{y}}_2 2\cos\Omega = \dot{\boldsymbol{y}}_{13}, \tag{3.116}$$

where

$$\begin{aligned}\Omega &:= \frac{2\pi\epsilon N_P}{N},\\ \dot{\boldsymbol{y}}_2 &:= \left[\left(\dot{\boldsymbol{y}}_2^{\langle 1\rangle}\right)^T,\ldots,\left(\dot{\boldsymbol{y}}_2^{\langle N_R\rangle}\right)^T\right]^T,\\ \dot{\boldsymbol{y}}_{13} &:= \left[\left(\dot{\boldsymbol{y}}_1^{\langle 1\rangle}+\dot{\boldsymbol{y}}_3^{\langle 1\rangle}\right)^T,\ldots,\left(\dot{\boldsymbol{y}}_1^{\langle N_R\rangle}+\dot{\boldsymbol{y}}_3^{\langle N_R\rangle}\right)^T\right]^T,\\ \dot{\boldsymbol{y}}_b^{\langle r\rangle} &:= \left[\dot{y}_b^{\langle r\rangle}[0],\ldots,\dot{y}_b^{\langle r\rangle}[N_P-1]\right]^T.\end{aligned}$$

The LSE of $\cos\Omega$ is

$$\hat{\cos}\,\Omega = \frac{1}{2}\mathcal{R}e\left\{(\dot{\boldsymbol{y}}_2)^\dagger\,\dot{\boldsymbol{y}}_{13}\right\} = \frac{1}{2\,||\dot{\boldsymbol{y}}_2||_2^2}\mathcal{R}e\left\{(\dot{\boldsymbol{y}}_2)^H\,\dot{\boldsymbol{y}}_{13}\right\}, \tag{3.117}$$

which yields the following CLosed-Form Estimator (CLFE):

$$\hat{\epsilon} = \pm\frac{N}{2\pi N_P}\cos^{-1}\left(\hat{\cos}\,\Omega\right). \tag{3.118}$$

Note that (3.118) is the extension of the estimator in [116] (Eq. (15)) to exploit the Rx array- and diversity gains. The sign ambiguity in (3.117) can be solved by taking the sign of the following rough CFO estimator:

$$\hat{\epsilon}' = \frac{N}{2\pi N_P}\arg\left\{\left[\dot{\boldsymbol{y}}_1^T,\dot{\boldsymbol{y}}_2^T\right]^*\left[\dot{\boldsymbol{y}}_2^T,\dot{\boldsymbol{y}}_3^T\right]^T\right\}. \tag{3.119}$$

To obtain estimates of $\dot{x}_{\mathrm{D;I}}^{\langle r\rangle}[n]$, $\dot{z}_{\mathrm{D}}^{\langle r\rangle}[n]$ and $\dot{z}_{\mathrm{I}}^{\langle r\rangle}[n]$ should be obtained first. For this purpose,

we rewrite Eq. (3.115) into the following matrix form:

$$\underbrace{\begin{bmatrix} \left(\dot{\boldsymbol{y}}_1^{\langle r\rangle}\right)^T \\ \left(\dot{\boldsymbol{y}}_2^{\langle r\rangle}\right)^T \\ \left(\dot{\boldsymbol{y}}_3^{\langle r\rangle}\right)^T \end{bmatrix}}_{\dot{\mathfrak{Y}}^{\langle r\rangle}} = \underbrace{\begin{bmatrix} 1 & 1 \\ e^{j\Omega} & e^{-j\Omega} \\ e^{j2\Omega} & e^{-j2\Omega} \end{bmatrix}}_{\mathfrak{f}_\Omega} \underbrace{\begin{bmatrix} \left(\dot{\boldsymbol{z}}_{\mathrm{D}}^{\langle r\rangle}\right)^T \\ \left(\dot{\boldsymbol{z}}_{\mathrm{I}}^{\langle r\rangle}\right)^T \end{bmatrix}}_{\dot{\mathfrak{Z}}^{\langle r\rangle}} + \underbrace{\begin{bmatrix} \left(\dot{\tilde{\boldsymbol{\eta}}}_1^{\langle r\rangle}\right)^T \\ \left(\dot{\tilde{\boldsymbol{\eta}}}_2^{\langle r\rangle}\right)^T \\ \left(\dot{\tilde{\boldsymbol{\eta}}}_3^{\langle r\rangle}\right)^T \end{bmatrix}}_{\dot{\mathfrak{n}}^{\langle r\rangle}}, \tag{3.120}$$

where $\dot{\boldsymbol{z}}_{\mathrm{D;I}}^{\langle r\rangle} = \left[\dot{z}_{\mathrm{D;I}}^{\langle r\rangle}[0], \ldots, \dot{z}_{\mathrm{D;I}}^{\langle r\rangle}[N_P-1]\right]^T$ and $\dot{\tilde{\boldsymbol{\eta}}}_b^{\langle r\rangle} = \left[\dot{\tilde{\eta}}_b^{\langle r\rangle}[0], \ldots, \dot{\tilde{\eta}}_b^{\langle r\rangle}[N_P-1]\right]^T$.

Now, $\dot{\mathfrak{Z}}^{\langle r\rangle}$ can be estimated by

$$\hat{\dot{\mathfrak{Z}}}^{\langle r\rangle} = \boldsymbol{A}^{\langle r\rangle}\dot{\mathfrak{Y}}^{\langle r\rangle}, \tag{3.121}$$

where $\boldsymbol{A}^{\langle r\rangle}$ is a 2×3 matrix and can be obtained by applying the following two different criteria:

1. Minimization of the cost function $\left\|\dot{\mathfrak{Z}}^{\langle r\rangle} - \boldsymbol{A}^{\langle r\rangle}\dot{\mathfrak{Y}}^{\langle r\rangle}\right\|_F^2$. In this case, we have

$$\boldsymbol{A}^{\langle r\rangle} = \left(\mathfrak{f}_\Omega\right)^\dagger, \forall r, \tag{3.122}$$

   which corresponds to an LSE [1].

2. Minimization of the cost function $E\left\{\left\|\dot{\mathfrak{Z}}^{\langle r\rangle} - \boldsymbol{A}^{\langle r\rangle}\dot{\mathfrak{Y}}^{\langle r\rangle}\right\|_F^2\right\}$. In this case, we have

$$\boldsymbol{A}^{\langle r\rangle} = \mathfrak{D}^{\langle r\rangle}\mathfrak{f}_\Omega^H\left(\mathfrak{f}_\Omega\mathfrak{D}^{\langle r\rangle}\mathfrak{f}_\Omega^H + \frac{1}{\rho^{\langle r\rangle}}\boldsymbol{I}_3\right)^{-1}, \tag{3.123}$$

   where $\rho^{\langle r\rangle}$ is the Rx SNR at the r^{th} Rx antenna and $\mathfrak{D}^{\langle r\rangle} = \mathrm{diag}\left\{\left[\frac{P_{\mathrm{D}}^{\langle r\rangle}}{P^{\langle r\rangle}}, \frac{P_{\mathrm{I}}^{\langle r\rangle}}{P^{\langle r\rangle}}\right]\right\}$ with $P_{\mathrm{D;I}}^{\langle r\rangle} = \frac{1}{N_P}E\left\{\left(\dot{\boldsymbol{z}}_{\mathrm{D;I}}^{\langle r\rangle}\right)^H\dot{\boldsymbol{z}}_{\mathrm{D;I}}^{\langle r\rangle}\right\}$ and $P^{\langle r\rangle} = P_{\mathrm{D}}^{\langle r\rangle} + P_{\mathrm{I}}^{\langle r\rangle}$. By assuming an approximate value $\hat{\upsilon}$ [2] for the Rx IRR $\upsilon^{\langle r\rangle} := \frac{P_{\mathrm{D}}^{\langle r\rangle}}{P_{\mathrm{I}}^{\langle r\rangle}}$ at all Rx branches, we can approximate $\mathfrak{D}^{\langle r\rangle}$ with $\mathfrak{D} = \mathrm{diag}\left\{\left[\frac{\hat{\upsilon}}{\hat{\upsilon}+1}, \frac{1}{\hat{\upsilon}+1}\right]\right\}, \forall r$. Thus, $\boldsymbol{A}^{\langle r\rangle}$ becomes independent of r. The estimation using (3.123) corresponds to an LMMSE.

In Sec. 3.5.6, the performance of the two estimators above will be compared based on simulation results.

With $\hat{\dot{\mathfrak{Z}}}^{\langle r\rangle}$ and $\hat{\epsilon}$, we can easily obtain estimates of $\dot{x}_{\mathrm{D;I}}^{\langle r\rangle}[n]$ from (3.115). Let

$$\dot{\boldsymbol{x}}_{\mathrm{D;I}}^{\langle r\rangle} = \left[\dot{x}_{\mathrm{D;I}}^{\langle r\rangle}[0], \ldots, \dot{x}_{\mathrm{D;I}}^{\langle r\rangle}[N_P-1]\right]^T$$

[1] This is true only when Ω is perfectly known.

[2] With realistic components, $\hat{\upsilon} = 200 \sim 1000$ can be assumed. Moderate deviation of $\hat{\upsilon}$ from the real IRR has negligible influence on the estimation.

and $\dot{\boldsymbol{X}}_{\mathrm{D;I}}^{\langle r\rangle} = \boldsymbol{F}^{N_P}\dot{\boldsymbol{x}}_{\mathrm{D;I}}^{\langle r\rangle}$. According to (3.105), $h_{1;2}^{\langle r,i\rangle}[n]$ can be estimated with $\dot{x}_{\mathrm{D}}^{\langle r\rangle}[n]$, while $h_{3;4}^{\langle r,i\rangle}[n]$ with $\dot{x}_{\mathrm{I}}^{\langle r\rangle}[n]$. Similar to the FDS estimation scheme in Sec. 3.4.6, the following relation can be obtained (when ignoring noise):

$$\dot{\boldsymbol{X}}_{\mathrm{D;I},\mathcal{I}_i}^{\langle r\rangle} = \boldsymbol{T}^{(i)}\boldsymbol{F}_{(\mathcal{I}_i,\mathcal{L}_{\mathrm{h}})}^{N_P}\boldsymbol{h}_{1;3}^{\langle r,i\rangle},\ \dot{\boldsymbol{X}}_{\mathrm{D;I},-\mathcal{I}_i}^{\langle r\rangle} = \acute{\boldsymbol{T}}^{(i)*}\boldsymbol{F}_{(-\mathcal{I}_i,\mathcal{L}_{\mathrm{h}})}^{N_P}\boldsymbol{h}_{2;4}^{\langle r,i\rangle}, \tag{3.124}$$

where $\boldsymbol{T}^{(i)}$ and $\acute{\boldsymbol{T}}^{(i)}$ are defined as in (3.65) and

$$\begin{aligned}\boldsymbol{h}_{1;2;3;4}^{\langle r,i\rangle} &= \left[h_{1;2;3;4}^{\langle r,i\rangle}[0],\ldots,h_{1;2;3;4}^{\langle r,i\rangle}[L_{\mathrm{h}}-1]\right]^T,\\ \mathcal{L}_{\mathrm{h}} &= \{0,\ldots,L_{\mathrm{h}}-1\}.\end{aligned}$$

Correspondingly, $\boldsymbol{h}_{1;2;3;4}^{\langle r,i\rangle}$ can be estimated with the following two methods:

1. The MLE:

$$\begin{aligned}\hat{\boldsymbol{h}}_{1;3}^{\langle r,i\rangle} &= \mathfrak{T}_{\mathrm{D}}^{(i)}\boldsymbol{T}^{(i)*}\dot{\boldsymbol{X}}_{\mathrm{D;I},\mathcal{I}_i}^{\langle r\rangle},\\ \hat{\boldsymbol{h}}_{2;4}^{(i)} &= \mathfrak{T}_{\mathrm{I}}^{(i)}\acute{\boldsymbol{T}}^{(i)}\dot{\boldsymbol{X}}_{\mathrm{D;I},-\mathcal{I}_i}^{\langle r\rangle},\end{aligned} \tag{3.125}$$

   with

$$\begin{aligned}\mathfrak{T}_{\mathrm{D}}^{(i)} &:= \left(\boldsymbol{F}_{(\mathcal{I}_i,\mathcal{L}_{\mathrm{h}})}^{N_P}\right)^{\dagger},\\ \mathfrak{T}_{\mathrm{I}}^{(i)} &:= \left(\boldsymbol{F}_{(-\mathcal{I}_i,\mathcal{L}_{\mathrm{h}})}^{N_P}\right)^{\dagger}.\end{aligned} \tag{3.126}$$

2. The LMMSE:

$$\begin{aligned}\hat{\boldsymbol{h}}_{1;3}^{\langle r,i\rangle} &= \mathfrak{Q}_{\mathrm{D}}^{(i)}\boldsymbol{T}^{(i)*}\dot{\boldsymbol{X}}_{\mathrm{D;I},\mathcal{I}_i}^{\langle r\rangle},\\ \hat{\boldsymbol{h}}_{2;4}^{(i)} &= \mathfrak{Q}_{\mathrm{I}}^{(i)}\acute{\boldsymbol{T}}^{(i)}\dot{\boldsymbol{X}}_{\mathrm{D;I},-\mathcal{I}_i}^{\langle r\rangle}\end{aligned} \tag{3.127}$$

   with

$$\begin{aligned}\mathfrak{Q}_{\mathrm{D}}^{(i)} &:= \left(\left(\boldsymbol{F}_{(\mathcal{I}_i,\mathcal{L}_{\mathrm{h}})}^{N_P}\right)^H\boldsymbol{F}_{(\mathcal{I}_i,\mathcal{L}_{\mathrm{h}})}^{N_P} + \frac{L_{\mathrm{h}}}{\rho^{\langle r\rangle}}\boldsymbol{I}_{L_{\mathrm{h}}}\right)^{-1}\left(\boldsymbol{F}_{(\mathcal{I}_i,\mathcal{L}_{\mathrm{h}})}^{N_P}\right)^H,\\ \mathfrak{Q}_{\mathrm{I}}^{(i)} &:= \left(\left(\boldsymbol{F}_{(-\mathcal{I}_i,\mathcal{L}_{\mathrm{h}})}^{N_P}\right)^H\boldsymbol{F}_{(-\mathcal{I}_i,\mathcal{L}_{\mathrm{h}})}^{N_P} + \frac{L_{\mathrm{h}}}{\rho^{\langle r\rangle}}\boldsymbol{I}_{L_{\mathrm{h}}}\right)^{-1}\left(\boldsymbol{F}_{(-\mathcal{I}_i,\mathcal{L}_{\mathrm{h}})}^{N_P}\right)^H,\end{aligned} \tag{3.128}$$

   where $\rho^{\langle r\rangle}$ is the SNR at each Rx antenna. To reduce complexity, a fixed value can be assumed for $\rho^{\langle r\rangle}$. In this case, both $\mathfrak{Q}_{\mathrm{D}}^{(i)}\boldsymbol{T}^{(i)*}$ and $\mathfrak{Q}_{\mathrm{I}}^{(i)}\acute{\boldsymbol{T}}^{(i)}$ can be regarded as know (and can be pre-computed).

In practice, when $\Omega \to 0$ and $\Omega \to \pm\pi$, the CLFE in (3.118) will suffer from high sensitivity to noise. Moreover, the condition number of $\mathfrak{f}_{\Omega}$ will become very large, resulting in large

estimation error for $\dot{\boldsymbol{z}}_{\mathrm{D;I}}^{\langle r\rangle}$. Sec. 3.5.6 will show that in such cases, the rough estimator $\hat{\epsilon}'$ will be much more accurate than the CLFE. Moreover, instead of applying (3.121), we should set

$$\hat{\dot{\boldsymbol{z}}}_{\mathrm{D}}^{\langle r\rangle} = \frac{1}{3}\left(\dot{\boldsymbol{y}}_1^{\langle r\rangle} + \dot{\boldsymbol{y}}_3^{\langle r\rangle} + \mathrm{sgn}\left(\cos\hat{\Omega}\right)\dot{\boldsymbol{y}}_2^{\langle r\rangle}\right),\ \hat{\dot{\boldsymbol{z}}}_{\mathrm{I}}^{\langle r\rangle} = \mathbf{0}_{N_P\times 1}, \tag{3.129}$$

which implies that the Rx-I/Q-imbalance will not be separately compensated for but jointly with the Tx-I/Q-imbalance and the MIMO channel. For the detection of such cases, we observe the relation $\frac{1}{N_R N_P} E\left\{\left|\left|\dot{\boldsymbol{y}}_{13} - 2\mathrm{sgn}\left(\cos\Omega\right)\dot{\boldsymbol{y}}_2\right|\right|_2^2\right\} \geq 6\tilde{\sigma}_{\mathrm{n}}^2$, which follows from (3.120) (we assume $E\left\{\left|\tilde{\eta}^{\langle r\rangle}[n]\right|^2\right\} = \tilde{\sigma}_{\mathrm{n}}^2$). The equality applies when $\Omega = 0$ or $\Omega = \pm\pi$. Accordingly, we can define the following metric:

$$P_\Delta := \frac{1}{N_R N_P}\left|\left|\dot{\boldsymbol{y}}_{13} - 2\mathrm{sgn}\left(\cos\Omega\right)\dot{\boldsymbol{y}}_2\right|\right|_2^2 - 6\zeta\tilde{\sigma}_{\mathrm{n}}^2, \tag{3.130}$$

where $\zeta \geq 1$ is an adjusting factor. Once $P_\Delta < 0$, both $\hat{\epsilon}'$ and (3.129) are applied. Otherwise, we apply $\left\|\mathbf{f}_{\hat{\Omega}}\hat{\dot{\mathbf{3}}}\right\|_F^2$ [1] as a further metric to switch between $\hat{\epsilon}$ and $\hat{\epsilon}'$, where $\hat{\dot{\mathbf{3}}} = \left[\hat{\dot{\mathbf{3}}}^{\langle 1\rangle}, \ldots, \hat{\dot{\mathbf{3}}}^{\langle N_R\rangle}\right]$. The estimator that leads to a larger $\left\|\mathbf{f}_{\hat{\Omega}}\hat{\dot{\mathbf{3}}}\right\|_F^2$ is chosen. Compared to [81], the metrics above allow soft switching.

To further improve the CFO estimation and the separation of $\dot{z}_{\mathrm{D}}^{\langle r\rangle}[n]$ and $\dot{z}_{\mathrm{I}}^{\langle r\rangle}[n]$, the following iterative processing can be applied. First, $\acute{\boldsymbol{y}}_b^{\langle r\rangle} = \dot{\boldsymbol{y}}_b^{\langle r\rangle} - \hat{\dot{\boldsymbol{z}}}_{\mathrm{I}}^{\langle r\rangle} e^{-j\hat{\Omega}(b-1)}, \forall b, r$ is calculated to eliminate the influence of Rx I/Q-imbalance on the received preamble. Afterwards, (3.119) is applied with $\acute{\boldsymbol{y}}_b$ instead of $\dot{\boldsymbol{y}}_b$ to obtain a new estimate of ϵ. With the new estimate of ϵ, (3.121) is used to obtain a new version of $\hat{\dot{\mathbf{3}}}^{\langle r\rangle}, \forall r$. The above calculation can be carried out iteratively.

3.5.4.3 Calculation of Compensation Coefficients

Now, we have the estimates of ϵ and $h_1^{\langle r,i\rangle}[n] \sim h_4^{\langle r,i\rangle}[n]$. According to Sec. 3.5.3, successful Rx-I/Q-imbalance compensation requires the fulfillment of the two conditions in (3.111). Since both conditions are equivalent, we only have to choose one of them. We consider that with realistic I/Q-imbalance parameters, $h_{\mathrm{D}}^{T(i);R\langle r\rangle}[n]$ would have much larger power gain than $h_{\mathrm{I}}^{T(i);R\langle r\rangle}[n]$. Thus, according to (3.106), $h_1^{\langle r,i\rangle}[n]$ would have much larger power gain than $h_{2;3;4}^{\langle r,i\rangle}[n]$ and can be estimated with much lower estimation error (due to noise). According to (3.110), $\vartheta_{\mathrm{I}}^{E\langle r,i\rangle}[n]$ consists partly of $h_1^{\langle r,i\rangle}[n]$. Thus, it should be used to obtain reliable compensation coefficients. From (3.104), (3.109) and (3.111), we obtain

$$\left(1 + jc^{\langle r\rangle}\right)\gamma_1^{\langle r,i\rangle}[n] + h^{C\langle r\rangle}[n] * \gamma_2^{\langle r,i\rangle}[n] = 0,\ \forall i \tag{3.131}$$

[1] This corresponds to the power of the signal part in (3.120).

with

$$\begin{aligned}\gamma_1^{\langle r,i\rangle}[n] &:= \left(h_1^{\langle r,i\rangle *}[n-n_\tau] + h_4^{\langle r,i\rangle}[n-n_\tau]\right) e^{-j\frac{2\pi}{N}\epsilon(n-n_\tau)},\\ \gamma_2^{\langle r,i\rangle}[n] &:= \left(-h_1^{\langle r,i\rangle *}[n] + h_4^{\langle r,i\rangle}[n]\right) e^{-j\frac{2\pi\epsilon n}{N}}.\end{aligned} \tag{3.132}$$

Eq. (3.131) can be rewritten with real valued signals as

$$\begin{aligned}-\gamma_{1,\mathrm{re}}^{\langle r,i\rangle}[n] &= -c\gamma_{1,\mathrm{im}}^{\langle r,i\rangle}[n] + h^{C\langle r\rangle}[n] * \gamma_{2,\mathrm{re}}^{\langle r,i\rangle}[n],\ \forall i\\ -\gamma_{1,\mathrm{im}}^{\langle r,i\rangle}[n] &= c\gamma_{1,\mathrm{re}}^{\langle r,i\rangle}[n] + h^{C\langle r\rangle}[n] * \gamma_{2,\mathrm{im}}^{\langle r,i\rangle}[n],\ \forall i.\end{aligned} \tag{3.133}$$

Let $V_{1;2}^{Re;Im,\langle r,i\rangle}[k] := \mathcal{F}_{N_P}\left\{\gamma_{1;2,\mathrm{re;im}}^{\langle r,i\rangle}[n]\right\}$ and $H^{C\langle r\rangle}[k] := \mathcal{F}_{N_P}\left\{h^{C\langle r\rangle}[n]\right\}$. Eq. (3.133) yields:

$$\underbrace{\begin{bmatrix} -V_1^{Re\langle r,1\rangle}[k] \\ -V_1^{Im\langle r,1\rangle}[k] \\ \vdots \\ -V_1^{Re\langle r,N_T\rangle}[k] \\ -V_1^{Im\langle r,N_T\rangle}[k] \end{bmatrix}}_{\boldsymbol{\nu}_k^{\langle r\rangle}} = \underbrace{\begin{bmatrix} -V_1^{Im\langle r,1\rangle}[k] & V_2^{Re\langle r,1\rangle}[k] \\ V_1^{Re\langle r,1\rangle}[k] & V_2^{Im\langle r,1\rangle}[k] \\ \vdots & \vdots \\ -V_1^{Im\langle r,N_T\rangle}[k] & V_2^{Re\langle r,N_T\rangle}[k] \\ V_1^{Re\langle r,N_T\rangle}[k] & V_2^{Im\langle r,N_T\rangle}[k] \end{bmatrix}}_{\boldsymbol{\Theta}_k^{\langle r\rangle}} \boldsymbol{\lambda}_k^{\langle r\rangle}, \tag{3.134}$$

with $\boldsymbol{\lambda}_k^{\langle r\rangle} = \left[c^{\langle r\rangle}, H^{C\langle r\rangle}[k]\right]^T$. Thus, $\boldsymbol{\lambda}_k^{\langle r\rangle}$ can be estimated by

$$\hat{\boldsymbol{\lambda}}_k^{\langle r\rangle} = \left(\boldsymbol{\Theta}_k^{\langle r\rangle}\right)^\dagger \boldsymbol{\nu}_k^{\langle r\rangle}. \tag{3.135}$$

Afterwards, $c^{\langle r\rangle}$ and $h^{C\langle r\rangle}[n]$ can be calculated by:

$$\hat{c}^{\langle r\rangle} = \frac{1}{N_{D,P}} \sum_{k\in\mathfrak{I}_{D,P}} \left(\hat{\boldsymbol{\lambda}}_k^{\langle r\rangle}\right)_1, \quad \hat{\boldsymbol{h}}^{C\langle r\rangle} = \left(\boldsymbol{F}_{(\mathfrak{I}_{D,P},\mathcal{L})}\right)^\dagger \hat{\boldsymbol{H}}^C_{\mathfrak{I}_{D,P}}, \tag{3.136}$$

with $\mathfrak{I}_{D,P} := \left\{-\frac{N_{D,P}}{2},\ldots,-1,1,\ldots,\frac{N_{D,P}}{2}\right\}$, $\boldsymbol{h}^{C\langle r\rangle} := \left[h^{C\langle r\rangle}[0],\ldots,h^{C\langle r\rangle}[L_\mathrm{c}-1]\right]^T$, $\mathcal{L} := \{0,\ldots,L_\mathrm{c}-1\}$ and $\boldsymbol{H}^{C\langle r\rangle}$ is a length-N_P column vector with $\left(\boldsymbol{H}^{C\langle r\rangle}\right)_k = H^{C\langle r\rangle}[k]$. Note that Tx antenna diversity is exploited in this calculation. Moreover, the influence of GB is taken into account in (3.136). Finally, since $V_{1;2}^{Re;Im\langle r,i\rangle}[k]$ is a conjugate symmetrical function of k, the calculation of (3.135) only needs to be carried out for $1 \le k \le \frac{N_{D,P}}{2}$.

To further reduce computational complexity, the DFT block size of $V_{1;2}^{Re;Im,\langle r,i\rangle}[k]$ can be reduced to a number N_V which just has to be larger than $L_\mathrm{h}+L_\mathrm{c}+n_\tau$. Furthermore, instead of $\mathfrak{I}_{D,P}$, a proper subcarrier index set $\mathfrak{I}_{D,V}$, with $|\mathfrak{I}_{D,V}| = N_{D,V}$, should be defined according to the GB size and the sampling rate.

Finally, with (3.110) and (3.109), we can calculate $h_{\mathrm{D;I}}^{E\langle r,i\rangle}[n]$ i.e. also $H_{\mathrm{D;I}}^{E\langle r,i\rangle}[k]$.

3.5.5 Joint Estimation Scheme Based on Iterative CFO- and Rx-I/Q-Imbalance Estimation

This scheme is developed directly based on the compensation structure in Fig. 3.39. This scheme uses a similar preamble. First, the preamble is applied to estimate ϵ and $h^C[n]$ in an iterative manner. Afterwards, the influence of the CFO and Rx I/Q-imbalance on the preamble is eliminated. Finally, the coefficients $H_{\mathrm{D;I}}^{E\langle r,i\rangle}[k]$ are calculated.

Note that the basic idea of the CFO and Rx I/Q-imbalance estimation is similar to that in [123]. However, our scheme is developed based on an Rx-I/Q-imbalance compensation structure with real-valued coefficients, which allows lower computational complexity[1]. Moreover, practical extension is developed to cope with the troublesome cases of $\Omega \to 0$ and $\Omega \to \pm\pi$.

3.5.5.1 Preamble Design

This scheme applies a similar preamble design as in Sec. 3.5.4.1. The same basic sequence is applied for each Tx antenna. However, the repetition number of this basic sequence can be as low as two. Let N_{rep} be the number of repetitions, the total length of the preamble is $N_{\mathrm{CP}} + N_{\mathrm{rep}} * N_P$.

3.5.5.2 Estimation Scheme

For simplicity of description, we first assume $N_{\mathrm{rep}} = 2$. The extension to preambles with $N_{\mathrm{rep}} > 2$ will be shown later. Similar to Sec. 3.5.4.2, $\dot{y}_b^{\langle r\rangle}[n]$ indicates the received signal of the b^{th} repetition of the basic sequence. This estimation scheme is based on the observation that assuming perfect CFO knowledge, perfect Rx I/Q-imbalance compensation coefficients and no noise, we have for each Rx- antenna

$$\left(\dot{\boldsymbol{y}}_{\mathrm{re},1}^{\langle r\rangle} + j\dot{\boldsymbol{Y}}_{\mathrm{CB},1}^{\langle r\rangle}\boldsymbol{h}^{\mathrm{C,Ext},\langle r\rangle}\right) e^{j\Omega} = \dot{\boldsymbol{y}}_{\mathrm{re},2}^{\langle r\rangle} + j\dot{\boldsymbol{Y}}_{\mathrm{CB},2}^{\langle r\rangle}\boldsymbol{h}^{\mathrm{C,Ext},\langle r\rangle} \tag{3.137}$$

with

$$\begin{aligned}\dot{\boldsymbol{Y}}_{\mathrm{CB},b}^{\langle r\rangle} &= \left[\dot{\boldsymbol{y}}_{\mathrm{re},b}^{\langle r\rangle}, \dot{\boldsymbol{Y}}_{\mathrm{im},b}^{\langle r\rangle}\right] \\ \boldsymbol{h}^{\mathrm{C,Ext},\langle r\rangle} &:= \left[c, \left(\boldsymbol{h}^{\mathrm{C},\langle r\rangle}\right)^T\right]^T,\end{aligned} \tag{3.138}$$

where $\dot{\boldsymbol{Y}}_{\mathrm{im},b}^{\langle r\rangle}$ is an $N_P \times L_{\mathrm{c}}$ Toeplitz matrix with the n_τ^{th} column equal to $\dot{\boldsymbol{y}}_{\mathrm{im},b}^{\langle r\rangle}$.

[1] Both for parameter estimation and the actual compensation.

Eq. (3.137) can be rewritten as

$$\underbrace{\begin{bmatrix} \dot{\boldsymbol{y}}_{\mathrm{re},1}^{\langle r\rangle}\cos\Omega - \dot{\boldsymbol{y}}_{\mathrm{re},2}^{\langle r\rangle} \\ \dot{\boldsymbol{y}}_{\mathrm{re},1}^{\langle r\rangle}\sin\Omega \end{bmatrix}}_{\boldsymbol{T}_{\epsilon}^{\langle r\rangle}} = \underbrace{\begin{bmatrix} \dot{\boldsymbol{Y}}_{\mathrm{CB},1}^{\langle r\rangle}\sin\Omega \\ \dot{\boldsymbol{Y}}_{\mathrm{CB},2}^{\langle r\rangle} - \dot{\boldsymbol{Y}}_{\mathrm{CB},1}^{\langle r\rangle}\cos\Omega \end{bmatrix}}_{\boldsymbol{R}_{\epsilon}^{\langle r\rangle}} \boldsymbol{h}^{\mathrm{C,Ext},\langle r\rangle}. \tag{3.139}$$

According to (3.139), if ϵ is known, $\boldsymbol{h}^{\mathrm{C,Ext},\langle r\rangle}$ can be estimated by

$$\hat{\boldsymbol{h}}^{\mathrm{C,Ext},\langle r\rangle} = \boldsymbol{R}_{\epsilon}^{\langle r\rangle\,\dagger}\boldsymbol{T}_{\epsilon}^{\langle r\rangle}. \tag{3.140}$$

Thus, we first carry out an initial CFO estimation by

$$\hat{\epsilon}^{\mathrm{init}} = \frac{N}{2\pi N_P}\arg\left\{\left(\dot{\boldsymbol{y}}_1^T\right)^*\dot{\boldsymbol{y}}_2\right\}, \tag{3.141}$$

where $\dot{\boldsymbol{y}}_b, \forall b = 1,2$ is defined as in Sec. 3.5.4.2. Afterwards, the initial CFO estimate is applied to (3.140) to obtain an initial estimate of $\boldsymbol{h}^{\mathrm{C,Ext},\langle r\rangle}, \forall r$, which is used to carry out Rx I/Q-imbalance compensation on the received preambles:

$$\acute{\dot{\boldsymbol{y}}}_b^{\langle r\rangle} = \dot{\boldsymbol{y}}_{\mathrm{re},b}^{\langle r\rangle} + j\dot{\boldsymbol{Y}}_{\mathrm{CB},b}^{\langle r\rangle}\boldsymbol{h}^{\mathrm{C,Ext},\langle r\rangle}. \tag{3.142}$$

Now, the operation in (3.141) is applied again, but with $\acute{\dot{\boldsymbol{y}}}_b^{\langle r\rangle}$ instead of $\dot{\boldsymbol{y}}_b^{\langle r\rangle}$, to obtain a new estimate of ϵ. This new CFO estimate is applied again to (3.140) to obtain a new estimate of $\boldsymbol{h}^{\mathrm{C,Ext},\langle r\rangle}, \forall r$. Afterwards, Rx I/Q-imbalance compensation is carried out with this new estimate. This process is repeated iteratively until a predefined allowable iteration number is exceeded.

After all iterations, a final CFO- and Rx I/Q-imbalance compensation is carried out on the received preamble sequences according to Fig. 3.39. We denote the received preamble sequences after this compensation as $\check{\dot{\boldsymbol{y}}}_b^{\langle r\rangle}$. First, we carry out averaging over the two repetitions:

$$\bar{\dot{\boldsymbol{y}}}^{\langle r\rangle} = \frac{1}{2}\sum_{b=1}^{2}\check{\dot{\boldsymbol{y}}}_b^{\langle r\rangle}. \tag{3.143}$$

Let $\bar{\dot{\boldsymbol{Y}}}^{\langle r\rangle} := \boldsymbol{F}^{N_P}\bar{\dot{\boldsymbol{y}}}^{\langle r\rangle}$. If we ignore the noise influence, the following relation exists:

$$\bar{\dot{\boldsymbol{Y}}}_{\mathcal{I}_i}^{\langle r\rangle} = \boldsymbol{T}^{(i)}\boldsymbol{F}_{(\mathcal{I}_i,\mathcal{L}_{\mathrm{h}})}^{N_P}\boldsymbol{h}_{\mathrm{D}}^{E\langle r,i\rangle}, \quad \bar{\dot{\boldsymbol{Y}}}_{-\mathcal{I}_i}^{\langle r\rangle} = \acute{\boldsymbol{T}}^{(i)*}\boldsymbol{F}_{(-\mathcal{I}_i,\mathcal{L}_{\mathrm{h}})}^{N_P}\boldsymbol{h}_{\mathrm{I}}^{E\langle r,i\rangle}. \tag{3.144}$$

Finally, we can obtain the MLE

$$\hat{\boldsymbol{h}}_{\mathrm{D}}^{E\langle r,i\rangle} = \mathfrak{T}_{\mathrm{D}}^{(i)}\boldsymbol{T}^{(i)*}\bar{\dot{\boldsymbol{Y}}}_{\mathcal{I}_i}^{\langle r\rangle}, \ \hat{\boldsymbol{h}}_{\mathrm{I}}^{E\langle r,i\rangle} = \mathfrak{T}_{\mathrm{I}}^{(i)}\acute{\boldsymbol{T}}^{(i)}\bar{\dot{\boldsymbol{Y}}}_{-\mathcal{I}_i}^{\langle r\rangle} \tag{3.145}$$

and the LMMSE

$$\hat{\boldsymbol{h}}_{\mathrm{D}}^{E\langle r,i\rangle} = \mathfrak{Q}_{\mathrm{D}}^{(i)} \boldsymbol{T}^{(i)*} \bar{\dot{\boldsymbol{Y}}}_{\jmath_i}^{\langle r\rangle}, \; \hat{\boldsymbol{h}}_{\mathrm{I}}^{E\langle r,i\rangle} = \mathfrak{Q}_{\mathrm{I}}^{(i)} \acute{\boldsymbol{T}}^{(i)} \bar{\dot{\boldsymbol{Y}}}_{-\jmath_i}^{\langle r\rangle}, \tag{3.146}$$

where $\mathfrak{T}_{\mathrm{D;I}}$ and $\mathfrak{Q}_{\mathrm{D;I}}$ are defined as in (3.126) and (3.128), respectively. Finally, we calculate $\hat{H}_{\mathrm{D;I}}^{E\langle r,i\rangle}[k] = \mathcal{F}_N \left\{ \hat{h}_{\mathrm{D;I}}^{E\langle r,i\rangle}[n] \right\}$.

Similar to the scheme in Sec. 3.5.4.2, the estimation scheme above will have poor performance when $\Omega \to 0$ or $\Omega \to \pm\pi$. The reason is that this scheme utilizes the phase rotation caused by CFO to identify the Rx I/Q-imbalance characteristic. However, this identification is impossible when $\Omega = 0$ or $\Omega = \pm\pi$. Actually, if we ignore the noise in these cases, $\boldsymbol{R}_{\epsilon}^{\langle r\rangle}$ and $\boldsymbol{T}_{\epsilon}^{\langle r\rangle}$ in (3.140) will become zero-valued.

To avoid this problem, we observe the following relation:

$$\frac{1}{N_P} E\left\{ \left\| \dot{\boldsymbol{y}}_1 e^{\jmath\Omega} - \dot{\boldsymbol{y}}_2 \right\|_2^2 \right\} \geq 2\tilde{\sigma}_{\mathrm{n}}^2, \tag{3.147}$$

from which the following soft-metric can be defined:

$$P'_{\Delta} := \frac{1}{N_P} \left\| \dot{\boldsymbol{y}}_1 e^{\jmath \frac{2\pi \hat{\epsilon} N_P}{N}} - \dot{\boldsymbol{y}}_2 \right\|_2^2 - 2\zeta\tilde{\sigma}_{\mathrm{n}}^2, \tag{3.148}$$

with ζ an adjusting factor. If $P'_{\Delta} > 0$, the iterative estimation scheme can be applied. However, if $P'_{\Delta} \leq 0$, we can assume that $\Omega \to 0$ or $\Omega \to \pm\pi$. In this case, we should omit the iterative estimation. Moreover, the initial CFO is used to carry out CFO correction on the received preamble. Based on the corrected preamble, joint Tx- and Rx I/Q-imbalance and MIMO channel estimation is carried out with the FDS-preamble based scheme in Sec. 3.4.6. This implies that no separate Rx I/Q-imbalance compensation is applied.

The proposed estimation scheme can be easily applied to preambles containing more than two repetitions of the basic sequence. To enable this, we just need to reorder the multiple basic repetitions into two augmented repetitions. These two augmented repetitions are allowed to have overlapped areas.

3.5.6 Simulation Results

3.5.6.1 Simulation Setups

The I/Q-imbalance parameters in Sec. 3.4.8 were applied. Moreover, the measured 60 GHz channels in [106] were used. As in Sec. 3.4.8, the following OFDM parameter sets are investigated: $N = 256, N_0 = 17$ and $N = 512, N_0 = 91$. Furthermore, we apply $N_T = 2, N_R = 2$, $L_{\mathrm{h}} = 32$ and $L_{\mathrm{c}} = 8$. Both the CLFE-based scheme in Sec. 3.5.4 (indicated as "SCH1") and the iterative scheme in Sec. 3.5.5 (indicated as "SCH2") were applied to estimate CFO, Tx- and Rx I/Q-imbalance and the MIMO channel. For "SCH1", the LSE (applying (3.122)) and

the LMMSE estimation (applying (3.123)) of $\dot{\mathfrak{z}}^{\langle r\rangle}$ are compared[1]. For "SCH2", the application of the real valued Rx-I/Q-imbalance compensation structure in Fig. 3.39 and that of a complex valued Rx-I/Q-imbalance compensation structure (as described in App. B.8 or in [123]) are compared. For both "SCH1" and "SCH2", both MLE and LMMSE[2] of $H^{E}_{\mathrm{D;I}}$ (corresponding to (3.125), (3.145) and (3.127), (3.146), respectively) are compared. When applying LMMSE, we assume a fixed value $10\log_{10}\rho^{\langle r\rangle} = 30\mathrm{dB}, \forall r$ for the calculation of $\mathfrak{Q}_{\mathrm{D;I}}$. For a fair comparison between "SCH1" and "SCH2", the same preamble was applied. No matter $N = 256$ or $N = 512$, the applied preamble consists of 3 repetitions of a basic sequence with $N_P = 256$ [3]. Thus, the total preamble length was 800. To apply "SCH2", the three repetitions were reordered to two augmented repetitions of length-512 [4] as described in Sec. 3.5.5.2.

As reference, the original iterative estimation scheme of [123] was also applied, which is indicated as "Hsu". This scheme uses a non-optimal preamble, which consists of two parts. The first part consists of M_{ST} repetitions of a length-N_{ST} short training sequence and is used for CFO and Rx-I/Q-imbalance estimation. The second half consists of M_{LT} repetitions of a length-N_{LT} long training sequence (each is attached a CP)[5] and is used for the estimation of $H^{E}_{D;I}[k], \forall k$. Thus, the total preamble length is $N_{TL} = M_{ST}N_{ST} + M_{LT}N_{LT} + (M_{LT}+1)N_{\mathrm{CP}}$. Two cases of the "Hsu" scheme were observed. The first case (indicated as "Hsu S") is that "Hsu" has the same preamble length as "SCH1/SCH2" i.e. $N_{TL} = 800$. Correspondingly, $M_{ST} = 5, N_{ST} = 64, M_{LT} = 2$ and $N_{LT} = 192$. The second case (indicated as "Hsu L") is that the first part of the preamble is already of length 800, with $M_{ST} = 12, N_{ST} = 64$. The second part of the preamble contains of $M_{LT} = 2$ OFDM symbols of regular length ($N_{LT} = N$). We will show that even with such a long preamble, "Hsu L" is still outperformed by our proposed schemes. Note that the CFO- and Rx-I/Q-imbalance estimation scheme of "Hsu" is almost the same as that of "SCH2,C" (App. B.8), except for the soft switching. To apply the "Hsu" scheme, the short training sequences are reordered into two augmented repetitions. The first- and the second augmented repetitions contain the first- and the last $(M_{ST}-1)^{\mathrm{th}}$ short training sequences, respectively.

Tab. 3.6 gives an overview of the abbreviation used in the simulation results. Tab. 3.7 lists the preamble overhead of the different schemes.

[1] Since the estimation of $\dot{\mathfrak{z}}^{\langle r\rangle}$ corresponds to the separation of $\dot{\boldsymbol{z}}^{\langle r\rangle}_{\mathrm{D}}$ and $\dot{\boldsymbol{z}}^{\langle r\rangle}_{\mathrm{I}}$, it is indicated by "SEP" in the simulation results.

[2] Both MLE and LMMSE can be decomposed in to two steps:1) LSE of coefficients on pilot subcarriers; 2) Interpolation of the LSE. Since the difference between MLE and LMMSE only lies in the interpolation, the corresponding simulation results are indicated by "INTP".

[3] Note that the preamble length is not directly related to the OFDM symbol length but the parameters N_T and L_{h} (see Sec. 3.5.4.1).

[4] With an overlapping area.

[5] These long training sequences are constructed as OFDM symbols whose subcarriers have constant amplitude and random phases.

Table 3.6: Abbreviations in Simulation Results

Abbreviation	Meaning
SCH1	The CLFE-based joint estimation scheme in Sec. 3.5.4
SCH2	The iterative joint estimation scheme in Sec. 3.5.5
SEP1	For SCH1: Estimation of $\dot{\mathbf{3}}^{\langle r \rangle}$ using LSE i.e. applying (3.122)
SEP2	For SCH1: Estimation of $\dot{\mathbf{3}}^{\langle r \rangle}$ using LMMSE i.e. applying (3.123)
R	For SCH2: apply the real valued Rx-I/Q-imbalance compensation structure (Sec. 3.5.5.2)
C	For SCH2: apply the complexed valued Rx-I/Q-imbalance compensation structure as in [123]
INTP1	For SCH1/SCH2: using the MLE in (3.125) or (3.145), respectively
INTP2	For SCH1/SCH2: using the LMMSE in (3.127) or (3.146), respectively
Hsu,S	The scheme in [123], with a preamble of length-800
Hsu,L	The scheme in [123], with a much longer preamble

Table 3.7: Preamble Overheads of Different Schemes (in Number of Samples)

Schemes	$N = 256$	$N = 512$
SCH1;SCH2;Hsu,S	800	800
Hsu,L	1376	1888

3.5.6.2 Estimation MSE as a Function of The CFO Value

Fig. 3.40 and 3.41 show the estimation MSEs[1] of the CFO, the Rx-I/Q-imbalance compensation coefficients and $H^E_{\mathrm{D;I}}$ as functions of ϵ ($N = 256$) [2]. While Fig. 3.40 shows the case with relatively low SNR (20 dB), Fig. 3.41 shows the case with relatively high SNR (35 dB). For comparison, the CFO estimations of (3.118), indicated by "Cosine", and that of (3.119), indicated "Rough", are included. As shown, the CFO MSEs of both the "Cosine"- and the "Rough" estimators depend strongly on ϵ. With $SNR = 20$ dB, the "Rough" estimator outperforms the "Cosine" estimator for a large range of ϵ values. However, with $SNR = 35$ dB, the "Cosine" estimator has lower MSE within the major ϵ range (except for ϵ values close to 0 or 0.5). For both SNR values, the soft switching method and iterative improvement proposed in "SCH1" allows MSE that is equal to or lower than the lower one between "Cosine" and "Rough". Especially with $SNR = 20$ dB, "SCH1" with "SEP2" can achieve much lower MSE than both "Cosine" and "Rough". Compared to "SCH1", both "SCH2" and Hsu's schemes have CFO MSE that is less dependent on ϵ, where "Hsu,S" has relatively high MSE floor. With most of the ϵ values, "SCH2,R/C" leads to the lowest CFO MSE.

With all the proposed schemes, the MSEs of the Rx-I/Q-imbalance compensation coefficients and $H^E_{\mathrm{D;I}}$ show "U" shapes over the observed ϵ range. The highest MSE are found with ϵ

[1] Unnormalized MSE is used for the estimation of both CFO- and Rx-I/Q-imbalance compensation coefficients, while normalized MSE is used for the estimation of $H^E_{\mathrm{D;I}}$.

[2] Since the MSE behavior with $\epsilon < 0$ is generally symmetric to that with $\epsilon > 0$, we only show the case with $\epsilon > 0$. Furthermore, the results with $N = 512$ are similar. When $N = 512$, the observed ϵ range becomes $0 \sim 1$.

values close to 0 or 0.5. The reason was that with such values, the distance between $e^{j\Omega}$ and $e^{-j\Omega}$ becomes quite small, leading to difficulties in the identification of the mirror interference generated by Rx-I/Q-imbalance. Although Hsu's schemes can achieve similar Rx-I/Q-imbalance MSE as the proposed schemes, they have much poorer estimations of $H^E_{\mathrm{D;I}}$ due to non-optimized preamble design [1]. Note that the "Hsu,S/L" schemes do not have MSE increase for ϵ values close to 0.5, since a smaller repetition distance was applied ($N_{ST} = 64$), which allows a larger range of CFO estimation range.

By comparing the MSE results of CFO and Rx-I/Q-imbalance compensation coefficients, we can see that: For "SCH1", "SEP1" allows better estimation of Rx-I/Q-imbalance compensation coefficients, while "SEP2" can lead to better CFO estimation[2]. Thus, we suggest to apply "SEP2" within the iterations to obtain CFO estimation and to apply "SEP1" in the final iteration to obtain the estimation of Rx-I/Q-imbalance compensation coefficients.

3.5.6.3 Estimation MSE as a Function of SNR

Fig. 3.42 and 3.43 show the estimation MSE of all relevant quantities as functions of SNR with $\{N = 256, N_0 = 17, \epsilon = 0.25\}$ and $\{N = 512, N_0 = 91, \epsilon = 0.5\}$, respectively. As reference, the CRLBs are included. As shown, the proposed schemes can achieve MSE close to the CRLB. It is also shown that the performance difference between MLE ("INTP1") and LMMSE ("INTP2") is significant only when the GB is relatively large [3]. As mentioned in Sec. 3.5.4.2 and 3.5.5.2, with a fixed assumed ρ value, the computational complexity of the LMMSE is identical to that of the MLE. Thus, we suggest to apply LMMSE. Furthermore, the CFO- and Rx-I/Q-imbalance MSE of the proposed schemes are similar to that of "Hsu,L" scheme, while the MSE of $H^E_{\mathrm{D;I}}$ with the proposed schemes (applying LMMSE) is much lower than that with Hsu's scheme. Remember that the "Hsu,L" scheme requires much higher preamble overhead than the proposed schemes (see Tab. 3.7).

3.5.6.4 Estimation MSE as a Function of the Iteration Number

Fig. 3.44 and 3.45 show the MSE of all related quantities as a function of the iteration number N_I with $\{N = 256, \epsilon = 0.15, SNR = 20\,\mathrm{dB}\}$ and $\{N = 256, \epsilon = 0.1, SNR = 35\,\mathrm{dB}\}$, respectively. The results for other ϵ- and SNR values as well as with $N = 512$ were found to be similar[4]. As shown, with $SNR = 20$ dB, all the schemes have MSE improvement of CFO estimation at the first iteration, where the improvement of "SCH2" is larger than that of "SCH1". We can also observe that further iteration only leads negligible improvement or even slight degradation. In contrast, the MSE of the Rx-I/Q-imbalance compensation coefficients and $H^E_{\mathrm{D;I}}$ with all

[1] Non-optimized in avoidance of inter-Tx-antenna interference and mirror interference.
[2] Better CFO estimation of "SEP2" is mainly achieved in the case of relatively low SNR.
[3] For "SCH1", the choice between MLE and LMMSE affects both the estimation of the Rx-I/Q-imbalance compensation coefficients and $H^E_{\mathrm{D;I}}$. However, for "SCH2", this choice only has influence on the estimation of $H^E_{\mathrm{D;I}}$.
[4] For "SCH1", the iteration gain of CFO estimation decreases as ϵ approaches 0.25 (for $N = 256$), since both "Cosine"- and "Rough" estimators can already provide very good estimation accuracy.

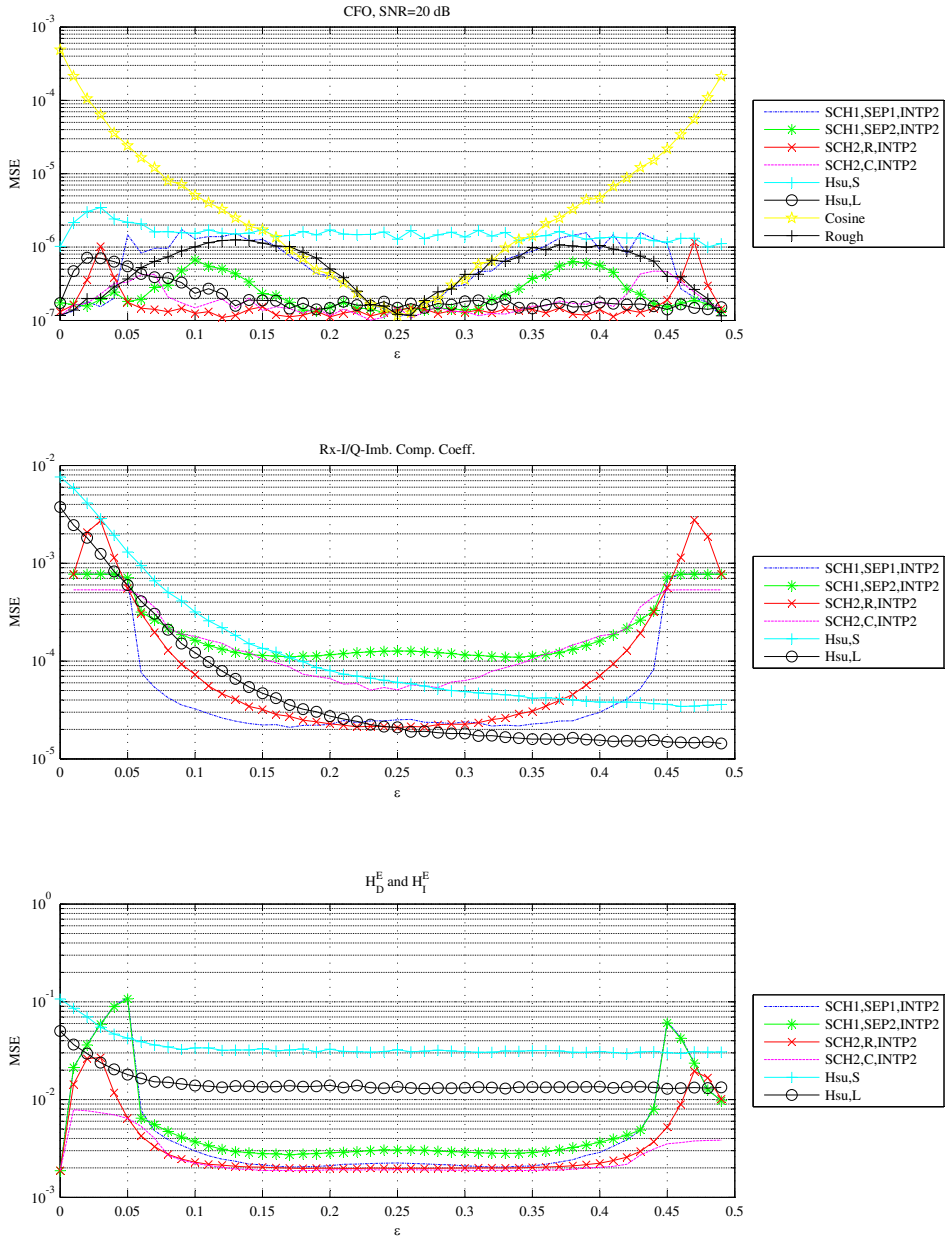

Figure 3.40: Estimation MSE as functions of ϵ with $N_I = 1, N = 256, SNR = 20$ dB.

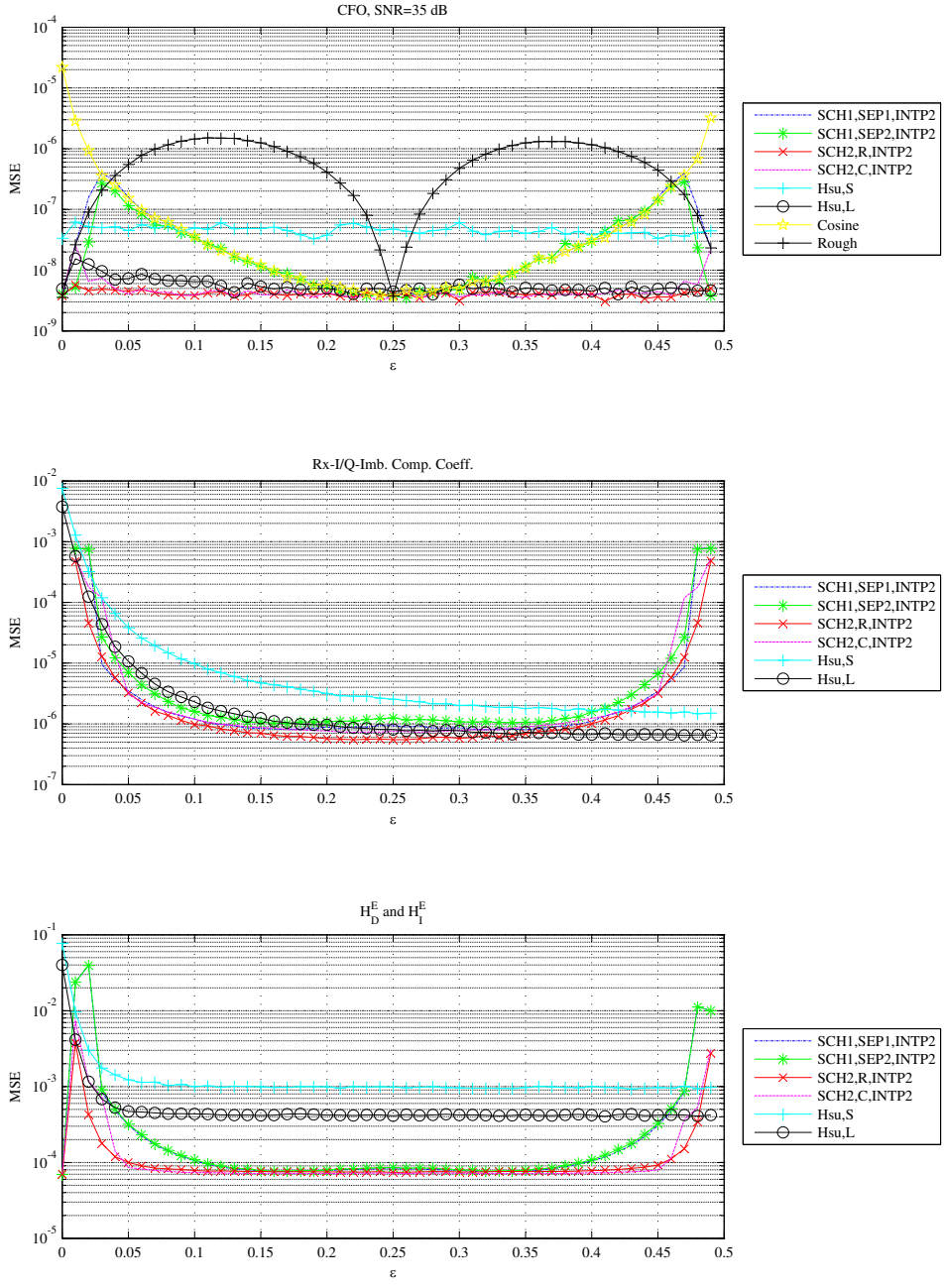

Figure 3.41: Estimation MSE as functions of ϵ with $N_I = 1, N = 256, SNR = 35$ dB.

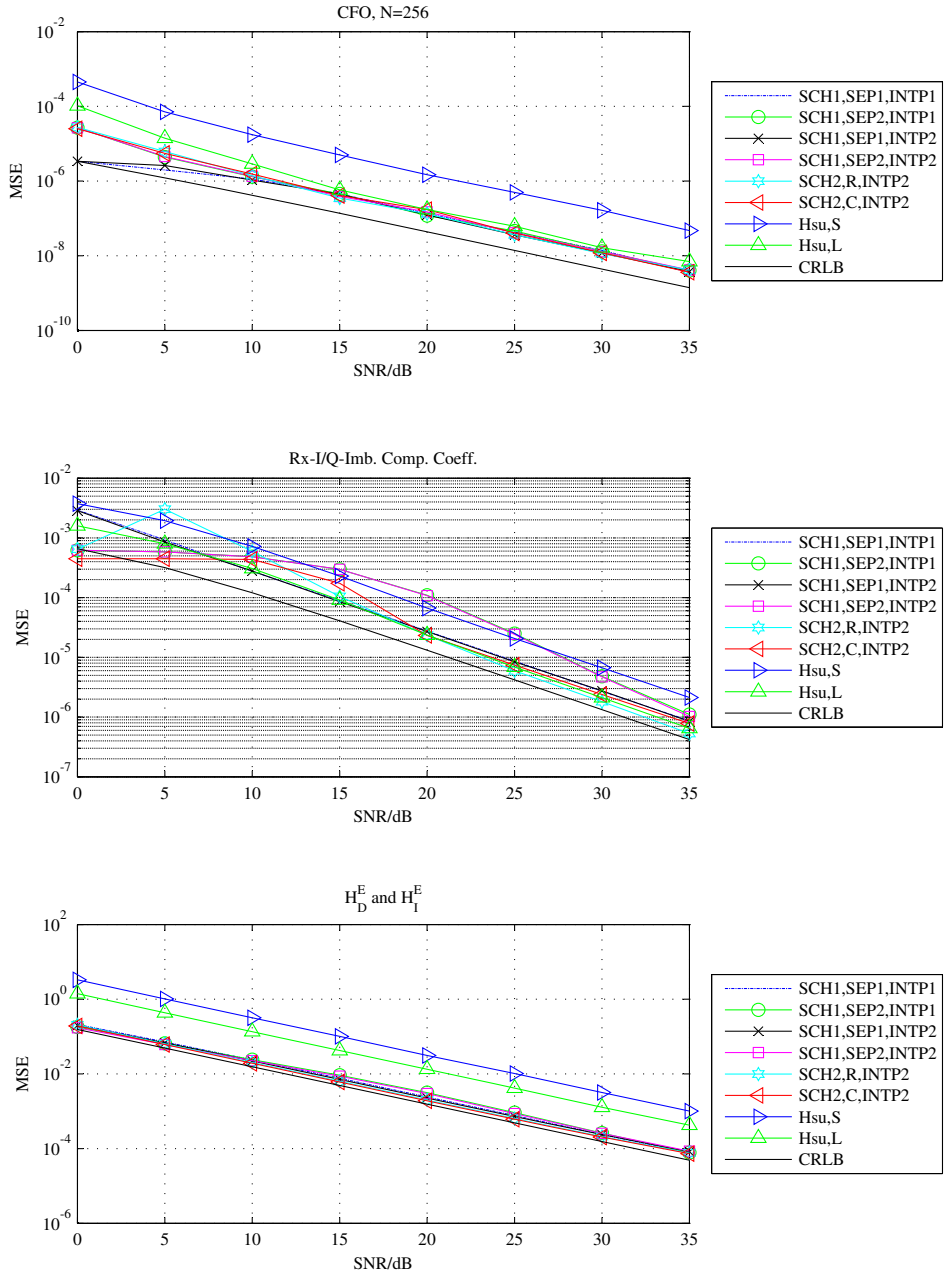

Figure 3.42: Estimation MSE as functions of SNR, $N_I = 1, N = 256, \epsilon = 0.25$

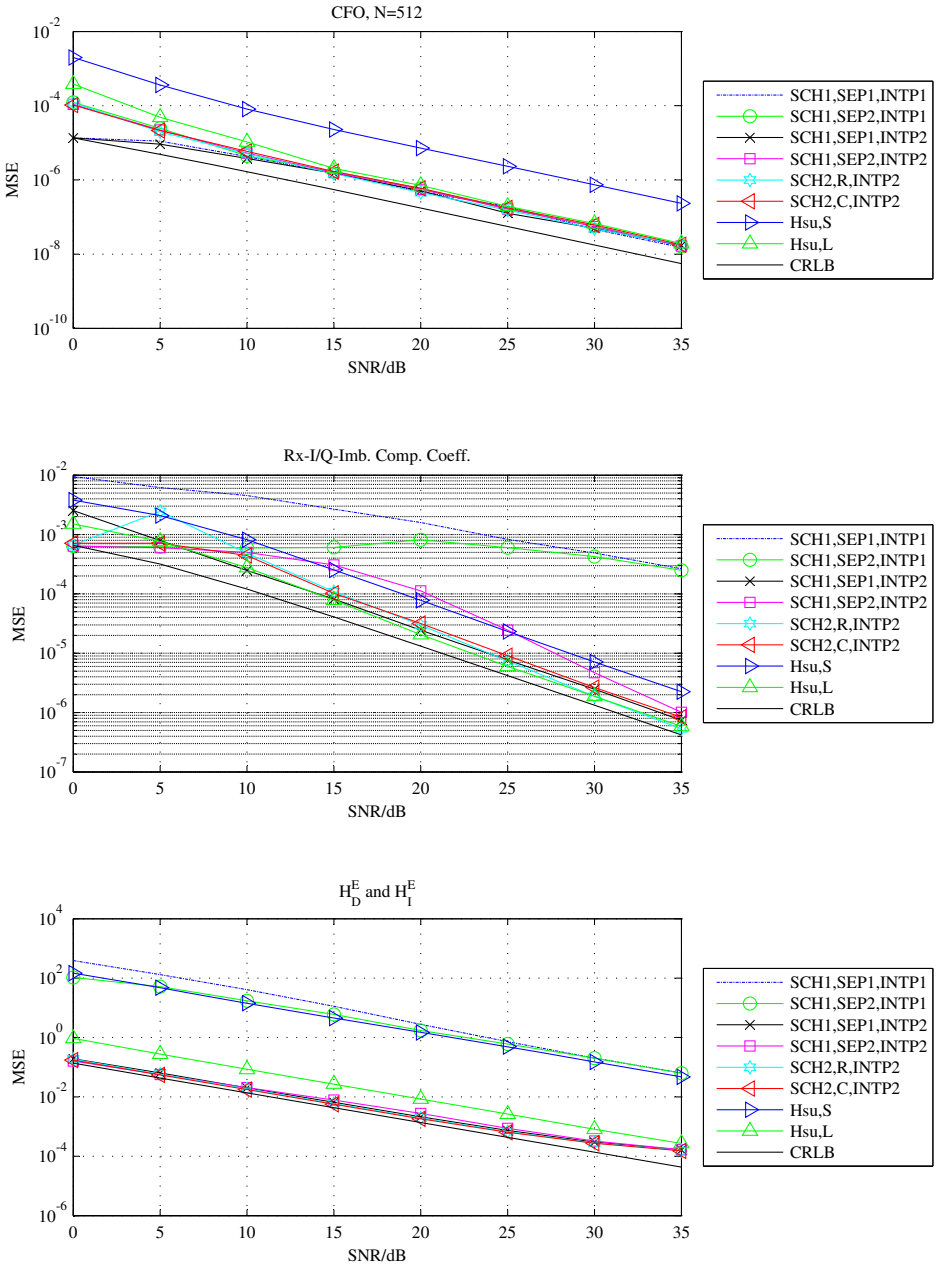

Figure 3.43: Estimation MSE as functions of SNR, $N_I = 1, N = 512, \epsilon = 0.5$

schemes is quite independent of N_I. With $SNR = 35$ dB, the schemes "SCH2" and "Hsu" have MSE improvement at the 1st iteration for both CFO- and $H^E_{\mathrm{D;I}}$ estimation, while almost no iteration gain can be observed for the estimation of Rx-I/Q-imbalance compensation coefficients. Furthermore, with this SNR value, "SCH1" does not benefit from iterative processing. By comparing Fig. 3.44 and 3.45, we can see that for the schemes "SCH2" and "Hsu", the higher the SNR, the larger the iteration gain (only for CFO and $H^E_{\mathrm{D;I}}$). In contrast, "SCH1" only benefits from iterative processing for CFO estimation at relatively low SNR region. Based on these results, we suggest to apply $N_I = 1$ for all the schemes to achieve a tradeoff between performance and complexity.

3.5.6.5 BER as Functions of SNR and The CFO Value

Except for the cases with the proposed schemes and Hsu's schemes, the following cases are also included in the BER simulation as reference: 1) With a CFO- and channel estimation and compensation scheme ignoring I/Q-imbalance ("No I/Q-Comp."); 2) Applying the compensation in Sec. 3.5.3 with perfect parameter estimation ("Perf. Est."); 3) Without impairments and assuming perfect channel estimation ("No Imp."). In the simulations, the CFO value was evenly distributed between 0 and $\frac{0.45N}{N_P}$. To avoid influence of residual CFO, only 8 OFDM symbols are transmitted within each signal frame [1]. The used modulation scheme was 16-QAM. Moreover, subcarrier-wise STC and ZF equalization (see Sec. 3.5.3) were applied. "Preamble-boosting" of 8 dB was applied for all schemes requiring parameter estimation. Fig. 3.46 and 3.47 show the BER as functions of SNR for $N = 256, N_0 = 17$ and $N = 512, N_0 = 91$, respectively. As shown, provided perfect parameters, the performance with the compensation in Sec. 3.5.3 can be as good as that without impairments. We can also see that the SNR losses (due to parameter estimation error) of the proposed schemes with "INTP2" are relatively small (within 0.9 dB)[2]. Note that the longer the OFDM symbol, the more ICI and CPE are caused by residual CFO. This may be the reason for the slightly higher SNR loss with $N = 512, N_0 = 91$. In contrast to the proposed schemes, both the "Hsu S/L" schemes and the scheme ignoring I/Q-imbalance have error floors. While the latter scheme suffers from model mismatch, the scheme in [123] mainly suffers from large estimation error of $H_{\mathrm{I}}^{E\langle r,i\rangle}[k], \forall k$, which is resulted from a non-optimized preamble design.

Fig. 3.48 shows the BER as a function of ϵ for both $N = 256, N_0 = 17$ and $N = 512, N_0 = 91$. As shown, these results comply with the MSE results in Fig. 3.40. Slight BER increase can be observed at about $\frac{\epsilon N_P}{N} = 0.05$ and $\frac{\epsilon N_P}{N} = 0.5$. Note that at both $\epsilon = 0$ and $\frac{\epsilon N_P}{N} = 0.5$, the separate Rx-I/Q-imbalance compensation is deactivated[3]. For $\epsilon = 0$, Rx-I/Q-imbalance can be co-modeled by $H^E_{\mathrm{D;I}}$. Thus, no model mismatch is present and no BER increase is observed. In contrast, $\frac{\epsilon N_P}{N} = 0.5$, Rx-I/Q-imbalance can not be co-modeled by $H^E_{\mathrm{D;I}}$ due to the CFO influence. The corresponding model mismatch results in considerable BER increase.

[1] This is just a simulation example to investigate the performance without the need of phase tracking.
[2] There is only small performance difference between the proposed schemes with "INTP2".
[3] Since separate estimation of the corresponding coefficients is impossible, see Sec. 3.5.4.2 and 3.5.5.2

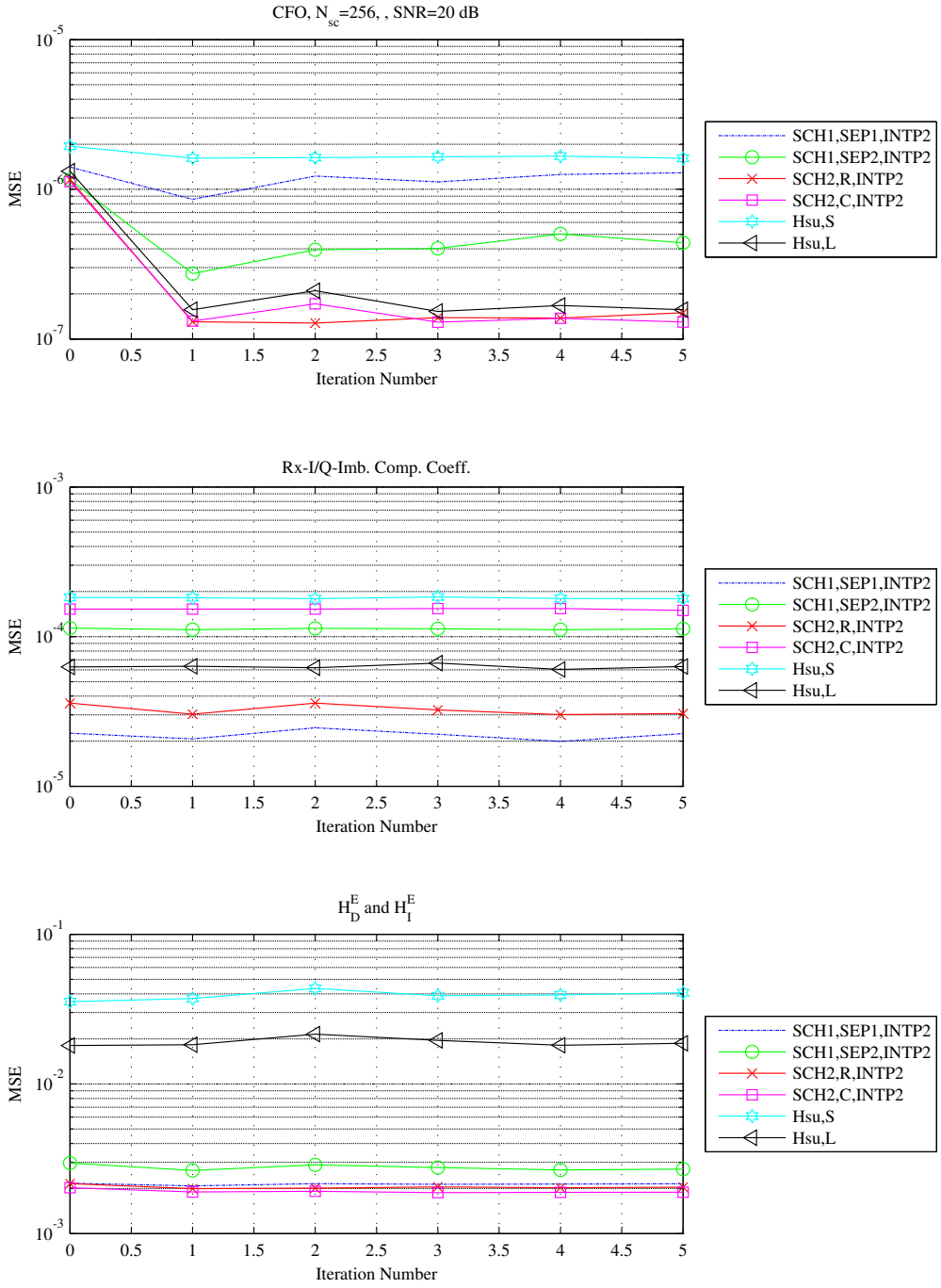

Figure 3.44: Estimation MSE as functions iteration number, $N = 256, \epsilon = 0.15$ and $SNR = 20$ dB.

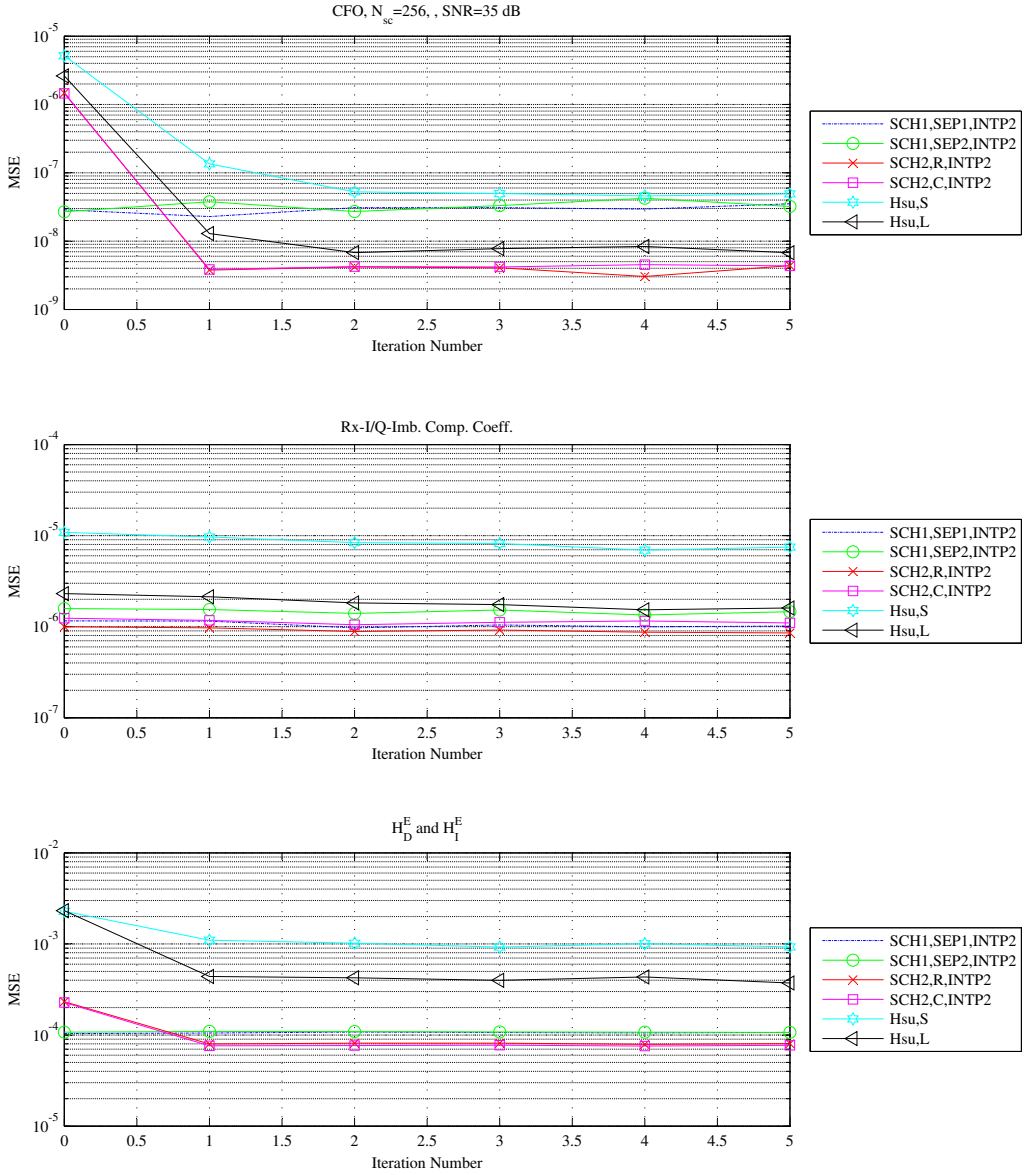

Figure 3.45: Estimation MSE as functions iteration number, $N = 256, \epsilon = 0.1$ and $SNR = 35$ dB.

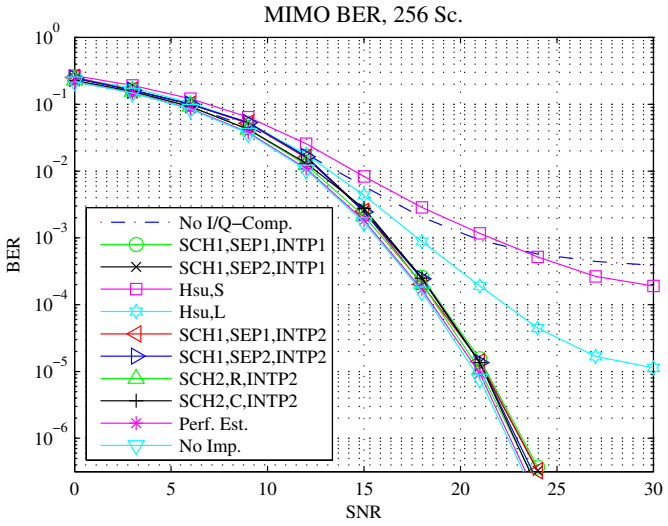

Figure 3.46: BER performance as a function of SNR, $N = 256, N_0 = 17$

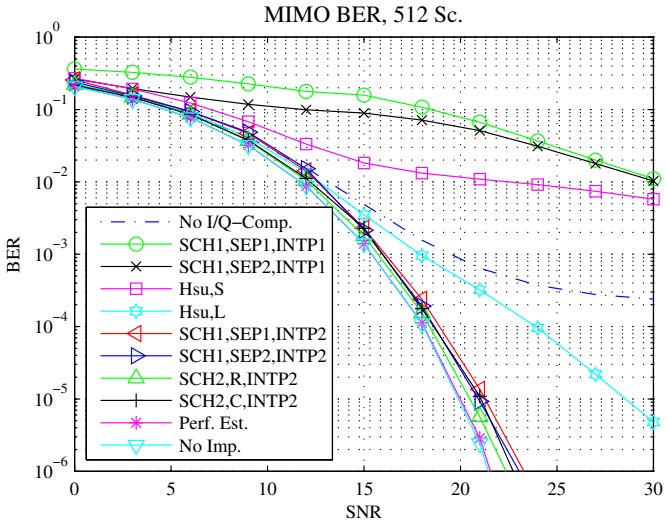

Figure 3.47: BER performance as a function of SNR, $N = 512, N_0 = 91$

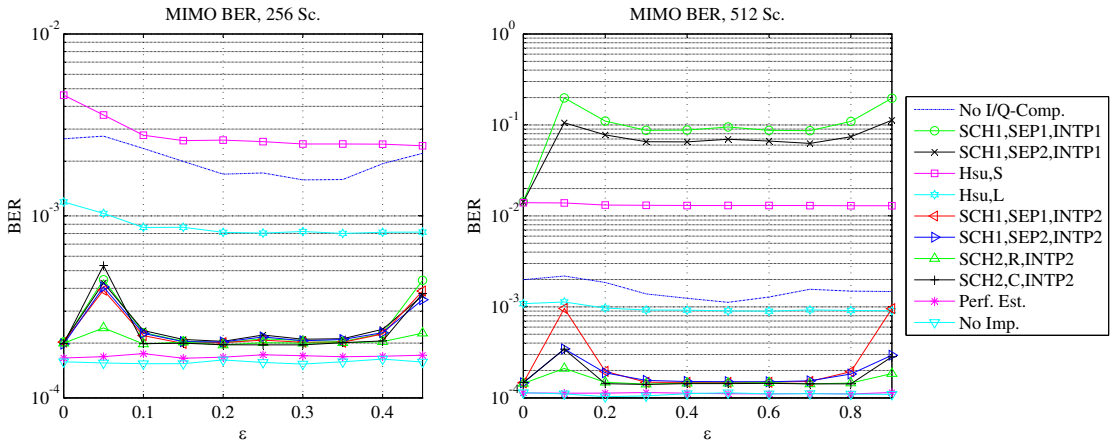

Figure 3.48: BER performance as a function of CFO. Left: $N = 256, N_0 = 17$; Right: $N = 512, N_0 = 91$; $SNR = 18$ dB

3.5.7 Computational Complexity Issues and Discussion

Similar to Sec. 3.4.9, the computational complexity is divided into three parts: parameter estimation, equalization matrix calculation and the actual compensation.

3.5.7.1 Computational Complexity of Parameter Estimation

Tab. 3.8 shows the computational complexity expressions of different schemes (in number of real MULs). By applying the simulation parameters, Fig. 3.49 can be obtained, which shows the number of required real MULs as a function of N_I for different schemes. As shown, the "Hsu" schemes have the highest computational complexity. The main reason is the inefficient calculation of $H^E_{\mathrm{D;I}}$ (see [90, 123]). Furthermore, "SCH1" has much lower computational complexity than "SCH2". The main reason was that the pseudo-inverse computation in (3.140) of "SCH2,R" and that in (B.8.26) of "SCH2,C" are quite costly. Compared to "SCH2,C", "SCH2,R" has lower computational complexity, since real valued computation is applied which considerably eased the pseudo-inverse computation in (3.140).

3.5.7.2 Computational Complexity of Equalization Matrix Calculation and the Actual Compensation

Tab. 3.9 and Tab. 3.10 summarize the computational complexity expressions of three different schemes for the calculation of equalization matrices and for the actual compensation, respectively. The three schemes only differ in the compensation method of the Tx-I/Q-imbalance and MIMO channel. These schemes include: 1) The applied joint Tx-I/Q-imbalance and MIMO channel compensation in Sec. 3.5.3 (indicated by "Joint Tx IQ+Ch.") [1]; 2) The separate Tx-

[1]The corresponding matrix equations can be found in Sec. 3.4.3.

Table 3.8: Computational Complexity of Different Schemes

Scheme	**Number of real MULs (per Rx antenna)**
SCH1	$352 + 8L_{\mathrm{c}}N_R + N_P N_R(129 + 2\log_2 N_P) + 2\,[22N_I(4 + N_P N_R)$ $+N_R N_T(4L_{\mathrm{h}} + 8L_{\mathrm{c}}L' + 2N\log_2 N + 4n_\tau + N_V \log_2 N_V)$ $+2N_R N_{V,D}(1 + L_{\mathrm{c}} + 10N_T)]$
SCH2,R	$2N_P + 2N_R N_P \log_2 N_P + 8L_{\mathrm{h}}L' N_R N_T + 4N_T N_R N \log_2 N +$ $4N_R N_{\mathrm{rep}} N_P + \frac{1}{3}N_R(N_I + 1)\,[(60 + 3N_{\mathrm{rep}})N_P +$ $L_{\mathrm{c}}\,(2 + 30N_P + L_{\mathrm{c}}(3 + L_{\mathrm{c}} + N_P) + 3N_{\mathrm{rep}}N_P)]$
SCH2,C	$2N_P + 2N_R N_P \log_2 N_P + 8L_{\mathrm{h}}L' N_R N_T + 4N_T N_R N \log_2 N +$ $4N_R N_{\mathrm{rep}} N_P + \frac{4}{3}N_R(N_I + 1)\,\big[9N_P + L_{\mathrm{c}}(-1 + L_{\mathrm{c}}^2 + 6N_P$ $+3L_{\mathrm{c}}N_P + 3N_{\mathrm{rep}}N_P)]$
Hsu	$2(M_{ST} - 1)N_{ST} + 44NN_T N_R \log_2 N + \frac{8}{3}L_{\mathrm{h}}N_T\,\big(-1 + 4L_{\mathrm{h}}^2 N_T^2$ $+3M_{LT}N_{LT}(N_R + 4N_T L_{\mathrm{h}})) + 4NRN_{TL} + \frac{4}{3}N_R(1 + N_I)$ $\big(9(M_{ST} - 1)N_{ST} + L_{\mathrm{c}}\,\big(-1 + L_{\mathrm{c}}^2 + (6 + 3L_{\mathrm{c}})(M_{ST} - 1)N_{ST} + 3N_{TL}\big)\big)$

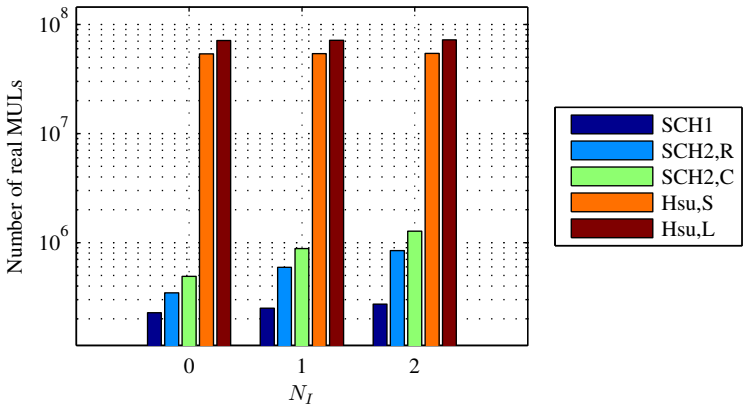

Figure 3.49: Numbers of required real MULs for different schemes as a function of N_I, $N = 256, N_0 = 17$

I/Q-imbalance and MIMO channel compensation in [90] (indicated by "Sep. Tx IQ+Ch."). In [90], general MIMO structures of Linear-Dispersion (LD) codes are considered, with STC and SM as special cases. It was assumed that at each subcarrier, n_s data symbols are encoded in κ consecutive OFDM symbols slots over N_T Tx antennas. Furthermore, in this scheme, the Tx-I/Q-imbalance is conducted subcarrier-wise in frequency domain; 3) The Tx-I/Q-imbalance is assumed to be already compensated for at the Tx (indicated by "No Tx IQ-Imb"). For all schemes, both real- and complex valued FIR filters (see Sec. 3.4.3 and Sec. B.8, respectively) are applied to compensate Rx-I/Q-imbalance (indicated by "R" and "C", respectively). The CFO compensation is done as described in Sec. 3.4.3. For simplicity, only ZF-equalization and STC are considered.

Table 3.9: Computational Complexity Expressions for Equalization Matrix Computation

Scheme	Nr. of real MULs
Joint Tx IQ+Ch.	$\frac{4}{3}N_D N_T(-1+4(1+6N_R)N_T^2)$
Sep. Tx IQ+Ch.	$\frac{2}{3}N_D n_s(-2+12\kappa^2 N_R^2+8n_s^2+3\kappa N_R(16n_s+N_T))$
No Tx IQ-Imb.	$\frac{4}{3}N_D N_T(-1+(1+6N_R)N_T^2)$

Table 3.10: Computational Complexity Expressions for the Actual Compensation

Scheme	Nr. of real MULs (per data symbol)
Joint Tx IQ+Ch.,R	$\frac{(6+L_c)N_R(N_{\mathrm{CP}}+N)}{N_D}+8N_T N_R$
Joint Tx IQ+Ch.,C	$\frac{(5+4L_c)N_R(N_{\mathrm{CP}}+N)}{N_D}+8N_T N_R$
Sep. Tx IQ+Ch.,R	$\frac{\kappa N_R((6+L_c)N_{\mathrm{CP}}+4N_D(\kappa N_R+n_s)+(6+L_c)N)}{N_D n_s}$
Sep. Tx IQ+Ch.,C	$\frac{\kappa N_R((5+4L_c)N_{\mathrm{CP}}+4N_D(\kappa N_R+n_s)+(5+4L_c)N)}{N_D n_s}$
No Tx IQ-Imb.,R	$\frac{(6+L_c)N_R(N_{\mathrm{CP}}+N)}{N_D}+4N_T N_R$
No Tx IQ-Imb.,C	$\frac{(5+4L_c)N_R(N_{\mathrm{CP}}+N)}{N_D}+4N_T N_R$

With the simulation parameters, the complexity comparison in Fig. 3.50 and Fig. 3.51 can be obtained[1]. As shown in Fig. 3.50, the "Sep. Tx IQ+Ch." scheme requires the highest computational complexity for equalization matrix calculation. The reason is that the subcarrier-wise calculation of the Tx-I/Q-imbalance compensation coefficients in [90] is quite costly. Complexity reduction can be achieved by selecting just a subset of subcarriers where such coefficients are calculated. Afterwards, interpolation should be applied. Compared to the "Sep. Tx IQ+Ch." scheme, the "Joint Tx IQ+Ch" scheme has lower computational complexity. Compared to both "Sep. Tx IQ+Ch."- and "Joint Tx IQ+Ch" schemes, the scheme assuming no Tx-I/Q-imbalance has much lower computational complexity.

Fig. 3.51 shows that for the actual compensation of all schemes, using complex FIR filters for Rx-I/Q-imbalance compensation requires much higher complexity than using real valued FIR filters. Furthermore, assuming the same filters for Rx-I/Q-imbalance compensation, the

[1]For scheme 2), we have $n_s = 2$ and $\kappa = 2$.

"Sep. Tx IQ+Ch." scheme requires the highest computational complexity for the actual compensation. The complexity of the "Joint Tx IQ+Ch." scheme is lower than that of the "Sep. Tx IQ+Ch." scheme but higher than that in the case without Tx-I/Q-imbalance.

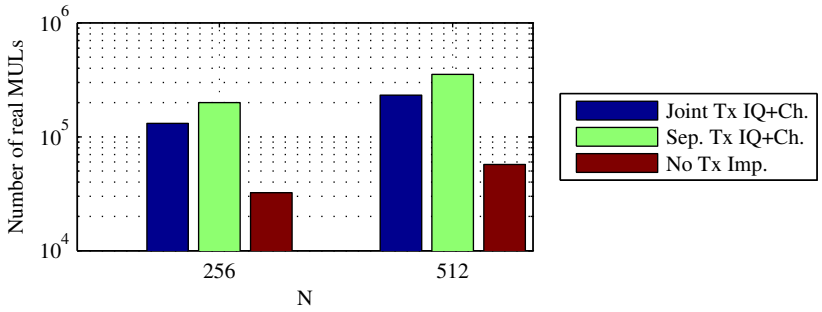

Figure 3.50: Computational complexity of different schemes for the calculation of the equalization matrix (for ZF signal equalization). STC is assumed.

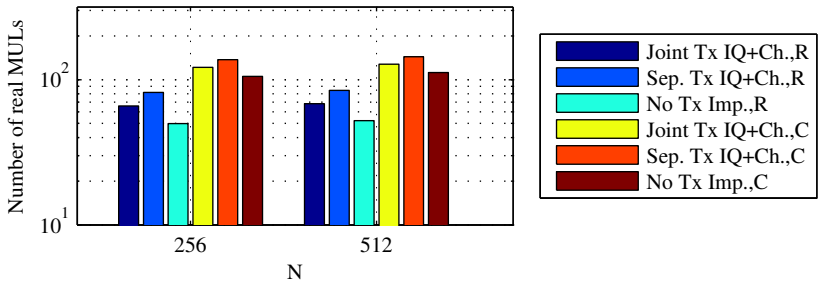

Figure 3.51: Computational complexity of different schemes for the actual compensation of CFO, I/Q-imbalance and the MIMO channels. STC is assumed.

3.5.7.3 Discussion

According to the analysis and the results in Sec. 3.4.9.1 and Sec. 3.4.9.2, conducting Tx-side Tx-I/Q-imbalance can considerably simplify the Rx signal processing. However, if Tx-I/Q-imbalance has to be compensated for at the Rx, it will be more efficient to compensate it jointly with the channels (assuming ZF-equalization). Moreover, it is much more efficient to apply real valued FIR filters to compensate for Rx-I/Q-imbalance. Compared to the state-of-the-art schemes, the proposed schemes require much lower computational complexity both for parameter estimation and impairment compensation. According to Sec. 3.5.6, the proposed schemes outperform the state of the art reference schemes. Thus, the proposed schemes are more suitable for the desired application. Among the proposed schemes, "SCH1" has the advantage of

lower computational complexity, while "SCH2" can work with less preamble overhead[1]. When both "SCH1" and "SCH2" apply three repetitions of the basic sequence as preamble, "SCH2" can achieve slightly better performance than "SCH1". Thus, similar to Sec. 3.4.9.3, we suggest to make the choice on the schemes based on the context and constraints of the system design as well as the advantages and disadvantages of the candidate schemes.

An interesting future extension of the work in this section may be to combine the bind Rx-I/Q-imbalance estimation scheme in [48] with preamble-based estimation of CFO, Tx-I/Q-imbalance and the MIMO channel. The reason is that the bind scheme in [48] may provide better Rx-I/Q-imbalance estimation than preamble-based schemes due to exploitation of the noise.

3.6 Efficient Multi-User Detection for the Uplink

3.6.1 Background and Overview

When considering the UL of broadband cellular systems with severely time-dispersive channels, CP-assisted Single-Carrier (SC) block transmission with Frequency Domain Equalization (FDE) is one of the most suitable techniques. Unlike OFDM systems, both the DFT and IDFT blocks are positioned at the Rx of the AP, keeping the signal processing complexity of the UT low. Moreover, SC signals have lower signal PAPR than OFDM signals and thus allow the application of low cost PA with high efficiency in the UTs [153]. Other advantages of SC transmission include low sensitivity to RF impairments e.g. CFO and the exploitation of frequency diversity in uncoded case [154].

At the AP, MUD is needed to separate the different user signals, which are affected by different propagation channels. As described in Sec. 3.2.1, DS-CDMA is applied in the UL of the 60 GHz WLAN system to enable MUD. Note that DS-CDMA is a special case of SC modulation and has the advantages of high capacity and flexibility [103]. By combining DS-CDMA with CP-assisted block transmission, efficient frequency domain receiver can be implemented. In [103], an iterative FD-MUD scheme was proposed for CP-assisted DS-CDMA systems. By applying IB-DFE as well as Successive Interference Cancellation (SIC), this scheme achieves performance close to the single-user Matched Filter Bound (MFB), which is an optimal performance bound [155]. However, IB-DFE with SIC requires relatively high computational complexity in the Rx. An elegant way to reduce the Rx computational complexity without degrading the performance is to drop the IB-DFE with SIC and apply Multiple Antenna Techniques (MAT). As will be shown in this thesis, proper MAT schemes can achieve even better performance than IB-DFE with SIC. In [156], a combination of MAT and the MUD scheme of [103] was presented, where spatial multiplexing was applied to enhance the transmission rate. Unlike [156], we propose a combination of MAT and the MUD scheme to achieve diversity gains. Finally, the proposed schemes in this section have been previously published in our work [43].

[1] Two repetitions of the basic sequence are sufficient for "SCH2", while "SCH1" requires three.

3.6.2 Signal Model

A CP-assisted DS-CDMA block transmission system with P users and one AP is considered. For simplicity, we begin with a system without antenna diversity i.e. with a SISO system. The extension to the cases with multiple Tx- and Rx antennas will be shown later. Note that the signal model used here follows that in [103].

Let $\boldsymbol{a}_p^M = [a_p[0], \ldots, a_p[M-1]]^T$ indicate a size-M data block transmitted by the p^{th} user, whose elements are drawn from a given constellation e.g. QPSK. If necessary, a block index b can be attached to $\boldsymbol{a}_p^M$, i.e. $\boldsymbol{a}_p^{M,b}$ indicates the b^{th} transmitted data block. The spreading code of the p^{th} user is $\boldsymbol{c}_p^K = [c_p[0], \ldots, c_p[K-1]]^T$, where the code length K is the same for all the users. We denote the corresponding chip block after code spreading as $\boldsymbol{s}_p^N = [s_p[0], \ldots, s_p[N-1]]^T$ with $N = MK$ and $s_p[n] = a_p[\lfloor \frac{n}{K} \rfloor] c_p[((n))_K]$. We further define $A_p[k] := \mathcal{F}_N \{a_p[n]\}$ and $S_p[k] := \mathcal{F}_N \{s_p[n]\}$.

Similar to the signal model as in [103], two length-N vectors, $\check{\boldsymbol{a}}_p^M = [\check{a}_p[0], \ldots, \check{a}_p[N-1]]^T$ and $\check{\boldsymbol{c}}_p^M = [\check{c}_p[0], \ldots, \check{c}_p[N-1]]^T$, are introduced, whose elements are defined as:

$$\check{a}_p[n] = \begin{cases} a_p[m], & n = mK; m = 0, \ldots, M-1 \\ 0, & \text{otherwise,} \end{cases} \tag{3.149}$$

$$\check{c}_p[n] = \begin{cases} c_p[n] & n = 0, \ldots, K-1 \\ 0 & n = K, \ldots, N-1. \end{cases} \tag{3.150}$$

The corresponding DFTs are written as $\check{A}_p[k] = \mathcal{F}_N \{\check{a}_p[n]\}$ and $\check{C}_p[k] = \mathcal{F}_N \{\check{c}_p[n]\}$, respectively. It was shown in [103] that:

$$S_p[k] = \check{A}_p[k] \check{C}_p[k], \, \forall k = 0, \ldots, N-1. \tag{3.151}$$

To maintain the periodicity of the received signal block even in multipath propagation environment, a CP is added to each chip block $\boldsymbol{s}_p^N$ at the Tx. This CP is removed after signal reception. The DFT of the corresponding received signal block is (see [103]):

$$\begin{aligned} Y[k] &= \sum_{p=1}^{P} \check{A}_p[k] \check{C}_p[k] H_p^{\text{ch}}[k] + N[k] \\ &= \sum_{p=1}^{P} \check{A}_p[k] H_p[k] + N[k] \end{aligned} \tag{3.152}$$

with $N[k]$ the spectral noise, $H_p^{\text{ch}}[k]$ the transmission channel FR for the p^{th} user and $H_p[k] := \check{C}_p[k] H_p^{\text{ch}}[k]$ the equivalent channel FR including the code-spreading. Note that except for the radio channel, $H_p^{\text{ch}}[k]$ also includes the influence of the RF component chain and the linear digital filtering.

It was shown in [103] that $\check{A}_p[k] = A_p[((k))_M]$. Thus, the following relation exists:

$$\check{A}_p[q + lM] = A_p[q], \forall q = 0, \ldots, M-1; l = 0, \ldots, K-1 \tag{3.153}$$

which implies a K^{th}-order frequency diversity effect in $Y[k]$.

3.6.3 Linear One-Stage MUD in SISO Case

According to [103], the linear one-stage detection of the transmitted data block in the frequency domain is performed as follows:

$$\widetilde{A}_p[q] = \sum_{l=0}^{K-1} Y[q + lM] G_p[q + lM];\ q = 0, 1, \ldots, M-1, \tag{3.154}$$

where $\widetilde{A}_p[q]$ is the reconstructed data symbol (in frequency domain) and $G_p[q+lM]$ is the spectral equalization coefficient of the p^{th} user at the $(q+lM)^{\text{th}}$ frequency point. These coefficients are determined according to the MMSE criterion, i.e. by minimizing the expectation:

$$E\left\{\left|\widetilde{A}_p[q] - A_p[q]\right|^2\right\}. \tag{3.155}$$

By applying Wirtinger-Calculus [157], the coefficients $G_p[q + lM]$ which minimize (3.155) suffice:

$$\frac{\partial}{\partial\, F_p^*[q + lM]}\, E\left\{\left|\widetilde{A}_p[q] - A_p[q]\right|^2\right\} = 0. \tag{3.156}$$

After substituting (3.154) into (3.156) and some straight forward manipulations, we obtain:

$$E\left\{\left(\sum_{l'=0}^{K-1} Y[q + l'M] G_p[q + l'\, M] - A_p[q]\right) Y^*[q + lM]\right\} = 0. \tag{3.157}$$

With (3.152), Eq. (3.157) can be rewritten as

$$E\left\{\left[\sum_{p'=1}^{P} A_{p'}^*[q] H_{p'}^*[q + lM] + N^*[q + lM]\right] \left[\sum_{l'=0}^{K-1}\left(\left\{\sum_{p''=1}^{P} A_{p''}[q] H_{p''}[q + l'M] + N[q + l'M]\right\} G_p[q + l'M]\right) - A_p[q]\right]\right\} = 0. \tag{3.158}$$

To solve Eq. (3.158), the following assumptions are made:

1. Zero-mean white noise: $E\{N[k]N^*[k']\} = 0, \forall k \neq k'$
2. Uncorrelated data: $E\left\{A_p[k]A_p^*[k']\right\} = 0, \forall k \neq k'$

3. Zero cross power spectral density of different users: $E\left\{A_p[k]A_{p'}^*[k]\right\} = 0, \forall p \neq p'$

4. Equal spectral power distribution of different users: $E\left\{|A_p[k]|^2\right\} = E\left\{|A_{p'}[k]|^2\right\}$

With the above assumptions, Eq. (3.158) can be simplified to the following equation:

$$\begin{aligned} H_p^*[q+lM] = \sum_{p'=1}^{P} H_{p'}^*[q+lM] \sum_{l'=0}^{K-1} H_{p'}[q+l'M]G_p[q+l'M] \\ + \alpha_p G_p[q+lM] \ , \end{aligned} \tag{3.159}$$

where $\alpha_p = \frac{E\left\{|N[q]|^2\right\}}{E\left\{|A_p[q]|^2\right\}}$. For each p and q, a Linear Equation System (LES) with K unknowns, $\{G_p[q+l'M]; l' = 0, \ldots, K-1\}$, has to be solved. According to (3.159), the LES can be written in the following matrix notation:

$$\boldsymbol{H}_{p,q}^* = \left[\alpha_p \boldsymbol{I}_K + \sum_{p'=1}^{P} \boldsymbol{H}_{p',q}^* \boldsymbol{H}_{p',q}^T\right] \boldsymbol{G}_{p,q} \ , \tag{3.160}$$

where

$$\boldsymbol{H}_{p,q} = [H_p[q+0\cdot M], \ldots, H_p[q+(K-1)M]]^T \ ,$$

$$\boldsymbol{G}_{p,q} = [G_p[q+0\cdot M], \ldots, G_p[q+(K-1)M]]^T \ .$$

By solving this LES, the equalization coefficients can be obtained.

3.6.4 Transmit Antenna Diversity Scheme

In this section, a MISO system with two Tx antennas is considered. The extension to more Tx antennas is possible. Based on the linear MUD in section 3.6.3, Alamouti's STC [158] is applied, which was originally developed for narrow-band transmission signals. For the application of STC, the system parameters should assure that the frequency spacing between the DFT components of the transmitted signal is within the channel coherence bandwidth, so that these components can be regarded as parallel transmitted narrow-band signals, which are suitable for STC. According to [158], the DFTs of consecutive data block pairs to be transmitted from the 1st and 2nd Tx antennas are $\left\{\boldsymbol{A}_p^{M,b_1}, -\boldsymbol{A}_p^{M,b_2\,*}\right\}$ and $\left\{\boldsymbol{A}_p^{M,b_2}, \boldsymbol{A}_p^{M,b_1\,*}\right\}$, respectively, where

$$\boldsymbol{A}_p^{M,b} = \left[A_p^b[0], \ldots, A_p^b[M-1]\right]^T \ .$$

Moreover, b_1 and b_2 are consecutive block indexes with $b_2 = b_1 + 1$. From [159], the corresponding time-domain data block pairs are $\left\{\boldsymbol{a}_p^{M,b_1}, -\left(\mathcal{OR}(\boldsymbol{a}_p^{M,b_2})\right)^*\right\}$ and $\left\{\boldsymbol{a}_p^{M,b_2}, \left(\mathcal{OR}(\boldsymbol{a}_p^{M,b_1})\right)^*\right\}$. This implies that the STC requires no extra DFT and IDFT operations but only simple time reverse operations, which enables simple implementation.

With (3.152) and (3.153), the DFTs of the two consecutive received blocks can be expressed as:

$$\begin{aligned} Y^{b_1}[k] &= \sum_{p=1}^{P} \left(\check{A}_p^{b_1}[k] H_p^{(1)}[k] + \check{A}_p^{b_2}[k] H_p^{(2)}[k] \right) + N^{b_1}[k], \\ Y^{b_2}[k] &= \sum_{p=1}^{P} \left(\check{A}_p^{b_1\,*}[k] H_p^{(2)}[k] - \check{A}_p^{b_2\,*}[k] H_p^{(1)}[k] \right) + N^{b_2}[k], \end{aligned} \tag{3.161}$$

where $H_p^{(i)}[k]$ is the equivalent channel FR corresponding to the i^{th} Tx antenna. At the AP, the STC decoder processes the received signal as follows:

$$\begin{aligned} \widetilde{A}_p^{b_1}[q] &= \frac{1}{2} \sum_{l=0}^{K-1} \left(Y^{b_1}[q+lM] G_p^{(1)}[q+lM] + Y^{b_2\,*}[q+lM] G_p^{(2)\,*}[q+lM] \right), \\ \widetilde{A}_p^{b_2}[q] &= \frac{1}{2} \sum_{l=0}^{K-1} \left(Y^{b_1}[q+lM] G_p^{(2)}[q+lM] - Y^{b_2\,*}[q+lM] G_p^{(1)\,*}[q+lM] \right), \end{aligned} \tag{3.162}$$

where $G_p^{(i)}[q+lM], \forall q, l$ are the equalization coefficients corresponding to the i^{th} transmission channel. Now, $G_p^{(1)}[q+lM]$ and $G_p^{(2)}[q+lM]$ must be jointly determined by minimizing the MSE $E\left\{ \left| \widetilde{A}_p^{b_1}[q] - A_p^{b_1}[q] \right|^2 \right\}$, which implies [157]:

$$\frac{\partial}{\partial\, G_p^{(i)\,*}[q+lM]} \; E\left\{ \left| \widetilde{A}_p^{b_1}[q] - A_p^{b_1}[q] \right|^2 \right\} = 0, \; \forall i = 1, 2. \tag{3.163}$$

Substituting (3.162) into (3.163) for $i = 1, 2$, we obtain the following equations:

$$\begin{aligned} E\Bigg\{ \Bigg[\sum_{l'=0}^{K-1} \frac{1}{2} \left(Y^{b_1}[q+l'M] G_p^{(1)}[q+l'M] + Y^{b_2\,*}[q+l'M] G_p^{(2)\,*}[q+l'M] \right) - A_p^{b_1}[q] \Bigg] \\ \frac{1}{2} Y^{b_1\,*}[q+lM] \Bigg\} = 0, \\ E\Bigg\{ \Bigg[\sum_{l'=0}^{K-1} \frac{1}{2} \left(Y^{b_1\,*}[q+l'M] G_p^{(1)\,*}[q+l'M] + Y^{b_2}[q+l'M] G_p^{(2)}[q+l'M] \right) - A_p^{b_1\,*}[q] \Bigg] \\ \frac{1}{2} Y^{b_2\,*}[q+lM] \Bigg\} = 0. \end{aligned} \tag{3.164}$$

We further substitute (3.161) into (3.164). In addition to the assumptions in section 3.6.3, we assume uncorrelated noise and data in different signal blocks, i.e. $E\left\{ N^{b_1}[k] N^{b_2\,*}[k] \right\} = 0$

and $E\left\{A_p^{b_1}[k]A_p^{b_2\,*}[k]\right\} = 0$, respectively. Finally, the equations become:

$$\begin{aligned} H_p^{(1)\,*}[q+lM] = \frac{1}{2}\sum_{p'=1}^{P}\sum_{l'=0}^{K-1}\Big[\Big(H_{p'}^{(1)\,*}[q+lM]H_{p'}^{(1)}[q+l'M]+ \\ H_{p'}^{(2)\,*}[q+lM]H_{p'}^{(2)}[q+l'M]\Big)G_p^{(1)}[q+l'M] + \Big(H_{p'}^{(1)\,*}[q+lM]H_{p'}^{(2)\,*}[q+l'M] \\ -H_{p'}^{(2)\,*}[q+lM]H_{p'}^{(1)\,*}[q+l'M]\Big)G_p^{(2)\,*}[q+l'M]\Big] + \frac{1}{2}\alpha_p G_p^{(1)}[q+lM]\ , \end{aligned} \tag{3.165}$$

$$\begin{aligned} H_p^{(2)\,*}[q+lM] = \frac{1}{2}\sum_{p'=1}^{P}\sum_{l'=0}^{K-1}\Big[\Big(H_{p'}^{(2)\,*}[q+lM]H_{p'}^{(1)\,*}[q+l'M]- \\ H_{p'}^{(1)\,*}[q+lM]H_{p'}^{(2)\,*}[q+l'M]\Big)G_p^{(1)\,*}[q+l'M] + \Big(H_{p'}^{(1)\,*}[q+lM]H_{p'}^{(1)}[q+l'M] \\ +H_{p'}^{(2)\,*}[q+lM]H_{p'}^{(2)}[q+l'M]\Big)G_p^{(2)}[q+l'M]\Big] + \frac{1}{2}\alpha_p G_p^{(2)}[q+lM]\ . \end{aligned} \tag{3.166}$$

For each p and q, an LES with $2K$ unknowns, $\left\{G_p^{(i)}[q+l'M]; i=1,2; l'=0,\ldots,K-1\right\}$, has to be solved. Eq. (3.165) and (3.166) can be written in the following matrix notation:

$$\begin{bmatrix} \boldsymbol{H}_{p,q}^{(1)\,*} \\ \boldsymbol{H}_{p,q}^{(2)} \end{bmatrix} = \begin{bmatrix} \boldsymbol{A}_{p,q} & \boldsymbol{B}_{p,q} \\ \boldsymbol{B}_{p,q}^{H} & \boldsymbol{A}_{p,q}^{*} \end{bmatrix} \begin{bmatrix} \boldsymbol{G}_{p,q}^{(1)} \\ \boldsymbol{G}_{p,q}^{(2)\,*} \end{bmatrix}, \tag{3.167}$$

where

$$\begin{aligned} \boldsymbol{H}_{p,q}^{(i)} &= \left[H_p^{(i)}[q+0\cdot M],\ldots,H_p^{(i)}[q+(K-1)M]\right]^T, \\ \boldsymbol{G}_{p,q}^{(i)} &= \left[G_p^{(i)}[q+0\cdot M],\ldots,G_p^{(i)}[q+(K-1)M]\right]^T, \end{aligned} \tag{3.168}$$

$$\begin{aligned} \boldsymbol{A}_{p,q} &= \frac{1}{2}\alpha_p \boldsymbol{I}_K + \frac{1}{2}\sum_{p'=1}^{P}\sum_{i=1}^{2}\left(\boldsymbol{H}_{p',q}^{(i)\,*}\boldsymbol{H}_{p',q}^{(i)T}\right), \\ \boldsymbol{B}_{p,q} &= \frac{1}{2}\sum_{p'=1}^{P}\left(\boldsymbol{H}_{p',q}^{(1)\,*}\boldsymbol{H}_{p',q}^{(2)H} - \boldsymbol{H}_{p',q}^{(2)\,*}\boldsymbol{H}_{p',q}^{(1)H}\right). \end{aligned} \tag{3.169}$$

By solving (3.167), the equalization coefficients can be obtained.

3.6.5 Receive Antenna Diversity Scheme

We assume that two Rx antennas are available. Let the received signal block of the r^{th} Rx antenna be:

$$Y^{\langle r\rangle}[k] = \sum_{p=1}^{P}\check{A}_p[k]H_p^{\langle r\rangle}[k] + N^{\langle r\rangle}[k], \tag{3.170}$$

where $H_p^{\langle r\rangle}[k]$ and $N^{\langle r\rangle}[k]$ are the equivalent channel FR and the noise spectrum of the r^{th} Rx antenna signal, respectively. The multi-user signal should be detected in the following way:

$$\widetilde{A}_p[q] = \sum_{l=0}^{K-1} \sum_{r=1}^{2} Y^{\langle r\rangle}[q+lM] G_p^{\langle r\rangle}[q+lM] \ , \tag{3.171}$$

where $G_p^{\langle r\rangle}[q+lM], \forall q, l$ are the equalization coefficients corresponding to the r^{th} Rx antenna and are determined by minimizing the MSE of (3.155), which implies:

$$\frac{\partial}{\partial\, G_p^{\langle r\rangle\,*}[q+lM]} \ E\left\{ \left| \widetilde{A}_p[q] - A_p[q] \right|^2 \right\} = 0, \ \forall r = 1, 2. \tag{3.172}$$

Similarly to the derivation in section 3.6.4, we substitute (3.171) and (3.170) into (3.172) and make the additional assumption of uncorrelated noise of different Rx antennas, i.e.,

$$E\left\{ N[k]^{\langle 1\rangle} N^{\langle 2\rangle\,*}[k] \right\} = 0.$$

Finally, the equalization coefficients can be calculated by solving the following matrix equation system:

$$\begin{bmatrix} \boldsymbol{H}_{p,q}^{\langle 1\rangle\,*} \\ \boldsymbol{H}_{p,q}^{\langle 2\rangle\,*} \end{bmatrix} = \begin{bmatrix} \boldsymbol{A}_{p,q}^{\langle 1\rangle} & \boldsymbol{B}_{p,q} \\ \boldsymbol{B}_{p,q}^{H} & \boldsymbol{A}_{p,q}^{\langle 2\rangle} \end{bmatrix} \begin{bmatrix} \boldsymbol{G}_{p,q}^{\langle 1\rangle} \\ \boldsymbol{G}_{p,q}^{\langle 2\rangle} \end{bmatrix}, \tag{3.173}$$

where

$$\begin{aligned} \boldsymbol{A}_{p,q}^{\langle r\rangle} &= \alpha_p \boldsymbol{I}_K + \sum_{p'=1}^{P} \boldsymbol{H}_{p',q}^{\langle r\rangle\,*} \boldsymbol{H}_{p',q}^{\langle r\rangle T}, \\ \boldsymbol{B}_{p,q} &= \sum_{p'=1}^{P} \boldsymbol{H}_{p',q}^{\langle 1\rangle\,*} \boldsymbol{H}_{p',q}^{\langle 2\rangle T}, \end{aligned} \tag{3.174}$$

and $\boldsymbol{H}_{p,q}^{\langle r\rangle}$ and $\boldsymbol{G}_{p,q}^{\langle r\rangle}$ are defined accordingly to (3.168).

3.6.6 MIMO Scheme

We consider a 2×2 MIMO configuration. At the Tx, STC is performed as described in section 3.6.4. Then, the consecutive received signal blocks corresponding to the r^{th} Rx antenna are:

$$\begin{aligned} Y^{b_1\langle r\rangle}[k] &= \sum_{p=1}^{P} \left(\check{A}_p^{b_1}[k] H_p^{\langle r,1\rangle}[k] + \check{A}_p^{b_2}[k] H_p^{\langle r,2\rangle}[k] \right) + N^{b_1\langle r\rangle}[k], \\ Y^{b_2\langle r\rangle}[k] &= \sum_{p=1}^{P} \left(\check{A}_p^{b_1\,*}[k] H_p^{\langle r,2\rangle}[k] - \check{A}_p^{b_2\,*}[k] H_p^{\langle r,1\rangle}[k] \right) + N^{b_2\langle r\rangle}[k], \end{aligned} \tag{3.175}$$

where $H_p^{\langle r,i\rangle}[k]$ is the FR of the equivalent channel between the i^{th} Tx antenna and the r^{th} Rx antenna. From (3.162) and (3.171), the FD-MUD should be done by:

$$\begin{aligned}\widetilde{A}_p^{b_1}[q] &= \frac{1}{2}\sum_{l=0}^{K-1}\sum_{r=1}^{2}\left(Y^{b_1\langle r\rangle}[q+lM]G_p^{\langle r,1\rangle}[q+lM] + Y^{b_2\langle r\rangle\,*}[q+lM]G_p^{\langle r,2\rangle\,*}[q+lM]\right),\\ \widetilde{A}_p^{b_2}[q] &= \frac{1}{2}\sum_{l=0}^{K-1}\sum_{r=1}^{2}\left(Y^{b_1\langle r\rangle}[q+lM]G_p^{\langle r,2\rangle}[q+lM] - Y^{b_2\langle r\rangle\,*}[q+lM]G_p^{\langle r,1\rangle\,*}[q+lM]\right),\end{aligned} \tag{3.176}$$

where $G_p^{\langle r,i\rangle}[q+lM], \forall q,l$ are the equalization coefficients corresponding to $H_p^{\langle r,i\rangle}[k]$. They are determined by minimizing the MSE $E\left\{\left|\widetilde{A}_p^{b_1}[q]-A_p^{b_1}[q]\right|^2\right\}$, which implies [157]:

$$\frac{\partial}{\partial\, G_p^{\langle r,i\rangle\,*}[q+lM]}\; E\left\{\left|\widetilde{A}_p^{b_1}[q]-A_p^{b_1}[q]\right|^2\right\} = 0,\ \forall i,r=1,2. \tag{3.177}$$

Similarly to the derivation in section 3.6.4, we substitute (3.176) and (3.175) into (3.177). With all the assumptions from sections 3.6.3, 3.6.4 and 3.6.5, we obtain the following matrix equation system for calculating the equalization coefficients:

$$\begin{bmatrix}\boldsymbol{H}_{p,q}^{\langle 1,1\rangle\,*}\\ \boldsymbol{H}_{p,q}^{\langle 2,1\rangle\,*}\\ \boldsymbol{H}_{p,q}^{\langle 1,2\rangle}\\ \boldsymbol{H}_{p,q}^{\langle 2,2\rangle}\end{bmatrix} = \begin{bmatrix}\boldsymbol{A}_{p,q}^{\langle 1\rangle} & \boldsymbol{B}_{p,q} & \boldsymbol{C}_{p,q}^{\langle 1\rangle} & \boldsymbol{D}_{p,q}\\ \boldsymbol{B}_{p,q}^{H} & \boldsymbol{A}_{p,q}^{\langle 2\rangle} & -\boldsymbol{D}_{p,q}^{T} & \boldsymbol{C}_{p,q}^{\langle 2\rangle}\\ \boldsymbol{C}_{p,q}^{\langle 1\rangle H} & -\boldsymbol{D}_{p,q}^{*} & \boldsymbol{A}_{p,q}^{\langle 1\rangle\,*} & \boldsymbol{B}_{p,q}^{*}\\ \boldsymbol{D}_{p,q}^{H} & \boldsymbol{C}_{p,q}^{\langle 2\rangle H} & \boldsymbol{B}_{p,q}^{T} & \boldsymbol{A}_{p,q}^{\langle 2\rangle\,*}\end{bmatrix}\begin{bmatrix}\boldsymbol{G}_{p,q}^{\langle 1,1\rangle}\\ \boldsymbol{G}_{p,q}^{\langle 2,1\rangle}\\ \boldsymbol{G}_{p,q}^{\langle 1,2\rangle\,*}\\ \boldsymbol{G}_{p,q}^{\langle 2,2\rangle\,*}\end{bmatrix}, \tag{3.178}$$

where

$$\begin{aligned}\boldsymbol{A}_{p,q}^{\langle r\rangle} &= \frac{1}{2}\alpha_p\boldsymbol{I}_K + \frac{1}{2}\sum_{p'=1}^{P}\sum_{i=1}^{2}\boldsymbol{H}_{p',q}^{\langle r,i\rangle\,*}\boldsymbol{H}_{p',q}^{\langle r,i\rangle T},\\ \boldsymbol{B}_{p,q} &= \frac{1}{2}\sum_{p'=1}^{P}\left(\boldsymbol{H}_{p',q}^{\langle 1,1\rangle\,*}\boldsymbol{H}_{p',q}^{\langle 2,1\rangle T} + \boldsymbol{H}_{p',q}^{\langle 1,2\rangle\,*}\boldsymbol{H}_{p',q}^{\langle 2,2\rangle T}\right),\\ \boldsymbol{C}_{p,q}^{\langle r\rangle} &= \frac{1}{2}\sum_{p'=1}^{P}\left(\boldsymbol{H}_{p',q}^{\langle r,1\rangle\,*}\boldsymbol{H}_{p',q}^{\langle r,2\rangle H} - \boldsymbol{H}_{p',q}^{\langle r,2\rangle\,*}\boldsymbol{H}_{p',q}^{\langle r,1\rangle H}\right),\\ \boldsymbol{D}_{p,q} &= \frac{1}{2}\sum_{p'=1}^{P}\left(\boldsymbol{H}_{p',q}^{\langle 1,1\rangle\,*}\boldsymbol{H}_{p',q}^{\langle 2,2\rangle H} - \boldsymbol{H}_{p',q}^{\langle 1,2\rangle\,*}\boldsymbol{H}_{p',q}^{\langle 2,1\rangle H}\right),\end{aligned} \tag{3.179}$$

and $\boldsymbol{H}_{p,q}^{\langle r,i\rangle}$ and $\boldsymbol{G}_{p,q}^{\langle r,i\rangle}$ are defined accordingly to (3.168).

3.6.7 Implementation and Complexity Considerations

The proposed MUD schemes involve solving PM LESs. According to (3.160), (3.167), (3.173) and (3.178), the parameter matrix of each LES is a $KN_TN_R \times KN_TN_R$ Hermitian matrix, where

N_T and N_R are the number of Tx and Rx antennas, respectively. Since the parameter matrices are Hermitian, the LES solutions can be efficiently implemented. For practical applications, a relatively small spreading factor K should be chosen to further reduce the complexity for solving the LES. This is possible with an FDMA/CDMA scheme, since not all users have to be separated in the code domain. Furthermore, the number of data symbols in each transmission block, M, is proportional to the number of LESs to be solved. Note that the calculation of the equalization coefficients $G_p[q + lM]$ only requires the channel information, the spreading code and the Rx SNR (to obtain α_p). These parameters can be assumed quasi constant within a communication frame whose duration is in the range of the channel coherence time. This implies that the equalization coefficients need only to be calculated once per signal frame. Thus, the demand on computation power is relaxed. The larger the channel coherence time, the lower the required computation power.

The proposed antenna diversity schemes require higher RF hardware complexity (for diversity branches) than the scheme in [103]. However, due to the linear one-stage Rx structure of the antenna diversity schemes, the computational complexity at the Rx is moderate or even lower (with MISO/SIMO) than that of IB-DFE SIC in [103]. Moreover, since no feedback loop is necessary, the diversity schemes are more time efficient.

Among the antenna diversity schemes, MIMO has the highest RF hardware complexity, since both the AP and P UTs must be equipted with diversity branches. MISO also requires diversity branches for all the P UTs. In contrast, SIMO only requires diversity branches at the AP and has the lowest RF hardware complexity. The computational complexity of the MIMO scheme is also the highest, while those of MISO and SIMO are almost the same. In section 3.6.8, it will be shown that SIMO achieves the best tradeoff between performance and complexity.

3.6.8 Simulation Results and Discussion

To simulate the proposed antenna diversity schemes for FD-MUD, we considered a CP-assisted DS-CDMA system with a spreading factor $K = 8$ and $M = 16$ data symbols in each data block. Furthermore, QPSK with Gray mapping was applied. The channel was Rayleigh fading with 16 independent fading taps and an exponential power delay profile. The applied antenna configurations are: SISO, SIMO (1×2), MISO (2×1) and MIMO (2×2). Under the assumptions of perfect synchronization, channel estimation and power control, the uncoded BER performance of the antenna diversity schemes were obtained from numerical simulations. To achieve fair comparison of the schemes, the total Tx power is the same for all antenna configurations. For the performance evaluation of the proposed schemes, the corresponding single-user MFB (see [155] and [160]) are included in the diagrams of all antenna configurations. Note that if ρ is the SNR of the received signal at an Rx antenna, the SNR per bit per user is calculated by $\frac{E_b}{\sigma_n^2} = \frac{\rho \cdot G_C}{P N_b}$, where $\frac{\sigma_n^2}{2}$ is the spectral power density of the white noise (see [97]), $G_C = K$ is the processing gain of the spectrum spreading and and N_b is the number of bits per modulation

symbol.

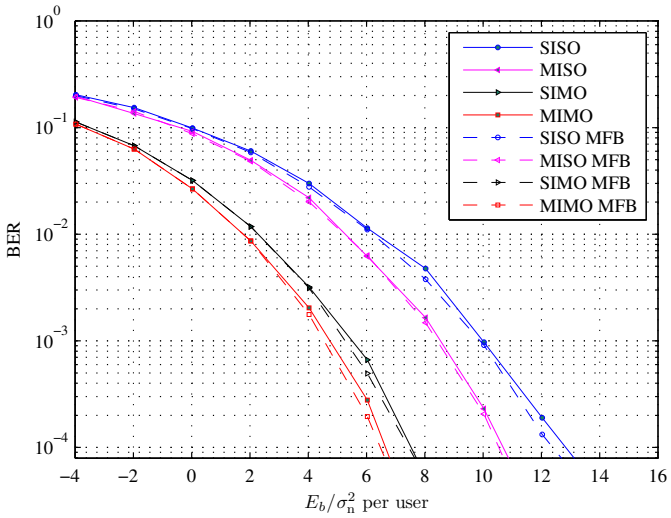

Figure 3.52: BER for a single-user scenario

Fig. 3.52 shows the BER in a single-user scenario with different antenna configurations. In this scenario, the performance of the antenna diversity schemes are very close to the corresponding MFBs, which verifies their effectiveness. Fig. 3.53 and 3.54 show the performance with $P = 4$ (half loaded case) and $P = 8$ (fully loaded case). We can see that the performance margins between the proposed schemes and the MFBs become larger as the number of users increases. The reason is that with severely frequency selective channels, the residual Multi-User Interference (MUI) and noise amplification caused by the MUD aggravate quickly with increasing user number. Thus, the system performance is degraded. However, the weaker the frequency selectivity, the closer the performance in multi-user case to that in single user case. From Fig. 3.53 and 3.54, we can see that SIMO and MIMO exhibit enormous performance improvement compared to SISO, indicating the fact that by exploiting spatial diversity, the influence of the channel frequency selectivity is mitigated and thus, the MUD becomes much more effective. In contrast, the improvement by MISO scheme is relatively small. The reason is that the MMSE algorithm can not afford perfect STC decoding and sufficient suppression of MUI and noise at the same time. Instead, it introduces Inter-Antenna-Interference (IAI, interference between signals from different Tx antennas) and finds a tradeoff between IAI, residual MUI and noise. As a result, the diversity exploitation is degraded. Thus, the performance improvement from SIMO to MIMO is not significant, either.

With the complexity analysis in section 3.6.7 and the simulation results, we can conclude that SIMO achieves the best tradeoff between performance and complexity (both RF hardware- and computational complexity). This conclusion complies with the design criterion of cellular systems that the complexity of the UTs should be kept low. Furthermore, while the

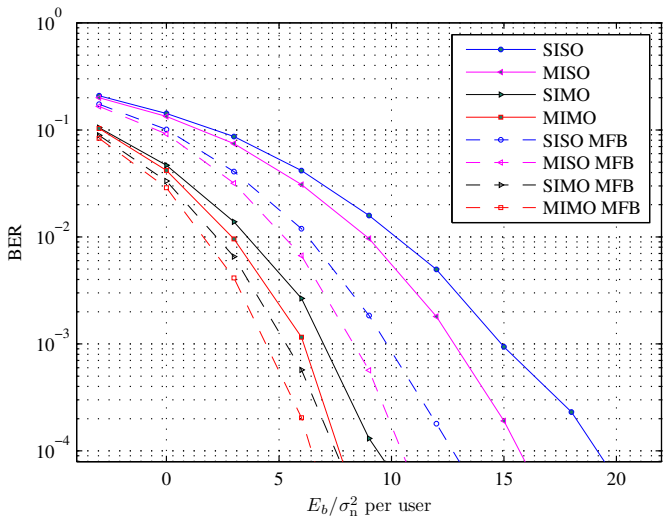

Figure 3.53: Average BER of each user, $P = 4$

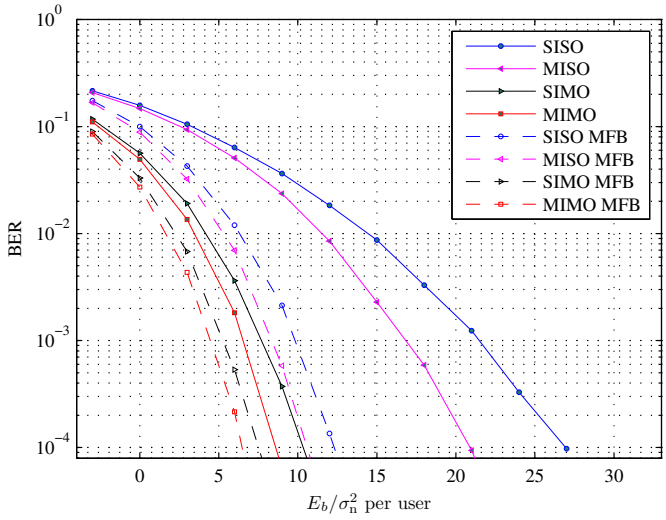

Figure 3.54: Average BER of each user, $P = 8$

IB-DFE SIC scheme in [103] only achieves performance close to the SISO MFB, the SIMO and MIMO schemes outperform both SISO and MISO single-user MFB. Although SIMO and MIMO schemes have higher RF hardware complexity than the scheme in [103], they show better performance and require only moderate or even lower (with SIMO) computational complexity. Thus, we can conclude that they are superior to IB-FDE with SIC.

3.7 Chapter Summary

In this chapter, the design of a 60 GHz WLAN was investigated. The IFE system was described as an example.

First, the overall system design was proposed, including the system configuration and frame structure. While OFDMA is used in the DL, CP-assisted DS-CDMA is applied in the UL. For the DL, performance simulation was carried out with the measured 60 GHz channels in an airplane cabin. In the simulation, STC and MRC were applied. Simulation shew that diversity gains of 11.7 dB and 13.13 dB can be achieved for LOS and OLOS, respectively. The worst case Tx power level is also derived from simulation.

Afterwards, the following specific aspects were investigated:

1. **Optimization of time domain windowing and GB size for cellular OFDM systems:** To reduce the sidelobes of OFDM signals for matching the spectral mask, we proposed to apply RC windowing in time domain. On the one hand, reducing the side-lobe allows smaller GB in frequency domain and leads to higher spectral efficiency. On the other hand, applying RC windowing requires more overhead in time domain and results in data rate decrease. To solve this problem, we have derived a mathematical model of the side-lobe power and finally obtained an expression of the data rate as a function of the ROF (of the RC window). Simulation results shew that the data rate function has a convex shape. Based on this function, the optimal ROF (as well as the optimal RC guard period and the optimal GB) can be found, which maximizes the data rate.

2. **Efficient joint estimation and compensation of I/Q-imbalance and the MIMO channel:** In practical systems with DCA, I/Q-imbalance effect can severely limit the system performance and should be compensated for. Since the 60 GHz WLAN system is intended for indoor scenarios, block-fading channels can be assumed. Based on the above considerations, we proposed three preamble based joint channel and Tx/Rx frequency-selective I/Q-imbalance compensation schemes for MIMO OFDM. The first and second schemes apply TDS- and FDS preambles, respectively. The third scheme applies a multi-functional preamble, which can also be used for frame detection/time synchronization (leading to overhead saving). All preambles have low overhead and consider the influence of NULL subcarriers. Numerical simulations have verified the effectiveness of the proposed schemes. While the TDS-based scheme is most robust, the FDS-based scheme has the

lowest computational complexity. Anyway, the multi-functional preamble based scheme is the most practical one that achieves the best tradeoff between performance, preamble overhead and computational complexity.

3. **Efficient joint estimation and compensation of CFO, I/Q-imbalance and the MIMO channel:** Here, the CFO is also included in the system model. Two preamble based joint CFO, Tx/Rx frequency-selective I/Q-imbalance and channel compensation schemes were proposed for MIMO OFDM. The first scheme applies three repetitions of a basic sequence and uses a closed-form CFO estimation. The second scheme applies two repetitions of the same basic sequence and uses iterative CFO- and Rx-I/Q-imbalance estimation. For both schemes, we have proposed soft metric based methods to solve the problems caused by some special CFO values (e.g CFO values close to zero). Numerical simulations have verified the effectiveness of the proposed schemes. While the second scheme provides slightly better performance and requires less preamble overhead, the first scheme has much lower computational complexity.

4. **Efficient multi-user detection for the uplink:** For the UL of the 60 GHz WLAN, CP-assisted DS-CDMA is applied, which allows low complexity frequency domain MUD. Based on this transmission scheme, we have proposed frequency domain MUD schemes with different antenna diversity configurations, including MISO, SIMO and MIMO. Simulation results shew that by exploiting diversity, the MUD performance can be significantly improved. It was also shown that SIMO exploits the diversity more effectively than MISO. Moreover, SIMO requires only multiple antennas at the AP i.e. lower hardware complexity. Finally, we could conclude that SIMO achieved the best tradeoff between performance and complexity (both RF hardware- and computational complexity).

Chapter 4

Summary and Conclusions

This thesis have proposed several enabling techniques for future broadband high speed wireless communications.

In the first part of this thesis (Ch. 2), the Smart-RF concept for cellular mobile systems was investigated with the emphasis on flexible and robust joint compensation of frequency selective I/Q-imbalance and modulator DC-offset at the transmitter of basestations. For this compensation, a low complexity compensation circuit was proposed, which requires only one real FIR filter and some minor operations. Moreover, two estimation schemes were developed: an Least-Square-Estimation (LSE) scheme and a simplified two-phase scheme. Both schemes allow to estimate with normal communication signals as reference. Thus, they are standard independent. Due to spectral gaps in the communication signals, the LSE scheme may suffer from ill-conditioned matrix problem. In contrast, the simplified scheme can achieve good performance that is almost independent of the communication signal characteristic. Complexity analysis has shown that proposed schemes require lower computational complexity than the state-of-the-art schemes. Furthermore, results form numerical simulations and HIL experiments have verified the the effectiveness of the proposed schemes. For the HIL experiment, the proposed compensation circuit was implemented in realtime in FPGAs. The achievable IRR on the experimental platform was as high as 55 dB. Finally, the HIL result has also verified the effectiveness of combining the proposed I/Q-imbalance compensation with PA pre-distortion.

In the second part of this thesis (Ch. 3), the design of a 60 GHz WLAN was investigated. An In-Flight Entertainment (IFE) system was described as an example. First, the overall system design was proposed, including the system configuration and frame structure. While OFDMA is used in the DL, CP-assisted DS-CDMA is applied in the UL. For the DL, performance simulation was carried out with the measured 60 GHz channels in an airplane cabin. Large diversity gains can be observed from the simulation results. Second, the optimization of time domain windowing and guardband size for cellular OFDM systems was studied. Based on mathematical modeling of the OFDM signal sidelobe power, we have developed a scheme to find the optimal roll-off-factor (of the time domain window), which maximizes the data rate and achieves the

best tradeoff between guardband- and windowing overhead. Third, the joint estimation and compensation of RF-impairments and the MIMO channel were investigated. Two different concepts of RF-impairment compensation were studied: 1) Joint digital compensation of frequency selective I/Q-imbalance and the MIMO channel assuming analog CFO compensation (via oscillator adjustment); 2) Joint digital compensation of CFO, frequency selective I/Q-imbalance and the MIMO channel. For each concept, efficient and effective preamble-based parameter estimation and compensation schemes were presented. The effectiveness of these schemes were verified by numerical simulation. Furthermore, complexity analysis was conducted to show that compared to the state-of-the-art schemes, the proposed schemes can achieve a good tradeoff between performance, preamble overhead and computational complexity. Finally, efficient antenna diversity schemes were proposed for the multi-user detection in uplink, including MISO, SIMO and MIMO schemes. Simulation results shew that by exploiting diversity, the MUD performance can be significantly improved. Moreover, the required computational complexity is much lower than that of a state-of-the-art scheme which applies iterative processing. Finally, we found out that among the proposed diversity schemes, SIMO can achieve the best tradeoff between performance and complexity (both RF hardware- and computational complexity).

Appendix for Chapter 2

A.1 Statistical and Spectral Characteristics of $s[n]$

According to [97], we have

$$R_{s_\Pi,s_\Pi}[l] = R_{s_\Pi,s_\Pi}[-l], \forall \Pi \in \{\text{re}, \text{im}\} \tag{A.1.1}$$

$$R_{s_{\text{re}},s_{\text{im}}}[-l] = R_{s_{\text{im}},s_{\text{re}}}[l]. \tag{A.1.2}$$

A proper process $s[n]$ has the following properties [95, 97]:

$$R_{s_{\text{re}},s_{\text{re}}}[l] = R_{s_{\text{im}},s_{\text{im}}}[l] \tag{A.1.3}$$

$$R_{s_{\text{re}},s_{\text{im}}}[l] = -R_{s_{\text{re}},s_{\text{im}}}[-l], \tag{A.1.4}$$

where (A.1.4) implies that $R_{s_{\text{re}},s_{\text{im}}}[0] = 0$. Recalling that $R_{s,s}[l] := \frac{1}{2}E\{s[n]s^*[n+l]\}$ is the ACF of $s[n]$, the following relation exists [97]:

$$R_{s,s}[l] = R_{s_{\text{re}},s_{\text{re}}}[l] - jR_{s_{\text{re}},s_{\text{im}}}[l]. \tag{A.1.5}$$

Now, we define

$$\begin{aligned} \Phi_{s_\Pi,s_\Pi}(\omega) &:= \mathcal{F}\left\{R_{s_\Pi,s_\Pi}[l]\right\}\big|_\omega, \forall \Pi \in \{\text{re}, \text{im}\} \\ \Phi_{s,s}(\omega) &:= \mathcal{F}\left\{R_{s,s}[l]\right\}\big|_\omega \end{aligned} \tag{A.1.6}$$

to be the Power Spectral Density (PSD) of $s_\Pi[n], \forall \Pi \in \{\text{re}, \text{im}\}$ and $s[n]$, respectively. Moreover, $\Phi_{s_\Pi,s_\Lambda}(\omega) := \mathcal{F}\left\{R_{s_\Pi,s_\Lambda}[l]\right\}\big|_\omega$ is the cross PSD between $s_\Pi[n]$ and $s_\Lambda[n], \forall \Pi, \Lambda \in \{\text{re}, \text{im}\}, \Pi \neq \Lambda$. From (A.1.5), we have

$$\Phi_{s,s}(\omega) = \Phi_{s_{\text{re}},s_{\text{re}}}(\omega) - j\Phi_{s_{\text{re}},s_{\text{im}}}(\omega). \tag{A.1.7}$$

According to [97], we have the following properties:

$$\Phi_{s_\Pi,s_\Pi}(\omega) \in \mathbb{R}^+ \quad \text{and} \quad \Phi_{s_\Pi,s_\Pi}(\omega) = \Phi_{s_\Pi,s_\Pi}(-\omega), \forall \Pi \in \{\text{re}, \text{im}\} \tag{A.1.8}$$

$$\Phi^*_{s_\Pi,s_\Lambda}(\omega) = \Phi_{s_\Lambda,s_\Pi}(\omega) \quad \text{and} \quad \Phi^*_{s_\Pi,s_\Lambda}(\omega) = \Phi_{s_\Pi,s_\Lambda}(-\omega), \forall \Lambda, \Pi \in \{\text{re}, \text{im}\} \tag{A.1.9}$$

where (A.1.4) implies that $R_{s_{\text{re}},s_{\text{im}}}[l]$ is an odd function. Correspondingly, we have

$$\Phi_{s_{\text{re}},s_{\text{im}}}(\omega) \in \mathbb{I} \quad \text{i.e.}\, \Phi_{s_{\text{re}},s_{\text{im}}}(\omega) = j\mathcal{I}m\left\{\Phi_{s_{\text{re}},s_{\text{im}}}(\omega)\right\}. \tag{A.1.10}$$

Furthermore, with (A.1.9), we obtain:

$$\Phi_{s_{\text{re}},s_{\text{im}}}(-\omega) = -\Phi_{s_{\text{re}},s_{\text{im}}}(\omega), \tag{A.1.11}$$

which indicates that $\Phi_{s_{\text{re}},s_{\text{im}}}(\omega)$ is also an odd function. With (A.1.5) and (A.1.10), Eq. (A.1.7) can be rewritten as:

$$\Phi_{s,s}(\omega) = \Phi_{s_{\text{re}},s_{\text{re}}}(\omega) + \mathcal{I}m\left\{\Phi_{s_{\text{re}},s_{\text{im}}}(\omega)\right\} \quad \text{with} \quad \Phi_{s,s}(\omega) \in \mathbb{R}^+. \tag{A.1.12}$$

With (A.1.8) and (A.1.11), we can easily show that:

$$\begin{aligned}
\max_\omega \Phi_{s,s}(\omega) &= \max_\omega \left(\Phi_{s_{\text{re}},s_{\text{re}}}(\omega) + \mathcal{I}m\left\{\Phi_{s_{\text{re}},s_{\text{im}}}(\omega)\right\}\right) = \max_\omega \left(\Phi_{s_{\text{re}},s_{\text{re}}}(\omega) + |\Phi_{s_{\text{re}},s_{\text{im}}}(\omega)|\right) \\
\min_\omega \Phi_{s,s}(\omega) &= \min_\omega \left(\Phi_{s_{\text{re}},s_{\text{re}}}(\omega) + \mathcal{I}m\left\{\Phi_{s_{\text{re}},s_{\text{im}}}(\omega)\right\}\right) = \min_\omega \left(\Phi_{s_{\text{re}},s_{\text{re}}}(\omega) - |\Phi_{s_{\text{re}},s_{\text{im}}}(\omega)|\right).
\end{aligned} \tag{A.1.13}$$

The statistical and spectral properties listed above will be used to derive asymptotic bounds on the condition number of $\boldsymbol{S}_{\text{LS}}$.

A.2 Proof of Lemma 1

Let λ be an eigenvalue of $\check{\boldsymbol{R}}$, there exist a column vector $\boldsymbol{u}$ so that

$$\check{\boldsymbol{R}}\boldsymbol{u} = \lambda \boldsymbol{u}. \tag{A.2.14}$$

With (2.47), the following relation exists:

$$\boldsymbol{R}\begin{bmatrix} 0 \\ \boldsymbol{u} \end{bmatrix} = \begin{bmatrix} 0 \\ \check{\boldsymbol{R}}\boldsymbol{u} \end{bmatrix} = \lambda \begin{bmatrix} 0 \\ \boldsymbol{u} \end{bmatrix}, \tag{A.2.15}$$

which indicates that λ is also an eigenvalue of $\boldsymbol{R}$.

The equation

$$\boldsymbol{R}\begin{bmatrix}\alpha\\ \boldsymbol{0}_{2L\times 1}\end{bmatrix}=\eta^2\begin{bmatrix}\alpha\\ \boldsymbol{0}_{2L\times 1}\end{bmatrix},\forall\alpha\neq 0 \tag{A.2.16}$$

indicates that η^2 is an eigenvalue of $\boldsymbol{R}$.

A.3 Proof of Lemma 2

Since $\lambda_m\left(\check{\boldsymbol{R}}\right)\geq 0,\forall m$ and

$$\lambda_{2L}\left(\check{\boldsymbol{R}}\right)\leq\frac{1}{2L}\sum_{m=1}^{2L+1}\lambda_m\left(\check{\boldsymbol{R}}\right)\leq\lambda_1\left(\check{\boldsymbol{R}}\right), \tag{A.3.17}$$

we can choose

$$\eta^2=\frac{1}{2L}\sum_{m=1}^{2L+1}\lambda_m\left(\check{\boldsymbol{R}}\right) \tag{A.3.18}$$

to ensure (2.50). By defining $\check{\boldsymbol{S}}_{\mathrm{LS}}:=[\boldsymbol{S}_{\mathrm{Toep,re}},\boldsymbol{S}_{\mathrm{Toep,im}}]$, we have $\check{\boldsymbol{R}}=\check{\boldsymbol{S}}_{\mathrm{LS}}^H\check{\boldsymbol{S}}_{\mathrm{LS}}$, yielding

$$\sum_{m=1}^{2L+1}\lambda_m\left(\check{\boldsymbol{R}}\right)=\mathrm{Trace}\left(\check{\boldsymbol{R}}\right)=\frac{1}{N}\left|\left|\check{\boldsymbol{S}}_{\mathrm{LS}}\right|\right|_F^2. \tag{A.3.19}$$

Substituting (A.3.19) into (A.3.18) yields:

$$\kappa\left(\boldsymbol{R}\right)=\kappa\left(\check{\boldsymbol{R}}\right)=\frac{\lambda_1\left(\check{\boldsymbol{R}}\right)}{\lambda_{2L}\left(\check{\boldsymbol{R}}\right)}. \tag{A.3.20}$$

A.4 Proof of Equation (2.93)

$$
\begin{aligned}
R_{\bar{s}_1\bar{s}_2}[l] &= E\left\{\bar{s}_1[n]\bar{s}_2^*[n-l]\right\} \\
&= E\left\{\left(s_{\mathrm{re}}[n] * \bar{h}[n]\right)\left(s_{\mathrm{im}}[n] * \bar{h}^*[n]\right)\right\} \\
&= E\left\{\left(\sum_{k=-\infty}^{\infty} \bar{h}[k] s_{\mathrm{re}}[n-k]\right)\right. \\
&\qquad \left.\left(\sum_{k'=-\infty}^{\infty} \bar{h}^*[k'] s_{\mathrm{im}}[n-l-k']\right)\right\} \\
&= \sum_{k=-\infty}^{\infty}\sum_{k'=-\infty}^{\infty} \bar{h}[k]\bar{h}^*[k'] E\left\{s_{\mathrm{re}}[n-k]\right. \\
&\qquad\qquad \left. s_{\mathrm{im}}[n-l-k']\right\} \\
&= \sum_{k=-\infty}^{\infty} \bar{h}[k] \sum_{k'=-\infty}^{\infty} \bar{h}^*[k'] R_{s_{\mathrm{re}}s_{\mathrm{im}}}[l+k'-k] \\
&\overset{k''=-k'}{=} \sum_{k=-\infty}^{\infty} \bar{h}[k] \sum_{k''=-\infty}^{\infty} \bar{h}^*[-k''] R_{s_{\mathrm{re}}s_{\mathrm{im}}}[l-k'-k] \\
&= \sum_{k=-\infty}^{\infty} \bar{h}[k] \left(\bar{h}^*[-(l-k)] * R_{s_{\mathrm{re}}s_{\mathrm{im}}}[(l-k)]\right) \\
&= \bar{h}[l] * \bar{h}^*[-l] * R_{s_{\mathrm{re}}s_{\mathrm{im}}}[l]
\end{aligned}
\tag{A.4.21}
$$

A.5 Proof of Equation (2.94)

$$
\begin{aligned}
R_{\bar{s}_1\bar{s}_2}[-l] &= \bar{h}[-l] * \bar{h}^*[l] * R_{s_{\mathrm{re}}s_{\mathrm{im}}}[-l] \\
&\overset{\text{using (2.90)}}{=} -\bar{h}[-l] * \bar{h}^*[l] * R_{s_{\mathrm{re}}s_{\mathrm{im}}}[l] \\
&= -\bar{h}^*[l] * \bar{h}[-l] * R_{s_{\mathrm{re}}s_{\mathrm{im}}}[l] \\
&= -\left(\bar{h}[l] * \bar{h}^*[-l] * R_{s_{\mathrm{re}}s_{\mathrm{im}}}[l]\right)^* \\
&= -R^*_{\bar{s}_1\bar{s}_2}[l].
\end{aligned}
\tag{A.5.22}
$$

Note that $R_{s_{\mathrm{re}}s_{\mathrm{im}}}[l] \in \mathcal{R}$.

A.6 Proof of Equation (2.103)

$$
\begin{aligned}
R_{\bar{s}_2\bar{s}_1}[l] &= \bar{h}[l] * \bar{h}^*[-l] * R_{s_{\mathrm{im}}s_{\mathrm{re}}}[l] \\
&\overset{\text{using (A.1.2)}}{=} \bar{h}[l] * \bar{h}^*[-l] * R_{s_{\mathrm{re}}s_{\mathrm{im}}}[-l] \\
&\overset{\text{using (A.1.4)}}{=} -\bar{h}[l] * \bar{h}^*[-l] * R_{s_{\mathrm{re}}s_{\mathrm{im}}}[l] \\
&= -R_{\bar{s}_1\bar{s}_2}[l].
\end{aligned}
\tag{A.6.23}
$$

A.7 Influence of the Signs of θ, ρ as well as the Values of υ_{re} and υ_{im} on the MSE of K_1

For proper signals, we have

$$\begin{aligned} MSE_{K_1} &= \left| \frac{(1-K_1^2)\frac{\theta}{\rho}}{K_1\left(\frac{\theta}{\rho}K_1 + j\right)} \right|^2 \\ &= \left| \frac{(1-K_1^2)}{K_1} \right|^2 \frac{\left|\frac{\theta}{\rho}\right|^2}{\left|\frac{\theta}{\rho}K_1 + j\right|^2} \end{aligned} \tag{A.7.24}$$

As seen, the signs of θ and ρ only have influence on the term $\left|\frac{\theta}{\rho}K_1 + j\right|^2$. With realistic I/Q-imbalance parameters, $\mathcal{I}m\{K_1\}$ is very small. Thus, this term can be approximated by

$$MSE_{K_1} \approx \left|\frac{\theta}{\rho}\mathcal{R}e\{K_1\} + j\right|^2 = \left|\frac{\theta}{\rho}\mathcal{R}e\{K_1\}\right|^2 + 1, \tag{A.7.25}$$

which is independent of the signs of θ and ρ.

For improper signals, we have

$$MSE'_{K_1} = \left| \frac{-j\upsilon + j(1-K_1)\upsilon_{\mathrm{re}} + (1-K_1^2)\theta}{K_1(\theta K_1 + j\rho)} \right|^2. \tag{A.7.26}$$

Since $|\upsilon| \gg |(1-K_1)\upsilon_{\mathrm{re}}|$, $|\upsilon| \gg |(1-K_1^2)\theta|$ and $|\mathcal{I}m\{K_1\}| \ll 1$, MSE'_{K_1} can be approximated by

$$MSE'_{K_1} \approx \frac{|\upsilon|^2}{|K_1|^2(|\theta\mathcal{R}e\{K_1\}|^2 + |\rho|^2)}, \tag{A.7.27}$$

which is independent of the signs of θ and ρ as well as the variation of υ_{re} and υ_{im} when fixing $|\upsilon|$.

A. APPENDIX FOR CHAPTER 2

Appendix for Chapter 3

B.1 Sidelobe Bound for an OFDM Signal with N_B OFDM Symbols

We extend Eq. (3.8) to describe an OFDM signal with N_B OFDM symbols as follows:

$$\acute{s}^{\mathrm{Ext}}(t) = \sum_{b=0}^{N_B-1} s_b(t) w(t - bT_{\mathrm{w}}), \tag{B.1.1}$$

where b is the index of the OFDM symbol. The frequency response of this signal can be written as:

$$\acute{S}^{\mathrm{Ext}}(f) = \sum_{k=-\frac{N}{2}}^{\frac{N}{2}-1} \left(\sum_{b=0}^{N_B-1} S_b[k] e^{-j2\pi f b T_{\mathrm{w}}} \right) W(f - k\Delta f). \tag{B.1.2}$$

With $|S_b[k]| \leq |S_{\max}|$ and the triangle inequality, the following relations can be obtained:

$$\left| \acute{S}^{\mathrm{Ext}}(f_\nu) \right|^2 \leq N_B^2 \left| S_{\max} \right|^2 \left(\sum_{k=-\frac{N}{2}}^{\frac{N}{2}-1} \left| W(f_\nu - k\Delta f) \right| \right)^2, \tag{B.1.3}$$

which provide an upper-bound on the sidelobe level at the frequency f_ν. Compared to (3.9), this upper-bound is just a scaled version with the factor N_B^2. It can be easily shown that the average spectral power of the interference signal within its bandwidth also scales with N_B^2. Therefore, the sidelobe reduction requirement remains the same as in (3.10). In other words, the analysis using a single OFDM symbol is equivalent to that using multiple OFDM symols.

B.2 Proof of Equation (3.72)

Here, we will prove that $S[k] = \mathcal{F}_N \{s[n]\}|_k = 0, \forall k \,\text{odd}$ results in $s[n + \frac{N}{2}] = -s[n], \forall n \in \mathcal{N}_1$. Since $s[n] = \frac{1}{N} \sum_{\substack{k \in \mathcal{I}_D \\ k \,\text{odd}}} S[k] e^{j \frac{2\pi kn}{N}}$, we have as proof $\forall n \in \mathcal{N}_1$:

$$s[n + \frac{N}{2}] = \frac{1}{N} \sum_{\substack{k \in \mathcal{I}_D \\ k \,\text{odd}}} S[k] e^{j \frac{2\pi k \left(n + \frac{N}{2}\right)}{N}} = \frac{1}{N} \sum_{\substack{k \in \mathcal{I}_D \\ k \,\text{odd}}} S[k] e^{j \frac{2\pi kn}{N}} \underbrace{e^{jk\pi}}_{=-1} = -\frac{1}{N} \sum_{\substack{k \in \mathcal{I}_D \\ k \,\text{odd}}} S[k] e^{j \frac{2\pi kn}{N}} = -s[n]. \tag{B.2.4}$$

B.3 Possible Combinations of the Compensation of Tx-, Rx-I/Q-Imbalance and the Radio Channel

Table B.1: Possible Combinations of the Compensation of Tx-, Rx-I/Q-Imbalance and the Radio Channel

Cases	**Tx-Rx-Comp.**	**Rx-Only-Comp.**
No CFO	Tx, Rx+Ch.	Tx+Ch.+Rx
	Tx, Rx,Ch.	Tx+Rx,Ch
With CFO	Tx, Rx+Ch. (e.g. PTEQ)	Rx, Tx+Ch.
	Tx, Rx,Ch.	Rx,Ch.,Tx
		Tx+Ch.+Rx (e.g. PTEQ)

Table B.2: Possible Combinations of the Tx-/Rx-I/Q-Imbalance of different Tx-/Rx Antennas of MIMO Systems

Cases	**Tx-I/Q-Imb.**	**Rx-I/Q-Imb.**
Tx-Rx-Comp.,no CFO	separate	separate, joint
Tx-Rx-Comp.,with CFO	separate	separate, joint (e.g. PTEQ)
Rx-Only-Comp.,no CFO	joint	joint
Rx-Only-Comp.,with CFO	joint	separate, joint (e.g. PTEQ)

In the tables above, "Tx-Rx-Comp." means Tx-side compensation of the Tx-I/Q-imbalance and Rx-side compensation of Rx-I/Q-imbalance (and CFO), while "Rx-Only-Comp." means Rx-side compensation of both Tx- and Rx-I/Q-imbalance (and CFO).

B.4 Proof of Shift Orthogonality of the Multi-Functional Preamble in Sec. 3.4.7

Let $s_{b,l}^{(i)}[n]$ be the circularly shifted version of $s_b^{(i)}[n]$ with

$$s_{b,l}^{(i)}[n] = s_b^{(i)}[((n-l))_N], \forall n \in \mathcal{N}, \forall 0 \leq l \leq L, \tag{B.4.5}$$

and

$$\begin{aligned} S_{b,l}^{(i)}[k] = \mathcal{F}_N\left\{s_{b,l}^{(i)}[n]\right\} = S_b^{(i)}[k]e^{-j\frac{2\pi kl}{N}} \\ \forall -\frac{N}{2} \leq k \leq \frac{N}{2}-1, \forall 0 \leq l \leq L. \end{aligned} \tag{B.4.6}$$

The shifted version of the short preambles will be $\left\{s_{b,l}^{(i)}[n], n = 0, \ldots, \frac{N}{2}-1\right\}$. The correlation between shifted short preambles of different Tx antennas can be expressed as:

$$\sum_{n=0}^{\frac{N}{2}-1} s_{b,l_0}^{(i_0)}[n] s_{b,l_1}^{(i_1)}[n], \forall i_0 \neq i_1, \forall 0 \leq l_0, l_1 \leq L. \tag{B.4.7}$$

Expressing $s_{b,l}^{(i)}[n]$ as IDFT of $S_{b,l}^{(i)}[k]$ according to (B.4.6), (B.4.7) can be rewritten as:

$$\begin{aligned} &\frac{1}{N^2}\sum_{n=0}^{\frac{N}{2}-1}\left(\sum_{\substack{k=-\frac{N}{2}\\ k\,\text{odd}}}^{\frac{N}{2}-1} S_b^{(i_0)*}[-k]e^{j\frac{2\pi k(n-l_0)}{N}}\right) \\ &\left(\sum_{\substack{k'=-\frac{N}{2}\\ k'\,\text{odd}}}^{\frac{N}{2}-1} S_b^{(i_1)}[k']e^{j\frac{2\pi k'(n-l_1)}{N}}\right) \\ &= \frac{1}{N^2}\sum_{\substack{k=-\frac{N}{2}\\ k\,\text{odd}}}^{\frac{N}{2}-1}\sum_{\substack{k'=-\frac{N}{2}\\ k'\,\text{odd}}}^{\frac{N}{2}-1} S_b^{(i_0)*}[-k]S_b^{(i_1)}[k']e^{-j\frac{2\pi(kl_0+k'l_1)}{N}} \\ &\sum_{n=0}^{\frac{N}{2}-1} e^{j\frac{2\pi(k+k')n}{N}}. \end{aligned} \tag{B.4.8}$$

With both odd numbers k and k', $(k+k')$ is an even number. Thus, $\sum_{n=0}^{\frac{N}{2}-1} e^{j\frac{2\pi(k+k')n}{N}}$

equals zeros except when $k + k' = 0$. Thus, (B.4.8) becomes

$$\frac{1}{2N} \sum_{\substack{k=-\frac{N}{2} \\ k \text{ odd}}}^{\frac{N}{2}-1} S_b^{(i_0)*}[k] S_b^{(i_1)}[k] e^{-j\frac{2\pi k(l_0+l_1)}{N}}. \tag{B.4.9}$$

From (3.77) and $\mathcal{I}_{i_0} \cap \mathcal{I}_{i_1} = \emptyset, \forall i_0 \neq i_1$, it is obvious that (B.4.9) equals zero.

B.5 Proof of Equation (3.83)

According to the definition in Sec. 3.4.7.2.1, $\bar{y}_b[n] = \sum_{i=1}^{N_T} \left(s_b^{(i)}[n] \circledast_N h_{\mathrm{D}}^{(i)}[n] + s_b^{(i)*}[n] \circledast_N h_{\mathrm{I}}^{(i)}[n] \right), \forall n \in \mathcal{N}$. First, we define $\bar{y}_{\mathrm{D}}^{(i)}[n] := s_b^{(i)}[n] \circledast_N h_{\mathrm{D}}^{(i)}[n]$ and $\bar{y}_{\mathrm{I}}^{(i)}[n] := s_b^{(i)*}[n] \circledast_N h_{\mathrm{I}}^{(i)}[n]$. Assuming $L < \frac{N}{2}$, we have the following expressions for $n \in \mathcal{N}_1$:

$$\begin{aligned} \bar{y}_{\mathrm{D}}^{(i)}[n] &= \sum_{m=0}^{L-1} h_{\mathrm{D}}^{(i)}[m] s_b^{(i)}[((n-m))_N], \\ \bar{y}_{\mathrm{D}}^{(i)}[n+\frac{N}{2}] &= \sum_{m=0}^{L-1} h_{\mathrm{D}}^{(i)}[m] s_b^{(i)}[\underbrace{n+\frac{N}{2}-m}_{\in [N/2-L+1, N-1]}]. \end{aligned} \tag{B.5.10}$$

With (3.72), (B.5.10) and $n-m \in \left[-L+1, \frac{N}{2}-L\right]$, the following relation can be obtained:

$$s_b^{(i)}[n+\frac{N}{2}-m] = \begin{cases} -s_b^{(i)}[n-m], & n-m \in \mathcal{N}_1 \\ -s_b^{(i)}[n-m+N], & n-m \in -\mathcal{N}_1 \end{cases}, \tag{B.5.11}$$

which is equivalent to $s_b^{(i)}[n+\frac{N}{2}-m] = -s_b^{(i)}[((n-m))_N]$. Thus,

$$\bar{y}_{\mathrm{D}}^{(i)}[n+\frac{N}{2}] = -\bar{y}_{\mathrm{D}}^{(i)}[n], \forall n \in \mathcal{N}_1, \tag{B.5.12}$$

Similarly, with $s_b^{(i)*}[n+\frac{N}{2}] = -s_b^{(i)*}[n], \forall n \in \mathcal{N}_1$, we can prove:

$$\bar{y}_{\mathrm{I}}^{(i)}[n+\frac{N}{2}] = -\bar{y}_{\mathrm{I}}^{(i)}[n], \forall n \in \mathcal{N}_1. \tag{B.5.13}$$

With (B.5.12), (B.5.13) and $\bar{y}_b[n] = \sum_{i=1}^{N_T} \left(\bar{y}_{\mathrm{D}}^{(i)}[n] + \bar{y}_{\mathrm{I}}^{(i)}[n] \right)$, Eq. (3.83) can be easily obtained.

B.6 Proof of the Fulfillment of the 3rd Design Rule with the Preamble in Sec. 3.4.7.1

The matrix $\mathbf{\Gamma}_b^{(i)}$ with circulant structure in (3.45) can be decomposed as

$$\mathbf{\Gamma}_b^{(i)} = \frac{1}{N}\boldsymbol{F}^H \boldsymbol{D}_b^{(i)} \boldsymbol{F}_{(:,\mathcal{L})}, \tag{B.6.14}$$

where $\boldsymbol{D}_b^{(i)}$ is a diagonal matrix containing the DFT-elements of $s_b^{(i)}[n]$ i.e. $\boldsymbol{D}_b^{(i)} = \text{diag}\left\{\left[S_b^{(i)}[-\frac{N}{2}], \ldots, S_b^{(i)}[\frac{N}{2}-1]\right]\right\}$ and $\mathcal{L} = \{0, \ldots, L-1\}$. Thus, we have

$$\mathbf{\Gamma}_b^{(i_0)^H} \mathbf{\Gamma}_b^{(i_1)*} = \frac{1}{N}\boldsymbol{F}_{(:,\mathcal{L})}^H \mathbf{\Delta}_b^{(i_0,i_1)} \boldsymbol{F}_{(:,\mathcal{L})}, \forall i_0, i_1 \tag{B.6.15}$$

where $\mathbf{\Delta}_b$ is a $N \times N$ diagonal matrix with the diagonal elements

$$\left(\mathbf{\Delta}_b^{(i_0,i_1)}\right)_{k,k} = \begin{cases} S_b^{(i_0)*}[k] S_b^{(i_1)*}[k], & k = -\frac{N}{2} \\ S_b^{(i_0)*}[k] S_b^{(i_1)*}[-k], & -\frac{N}{2}+1 \leq k \leq \frac{N}{2}-1 \end{cases}. \tag{B.6.16}$$

Applying (B.6.15) to design rule 3) yields

$$\begin{aligned} \sum_{b=1}^{2} \mathbf{\Gamma}_b^{(i_0)^H} \mathbf{\Gamma}_b^{(i_1)*} &= \frac{1}{N}\boldsymbol{F}_{(:,\mathcal{L})}^H \left(\sum_{b=1}^{2} \mathbf{\Delta}_b^{(i_0,i_1)}\right) \boldsymbol{F}_{(:,\mathcal{L})} \\ &= \mathbf{0}_L, \forall i_0, i_1, \end{aligned} \tag{B.6.17}$$

which is fulfilled when

$$\sum_{b=1}^{2} \mathbf{\Delta}_b^{(i_0,i_1)} = \mathbf{0}_L, \forall i_0, i_1. \tag{B.6.18}$$

Now, we consider the subcarrier selection cases in 3.4.7.1.2 and assume that the subcarrier $k = -\frac{N}{2}$ is within the guardband. In case 1), $\mathcal{I}_{i_0} = -\mathcal{I}_{i_1}$ with $i_0 \neq i_1$, we have

$$\left(\sum_{b=1}^{2} \mathbf{\Delta}_b^{(i_0,i_1)}\right)_{k,k} = \begin{cases} 0, & k \notin \mathcal{I}_{i_0} \\ \sum_{b=1}^{2} S_b^{(i_0)*}[k] S_b^{(i_1)*}[-k], & k \in \mathcal{I}_{i_0} \end{cases}. \tag{B.6.19}$$

For $k \in \mathcal{I}_{i_0}$, we have for each $k = \mathcal{I}_{i_0}(\kappa)$ the following relation:

$$\begin{aligned} S_b^{(i_0)*}[k] &= T_b^{(i_0)}[\kappa], \\ S_b^{(i_1)*}[-k] &= T_b^{(i_1)}[\kappa'], \end{aligned} \tag{B.6.20}$$

where κ' is defined as in Sec. 3.4.7.3. With (B.6.19) and (B.6.20), the requirement of (B.6.18) can be transformed to

$$\sum_{b=1}^{2} T_b^{(i_0)*}[\kappa] T_b^{(i_1)*}[\kappa'], \forall \kappa = 0, \ldots, L' - 1, \tag{B.6.21}$$

which is equivalent to Eq. (3.97). In case 2), $\mathcal{I}_i = -\mathcal{I}_i$. Eq. (B.6.18) to Eq. (B.6.21) apply with $i_0 = i_1 = i$. Particularly, by applying $i_0 = i_1 = i$, Eq. (B.6.21) is equivalent to Eq. (3.100). Since the preamble designs in case 1) and 2) fulfill Eq. (3.97) and Eq. (3.100), respectively, the 3$^{\text{rd}}$ design rule is fulfilled. In case 3), $\mathcal{I}_{i_0} \cap (-\mathcal{I}_{i_0}) = \emptyset, (-\mathcal{I}_{i_0}) \cap \mathcal{I}_{i_1} = \emptyset, \forall i_1 \neq i_0$. We have

$$S_b^{(i_0)*}[k] S_b^{(i_1)*}[-k] = 0, \forall k \in \mathcal{I}_{i_0}, \tag{B.6.22}$$

which implies (B.6.18) according to (B.6.19). Thus, the 3$^{\text{rd}}$ design rule is also fulfilled in this case.

B.7 Derivation of the Relation between DMOD input and ALP output in Sec. 3.5.2

The relation between $v(t)$ and the ALP outputs $y_{\text{re}}(t)$ and $y_{\text{im}}(t)$ can be written as

$$\begin{aligned}
y_{\text{re}}(t) =& \frac{1}{2}\Bigg[v_{\text{re}}(t) \Bigg(\underbrace{\cos\left(2\pi\left(2f_c + \Delta f\right)t\right)}_{\text{suppressed by ALP}} + \cos\left(2\pi\Delta f t\right) \Bigg) \\
& - v_{\text{im}}(t) \Bigg(\underbrace{\sin\left(2\pi\left(2f_c + \Delta f\right)t\right)}_{\text{suppressed by ALP}} - \sin\left(2\pi\Delta f t\right) \Bigg) \Bigg] * h^{RI}(t) \\
=& \frac{1}{2}\left[v_{\text{re}}(t)\cos\left(2\pi\Delta f t\right) + v_{\text{im}}(t)\sin\left(2\pi\Delta f t\right) \right] * h^{RI}(t) \\
y_{\text{im}}(t) =& \frac{1}{2} g^R \Bigg[-v_{\text{re}}(t) \Bigg(\underbrace{\sin\left(2\pi\left(2f_c + \Delta f\right)t + \varphi^R\right)}_{\text{suppressed by ALP}} + \sin\left(2\pi\Delta f t + \varphi^R\right) \Bigg) \\
& - v_{\text{im}}(t) \Bigg(\underbrace{\cos\left(2\pi\left(2f_c + \Delta f\right)t + \Delta\varphi^R\right)}_{\text{suppressed by ALP}} - \cos\left(2\pi\Delta f t + \varphi^R\right) \Bigg) \Bigg] * h^{RQ}(t) \\
=& \frac{1}{2} g^R \left[-v_{\text{re}}(t)\sin\left(2\pi\Delta f t + \Delta\varphi^R\right) + v_{\text{im}}(t)\cos\left(2\pi\Delta f t \Delta + \varphi^R\right) \right] * h^{RQ}(t),
\end{aligned} \tag{B.7.23}$$

where the Rx index r is omitted for simplicity. Substituting Eq. (B.7.23) into $y(t) = y_{\mathrm{re}}(t) + jy_{\mathrm{im}}(t)$, (3.102) can be obtained.

B.8 Alternative Scheme for Joint CFO and Rx-I/Q- Imbalance Estimation Using Complex-Valued Compensation Filters

Except for the real valued Rx-I/Q-imbalance compensation structure in Sec. 3.5.3, a complex valued filter based compensation can also be applied (as described in [123]). The Rx-I/Q-imbalance compensation using a complex valued filter can be expressed as:

$$\acute{y}^{\langle r\rangle}[n] = y^{\langle r\rangle}[n] - y^{\langle r\rangle *}[n] * \rho^{C,\langle r\rangle}[n], \tag{B.8.24}$$

where $\rho^{C}[n]$ denotes a length-L_{c} complex valued FIR filter with a dominant tap index n_τ. Providing perfect Rx-I/Q-imbalance compensation coefficients, we have the following relation, which is equivalent to Eq. (3.137):

$$\left(\dot{\boldsymbol{y}}_1^{\langle r\rangle} - \dot{\mathbb{Y}}_1^{\langle r\rangle *}\boldsymbol{\rho}^{C,\langle r\rangle}\right) e^{j\Omega} = \dot{\boldsymbol{y}}_2^{\langle r\rangle} - \dot{\mathbb{Y}}_2^{\langle r\rangle *}\boldsymbol{\rho}^{C,\langle r\rangle}, \tag{B.8.25}$$

where $\boldsymbol{\rho}^{C,\langle r\rangle} = \left[\rho^{C,\langle r\rangle}[0], \ldots, \rho^{C,\langle r\rangle}[L_{\mathrm{c}}-1]\right]^T$ and $\dot{\mathbb{Y}}_b^{\langle r\rangle}$ is a $N_P \times L_{\mathrm{c}}$ Toeplitz matrix with the n_τ^{th} column equal to $\dot{\boldsymbol{y}}_b^{\langle r\rangle}$. Based on (B.8.25), if we have a temporary estimate of ϵ i.e. Ω, the filter $\boldsymbol{\rho}^{C,\langle r\rangle}$ can be obtained by

$$\begin{aligned} \hat{\boldsymbol{\rho}}^{C,\langle r\rangle} &= {\mathbb{R}_\epsilon^{\langle r\rangle}}^{\dagger}\mathbb{T}_\epsilon^{\langle r\rangle}, \\ \mathbb{R}_\epsilon^{\langle r\rangle} &:= \dot{\mathbb{Y}}_1^{\langle r\rangle *}e^{j\Omega} - \dot{\mathbb{Y}}_2^{\langle r\rangle *}, \\ \mathbb{T}_\epsilon^{\langle r\rangle} &:= \dot{\boldsymbol{y}}_1^{\langle r\rangle}e^{j\Omega} - \dot{\boldsymbol{y}}_2^{\langle r\rangle}. \end{aligned} \tag{B.8.26}$$

An alternative joint CFO- and Rx-I/Q-imbalance scheme can be obtained by replacing (3.140) with (B.8.26) in Sec. 3.5.5.2 (The other steps of the scheme in Sec. 3.5.5.2 remains unchanged).

References

[1] M. Peter, W. Keusgen, and J. Luo, "A survey on 60 GHz broadband communication: Capability, applications and system design," *European Microwave Week 2008, Amsterdam*, pp. 1–4, Oct. 2008. xv, 2, 3

[2] L. Ding, Z. Ma, D. R. Morgan, M. Zierdt, and G. Tong Zhou, "Compensation of frequency-dependent gain/phase imbalance in predistortion linearization systems," *IEEE Transactions on Circuits and Systems I: Regular Papers*, vol. 55, no. 1, pp. 390–397, 2008. xv, 7, 11, 12, 13, 16, 19, 33, 37, 39, 59

[3] L. Anttila, M. Valkama, and M. Renfors, "Frequency-selective I/Q mismatch calibration of wideband direct-conversion transmitters," *Circuits and Systems II: Express Briefs, IEEE Transactions on*, vol. 55, no. 4, pp. 359–363, April 2008. xv, 4, 9, 10, 11, 12, 13, 16, 17, 19, 37, 39, 59

[4] G. Fettweis, F. Guderian, and S. Krone, "Entering the path towards Terabit/s wireless links," *Proceedings of the Design Automation and Test in Europe (DATE'11),Grenoble, France*, 2011. 1

[5] M. Valkama, "Advanced I/Q signal processing for wideband receivers: Models and algorithms," *Phd thesis, Tampere University of Technology*, 2001. 2

[6] M. Valkama, J. Pirskanen, and M. Renfors, "Signal processing challenges for applying software radio principles in future wireless terminals: An overview," *Int. Journal of Communication Systems*, vol. 15, pp. 741–769, Oct. 2002. 2

[7] U. Li, S. Mclaughlin, D. G. M. Cruickshank, and X. Wei, "Towards multi-mode terminals," *IEEE Vehicular Technology Magazine*, vol. 1, no. 4, pp. 17–24, 2006. 2

[8] A. Baschirotto, R. Castello, F. Campi, G. Cesura, M. Toma, R. Guerrieri, R. Lodi, L. Lavagno, and P. Malcovati, "Baseband analog front-end and digital back-end for reconfigurable multi-standard terminals," *IEEE Circuits and Systems Magazine*, vol. 6, no. 1, pp. 8–28, 2006. 2

[9] F. Agnelli, G. Albasini, I. Bietti, A. Gnudi, A. Lacaita, D. Manstretta, R. Rovatti, E. Sacchi, P. Savazzi, F. Svelto, E. Temporiti, S. Vitali, and R. Castello, "Wireless multistandard terminals: system analysis and design of a reconfigurable rf front-end," *IEEE Circuits and Systems Magazine*, vol. 6, no. 1, pp. 38–59, 2006. 2

[10] L. Maurer, G. Hueber, T. Dellsperger, T. Burger, M. Huemer, and R. Weigel, "A frequency agile terminal receiver for wireless multi-standard applications," in *Proc. IEEE Radio and Wireless Symp*, 2006, pp. 291–294. 2

[11] R. Kakerow and G. Boeck, "Reconfigurable receiver approach for future wireless terminals," *Analog Integrated Circuits and Signal Processing*, vol. 59, pp. 105–115, 2009, 10.1007/s10470-008-9249-7. [Online]. Available: http://dx.doi.org/10.1007/s10470-008-9249-7 2

[12] G. Hueber, Y. Zou, K. Dufrene, R. Stuhlberger, and M. Valkama, "Smart front-end signal processing for advanced wireless receivers," *Selected Topics in Signal Processing, IEEE Journal of*, vol. 3, no. 3, pp. 472 –487, june 2009. 2, 4, 7

[13] J. Platz, G. Strasser, K. Feilkas, L. Maurer, and A. Springer, "A direct up-conversion transmitter with integrated prescaler for reconfigurable multi-band/multi-standard base stations," in *Radio Frequency integrated Circuits (RFIC) Symposium, 2005. Digest of Papers. 2005 IEEE*, june 2005, pp. 487 – 490. 2

[14] B. Haberland, W. Koenig, A. Pascht, and U. Weiss, "Software defined radio: A promising technology for multi-standard base stations," *Alcatel Telecommunications Review, White Paper*, 2005. 2

[15] N. Lashkarian, E. Hemphill, H. Tarn, H. Parekh, and C. Dick, "Reconfigurable digital front-end hardware for wireless base-station transmitters: Analysis, design and fpga implementation," *Circuits and Systems I: Regular Papers, IEEE Transactions on*, vol. 54, no. 8, pp. 1666 –1677, aug. 2007. 2

[16] G. Fettweis, M. Lohning, D. Petrovic, M. Windisch, P. Zillmann, and W. Rave, "Dirty RF: a new paradigm," *PIMRC05. IEEE 16th International Symposium on*, vol. 4, p. Vol. 4, Sept. 2005. 2, 8

[17] S. Woo, D. Lee, K. Kim, Y. Hur, C.-H. Lee, and J. Laskar, "Combined effects of rf impairments in the future ieee 802. 11n wlan systems," in *Proc. VTC 2005-Spring Vehicular Technology Conf. 2005 IEEE 61st*, vol. 2, 2005, pp. 1346–1349. 2

[18] S. Woo, H. Yu, J. Lee, C.-H. Lee, and J. Laskar, "Effects of rf impairments in transmitter for the future beyond-3g communications systems," in *Proc. IEEE Int. Symp. Circuits and Systems ISCAS 2006*, 2006. 2

[19] T. C. W. Schenk and E. R. Fledderus, "Rf impairments in high-rate wireless systems - understanding the impact of tx/rx-asymmetry," in *Proc. 3rd Int. Symp. Communications, Control and Signal Processing ISCCSP 2008*, 2008, pp. 117–122. 2

[20] Q. Zou, M. Mikhemar, and A. H. Sayed, "Digital compensation of rf nonlinearities in software-defined radios," in *Proc. IEEE Int. Conf. Acoustics, Speech and Signal Processing ICASSP 2008*, 2008, pp. 2921–2924. 2

[21] D. Tandur, C.-Y. Lee, and M. Moonen, "Efficient compensation of rf impairments for ofdm systems," in *Proc. IEEE Wireless Communications and Networking Conf. WCNC 2009*, 2009, pp. 1–6. 2

[22] G. Hueber and R. Staszewski, "Rf impairment compensation for future radio systems," in *Multi-Mode / Multi-Band RF Transceivers for Wireless Communications:Advanced Techniques, Architectures, and Trends.* IEEE, 2011, pp. 451–496. 2

[23] *Smart-RF project: www.smart-rf.de.* 2, 77

[24] P. Smulders, "Exploiting the 60 ghz band for local wireless multimedia access: prospects and future directions," *Communications Magazine, IEEE*, vol. 40, no. 1, pp. 140 –147, jan 2002. 3

[25] D. Sommer and G. Fettweis, "Coherent OFDM transmission at 60 GHz," *Vehicular Technology Conference, 1999. VTC 1999 - Fall. IEEE VTS 50th*, vol. 3, pp. 1545–1549 vol.3, 1999. 3

[26] J. Noreus, M. Flament, A. Alping, and H. Zirath, "System considerations for hardware parameters in a 60 ghz wlan," in *Symposium on Gigahertz Electronics, Gothenburg*, 2000. 3

[27] A. Siamarou, "Broadband wireless local-area networks at millimeter waves around 60 ghz," *Antennas and Propagation Magazine, IEEE*, vol. 45, no. 1, pp. 177 – 181, feb 2003. 3

[28] A. Seyedi and D. Birru, "On the design of a multi-gigabit short-range communication system in the 60ghz band," in *Consumer Communications and Networking Conference, 2007. CCNC 2007. 4th IEEE*, jan. 2007, pp. 1 –6. 3

[29] S. Krone, F. Guderian, G. Fettweis, M. Petri, M. Piz, M. Marinkovic, M. Peter, R. Felbecker, and W. Keusgen, "Physical layer design, link budget analysis, and digital baseband implementation for 60 GHz short-range applications," *International Journal of Microwave and Wireless Technologies*, 2011. 3

[30] B. Schulte, M. Peter, R. Felbecker, W. Keusgen, R. Steffen, H. Schumacher, M. Hellfeld, A. Barghouthi, S. Krone, F. Guderian, G. Fettweis, and V. Ziegler, "60 GHz WLAN

applications and implementation aspects," *EuMA Int. J. Microw. Wirel. Technol. (Special Issue on 60 GHz Communication Systems)*, 2011. 3

[31] E. Perahia, C. Cordeiro, M. Park, and L. Yang, "IEEE 802.11ad: Defining the next generation multi-Gbps Wi-Fi," in *Consumer Communications and Networking Conference (CCNC), 2010 7th IEEE*, jan. 2010, pp. 1 –5. 3, 82

[32] J. Luo, A. Kortke, and W. Keusgen, "Throughput maximization of a hybrid dynamic frame aggregation and block-ACK scheme for 60 GHz high speed communications." 21st Annual IEEE International Symposium on Personal, Indoor and Mobile Radio Communications (PIMRC), 2010. 3

[33] A. C. Ulusoy and H. Schumacher, "A system-on-package analog synchronous QPSK demodulator for ultra-high rate 60 GHz wireless communications," in *International Microwave Symposium, Baltimore*, 2011. 3

[34] A. Abidi, "Direct-conversion radio transceivers for digital communications," *Solid-State Circuits, IEEE Journal of*, vol. 30, no. 12, pp. 1399 –1410, dec 1995. 3

[35] D. Dardari, V. Tralli, and A. Vaccari, "A theoretical characterization of nonlinear distortion effects in ofdm systems," *IEEE Transactions on Communications*, vol. 48, no. 10, pp. 1755–1764, 2000. 4, 8

[36] M. Valkama, A. Shahed hagh ghadam, L. Anttila, and M. Renfors, "Advanced digital signal processing techniques for compensation of nonlinear distortion in wideband multicarrier radio receivers," *Microwave Theory and Techniques, IEEE Transactions on*, vol. 54, no. 6, pp. 2356 –2366, june 2006. 4

[37] J. Luo, A. Kortke, and W. Keusgen, "Joint calibration of frequency selective time variant I/Q-imbalance and modulator DC-offset error in broadband direct-conversion transmitters," *ICCCAS'09*, pp. 255–259, July 2009. 5, 6, 10, 11, 12, 13

[38] ——, "Semi-blind iterative joint estimation of frequency selective I/Q-imbalance and modulator offset error in direct-conversion transmitters," in *IEEE Conference VTC 2010-Fall*, 2010. 5, 11, 12, 13, 41, 42, 60, 70

[39] J. Luo, W. Keusgen, A. Kortke, and M. Peter, "A design concept for a 60GHz wireless in-flight entertainment system." Calgary, Canada: IEEE 68th VTC 2008-Fall. 5, 6

[40] J. Luo, W. Keusgen, and A. Kortke, "Optimization of time domain windowing and guardband size for cellular OFDM systems." Calgary, Canada: IEEE 68th VTC 2008-Fall, 2008. 5, 6, 95

[41] J. Luo, A. Kortke, and W. Keusgen, "Efficient channel estimation schemes for MIMO OFDM systems with NULL subcarriers," in *IEEE VTC 2008-Fall, Calgary, Canada*, 2008. 5, 44, 119, 120, 121, 124, 134

[42] J. Luo, W. Keusgen, and A. Kortke, "Preamble designs for efficient joint channel and frequency-selective I/Q-imbalance compensation in MIMO OFDM systems," *Wireless Communications and Networking Conference (WCNC'10)*, pp. 1 –6, 18-21 2010. 5, 6, 11, 109, 111

[43] J. Luo, A. Kortke, and W. Keusgen, "Antenna diversity schemes for uplink frequency-domain multiuser detection in CP-assisted DS-CDMA systems," in *Communications, 2009. ICC '09. IEEE International Conference on*, june 2009, pp. 1 –5. 5, 6, 173

[44] J. Luo, W. Keusgen, and A. Kortke, "Preamble based joint CFO, frequency-selective I/Q-imbalance and channel estimation and compensation in MIMO OFDM systems," *IEEE 74th VTC 2008-Fall, San Francisco, USA*, 2011. 5, 6, 11, 109, 142, 143

[45] Y. Zou, M. Valkama, and M. Renfors, "Pilot-based compensation of frequency-selective I/Q imbalances in direct-conversion OFDM transmitters," *Vehicular Technology Conference, 2008. VTC 2008-Fall. IEEE 68th*, pp. 1–5, Sept. 2008. 7, 11, 12, 112

[46] L. Anttila, P. Handel, and M. Valkama, "Joint mitigation of power amplifier and I/Q modulator impairments in broadband direct-conversion transmitters," *IEEE Transactions on Microwave Theory and Techniques*, vol. 58, no. 4, pp. 730–739, 2010. 7, 8, 10, 11, 12, 13, 19

[47] L. Ding, Z. Ma, D. Morgan, M. Zierdt, and G. Zhou, "Frequency-dependent modulator imbalance in predistortion linearization systems: modeling and compensation," *Signals, Systems and Computers, 2003. Conference Record of the 37th Asilomar Conference on*, vol. 1, pp. 688–692 Vol.1, Nov. 2003. 7, 9, 10, 11, 12, 13, 16, 17, 19, 33

[48] L. Anttila, M. Valkama, and M. Renfors, "Circularity-based I/Q imbalance compensation in wideband direct-conversion receivers," *Vehicular Technology, IEEE Transactions on*, vol. 57, no. 4, pp. 2099–2113, July 2008. 7, 51, 74, 108, 109, 143, 173

[49] R. Raich and G. T. Zhou, "On the modeling of memory nonlinear effects of power amplifiers for communication applications," in *Proc. IEEE 10th and the 2nd Signal Processing Education Workshop Digital Signal Processing Workshop*, 2002, pp. 7–10. 8

[50] C. Crespo-Cadenas, J. Reina-Tosina, and M. J. Madero-Ayora, "Volterra series approach to behavioral modeling: Application to an fet amplifier," in *Proc. Asia-Pacific Microwave Conf. APMC 2006*, 2006, pp. 445–448. 8

[51] B. Schubert, J. Liszewski, and W. Keusgen, "Identification of the volterra kernels of nonlinear power amplifiers," in *Proc. Int. Conf. Communications, Circuits and Systems ICCCAS 2009*, 2009, pp. 767–771. 8, 73

[52] H. Zhou, G. Wan, and L. Chen, "A nonlinear memory power amplifier behavior modeling and identification based on memory polynomial model in soft-defined shortwave transmitter," in *Proc. 6th Int Wireless Communications Networking and Mobile Computing (WiCOM) Conf*, 2010, pp. 1–4. 8

[53] L. Anttila, P. Hndel, O. Myllri, and M. Valkama, "Recursive learning-based joint digital predistorter for power amplifier and I/Q modulator impairments," *International Journal of Microwave and Wireless Technologies*, vol. 2, pp. 173–182, 2010. 8, 10, 12, 13

[54] S. Han, "An effective slm-prsc hybrid scheme for ofdm papr reduction based on repeated utilization of identical prsc sequences in time domain," in *Proc. IEEE Asia Pacific Conf. Circuits and Systems APCCAS 2006*, 2006, pp. 298–301. 8

[55] B. S. Krongold and D. L. Jones, "An active-set approach for OFDM PAR reduction via tone reservation," *IEEE Transactions on Signal Processing*, vol. 52, no. 2, pp. 495–509, 2004. 8

[56] S. H. Han and J. H. Lee, "An overview of peak-to-average power ratio reduction techniques for multicarrier transmission," *IEEE Wireless Communications Magazine*, vol. 12, no. 2, pp. 56–65, 2005. 8

[57] P. Boonsrimuang, K. Mori, T. Paungma, and H. Kobayashi, "Papr reduction method for ofdm signal by using dummy sub-carriers," in *Proc. 1st Int Wireless Pervasive Computing Symp*, 2006, pp. 1–5. 8

[58] S. B. Slimane, "Peak-to-average power ratio reduction of ofdm signals using broadband pulse shaping," in *Proc. VTC 2002-Fall Vehicular Technology Conf. 2002 IEEE 56th*, vol. 2, 2002, pp. 889–893. 8

[59] L. Ding, G. T. Zhou, D. R. Morgan, Z. Ma, J. S. Kenney, J. Kim, and C. R. Giardina, "A robust digital baseband predistorter constructed using memory polynomials," *IEEE Transactions on Communications*, vol. 52, no. 1, pp. 159–165, 2004. 8

[60] J. Liszewski, B. Schubert, W. Keusgen, and A. Kortke, "Low-complexity fpga implementation of volterra predistorters for power amplifiers," in *Proc. IEEE Topical Conf. Power Amplifiers for Wireless and Radio Applications (PAWR)*, 2011, pp. 41–44. 8, 73, 77

[61] C. F. Lanzani and G. K. D. Boppana, "Remote radio heads and the evolution towards 4G networks," *Technical white paper from Radiocomp and Altera*, 2009. 8

[62] A. Gokceoglu, A. Ghadam, and M. Valkama, "Effects of power amplifier memory on adaptive feedforward linearizers," in *Wireless Communication Systems. 2008. ISWCS '08. IEEE International Symposium on*, oct. 2008, pp. 304 –308. 8

[63] S. Burglechner, A. Shahed Hagh Ghadam, A. Springer, M. Valkama, and G. Hueber, "Dsp oriented implementation of a feedforward power amplifier linearizer," in *Circuits and Systems, 2009. ISCAS 2009. IEEE International Symposium on*, may 2009, pp. 1755 –1758. 8

[64] J. K. Cavers, "The effect of quadrature modulator and demodulator errors on adaptive digital predistorters for amplifier linearization," *IEEE Transactions on Vehicular Technology*, vol. 46, no. 2, pp. 456–466, 1997. 10, 11, 12

[65] ——, "New methods for adaptation of quadrature modulators and demodulators in amplifier linearization circuits," *IEEE Transactions on Vehicular Technology*, vol. 46, no. 3, pp. 707–716, 1997. 10, 11, 12

[66] Y.-D. Kim, E.-R. Jeong, and Y. H. Lee, "Adaptive compensation for power amplifier nonlinearity in the presence of quadrature modulation/demodulation errors," *IEEE Transactions on Signal Processing*, vol. 55, no. 9, pp. 4717–4721, 2007. 10

[67] D. S. Hilborn, S. P. Stapleton, and J. K. Cavers, "An adaptive direct conversion transmitter," *IEEE Transactions on Vehicular Technology*, vol. 43, no. 2, pp. 223–233, 1994. 10, 11, 12

[68] F. Gregorio, J. Cousseau, S. Werner, T. Riihonen, and R. Wichman, "Compensation of iq imbalance and transmitter nonlinearities in broadband mimo-ofdm," in *Circuits and Systems (ISCAS), 2011 IEEE International Symposium on*, may 2011, pp. 2393 –2396. 10, 11, 12, 13

[69] M. Windisch and G. Fettweis, "Adaptive I/Q imbalance compensation in low-IF transmitter architectures," in *Vehicular Technology Conference, 2004. VTC2004-Fall. 2004 IEEE 60th*, vol. 3, sept. 2004, pp. 2096 – 2100 Vol. 3. 10, 11, 12, 13, 19

[70] M. Faulkner, T. Mattsson, and W. Yates, "Automatic adjustment of quadrature modulators," *Electronics Letters*, vol. 27, no. 3, pp. 214–216, 1991. 11, 12

[71] J. K. Cavers and M. W. Liao, "Adaptive compensation for imbalance and offset losses in direct conversion transceivers," *IEEE Transactions on Vehicular Technology*, vol. 42, no. 4, pp. 581–588, 1993. 11, 12

[72] R. Marchesani, "Digital precompensation of imperfections in quadrature modulators," *Communications, IEEE Transactions on*, vol. 48, no. 4, pp. 552–556, Apr 2000. 11, 12

[73] X. Huang and M. Caron, "Gain/phase imbalance and DC offset compensation in quadrature modulators," in *Circuits and Systems, 2002. ISCAS 2002. IEEE International Symposium on*, vol. 4, 2002, pp. IV–811 – IV–814 vol.4. 11, 12

[74] J. Tubbax, B. Come, L. Van der Perre, S. Donnay, M. Moonen, and H. De Man, "Compensation of transmitter iq imbalance for ofdm systems," in *Acoustics, Speech, and Signal Processing, 2004. Proceedings. (ICASSP '04). IEEE International Conference on*, vol. 2, may 2004, pp. ii – 325–8 vol.2. 11

[75] L. Angrisani and R. Colella, "Detection and evaluation of i/q impairments in rf digital transmitters," *Science, Measurement and Technology, IEE Proceedings* -, vol. 151, no. 1, pp. 39 – 45, jan. 2004. 11, 12

[76] T. Schenk, P. Smulders, and E. Fledderus, "Estimation and compensation of TX and RX IQ imbalance in OFDM-based MIMO systems," *Radio and Wireless Symposium, 2006 IEEE*, pp. 215–218, Jan. 2006. 11, 109

[77] A. Tarighat and A. Sayed, "Joint compensation of transmitter and receiver impairments in OFDM systems," *Wireless Communications, IEEE Transactions on*, vol. 6, no. 1, pp. 240 –247, jan. 2007. 11

[78] A. Cantoni and J. Tuthill, "Digital compensation of frequency dependent imperfections in direct conversion i-q modulators," in *Proc. IEEE Int. Symp. Circuits and Systems ISCAS 2007*, 2007, pp. 269–272. 11, 12

[79] E. Lopez-Estraviz, S. De Rore, F. Horlin, and A. Bourdoux, "Pilot design for joint channel and frequency-dependent transmit/receive IQ imbalance estimation and compensation in OFDM-based transceivers," *ICC '07. IEEE International Conference on*, pp. 4861–4866, June 2007. 11, 108, 109, 110, 111, 118, 121, 132, 133

[80] L. Angrisani, M. D'Arco, and M. Vadursi, "Clustering-based method for detecting and evaluating I/Q impairments in radio-frequency digital transmitters," *Instrumentation and Measurement, IEEE Transactions on*, vol. 56, no. 6, pp. 2139 –2146, dec. 2007. 11, 12

[81] H. Lin, X. Zhu, and K. Yamashita, "Hybrid domain compensation for analog impairments in OFDM systems," *IEEE Global Telecommunications Conference (GLOBECOM'08)*, 2008. 11, 109, 142, 143, 144, 146, 153

[82] Y. Zou, M. Valkama, and M. Renfors, "Analysis and compensation of transmitter and receiver I/Q imbalances in space-time coded multiantenna OFDM systems," in *EURASIP Journal on Wireless Communications and Networking, vol. 2008, Article ID 391025*, 2008. 11, 109, 110, 133, 135, 138, 139

[83] E. K. S. Au, Z. Lei, and F. P. S. Chin, "Exploiting the diversity gain of transmitter i/q imbalance in single-antenna ofdm systems," *IEEE Global Telecommunications Conference, GLOBECOM 2009*, pp. 1 –5, nov. 2009. 11, 108, 109, 110

[84] M. de Noronha Neto, R. Souza, A. Barreto, and A. Cavalcante, "Exploiting I/Q imbalance in direct conversion transceivers for improving the performance of a V-BLAST OFDM

system," *IEEE 69th Vehicular Technology Conference, Spring 2009.*, pp. 1 –5, 26-29 2009. 11, 108, 109, 110

[85] B. Narasimhan, S. Narayanan, N. Al-Dhahir, and H. Minn, "Digital baseband compensation of joint TX/RX frequency-dependent I/Q imbalance in mobile MIMO-OFDM transceivers," *Information Sciences and Systems, 2009. CISS 2009. 43rd Annual Conference on*, pp. 545–550, March 2009. 11, 110

[86] H. Minn and D. Munoz, "Pilot designs for channel estimation of OFDM systems with frequency-dependent I/Q imbalances," *Wireless Communications and Networking Conference (WCNC'09)*, pp. 1–6, April 2009. 11, 110, 112, 113, 124

[87] S. A. Bassam, S. Boumaiza, and F. M. Ghannouchi, "Block-wise estimation of and compensation for i/q imbalance in direct-conversion transmitters," *IEEE Transactions on Signal Processing*, vol. 57, no. 12, pp. 4970–4973, 2009. 11, 12

[88] J. Luo, A. Kortke, and W. Keusgen, "Efficient self-calibration of frequency-dependent I/Q-imbalance in direct-conversion OFDM transceivers," in *Circuits and Systems, ISCAS 2009*, pp. 413–416. 11, 12, 108, 110

[89] H. Cao, A. Soltani Tehrani, C. Fager, T. Eriksson, and H. Zirath, "I/Q imbalance compensation using a nonlinear modeling approach," *IEEE Transactions on Microwave Theory and Techniques*, vol. 57, no. 3, pp. 513–518, 2009. 11, 12, 13, 16

[90] C.-J. Hsu and W.-H. Sheen, "Joint estimation and compensation of transmitter and receiver radio impairments in MIMO-OFDM receivers," in *Int. Sym. on Personal, Indoor and Mobile Radio Communications (PIMRC'09)*, 2009. 11, 109, 110, 142, 143, 144, 146, 169, 171

[91] A. Kiayani, L. Anttila, O. Myllari, and M. Valkama, "Prototype implementation and rf performance measurements of dsp based transmitter i/q imbalance calibration," in *Proc. 7th Int Communication Systems Networks and Digital Signal Processing (CSNDSP) Symp*, 2010, pp. 484–489. 11, 12, 13

[92] S. K. Mitra, *Digital Signal Processing - A Computer-Based Approach*, 2nd, Ed. McGraw-Hill, 2001. 17, 22

[93] D. G. Manolakis, V. K. Ingle, and S. M. Kogon, *Statistical and Adaptive Signal Processing*. Artech house, 2005. 27, 48

[94] H. Gazzah, P. Regalia, and J.-P. Delmas, "Asymptotic eigenvalue distribution of block Toeplitz matrices and application to blind SIMO channel identification," in *Information Theory, IEEE Transactions on*, vol. 47, no. 3, mar 2001, pp. 1243 –1251. 29, 30

[95] F. Neeser and J. Massey, "Proper complex random processes with applications to information theory," *Information Theory, IEEE Transactions on*, vol. 39, no. 4, pp. 1293–1302, Jul 1993. 29, 189

[96] E. A. Lee and D. G. Messerschmitt, *Digital Communication*, 2nd ed. Kluwer, 1994. 29

[97] J. G. Proakis, *Digital Communications*. McGraw-Hill, 1983. 29, 49, 181, 189, 190

[98] ——, *Algorithms for Statistical Signal Processing*. Prentice Hall, 2002. 35

[99] M. Windisch and G. Fettweis, "Standard-independent I/Q imbalance compensation in ofdm direct-conversion receivers." Dresden, Germany: Proc. 9th Intl. OFDM Workshop (InOWo), September 2004, pp. 57–61. 37

[100] V. Jungnickel, V. Pohl, S. Nonnig, and C. von Helmolt, "A physical model of the wireless infrared communication channel," *Selected Areas in Communications, IEEE Journal on*, vol. 20, no. 3, pp. 631–640, Apr 2002. 81

[101] C. Zhu, Y. Kim, O. Aboul-magd, and C. Ngo, "Multi-user support in next generation wireless LAN," in *Consumer Communications and Networking Conference (CCNC), 2011 IEEE*, jan. 2011, pp. 1120 –1121. 82

[102] "IEEE standard for local and metropolitan area networks part 16: Air interface for fixed broadband wireless access systems," *IEEE Std 802.16-2004 (Revision of IEEE Std 802.16-2001)*, 2004. 84, 86

[103] P. Silva and R. Dinis, "Frequency-domain multiuser detection for CP-assisted DS-CDMA signals," *Vehicular Technology Conference, 2006. VTC 2006-Spring. IEEE 63rd*, vol. 5, pp. 2103–2108, 7-10 May 2006. 86, 87, 173, 174, 175, 181, 184

[104] L. Nuaymi, *WiMAX Technology for Broadband Wireless Access*. Wiley, 2007. 86

[105] S. M. Alamouti, "A simple transmit diversity technique for wireless communications," *IEEE J. Select. Areas Commun.*, vol. 16, no. 8, Oct. 1998. 88, 89

[106] M. Peter, W. Keusgen, and A. Kortke, "Measurement and analysis of the 60 GHz invehicular broadband radio channel." Baltimore, USA: 66th Vehicular Technology Conference, VTC'07-Fall, 2007. 89, 91, 92, 101, 102, 157

[107] E. P. Lawrey, "Adaptive techniques for multiuser OFDM," Ph.D. dissertation, School of Engineering, James Cook University, Dec. 2001. 93, 95

[108] S. Brandes, I. Cosovic, and M. Schnell, "Reduction of out-of-band radiation in OFDM systems by insertion of cancellation carriers," *Communications Letters, IEEE*, vol. 10, no. 6, pp. 420–422, June 2006. 93

[109] I. Cosovic, S. Brandes, and M. Schnell, "Subcarrier weighting: a method for sidelobe suppression in OFDM systems," *Communications Letters, IEEE*, vol. 10, no. 6, pp. 444–446, June 2006. 93

[110] I. Cosovic and T. Mazzoni, "Suppression of sidelobes in OFDM systems by multiple-choice sequences," *Eur. Trans. Telecomms.*, vol. 17, pp. 623–630, 2006. 93

[111] H. Mahmoud and H. Arslan, "Sidelobe suppression in OFDM-based spectrum sharing systems using adaptive symbol transition," *Communications Letters, IEEE*, vol. 12, no. 2, pp. 133–135, February 2008. 93, 95

[112] M. Feuerstein, K. Blackard, T. Rappaport, S. Seidel, and H. Xia, "Path loss, delay spread, and outage models as functions of antenna height for microcellular system design," *Vehicular Technology, IEEE Transactions on*, vol. 43, no. 3, pp. 487–498, Aug 1994. 96, 98

[113] B. Razavi, "Design considerations for direct-conversion receivers," *Circuits and Systems II: Analog and Digital Signal Processing, IEEE Transactions on*, vol. 44, no. 6, pp. 428 –435, jun 1997. 106

[114] M. Valkama, M. Renfors, and V. Koivunen, "Compensation of frequency-selective I/Q imbalances in wideband receivers: models and algorithms," *SPAWC '01, 2001 IEEE*, pp. 42–45, 2001. 108, 113

[115] G. Xing, M. Shen, and H. Liu, "Frequency offset and I/Q imbalance compensation for ofdm direct-conversion receivers," *Int. Conf. on Acoustics, Speech, and Signal Processing (ICASSP'03)*, 6-10 2003. 108, 142, 143

[116] S. De Rore, E. Lopez-Estraviz, F. Horlin, and L. Van der Perre, "Joint estimation of carrier frequency offset and IQ imbalance for 4G mobile wireless systems," *Int. Conf. on Communications (ICC'06)*, 2006. 108, 142, 143, 149, 150

[117] H. Lin, X. Zhu, and K. Yamashita, "Pilot-aided low-complexity CFO and I/Q imbalance compensation for OFDM systems," *ICC'08, IEEE International Conference on*, pp. 713 –717, 19-23 2008. 108, 142, 143, 144, 146

[118] C.-J. Hsu, R. Cheng, and W.-H. Sheen, "Joint least squares estimation of frequency, DC Offset, I-Q imbalance, and channel in MIMO receivers," *Vehicular Technology, IEEE Transactions on*, vol. 58, no. 5, pp. 2201 –2213, jun 2009. 108, 142, 143

[119] L. L. Jr., M. Kurosaki, and H. Ochi, "Low complexity compensation of frequency dependent I/Q imbalance and carrier frequency offset for direct conversion receivers," in *International Symposium on Circuits and Systems (ISCAS'10)*, Paris, France, 2010. 108, 142, 143

[120] Y.-H. Chung and S.-M. Phoong, "Joint estimation of I/Q imbalance, CFO and channel response for MIMO OFDM systems," *Communications, IEEE Transactions on*, vol. 58, no. 5, pp. 1485 –1492, May 2010. 108, 142, 143

[121] J. Gao, X. Zhu, H. Lin, and A. Nandi, "Independent component analysis based semi-blind I/Q imbalance compensation for MIMO ofdm systems," *Wireless Communications, IEEE Transactions on*, vol. 9, no. 3, pp. 914 –920, march 2010. 108, 109, 110

[122] S. Harada and R. Prasad, *Multicarrier techniques for 4G mobile communications*. Artech house, 2003. 108

[123] C.-J. Hsu and W.-H. Sheen, "Compensation of cascaded radio impairments in MIMO-OFDM systems with direct-conversion architecture," in *Global Mobile Congress (GMC)*, 2010. 108, 109, 142, 143, 144, 146, 155, 158, 159, 165, 169, 201

[124] Y. Zou, M. Valkama, and M. Renfors, "Compensation of frequency-selective I/Q imbalances in space-time coded multi-antenna OFDM systems," *ISCCSP. 3rd International Symposium on*, March 2008. 108, 109, 110, 112, 113, 114, 133, 135, 138, 139

[125] D. Munoz and H. Minn, "Pilot designs with guard bands for channel estimation of MIMO OFDM systems with frequency-dependent i/q imbalances," *IEEE, Vehicular Technology Conference Fall (VTC'09-Fall)*, pp. 1 –5, 20-23 2009. 108, 109, 110, 111, 113, 116, 117, 118, 132, 138, 139, 142

[126] H. Minn and D. Munoz, "Effect of I/Q imbalance on pilot design for MIMO OFDM channel estimation," *IEEE Global Telecommunications Conference (GLOBECOM'09)*, pp. 1 –5, nov. 2009. 108, 109, 110, 111, 113, 116, 117, 118, 132, 138, 139, 142

[127] ——, "Pilot designs for channel estimation of MIMO OFDM systems with frequency-dependent I/Q imbalances," *IEEE Transactions on Communications*, vol. 58, no. 8, pp. 2252–2264, 2010. 108, 109, 110, 111, 113, 116, 117, 118, 132, 138, 139, 142

[128] R. Rao and B. Daneshrad, "I/Q mismatch cancellation for MIMO-OFDM systems," *PIMRC 2004*, vol. 4, pp. 2710–2714 Vol.4, Sept. 109, 110

[129] A. Tarighat and A. Sayed, "MIMO OFDM receivers for systems with IQ imbalances," *Signal Processing, IEEE Transactions on*, vol. 53, no. 9, pp. 3583–3596, Sept. 2005. 109, 110, 114, 140

[130] J. Gao, X. Zhu, H. Lin, and A. Nandi, "Kalman filtering based compensation for I/Q imbalance and CFO in time-varying MIMO OFDM systems," *Global Telecommunications Conference, 2009. GLOBECOM 2009. IEEE*, pp. 1 –6, nov. 2009. 109, 142, 143

[131] T. Schenk, P. Smulders, and E. Fledderus, "Estimation and compensation of frequency selective TX/RX IQ imbalance in MIMO OFDM systems," *ICC '06. IEEE*, vol. 1, pp. 251–256, June 2006. 109, 110

[132] J. Feigin and D. Brady, "Joint transmitter/receiver I/Q imbalance compensation for direct conversion OFDM in packet-switched multipath environments," *Signal Processing, IEEE Transactions on*, vol. 57, no. 11, pp. 4588 –4593, 2009. 109, 142

[133] D. Tandur and M. Moonen, "Digital compensation of RF imperfections for broadband wireless systems," in *Communications and Vehicular Technology in the Benelux, 2007 14th IEEE Symposium on*, nov. 2007, pp. 1 –5. 109

[134] ——, "Joint adaptive compensation of transmitter and receiver IQ imbalance under carrier frequency offset in OFDM-based systems," *Signal Processing, IEEE Transactions on*, vol. 55, no. 11, pp. 5246 –5252, nov. 2007. 109

[135] ——, "Compensation of RF impairments in MIMO OFDM systems," in *Int. Conf. on Acoustics, Speech and Signal Processing (ICASSP'08)*, Washington, USA, 2008. 109, 142, 143

[136] H. Kamata, K. Sakaguchi, and K. Araki, "An effective IQ imbalance compensation scheme for MIMO-OFDM communication system," *PIMRC05. IEEE 16th International Symposium on*, vol. 1, pp. 181–185, Sept. 2005. 110

[137] M. Cao and H. Ge, "I/Q imbalance mitigation for STBC MIMO-OFDM communication systems," *IEEE International Conference on, ICASSP'08*, pp. 3093–3096, 31 2008-April 4 2008. 110

[138] B. Narasimhan, D. Wang, S. Narayanan, N. Al-Dhahir, and H. Minn, "Digital baseband compensation for mobile SFBC-OFDM systems with receiver I/Q imbalance," *Global Telecommunications Conference (IEEE GLOBECOM'08)*, pp. 1–5, 30 2008-Dec. 4 2008. 110

[139] Y. Shen and E. Martinez, *Channel Estimation in OFDM Systems*, application note ed., Freescale Semiconductor, 2006. 110, 128, 135, 138

[140] M. Morelli and U. Mengali, "A comparison of pilot-aided channel estimation methods for OFDM systems," *Signal Processing, IEEE Transactions on*, vol. 49, no. 12, pp. 3065–3073, Dec 2001. 111, 117

[141] C. Suh, C.-S. Hwang, and H. Choi, "Preamble design for channel estimation in MIMO-OFDM systems," *GLOBECOM'03*, vol. 1, 2003. 111, 117, 118

[142] S. M. Kay, *Fundamentals of Statistical Signal Processing: Estimation Theory*. Prentice Hall, 1993. 111, 117

[143] P. Wolniansky, G. Foschini, G. Golden, and R. Valenzuela, "V-BLAST: an architecture for realizing very high data rates over the rich-scattering wireless channel," *ISSSE 1998 URSI*, pp. 295–300, Sep-2 Oct. 116

[144] E. De Carvalho and D. Slock, "Cramer-Rao bounds for semi-blind, blind and training sequence based channel estimation," *Signal Processing Advances in Wireless Communications, IEEE Workshop*, pp. 129 –132, apr 1997. 117

[145] H. Meyr, M. Moeneclaey, and S. A. Fechtel, *Digital Communication Receivers*. John Wiley & Sons, 1998. 117

[146] S. Song and A. Singer, "Pilot-aided OFDM channel estimation in the presence of the guard band," *Communications, IEEE Transactions on*, vol. 55, no. 8, pp. 1459 –1465, aug. 2007. 118

[147] S. Narahashi and T. Nojima, "New phasing scheme of n-multiple carriers for reducing peak-to-average power ratio," *Electronics Letters*, vol. 30, no. 17, pp. 1382–1383, Aug 1994. 119

[148] T. Schmidl and D. Cox, "Robust frequency and timing synchronization for ofdm," *Communications, IEEE Transactions on*, vol. 45, no. 12, pp. 1613–1621, Dec 1997. 125, 135

[149] M. Schellmann, V. Jungnickel, and C. von Helmolt, "On the value of spatial diversity for the synchronisation in MIMO-OFDM systems," *PIMRC'05, IEEE 16th International Symposium on*, vol. 1, pp. 201–205, Sept. 2005. 125, 127

[150] M. Peter, W. Keusgen, A. Kortke, and M. Schirrmacher, "Measurement and analysis of the 60 GHz in-vehicular broadband radio channel," *IEEE 66th VTC-2007 Fall.*, pp. 834–838, 30 2007-Oct. 3. 132

[151] G. Gil, I. hyun Sohn, Y. Lee, Y. I. Song, and J. K. Park, "Joint ml estimation of I/Q mismatch, DC offset, carrier frequency, and channel for direct-conversion receivers," in *Vehicular Technology Conference, 2003. VTC 2003-Spring. The 57th IEEE Semiannual*, vol. 4, april 2003, pp. 2348 – 2352 vol.4. 142

[152] J. Tubbax, A. Fort, L. Van der Perre, S. Donnay, M. Engels, M. Moonen, and H. De Man, "Joint compensation of IQ imbalance and frequency offset in OFDM systems," in *Global Telecommunications Conference, 2003. GLOBECOM '03. IEEE*, vol. 4, dec. 2003, pp. 2365 – 2369 vol.4. 142

[153] D. Falconer, S. Ariyavisitakul, A. Benyamin-Seeyar, and B. Eidson, "Frequency domain equalization for single-carrier broadband wireless systems," *Communications Magazine, IEEE*, vol. 40, no. 4, pp. 58–66, Apr 2002. 173

[154] A. Czylwik, "Synchronization for single carrier modulation with frequency domain equalization," *Vehicular Technology Conference, 1998. VTC 98. 48th IEEE*, vol. 3, pp. 2277–2281 vol.3, May 1998. 173

[155] F. Ling, "Matched filter-bound for time-discrete multipath Rayleigh fading channels," *Communications, IEEE Transactions on*, vol. 43, no. 234, pp. 710–713, Feb/Mar/Apr 1995. 173, 181

[156] P. Silva and R. Dinis, "Multiuser detection for the uplink of prefix-assisted DS-CDMA systems employing multiple transmit and receive antennas," *Vehicular Technology Conference, 2006. VTC-2006 Fall. 2006 IEEE 64th*, pp. 1–5, Sept. 2006. 173

[157] W. Wirtinger, "Zur formalen Theorie der Funktionen von mehr komplexen Vernderlichen," *Mathematische Annalen*, vol. 97:357-375, 1927. 175, 177, 180

[158] S. Alamouti, "A simple transmit diversity technique for wireless communications," *Selected Areas in Communications, IEEE Journal on*, vol. 16, no. 8, pp. 1451–1458, Oct 1998. 176

[159] S. Reinhardt, T. Buzid, and M. Huemer, "MIMO extensions for SC/FDE systems," *Wireless Technology, 2005. The European Conference on*, pp. 109–112, 3-4 Oct. 2005. 176

[160] A. Naguib, "On the matched filter bound of transmit diversity techniques," *Communications, 2001. ICC 2001. IEEE International Conference on*, vol. 2, pp. 596–603 vol.2, 2001. 181